On the role of surface rheology in a two-phase MHD flow

Jules Delacroix

UNIVERSITÉ GRENOBLE ALPES

THÈSE

Pour obtenir le grade de

DOCTEUR DE L'UNIVERSITÉ GRENOBLE ALPES

Spécialité : Mécanique des fluides, Procédés, Energétique

Arrêté ministériel : 7 août 2006

Présentée par

Jules DELACROIX

Thèse dirigée par Laurent DAVOUST

préparée au sein du Laboratoire de Sciences et Ingénierie des Matériaux et Procédés (SIMaP), groupe Elaboration par Procédés Magnétiques (EPM)
dans l'Ecole Doctorale Ingénierie-Matériaux Mécanique Energétique Environnement Procédés Production (I-MEP²)

Rôle de la rhéologie de surface dans un écoulement diphasique MHD.
On the role of surface rheology in a two-phase MHD flow.

Thèse soutenue publiquement le 14/12/2015,
devant le jury composé de :

M. Valéry BOTTON
Professeur, INSA Lyon, Rapporteur
M. Laurent DAVOUST
Professeur, Grenoble INP, Directeur de thèse
M. Eric GONCALVES DA SILVA
Professeur, Institut P' – ENSMA, Président
M. Alban POTHERAT
Professeur, Coventry University, Examinateur
M. Benoit SCHEID
Chercheur qualifié F.R.S-FNRS, Université libre de Bruxelles, Rapporteur

Acknowledgements

Mes premières pensées vont vers Laurent. Laurent Davoust est un personnage peu commun: son expertise, son professionnalisme, et son réel humanisme ont été d'un immense soutien. C'est grâce à lui que ce projet a été mis en place, que des points cruciaux ont pu être soulevés et débloqués, que ma motivation est restée sans faille. Un grand merci à toi Laurent: tu m'as (re)donné le virus de la science.

Je tiens à nommer ici tout particulièrement l'équipe technique d'EPM: Christian, Patrick, Benjamin, Gaby, Denis…ont tous concouru à la bonne réalisation de cette thèse. Mes chaleureux remerciements à tous.

J'ai également une pensée pour tout le reste du groupe EPM, spécialement le professeur Yves Fautrelle, Jacqueline Etay, Marianno, Guy, Khadija…et tous ceux que j'oublie de citer. Un grand merci à Jonathan Deseure, du LEPMI, pour sa gentillesse et sa disponibilité, et pour le prêt déterminant de matériel de mesure ultra-sensible. J'y adjoins également deux excellentes personnes et redoutables scientifiques, qui m'ont aidé plus d'une fois: Johannes et Etienne, merci à vous. Merci également à tous les stagiaires que j'ai pu encadrer: Guillaume, Elena, Emeline. Leur contribution à ce travail est loin d'être négligeable.

Merci à l'Etat français, qui m'a permis de mener à bien mes projets d'étude dans des conditions exceptionnelles.

Je souhaite exprimer toute ma gratitude au jury, pour sa patience lors de la lecture de ce manuscrit. Je tiens à remercier les professeurs Valery Botton et Benoit Scheid d'avoir accepté de rapporter sur ce mémoire.

Enfin, il est certaines personnes pour lesquelles les mots sont inutiles. A ma femme Janina, sans l'amour et le dévouement de laquelle cette aventure n'aurait aucun sens. A mon futur fils, Hugo, pour les moments de bonheur à venir. A ma mère Claire et à mon père Eric, pour leur amour et leur présence. A ma sœur Charlotte et à mon frère Hubert. A toute ma famille et ma belle-famille. A Mimine, Dune et Forest.

"All that is gold does not glitter."
J. R. R. Tolkien, The Lord of The Rings, The Fellowship of the Ring.

List of Figures

I.A.1 Typical stratified and dispersed flows 5
I.A.2 Fundamental stratified MHD flows 6
I.A.3 Industrial stratified MHD flows 7
I.A.4 Fundamental dispersed MHD flows 7
I.A.5 Industrial dispersed MHD flows: application to GEN-IV MSFR fission reactor 8
I.A.6 ITER, the world's largest Tokamak 9
I.A.7 Typical layout of MHD liquid/gas flow 10

I.B.1 The induction principle 12
I.B.2 The Hartmann flow 13
I.B.3 Slow viscous flow past spheres 15
I.B.4 Experimental techniques for determining surface tension γ . 16
I.B.5 The deep-channel surface viscometer 17
I.B.6 Experimental evidence of the interaction between oxidation and MHD 18
I.B.7 Gallium and Indium exchange rates 20
I.B.8 Interfacial tension of a gradually oxidising Galinstan sample 21
I.B.9 Gel behaviour and varying apparent bulk viscosity of gradually oxidising Galinstan sample 22

II.A.1 Electromagnetic force 35
II.A.2 Inlet/Outlet BCs 40
II.A.3 Interface oxidation and electromagnetic BCs 41

II.B.1 Gibbs (macroscale) and Guggenheim (microscale) view of a fluid interface 44
II.B.2 Definition of in-excess surface quantities 45
II.B.3 Interfacial tension and soap film 47
II.B.4 Surface shear viscosity 48
II.B.5 Surface dilatational viscosity 49

II.C.1 Overall mathematical coupling 53

III.A.1 The classical layout of the deep-channel surface viscometer . 58
III.A.2 Stokes flow and surface viscous shearing in the literature . . 61

III.A.3 Inertial effects and surface viscosities in the literature 63
III.A.4 The annular MHD viscometer 64

III.B.1 Subregions of the flow 68
III.B.2 Two-way coupling between the bulk and surface flows. . . . 71
III.B.3 $v^{\star}_{\theta S}(r^{\star})$ at various values of Ha and Bo_{η_S}. 84
III.B.4 Velocity and magnetic induction for two asymptotic cases . 86
III.B.5 Electric current density and Lorentz force density for two asymptotic cases 87
III.B.6 Line graphs of velocity and electric current with respect to various $(\mathrm{Ha}, \mathrm{Bo}_{\eta_S})$ values 89
III.B.7 Geometry and boundary conditions for 2-D numerical computation 93
III.B.8 Lubrication gaps of the annular MHD viscometer for tackling the boundary data discontinuity problem 95
III.B.9 2-D Mesh 96
III.B.10 Comparison between 2-D analytical and numerical results . 96
III.B.11 Consequences of the numerical treatment of boundary data discontinuity 97
III.B.12 Lower Ha-limit of agreement between analytical and numerical results 98

III.C.1 Geometry and boundary conditions for 2-D 1/2 numerical computation 103
III.C.2 2-D 1/2 Mesh 107
III.C.3 Numerical benchmark for the hydrodynamic 2-D ½ flow . . 108
III.C.4 Impact of varying surface rheology on the purely hydrodynamic 2-D ½ flow patterns 110
III.C.5 Analytical and numerical benchmark for the 2-D ½ modelling when neglecting inertial effects 112
III.C.6 Scaling law for the different flow regimes of the annular MHD viscometer 113
III.C.7 Azimuthal electric current, surface shear effect 115
III.C.8 Electric current density and MHD swirling flow: overall flow patterns linked to surface viscous shear 117
III.C.9 Velocity, Lorentz force density and MHD swirling flow: overall flow patterns, surface shear effect 118
III.C.10 Velocity, MHD swirling flow and counter-rotating vortex: surface dilatation effect 119
III.C.11 Curl of the centrifugal force and counter-rotating vortex . . 121
III.C.12 Azimuthal electric current, surface dilatation effect 121
III.C.13 Electric current density and MHD swirling flow: overall flow patterns linked to surface viscous dilatation 123
III.C.14 Velocity, Lorentz force density and MHD swirling flow: overall flow patterns, surface dilatation effect 124

III.D.1 CAD overview of Madip . . . 128
III.D.2 Photograph of Madip . . . 129
III.D.3 The annular viscometer of Madip . . . 129
III.D.4 Cross-sectional view of the annular channel . . . 130
III.D.5 CAD view of the gas circuit of Madip . . . 131
III.D.6 The gas panel of Madip . . . 132
III.D.7 The chemical reactor of Madip . . . 132
III.D.8 Instrumentation devoted to the gas circuit of Madip . . . 134
III.D.9 Electromagnet system of Madip . . . 135
III.D.10 Optical test-bench of Madip . . . 136
III.D.11 Instrumentation of Madip . . . 137
III.D.12 Glove-box and centrifuge used for preparing the alloy and the tracers . . . 137
III.D.13 Bubbler system configurations for argon sweeping and transferring galinstan . . . 138
III.D.14 Operating annular MHD viscometer and PTV technique . . . 139
III.D.15 Measurement of the liquid metal height in the annular channel of Madip . . . 140
III.D.16 HCl layer experiment . . . 142
III.D.17 Surface radial velocity data points for the HCl experiment . . . 143
III.D.18 Surface azimuthal velocity data points for the HCl experiment 144
III.D.19 Reactor experiment: picture of the partially oxidised interface 147
III.D.20 Surface azimuthal velocity data points and curve fitting for the reactor experiment, for Re=1351 . . . 149
III.D.21 Surface azimuthal velocity data points and curve fitting for the reactor experiment, for Re=4494 . . . 150
Concl. 1 Future prospects. . . . 156

D.1 Overall layout of the bubble MHD problem . . . 166
D.2 Equivalence between a bubble rising in a fluid at rest at its terminal velocity, and the flow past a stationary bubble . . . 167
D.3 Shape regimes map for bubbles and drops . . . 169
D.4 Flow past a sphere and drag force . . . 170
D.5 Stokes and Basset flow streamlines . . . 173
D.6 Steady wake behind rigid spheres . . . 174
D.7 Flow coefficients of a sphere at intermediate Re_p values . . . 175
D.8 Absence of wake for gaseous spheres at intermediate Re_p values 176
D.9 Flow confinement . . . 177
D.10 Drag correction due to flow confinement . . . 177
D.11 Structure of the MHD flow around a sphere when $Ha, N \gg 1$ 182
D.12 Typical MHD flow patterns past a sphere when $Ha, N \gg 1$. 185
D.13 Hunt's wake past a truncated cylinder . . . 188
D.14 Electric current streamlines for different MHD flows past obstacles . . . 189

D.15 Drag coefficients of spheres placed in a MHD flow: numerical and experimental results 190
D.16 Geometry and boundary conditions for the upcoming numerical simulations of the bubble MHD problem 191

E.1 Typical layout of eddy current method 198
E.2 Global electric circuit of Micmac 201
E.3 Some Micmac results 202

List of Tables

I.B.1 Bulk physical properties of Galinstan, compared to mercury 19

III.D.1 Dimensioning criteria 127
III.D.2 Surface viscous shear fitting values 148

Nomenclature

Symbol	Description	Unit
Units		
[A]	Ampère	
[°C]	Celsius degree	
[C]	Coulomb	
[F]	Farad	
[H]	Henry	
[K]	Kelvin	
[kg]	Kilogram	
[m]	Metre	
[mol]	Mol	
[N]	Newton	
[Ω]	Ohm	
[Pa]	Pascal	
[ppm]	Parts per million	
[px]	Pixel	
[rpm]	Rounds per minute	$[\mathrm{min}^{-1}]$
[S]	Siemens	
[s]	Second	
[T]	Tesla	
[Torr]	Torr	$[1.3 \times 10^2\,\mathrm{Pa}]$
[V]	Volt	

Chemistry

c	Molar concentration	$[\mathrm{mol{\cdot}L^{-1}}]$
pH	Hydrogen potential	[1]
x	Mass fraction	[ppm]

Electricity

L	Inductance	[H]
N	Number of turns	[1]
Φ	Magnetic flux	$[\mathrm{T{\cdot}m^2}]$
R	Electric resistance	[Ω]
τ	Eddy-current time constant (Micmac experiment)	[s]
V	Voltage	[V]

Electromagnetism

$\vec{A}$	Magnetic vector potential	$[\mathrm{T{\cdot}m}]$
A	Typical magnetic vector potential	$[\mathrm{T{\cdot}m}]$
$\vec{B}$	Magnetic field	[T]
$\vec{b}$	Magnetic induction	[T]
$\vec{B}_{\mathrm{ext}}, \vec{B}_0$	External magnetic field	[T]
b	Typical magnetic induction	[T]
B, B	Typical magnetic field	[T]
$\vec{E}$	Electric field	$[\mathrm{V{\cdot}m^{-1}}]$
E	Typical electric field	$[\mathrm{V{\cdot}m^{-1}}]$
e	Electromotive force	[V]
ϵ	Electric permittivity	$[\mathrm{F{\cdot}m^{-1}}]$
$\vec{F}_{\mathrm{em}}$	Electromagnetic force	[N]
$\vec{f}_{\mathrm{em}}$	Electromagnetic force density	$[\mathrm{N{\cdot}m^{-3}}]$
$\vec{f}_{\mathrm{L}}$	Lorentz force density	$[\mathrm{N{\cdot}m^{-3}}]$

f_{L}	Typical Lorentz force density	[N·m^{-3}]
$\vec{j}$	Electric current density	[A·m^{-2}]
J, J	Typical electric current density	[A·m^{-2}]
μ	Magnetic permeability	[H·m^{-1}]
Φ	Typical electric potential	[V]
ϕ	Electric potential	[V]
ψ	Elsasser variable	[1]
Q	Electric point charges	[C]
q	Electric charge density	[C·m^{-3}]
σ	Electrical conductivity	[S·m^{-1}]
τ_r	Electric charge relaxation time	[s]
τ_t	Electromagnetic field transit time	[s]
$\vec{u}$	Electric point charge velocity	[m·s^{-1}]

Fluid Mechanics

α	Axial angular momentum	[m^2·s^{-1}]
β	Sliding friction coefficient	[Pa·s·m^{-1}]
β	Slip length coefficient	[m]
C_d	Drag coefficient	[1]
$\vec{F}_d$	Drag force	[N]
η	(Bulk) dynamic viscosity	[Pa·s]
$\vec{F}$	Force	[N]
$\vec{f}$	Force (volume) density	[N·m—3]
$\vec{g}$	Gravity	[N]
l_c	Capillary length	[m]
L_w	Length of the recirculation area (bubble wake)	[m]
Ω	Angular speed	[rad·s^{-1}]
ω	Vorticity field	[s^{-1}]
$\overline{p}, p$	Pressure, pressure corrected by gravity	[Pa]

P	Typical pressure	[Pa]
ψ	Spherical stream function	$[m^3 \cdot s^{-1}]$
Q	Flow-rate	$[m^3 \cdot s^{-1}]$
ρ	Density	$[kg \cdot m^{-3}]$
$\overrightarrow{\overrightarrow{T}}$	Bulk mechanical stress tensor	[Pa]
$\vec{v}$	Velocity field	$[m \cdot s^{-1}]$
V, V	Typical velocity	$[m \cdot s^{-1}]$
W	Mechanical work	[J]

Surface Rheology

div_S	(Scalar) Surface divergence operator	$[m^{-1}]$
$\overrightarrow{\mathrm{div}}_S$	(Vector) Surface divergence operator	$[m^{-1}]$
η_S	Surface shear viscosity	$[kg \cdot s^{-1}]$
$\vec{f}_S$	Force (surface) density	$[N \cdot m^{-2}]$
γ	Surface tension	$[N \cdot m^{-1}]$
$\overrightarrow{\overrightarrow{\mathrm{grad}}}_S$	(Matrix) Surface gradient operator	$[m^{-1}]$
$\overrightarrow{\overrightarrow{I_S}}$	Surface projection tensor	[1]
$\varkappa_S$	Surface dilatational viscosity	$[kg \cdot s^{-1}]$
ρ_S	Surface density	$[kg \cdot m^{-2}]$
$\overrightarrow{\overrightarrow{T_S}}$	Surface mechanical stress tensor	$[N \cdot m^{-1}]$
$\vec{v}_S$	Surface velocity field	$[m \cdot s^{-1}]$

Heat Transfer

T	Temperature	[K] or [°C]

Geometry

ATL, ATR, ABL, ABR	Bottom and/or top left and/or right, adjacent regions	
C	(Flow) Core region	
$(O, \vec{e}_x, \vec{e}_y, \vec{e}_z)$	Cartesian system of coordinates	

χ	Aspect ratio	[1]
$(O,\vec{e}_n$ or $\vec{n},\vec{e}_s,\vec{e}_t)$	Curvilinear system of coordinates (normal, tangential 1, tangential 2)	
$(O,\vec{e}_r,\vec{e}_\theta,\vec{e}_z)$	Cylindrical system of coordinates	
d	Bubble diameter	[m]
R	Bubble radius	[m]
δ	Typical boundary layers thickness; annular channel bottom gap	[m]
e	Typical oxide layer thickness	[m]
h	Annular channel height	[m]
HB, HT	Bottom or Top Hartmann layers	
IC	Corner regions	
L	Typical scale length; duct half-height	[m]
λ	Blockage ratio $d/2L$	[1]
n	Curvilinear (normal) n-coordinate	[m]
φ	Spherical φ-coordinate	[° or rad]
r	Cylindrical or spherical r-coordinate	[m]
r_i	Annular channel inner radius	[m]
r_o	Annular channel outer radius	[m]
S	Interfacial region	
s	Curvilinear (tangential) s-coordinate	[m]
SL, SR	Left or Right Shercliff layers	
$(O,\vec{e}_r,\vec{e}_\theta,\vec{e}_\varphi)$	Spherical system of coordinates	
t	Curvilinear (tangential) t-coordinate	[m]
θ	Cylindrical or spherical θ-coordinate	[° or rad]
x	Cartesian x-coordinate	[m]
x	Curvilinear ξ-coordinate	[m]
y	Cartesian y-coordinate	[m]
z	Cartesian or cylindrical z-coordinate	[m]
ζ	Curvilinear ζ-coordinate	[m]

Dimensionless numbers

Bo_{η_S}	Surface shear Boussinesq number ($=\frac{\eta_S}{\eta L}$)	[1]
$\mathrm{Bo}_{\varkappa_S}$	Surface dilatation Boussinesq number ($=\frac{\varkappa_S}{\eta L}$)	[1]
Eo	Eötvös number ($=\frac{\rho g d^2}{\gamma}$)	[1]
Ha	Hartmann number ($=B_0 L\sqrt{\frac{\sigma}{\eta}}$)	[1]
$\mathrm{Ha_p}$	Particulate Hartmann number ($=\frac{B_0 d\sqrt{\sigma}}{\sqrt{\eta}}$)	[1]
Mo	Morton number ($=\frac{\eta^4 \rho g}{\rho^2 \gamma^3}$)	[1]
N	Stuart number ($=\frac{\mathrm{Ha}^2}{\mathrm{Re}}$)	[1]
$\mathrm{N_p}$	Particulate Stuart number ($=\frac{\mathrm{Ha_p}^2}{\mathrm{Re_p}}$)	[1]
Re	Reynolds number ($=\frac{\rho V L}{\eta}$)	[1]
$\mathrm{Re_p}$	Particulate Reynolds number ($=\frac{\rho V d}{\eta}$)	[1]
Rm	Magnetic Reynolds number ($=\mu\sigma V L$)	[1]
R_ω	Shielding parameter ($=\frac{\mu\sigma L^2}{\tau}$)	[1]

Mathematics

*,*	Dimensionless notations	
*	Mathematical adjoint notation	
$\mathscr{I}$	Modified Bessel function of the first kind	
$\mathscr{J}$	Bessel function of the first kind	
$\mathscr{K}$	Modified Bessel function of the second kind	
$\mathscr{Y}$	Bessel function of the second kind	
cosh	Hyperbolic cosine function	
$\times$	Cross product	
$\overrightarrow{\mathrm{curl}}$	Curl operator	$[\mathrm{m}^{-1}]$
d	Differentiation operator	
δ	Inexact differentiation operator	
∂	Partial differentiation operator	

$\Im$	Differential operator	
div	(Scalar) Divergence operator	$[m^{-1}]$
$\overrightarrow{\text{div}}$	(Vector) Divergence operator	$[m^{-1}]$
$f, g, h \ldots$	Arbitrary mathematical functions	
G	Green function	
$\overrightarrow{\text{grad}}$	(Vector) Gradient operator	$[m^{-1}]$
$\Longrightarrow$ grad	(Matrix) Gradient operator	$[m^{-1}]$
$\overrightarrow{I}$	Identity tensor	[1]
$\int$	Integral	
Δ	(Scalar) Laplacian operator; local difference operator	$[m^{-2};1]$
$\vec{\Delta}$	(Vector) Laplacian operator	
$\| \|$	Euclidean norm	
$O()$	Landau big O notation	
$o()$	Landau little o notation	
∂	Partial differential operator	
$\bullet$	Ordinary matrix product	
$\cdot$	Scalar product	
$\otimes$	Tensor product	
$\mathbb{R}^3$	Real space	
S	Control surface	$[m^2]$
sinh	Hyperbolic sine function	
$\sum$	Sum	
$\Rightarrow$	Tensor notation	
tr	Matrix trace	
$\top$	Transpose operator	
$\oplus$	Subspace mathematical union	
V	Control volume	$[m^3]$
$\rightarrow$	Vector notation	

Other notations

AC	Alternating Current	
App.	Appendix	
Ba	Basset solution	
BC	Boundary Condition	
Br	Branover solution	
CAD	Computer-aided design	
Chap.	Chapter	
Clift	Clift solution	
Co	Couette solution	
Cst	Constant notation	
CPU	Central processing unit	
Da	Davoust solution	
DC	Direct Current	
DNS	Direct Numerical Simulation	
Ed	Edwards solution	
ϵ	Mean absolute error	[1]
Eq.	Equation	
Exp.	Experimental	
Fig.	Figure	
GEN-IV	Fourth generation of nuclear power plants	
Gotoh	Gotoh solution	
HL	Hirsa Lopez solution	
Hunt	Hunt solution	
ITER	International Thermonuclear Experimental Reactor	
Madip	*Magnétohydrodynamique diphasique*	
MHD	Magnetohydrodynamics	
Micmac	*Mesure inductive de la conductivité des matériaux (électro)conducteurs*	

MSFR	Molten-Salt Fast-Spectrum Reactor	
TBM	Test-Blanket Modules	
MS	Mannheimer Shechter solution	
ODE	Ordinary Differential Equation	
$\boldsymbol{P}$	Generic physical property	
PDE	Partial Differential Equation	
POM	Polyoxymethylene	
Ψ	Amount of $\boldsymbol{P}$ in a given volume	
ψ	Amount of $\boldsymbol{P}$ per unit volume	
PTV	Particle Tracking Velocimetry	
R&D	Research and Development	
Reitz	Reitz solution	
Sec.	Section	
Sh	Shercliff solution	
St	Stokes solution	
t	Time	[s]
Tab.	Table	
τ	Typical time	[s]
VOF	Volume of fluid numerical method	
Wham	Wham solution	

Contents

Acknowledgements iii

List of figures iv

List of tables viii

Nomenclature ix

Contents xviii

I Introduction 1

I.A Of electroconductive multiphase flows 5

I.A.1 Stratified and dispersed flows 5

I.A.2 (Re-)considering the MHD/interface interactions 9

I.B MHD/Surface rheology: enhancing an original coupling 11

I.B.1 Two well-known but distinct fields 11

I.B.2 The choice of Galinstan as working fluid 18

I.C Bridging the gap between MHD and surface rheology 23

I.C.1 Overall approach 23

I.C.2 Main assumptions 24

I.C.3 Outlines 25

II Fundamentals 27

II.A Introduction to magnetohydrodynamics 29

II.A.1 Review of electromagnetism in an electroconductive fluid . . . 29

II.A.2 Review of electroconductive fluid mechanics. 35

II.A.3 Initial and boundary conditions 37

II.B Introduction to surface rheology **43**

II.B.1 From the microscale to the macroscale view of a fluid interface . 43

II.B.2 Interfacial transport of momentum 46

II.C Strong coupling **53**

III Surface rheology and stratified MHD flow: the annular MHD viscometer **55**

III.A Physical outlines of the annular MHD viscometer **57**

III.A.1 The hydrodynamic annular viscometer: state-of-the-art 57

III.A.2 The annular MHD viscometer: an original layout 64

III.B 2-D annular MHD flow and surface viscous shearing **67**

III.B.1 2-D analytical study of the annular MHD viscometer 67

III.B.2 2-D numerical study of the annular MHD viscometer 92

III.B.3 Conclusion: what about inertia? 98

III.C 2-D $^1/_2$ topology of the MHD viscometer: inertia and surface dilatation **101**

III.C.1 Physical modelling and numerical implementation 101

III.C.2 Results and interpretations 107

III.C.3 Conclusion and final scaling laws towards the experimental test-bench 125

III.D MHD and surface viscosities: Madip, first experimental investigations **126**

III.D.1 Scaling laws for dimensioning the experimental set-up 126

III.D.2 Instrumentation and technical developments. 126

III.D.3 Experimental protocol 136

III.D.4 First experimental campaigns: qualitative/quantitative results . . 141

Conclusion **153**

Appendices 157

A Mannheimer and Schechter's modelling of the annular channel viscometer 159

B Davoust and Huang's modelling of the annular channel viscometer 161

C Shercliff's modelling of the MHD flow in a square duct 163

D A first approach to bubble MHD 165

D.1 Motivation, physical issues and assumptions for the bubble MHD problem . . . 165

D.2 Hydrodynamic flow past a sphere: state-of-the-art . . . 172

D.3 MHD flow around an obstacle in the presence of a transverse magnetic field . . . 180

D.4 Some hints at the numerical implementation of the bubble MHD problem . . . 191

E Electrical conductivity of liquid metals: the Micmac experiment 197

E.1 Motivation and state-of-the-art . . . 197

E.2 The Micmac experiment . . . 201

References 203

Bibliography 211

Publications and conferences 212

Part I

Introduction

AMONG *the numerous media involved in human activities, the electroconductive media (including metals) are given a prominent place. They are ubiquitous. Construction industry, power plants, car industry, aeronautics, aerospace industry…every single human activity bears, at some point of a given process or another, on the ability of a given medium to carry electricity.*

The best-known electroconductive media are metals. Extracted from the earth's crust, they are melted, purified, quenched, manufactured at will. Their electrical, thermal, mechanical properties are hardly matched. They are mostly used at solid state, their most common state at room temperature. However, their aforementioned interesting physical properties relies heavily on the way metals are processed at liquid state, during the smelting process, in the blast furnaces. Besides, there are numerous applications where liquid metals are directly used, for instance, as reference fluids in fundamental magnetohydrodynamic experiments, or as coolants for future nuclear power plants in the nuclear industry. Thus, improving scientific knowledge on the liquid state of metals meets both fundamental and industrial concerns.

Let us consider a metal at its liquid state. A majority of metals has a special affinity with oxygen, so that solid particles made of metallic oxides may exist either in the liquid bath, or at an hypothetical interface between the liquid metal and a gaseous phase. The latter may surround the liquid bath (working atmosphere for free surface layouts). Gaseous pockets can also be included inside the metal, either involuntarily (accidental boiling, trapped gas), or on purpose (bubble injection). As such, a metallic bath may form an heterogeneous medium, where liquid, solid and gaseous phases coexist. When put in motion, a liquid metal flow may therefore constitute an electroconductive multiphase flow.

One outstanding feature of electroconductive flows is that they can be driven by means of an outer magnetic field. Magnetohydrodynamics (MHD) covers those phenomena where the velocity and the magnetic fields are coupled. Because of this interaction, an electromagnetic force appears (called the Lorentz force) strongly influencing the fluid flow. Besides, in MHD, and contrary to classical hydrodynamics, the role of boundary layers is particularly enhanced. They indeed govern directly the electromagnetic force, and as such, they are able to influence actively *the core-flow, modifying it by an order of magnitude, depending on the electrical nature of the boundary conditions.*

The MHD of single-phase flows has been extensively studied. However, as far as MHD multiphase flows are concerned, several issues arise due to the heterogeneous aspect of the considered medium. More particularly, the critical role played by the boundary layers in MHD questions the relevance of the modelling of MHD boundary conditions. For instance, the electrical and mechanical behaviour of a liquid/gas interface may evolve according to its level of purity, i.e. *its state of oxidation for liquid metals. A gradually oxidising interface might in turn strongly impact the MHD bulk flow, leading to a variety of MHD flow patterns. This critical issue leads to the guiding principle of this PhD work.*

How does the alteration of the behaviour of a liquid metal/gas interface, through oxidation processes, may affect a supporting MHD bulk flow?

Undoubtedly, this common thread arouses a lot of resulting issues: how to model a liquid metal/gas interface? What are the surface properties characterising this interface?

Can we measure them? And how to relate them to a MHD bulk flow? All these questions show the necessity to highlight the interactions between MHD and the field of science that studies the mechanical properties of fluid interfaces, i.e. *surface rheology. As a consequence, we shall consistently emphasize the original coupling between MHD and surface rheology in this study. This coupling constitutes a background step towards multiphase MHD.*

This first part constitutes the general introduction to this coupling issue. The fundamental and industrial applications potentially affected are emphasised. Then, the originality of the coupling between MHD and surface rheology is highlighted, the state-of-the-art being surprisingly reduced to its smallest portion. Afterwards, the selection of the model liquid metal, i.e. *the eutectic alloy called Galinstan, is justified. Finally, the outlines of this work are unveiled, along with the overall methodology.*

I.A Of electroconductive multiphase flows

Modelling of MHD multiphase flows has recently become an issue of major interest, given the fundamental and industrial applications potentially affected. This chapter recapitulates some of these applications, introducing a first distinction between stratified and dispersed flows. Then, the focus is put on a typical layout of a MHD liquid/gas flow, which allows us to highlight the interest of (re)considering the interactions between a gradually oxidising interface and a bulk MHD flow.

I.A.1 Stratified and dispersed flows

Basically, there are two asymptotic cases considering the topology of multiphase flows: the so-called *stratified* and *dispersed* topologies. They cover two distinct classes of multiphase flow layouts: those where, *e.g.*, the liquid and gaseous phases individually form homogeneous media separated by a unique interface, corresponding to the stratified layout; and those where the two phases are mingled, with the existence of more or less large inclusions, depending on the prevailing phase, corresponding to the dispersed layout. Two typical examples are (stratified) free surface and (dispersed) bubbly flows, as illustrated in Fig. I.A.1. Such a distinction is not meaningless: MHD multiphase processes often involve one or the other kind of flows. Let us first focus on a set of stratified MHD flows, and the associated fundamental and industrial issues.

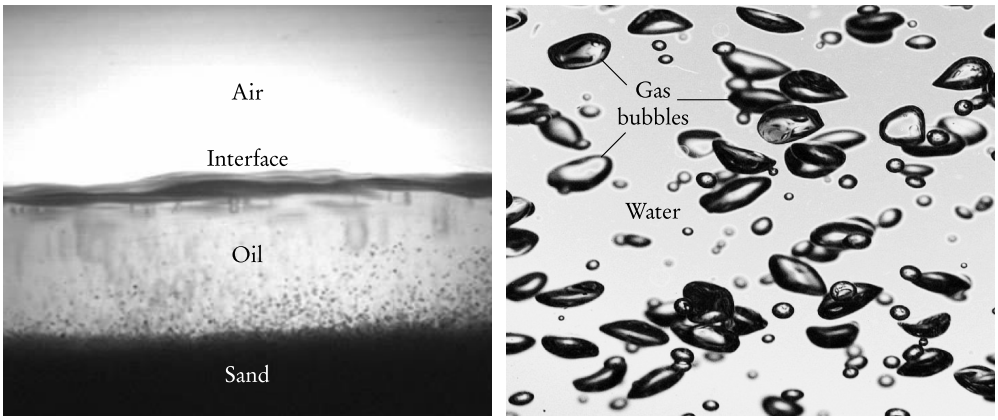

(a) – Oil/Air stratified flow, on a sand bed [1]. **(b)** – Water/Gas bubbly flow [2].

Figure I.A.1 – Typical stratified and dispersed flows.

I.A.1.a Stratified MHD flows

Stratified MHD flows are historically at the root of fundamental MHD. One of the first laboratory experiments carried out using mercury indeed consisted of a mercury free-surface bath, entrained by a rotating annular strong magnet [3], as shown in Fig. I.A.2(a). The conclusions of these experiments "clarified and stimulated research in MHD" for the following decades, about such concepts as "analogies between MHD and rotating fluids or two-dimensional flow structures" [4]. Over the past few years, such stratified flows have received growing attention, in link with the fundamental study of the interactions between the bulk MHD flow and an oxidising surface (see *e.g.* [5]) as displayed in Fig. I.A.2(b). We shall go back later on this particular point.

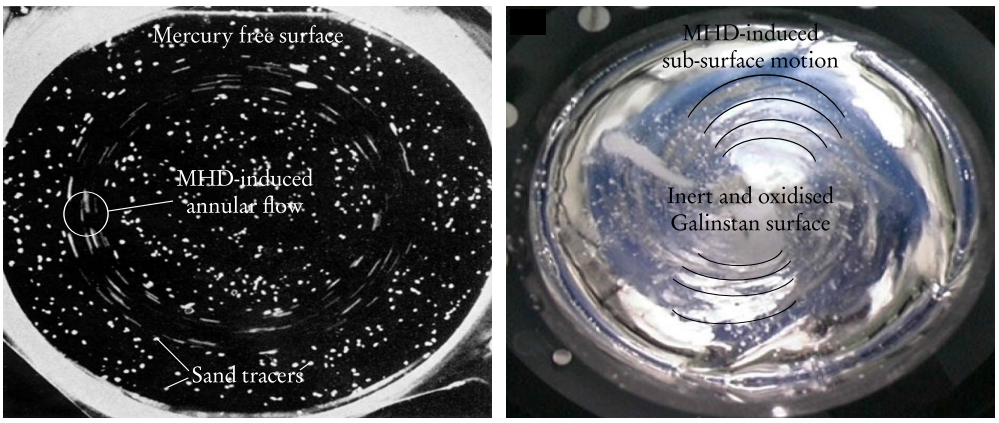

(a) – Experimental evidence of the electromagnetic blocking [3].

(b) – Galinstan (eutectic metallic alloy) oxide layer and MHD swirling flow [5].

Figure I.A.2 – Fundamental stratified MHD flows.

In the industry, magnetic fields are often used in the processing of liquid metals to dampen unwanted fluid motion at free surfaces, or stir the liquid in a contactless way. The best-known illustration of such industrial stratified MHD flows is the so-called cold crucible induction melting process, presented in Fig. I.A.3. By means of an alternating current (AC) flowing through an inductor, eddy currents are induced in the sectored crucible, and then in the metallic load. This allows both for heating (Joule heating) and stirring (Lorentz force) the melting metal. After quenching, a typical dome-shaped surface is found at the metal/air interface, due to electromagnetic pressure, as seen in Fig. I.A.3(b). Some patches of metallic oxides can be noted. One of the aim of the electromagnetic stirring is to make these oxides adsorb preferentially at the interface during the smelting process, to reach the highest purity inside the ingot.

I.A.1.b Dispersed MHD flows

The MHD of dispersed flows has recently become a leading fundamental issue, given the growing number of publications related to this particular topic. Two cases must be distinguished, corresponding either to the case of a gaseous phase surround-

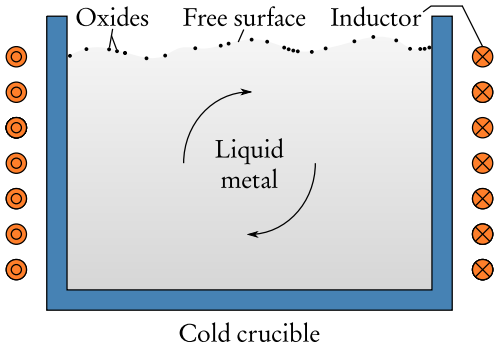

(a) – Cold crucible induction melting principle.

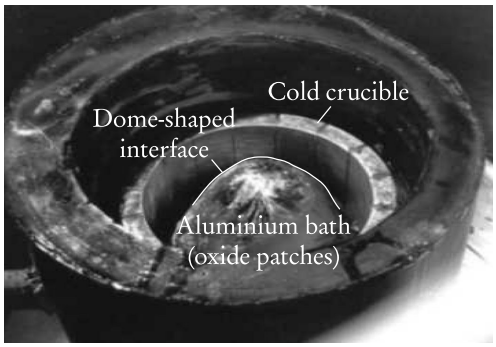

(b) – Photograph of the dome-shaped oxidised surface of an aluminium bath, under the influence of an AC field [6].

Figure I.A.3 – Industrial stratified MHD flows.

ing metallic droplets, or to the case of gaseous inclusions suspended into a supporting liquid metal flow. The first case can be illustrated by the fundamental issue of electromagnetic levitation by means of the Lorentz force [6], as shown in Fig. I.A.4(a). The non-spherical shape of the levitating droplet is due to the balance between repulsive electromagnetic pressure (prevailing near the inductors) and capillary effects (prevailing in the gap). In addition to the stratified layouts previously exposed, this fundamental application is another occurrence of the competition between surface properties and bulk MHD. The second case encompasses the MHD of bubbly flows inside liquid metals. In Fig. I.A.4(b), the typical electric current density distribution around an Argon bubble rising in Galinstan (eutectic alloy) is numerically investigated by means of direct numerical simulation (DNS).

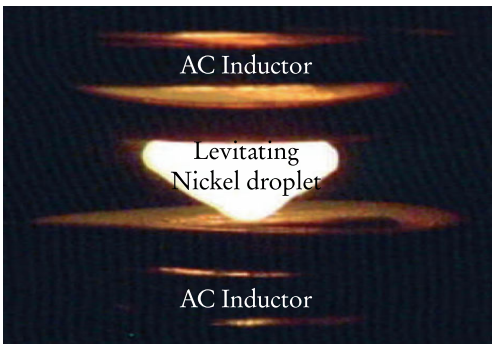

(a) – Electromagnetic levitation of a Nickel droplet [6].

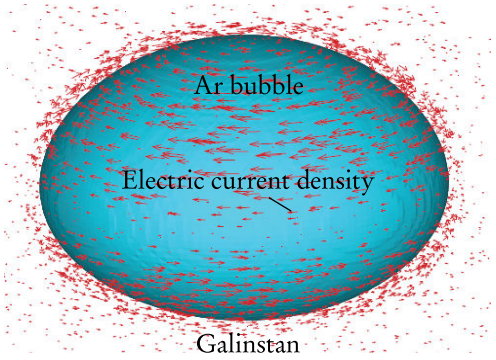

(b) – Direct numerical simultion of the MHD of a single gas bubble suspended into Galinstan. Arrows: electric current density distribution [7].

Figure I.A.4 – Fundamental dispersed MHD flows.

From the industrial point of view, the MHD of dispersed flows may become a critical issue in the next few years, especially in the nuclear industry. In view of the

fourth generation (GEN-IV) of nuclear power plants, the concept of molten-salt fast-spectrum reactors (MSFR) has been proposed, of which a conceptual design is displayed in Fig. I.A.5(a) (see [8]). The Thorium-based fuel must be retreated and recycled, essentially for corrosion reasons. An original on-line extraction method consists in capturing the fission products (metallic particles or gaseous products), either by diffusion in He bubbles, or adsorption at the surface of these bubbles, injected inside the deprecated salt. In parallel, an electromagnetic device for interface melting and stirring of two-phase systems has been developed by a Grenoble team [9], with special application to pyrometallurgical transfer from the salt to a metallic slag. Its principle is exposed in Fig. I.A.5(b). The two approaches could be combined, to maximise the waste extraction efficiency. Once again, the interplay between interface conditions and bulk MHD is vital for the process.

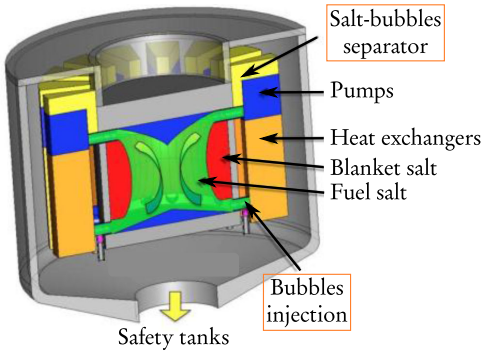

(a) – Schematic MSFR design, showing the implementation of the on-line waste treatment in the nuclear reactor [8].

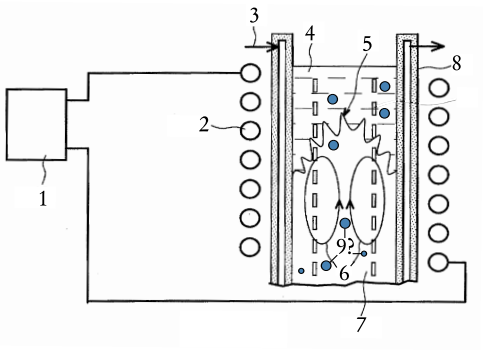

(b) – Sketch of the electromagnetic device for interface melting and stirring [9]. 1: electric power unit, with built-in frequency modulation facilities. 2: inductor. 3: coolant. 4: upper phase. 5: interface. 6: electromagnetic stirring. 7: lower phase. 8: cold crucible. 9: possible bubbles injection.

Figure I.A.5 – Industrial dispersed MHD flows: application to GEN-IV MSFR fission reactor.

In a long-term view, the issue of the dispersed MHD flows may appear in link with the design of nuclear fusion reactors (also called Tokamak, with reference to the plasma levitating concept). The international thermonuclear experimental reactor (ITER) project, currently developed next to the Cadarache facility, aims at demonstrating the sustainability of Deuterium/Tritium fusion for the production of electric power. Due to the limited supply of Tritium, currently estimated at 20 kg worldwide, a breeding-blanket concept must be designed in order to generate Tritium, as shown in Fig. I.A.6. Tritium can be produced within the Tokamak when neutrons escaping the plasma interact with a specific element, Lithium, contained in the blanket. In addition to this necessary feature, the blanket must provide an efficient heat removal from the levitating plasma, allowing for the conversion of nuclear power [10]. Among the various test blanket modules (TBM) proposed to address these issues, those based on Li-containing liquid as breeder and coolant are focusing attention (see, *e.g.*, a review about a possible concept of liquid Li/Pb TBM in [11]).

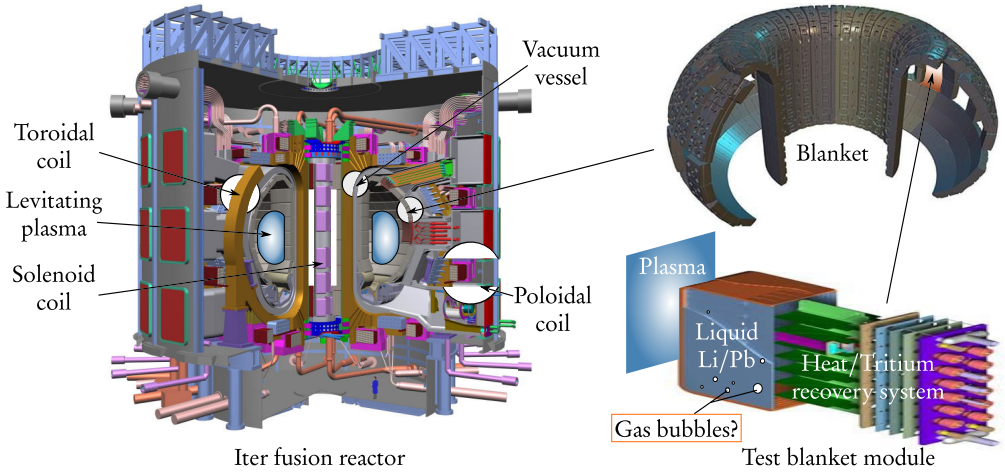

Figure I.A.6 – ITER, the world's largest Tokamak. Left part: global view of the reactor [12]. Right part, top: conceptual design of the blanket [10]. Right part, bottom: a possible TBM design [13].

As shown in Fig. I.A.6, the ITER magnet system includes 18 superconducting toroidal field and 6 poloidal field coils, a central solenoid, and a set of correction coils that magnetically confine, shape, and control the plasma inside the vacuum vessel [10]. The interplay between the liquid metal motion and the strong magnetic fields generated by the magnet system leads to a MHD flow inside liquid Li/Pb. The resultant Lorentz force generates a pressure drop, which degrades convective heat transfer. The solution of injecting gas bubbles in the blanket has been proposed [14]. It is not obvious that the flow shall adopt either a dispersed topology (bubbly flow) or a stratified topology (presence of an annular film around a liquid metal core) topology. The purpose remains nonetheless the same: to lower the MHD pressure drop, either by reducing the apparent electrical conductivity of the fluid (dispersed flow), or by activating particular MHD layers, called the Hartmann layers (see hereafter), that are able to increase the magnitude of the core velocity field (annular flow). Of course, even if this solution contributes to a better convective heat transfer, the injection of a gaseous phase degrades the conductive part of heat removal, either by lowering the apparent thermal conductivity (bubbly flow), or by reducing the conducto-convective coefficient at the TBM walls (stratified flow). A trade-off must be found between these two phenomena, with the aim to enhance as much as possible the Nusselt number (see, *e.g.*, [15] for such considerations in the case of an annular flow). Whatever it be, the breeding blanket heat transfer issue is another point illustrating the industrial and fundamental needs for a better understanding of MHD multiphase flows, with special care about the influence of surface properties on bulk MHD.

I.A.2 (Re-)considering the MHD/interface interactions

All the previously exposed fundamental and industrial applications share common features, which yield the definition of a typical layout of MHD multiphase flows

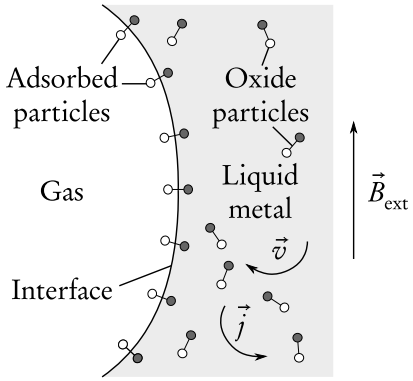

Figure I.A.7 – Typical layout of MHD liquid/gas flow.

(whether it be a stratified or dispersed structure), displayed in Fig. I.A.7. In this figure, we can first point out that due to internal motion $\vec{v}$ inside the electroconductive fluid, in interaction with the outer magnetic field $\vec{B}_{\text{ext}}$, electric currents are developing, leading to the emergence of a MHD flow. Moreover, if a gaseous phase is added to form a heterogeneous liquid/gas medium, complex interactions between the two phases are expected to influence the overall MHD flow. More particularly, the role that may be played by the liquid/gas interface is a crucial issue. If the focus is placed on the liquid surface, particles stemming from physico-chemical processes such as corrosion due to redox reactions or mechanical abrasion, can adsorb at this interface. Depending on its level of contamination, the mechanical and electric properties of the interface can be greatly modified. This interface constituting one boundary condition of the MHD problem, a major impact is expected on the topology of the supporting MHD flow, especially as boundary layers in MHD may significantly alter the core-flow (see Sec. I.B.1.a). Consequently, the particular coupling between MHD and varying surface properties of a liquid metal is worthy of investigation, as the physical insight is expected to be significant. This leads to the definition of the main issue of this work.

How does the alteration of a liquid metal/gas interface, due to oxidation processes, may affect a supporting permanent MHD flow?

This main topic encompasses several issues that we should address. The question of how to model a gradually oxidising interface between a liquid metal and a gas must be solved. What kind of surface parameters necessarily stem from this modelling? Have they ever been measured, or, if not, can we implement an existing measurement method to get access to the values of such parameters? Finally, how can we relate a change in surface properties to a MHD bulk flow? Do the effects of such a coupling depend on the structure of the multiphase flow, either dispersed or confined? Prior to any investigation of our own, let us draw up a state-of-the art of the existing work about such an original coupling between bulk MHD and what we shall call the surface rheology of a liquid metal, which covers those physico-chemical phenomena governing the dynamics at a given liquid surface.

I.B MHD/Surface rheology: enhancing an original coupling

In this chapter, some basic notions of MHD and surface rheology are separately introduced. Our purpose is not so much giving a detailed review about physical phenomena, equations, boundary conditions, etc. (see rather Part II), as showing how the coupling between MHD and surface rheology can reveal insightful, through a set of selected study cases. This heuristic approach allows us to show that despite promising features, such a coupling constitutes an original approach, given the relatively reduced literature in link with this particular topic. Finally, the choice of Galinstan as the working fluid is motivated, with respect to its promising bulk and surface properties.

I.B.1 Two well-known but distinct fields

I.B.1.a Major features of MHD

Historical development

MHD investigates the interplay between the hydrodynamics of electroconductive fluids and electromagnetism, and bears on the induction principle. Historically, Faraday is considered as the discoverer of MHD, in its attempt to measure the flow-rate of the Thames (1840), similarly to how it is now measured for liquid metals (the measurement failed due to the low electrical conductivity of water). However, most of MHD theory and applications were discovered during the twentieth century. Two main periods can be distinguished, corresponding to the two main classes of MHD problems: those based on Lorentz induction, or those based on Neumann induction.

Until the early 1980s, a typical MHD system consists in the motion of a given electroconductive medium, subjected to an outer direct current (DC) magnetic field: this is Lorentz induction, as illustrated in Fig. I.B.1(a). The corresponding MHD shall be qualified as "dynamic" MHD in this study. Alternatively, since the mid-1980s, a new kind of MHD problems has emerged: currents can also be induced when the electroconductive medium is subjected to an external alternative current (AC) field, generated by a conductor crossed by an AC electric current. This is Neumann induction, described in Fig. I.B.1(b), which introduces frequency as a new MHD parameter. The corresponding MHD shall be qualified as "frequency" MHD in this study. For both types of MHD layouts, there are two main consequences, the first of which being that an induced magnetic field linked to eddy currents appears, perturbing the original magnetic field. The second consequence is that an electromagnetic force appears

due to the interaction between these currents and the magnetic field, perturbing the original motion: the Lorentz force.

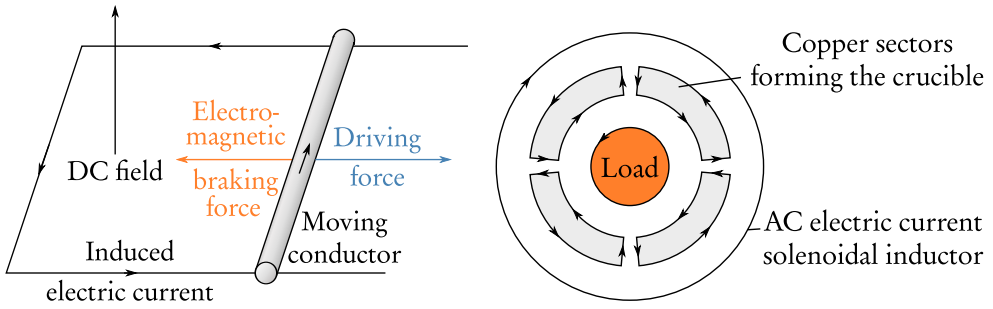

(a) – Lorentz induction for a moving electroconductive rod.

(b) – Neumann induction of electric currents inside a cold crucible [16]. Arrows represent the electric current direction.

Figure I.B.1 – The induction principle.

In this study, the focus is particularly put on dynamic MHD problems, *i.e.* with an outer DC field. Keeping in mind the coupling with varying interface properties acting as boundary conditions for bulk MHD flows, it seems meaningful to focus our research on particular MHD effects linked to boundary conditions. And, indeed, one of the most outstanding features of dynamic MHD involves the active behaviour of particular boundary layers, called the Hartmann layers. They are now introduced through a particularly insightful study case: the Hartmann flow.

The Hartmann flow: highlighting active boundary layers

The Hartmann flow is one of the cornerstones of MHD, equivalent to the Poiseuille flow in classical hydrodynamics [4]. This study case is named after J. Hartmann, who first described this elementary MHD flow when he achieved the first success of MHD, *i.e.* the electromagnetic pump, in 1918, and then analysed its behaviour [17, 18]. Let us consider the fully-developed steady laminar flow of an electroconductive fluid between two infinite and planar parallel walls, subjected to a steady and homogeneous magnetic field $\vec{B}_0 = B_0\vec{e}_z$, as described in Fig. I.B.2. The interplay between fluid motion $\vec{v} = v_x(z)\vec{e}_x$ and the outer magnetic field induces electric current densities $\vec{j} = j_y(z)\vec{e}_x$ inside the fluid. Then, three flow areas can be distinguished:

- the core-flow region C, essentially governed by the effects stemming from pressure gradient and electromagnetic forces;
- and the two boundary layers, namely HT (top boundary layer) and HB (bottom boundary layer), due to the shear induced by the motionless walls, and governed by viscous and electromagnetic effects.

Anticipating Sec. II.A.2.c, where it is more formally defined, let us introduce a dimensionless number that expresses the ratio between electromagnetic and viscous effects, called the Hartmann number, and denoted Ha. These particular layers, whose normal is parallel to the outer magnetic field, are called the *Hartmann layers*. Let us

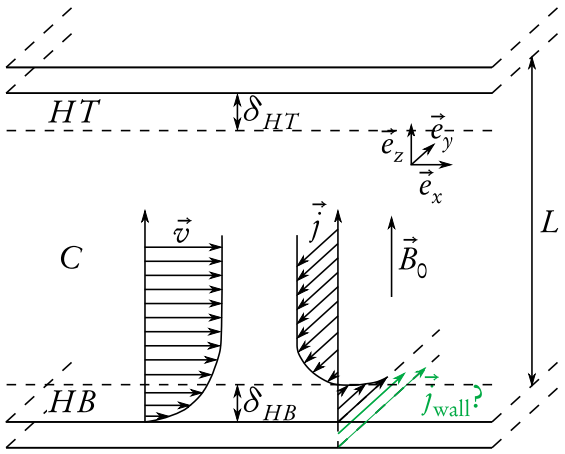

Figure I.B.2 – The Hartmann flow.

now switch to a dimensionless description of the physical problem, the dimensionless physical quantities being superscripted *. The typical dimensionless thickness of the Hartmann layers, denoted $\delta^\star_{HB(HT)}$, is $\delta^\star_{HB(HT)} = 1/\text{Ha}$. Focusing on the bottom part of the flow, the velocity field can be expressed as:

$$v_x^\star(z^\star) = v_{xC}^\star(z^\star) + v_{xHB}^\star(z^\star).$$

The first and the second terms on the right-hand side of previous equation represents the core contribution and the Hartmann layer contribution to the velocity field, respectively. The velocity profile $v^\star_{xHB}(z^\star)$ is such that it matches the zero value at the walls in common with classical hydrodynamics (Blasius layer). However, the Hartmann layer has also another striking feature, which makes it differ fundamentally from "passive" boundary layers. This "active" role is demonstrated by the study of electric current densities, which can be written, similarly to velocity:

$$j_y^\star(z^\star) = j_{yC}^\star(z^\star) + j_{yHB}^\star(z^\star).$$

The "active" denomination stems from the fact that the electric current flowing in the Hartmann layer is found to be proportional to the core velocity. If we reason in term of scaling analysis:

$$V_C^\star \sim \frac{J_{HB}^\star}{\text{Ha}},$$

where $V_C^\star$ is the typical dimensionless core velocity and $J_{HB}^\star$ is the typical order of magnitude of $j_{yHB}^\star$. The previous relation shows how the Hartmann layers controls the outer flow, by means of the electric current density flowing along them. It is important to point out that the electric circuit relies heavily on the electrical nature of the walls. In the vicinity of a very conductive wall, there is no longer the need for the electric current density to flow in the Hartmann layer, since the electric circuit closes up inside the walls (see $\vec{j}_{\text{wall}}$ in Fig. I.B.2). In this case, $J_{HB}^\star \sim O(1/\text{Ha})$, and

$V_C^\star \sim O(1/\mathrm{Ha}^2)$: the Hartmann layers are said electrically *inactive*. Conversely, if the walls are insulating, the conservation of electric current leads to:

$$J_C^\star * O(1) = J_{HB}^\star * \delta_{HB}^\star,$$

and the typical dimensionless core velocity is then deduced: $V_C^\star \sim O(1/\mathrm{Ha})$. The Hartmann layers are said electrically *active*.

The Hartmann flow study case has allowed us to highlight the particular role played by the Hartmann layers in classical MHD. The electrical influence of the walls completely modifies the electric circuit and results in a major impact on the topology of the MHD flow. Given the unique properties of the Hartmann layers, we could expect significant changes considering varying dynamic boundary conditions this time. In order to describe dynamically evolving boundaries and write the corresponding boundary conditions, and then analyse the impact on bulk MHD, we must turn to surface rheology, which is now phenomenologically introduced.

I.B.1.b Major features of surface rheology

Historical development

In classical hydrodynamics (*e.g.* [19]), boundary conditions at free fluid interface often omit an explicit description of interfacial (or surface) rheology. The normal stress boundary condition at the liquid surface is seen as a continuity condition imposed upon the normal component of the fluid stress tensor, with a possible discontinuity arising at a curved interface due to the interfacial (or surface) tension. This approximative description of fluid interfaces is often justified, due to a small fluid surface-to-volume ratio in the considered problems. In this case, bulk hydrodynamics is not significantly altered by surface boundary conditions. However, when the fluid system exhibits a large specific surface, as it is the case for instance for colloidal dispersions or bubbly flows, there is the need for an accurate description of the interfacial mechanics, especially when the interface under consideration is gradually populated by surface-active agents (surfactants, *e.g.* detergent, wetting agent…), because this interface might in turn strongly interact with bulk flow. The need for such a description has given birth to surface rheology [20].

Two main periods can be distinguished in the historical development of surface rheology. Until the beginning of the 1960s, the development of surface rheology was linked to a historical problem of chemical engineering, *i.e.* the fluid flow around an insulated bubble, which is introduced hereafter as a study case. The controversy about the discrepancies between theoretical and experimental work allowed to clarify very important notions such as the Marangoni effect, due to surface tension gradients, and the concept of surface viscosities. This intense scientific discussion led to a unified description of material interfaces of arbitrary curvature, formulated by Scriven [21]. Since this work, the effort has been mainly made on experimental developments in order to allow consistent measurements of interfacial rheological properties (see hereafter for a collection of experimental techniques). In parallel, recent computational progress allowed for the investigation of the drainage and stability of thin liquid films, with potential applications in the dynamical control of foams and emulsions [20].

Creeping flow around a fluid droplet

A spherical fluid droplet should settle more rapidly under buoyancy than would a comparable solid sphere, as stated by the Hadamard-Rybczynski theory [22, 23], which generalised the Stokes' original law for rigid spheres [24]. As displayed in Fig. I.B.3(a), the particle causes significant streamlines curvature. Internal spherical vortices and a non-zero surface velocity v_S along the particle surface S are predicted in the case of a fluid particle. In the case of a rigid sphere, no internal motion and a vanishing surface velocity are expected. However, experimental observations show that the settling velocity for small bubbles and drops tend to deviate from Hadamard-Rybczynski predictions, the internal circulation being hardly noticeable [25]. In order to explain this discrepancy, two explanations were originally proposed. On the one hand, Boussinesq suggested that the liquid surface could be covered by a monolayer which would act as a viscous 2-D membrane. In addition to surface tension, two surface viscosities, surface shear viscosity and surface dilatational viscosity, were introduced to describe the retarded fluid motion [26]. On the other hand, Frumkin and Levich postulated that the anomalous experimental results could be explained by the presence of surfactants at the surface of the droplets [27]. Because of the droplet motion, these surfactants could be swept to the rear of the droplet, leading to surface tension gradients. The resulting Marangoni effect would be generated with the emergence of a tangential (chemical) stress, retarding surface motion (see Fig. I.B.3(b)).

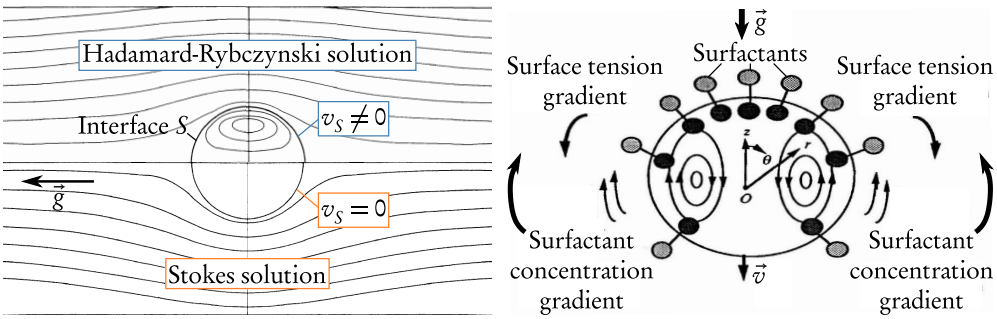

(a) – Streamlines relative to sphericle particle suspended in a creeping flow. Top: Hadamard-Rybczynski solution, bottom: Stokes' solution [25].

(b) – Surface tension gradients created by the convective sweeping of adsorbed surfactants to the rear of the settling droplet [20].

Figure I.B.3 – Slow viscous flow past spheres.

The permanent settling of a contaminated bubble is a remarkable system which enables to introduce the three typical surface rheological properties characterising an interface between two fluids, gradually contaminated by surfactants: surface tension γ, surface shear viscosity η_S and surface dilatational viscosity $\varkappa_S$. A more extensive review of the physical phenomena associated with each parameter is given in Sec. II.B, along with the presentation of the unified Boussinesq-Scriven theory. These param-

eters are defined in order to explain significantly different hydrodynamic layouts in permanent regime. Depending on its level of saturation in surfactants, the rheological behaviour of a liquid/gas interface can be greatly modified, *e.g.* evolving from a slip to a no-slip boundary condition. Now, in the following section, we briefly define the state-of-the-art of the surface rheology of liquid metals, and the experimental means at our disposal to access the values of surface tension and viscosities.

Accessing the surface rheology of liquid metals

Whatever the fluid system considered, the best-known rheological parameter is surface tension γ. As previously said, flow layouts with small specific surface do not need an accurate description of fluid interface, except for surface tension, which governs the pressure discontinuity occurring at a curved interface. A collection of classical techniques to measure γ is summarised in [20], that we can divide into two main categories. The first kind of instrumental devices bears on the measurement of the force that is necessary to stretch the interface, according to the Wilhelmy's or Du Nouy's principle. The Langmuir trough is one of the oldest techniques for measuring the surface tension of a newly created surfactant monolayer at a liquid/gas interface (see Fig. I.B.4(a)). The second category bears on what we generically call the drop shape method: surface tension is recovered by fitting the shape of a (sessile or pendant) drop to a constitutive law, the Young-Laplace equation (see Fig. I.B.4(b)). For liquid metals, the drop-shape methods are favoured, because they do not require a large quantity of fluid. With such methods, the surface tension of such liquid metals as Galinstan is known, with respect to temperature [28] and to surface oxidation [29].

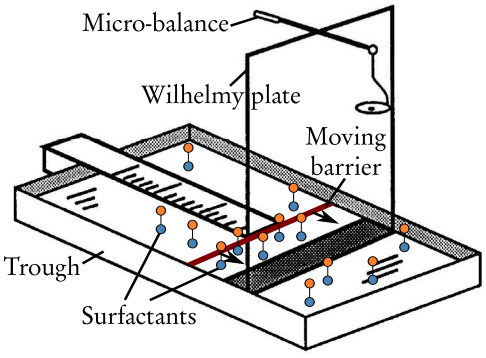

(a) – Langmuir trough. The monolayer area is varied through the moving barrier. The Wilhelmy plate is submitted to the force resulting from capillarity effects [20].

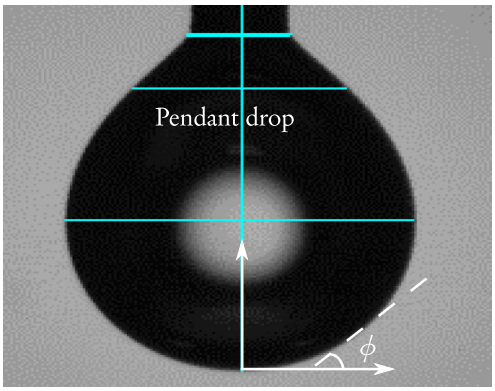

(b) – Pendant drop method. The angle ϕ allows for shape fitting [30].

Figure I.B.4 – Experimental techniques for determining surface tension γ.

With respect to surface shear and dilatational viscosities, a critical issue to be addressed is the existence of Marangoni stresses due to surface tension gradients, which could interfere with the measurement of η_S and $\varkappa_S$. Among the various designs of

surface viscometers, the annular channel viscometer "may be regarded as the most effective, owing to its relative sensitivity, exactness of theoretical description, and simplicity of technique and analysis" [20]. The original design proposed by Mannheimer and Schechter [31] (see Fig. I.B.5) can be recommended in order to measure both η_S and $\varkappa_S$, independently of γ [32].

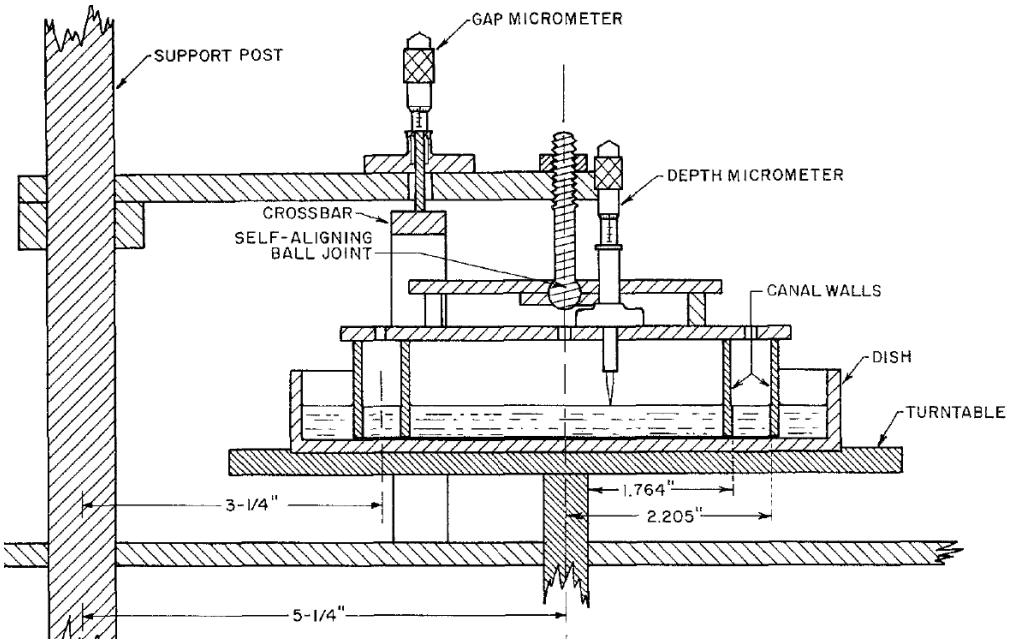

Figure I.B.5 – Schematic cross-section of the deep-channel surface viscometer [31].

I.B.1.c An original coupling

The MHD of single-phase laminar flows has been extensively studied for many years. The flow can be either confined [33], or may have a free surface [3, 34]. In the case of duct flows, the walls can have infinite electrical conductivity [4], no conductivity [33], mixed infinite and vanishing conductivities [35], or arbitrary conductivity [36]. However, the fundamental issue of varying mechanical boundary conditions between slip and no-slip conditions still remains an undisclosed topic.

Moreover, little is actually known about the surface rheology of liquid metals when they are progressively oxidized. The viscoelastic properties of liquid metals have been experimentally investigated by several authors (see, *e.g.*, [29, 37, 38, 39, 40, 41]). These authors have highlighted the preponderant role of the interface level of oxidation on different mechanical properties, such as the response to imposed elastic stresses, surface tension, and contact angles... however, these results do not address neither the issue of surface rheological transport, nor the coupling with MHD.

There are only a couple of articles dealing with the interplay between the oxidation state of a given interface and MHD; see, *e.g.*, the generation of oscillatory flow patterns influenced by surface oxidation [5], in the case of a liquid metal subjected to

a rotating magnetic field (Fig. I.B.6(a)); or the Eurofer (ITER blanket material) corrosion by the flow of the eutectic alloy Li/Pb, stimulated by the presence of a strong magnetic field [42] (Fig. I.B.6(b)). These two studies omit nonetheless any reference to interfacial transport. Finally, the reduced literature about this topic leads us to the conclusion that the coupling between MHD and surface rheology is fairly original.

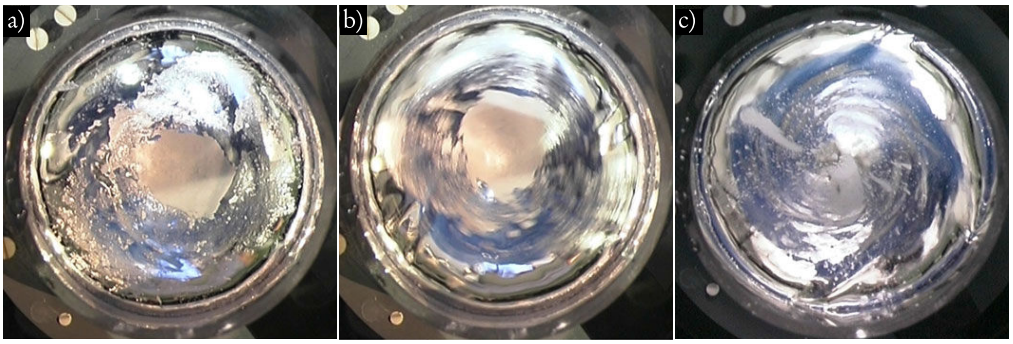

(a) – Intermittent behaviour caused by surface oxidation in a Galinstan (eutectic Ga-In-Sn) flow driven by a rotating magnetic field [5]. a): oxide layer at rest, b) oxide layer in motion, c) closed oxide layer at rest in presence of an intense swirling motion of the fluid beneath.

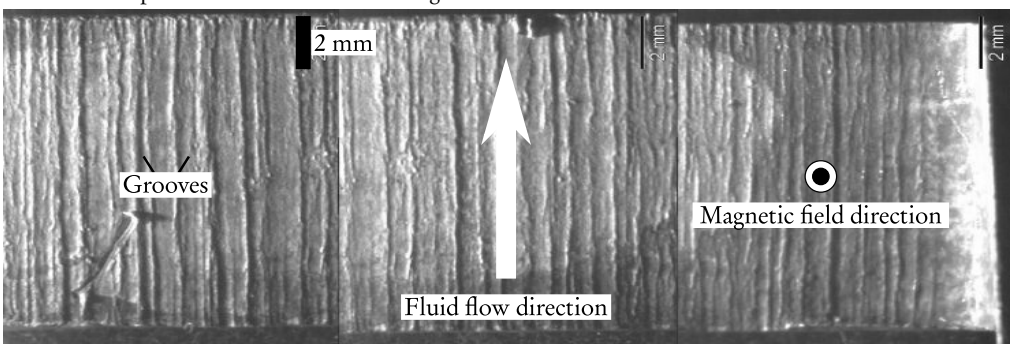

(b) – Optical microscopy observation of the Eurofer surface [42]. The corroded surface exhibits grooved aligned with the fluid velocity, with periodic patterns, enhanced by MHD interactions.

Figure I.B.6 – Experimental evidence of the interaction between oxidation and MHD.

So far, we have been undertaking an intellectual approach, concluding to the insightful aspect of the coupling between MHD and surface rheology. However, all this thought process would reveal pointless, if we are not able to relate it to a medium capable of highlighting this particular coupling. This brings us to the following section, concerning the choice of Galinstan as the model system all along this thesis work.

I.B.2 The choice of Galinstan as working fluid

In this section, the choice of Galinstan as the model system is justified. First, its bulk physical properties are detailed. Then, its promising interfacial characteristics are introduced, along with some interesting dedicated applications, making Galinstan the ideal candidate for investigating the coupling between MHD and surface rheology.

I.B.2.a Galinstan as the new model fluid system in MHD

Galinstan is a eutectic gallium-indium-tin alloy ($Ga_{67\%}In_{20.5\%}Sn_{12.5\%}$ for the usual chemical composition in wt %). Galinstan properties are collected in Tab. I.B.1, according to [28, 43], and are compared to those of mercury. The ternary system GaInSn involves an eutectic composition which is liquid at room temperature, with a low-temperature melting point, depending on the chemical composition. Usually, experimental studies on an industrial scale with liquid metals require special effort on the test-bench designs, in order to reach the liquidus point. A threshold temperature $T > 100$ °C can be defined, from which most of standard instrumental devices should be replaced with heat-resistant devices. The low melting-point of Galinstan constitutes a decisive advantage for implementing cost-saving model experiments.

Property	Galinstan	Mercury
Boiling point (°C)	> 1300	357
Melting point (°C)	-19	-38.8
Vapour pressure (Pa)	$< 10^{-6}$ (at 500 °C)	$\sim 10^{-1}$ (at 20 °C)
Water compatibility	Insoluble	Soluble
Density ($kg{\cdot}m^{-3}$)	6360 (at 20 °C)	13530 (at 20 °C)
Dynamic viscosity (Pa·s)	2.14×10^{-3} (at 20 °C)	1.55×10^{-3} (at 20 °C)
Electrical conductivity ($S{\cdot}m^{-1}$)	3.29×10^{6} (at 20 °C)	10^{6} (at 20 °C)
Magnetic permeability ($H{\cdot}m^{-1}$)	$4\pi \times 10^{-7}$	$4\pi \times 10^{-7}$

Table I.B.1 – Bulk physical properties of Galinstan, compared to mercury [28, 43].

Galinstan exhibits attractive handling properties, owing to the low reactivity and toxicity of its components. Compared to the historical operating fluid in liquid metal experimental facilities, *i.e.* mercury, Galinstan does not evaporate at room temperature; rather, its vapour pressure is extremely low. Unlike many liquid metals, Galinstan is chemically compatible with a variety of metals (with the notable exception of aluminium and its alloys), plastic, rubbers, and glasses at low temperature.

In recent decades, Galinstan has progressively replaced mercury as the classical MHD model system, in most studies devoted to liquid metal MHD flows (see *e.g.* [44, 45, 46, 47, 48] for recent applications). First, the ratio $\sqrt{\sigma/\eta}$ for Galinstan is roughly 50 % higher than for mercury, where σ and η are the electrical conductivity and the dynamic viscosity of the liquid metal under consideration, respectively. Moreover, the ratio ρ/η for Galinstan is 3 times as low as for mercury, where ρ is the fluid den-

sity. These are very interesting properties, because it allows for a wide range of values of MHD scaling parameters. Indeed, the Reynolds number Re and the Hartmann number Ha (see Sec. II.A.2.c) can reach lower or higher values, respectively, than for mercury (for a given experimental facility). The difficulty to reach very low velocities often prevents one from accessing to small Re values, corresponding to the (viscous) Stokes flow regime. In parallel, large Ha values are difficult to obtain, because imposing a strong outer magnetic field is a challenging issue. Consequently, Galinstan has generally better MHD parameters than those of mercury. This flexibility about some MHD scaling parameters is also comfortable, because this gives a physical meaning to the wide range of values tested for these parameters, in the analytical and numerical parts of this study.

Finally, one of the rare drawbacks of Galinstan is price, which can vary widely with world market demand (Fig. I.B.7). It is a major constraint in the design of industrial scale MHD experiment, requiring large volumes of fluid, which can reveal extremely expensive. Recycling techniques are then most valuable [49].

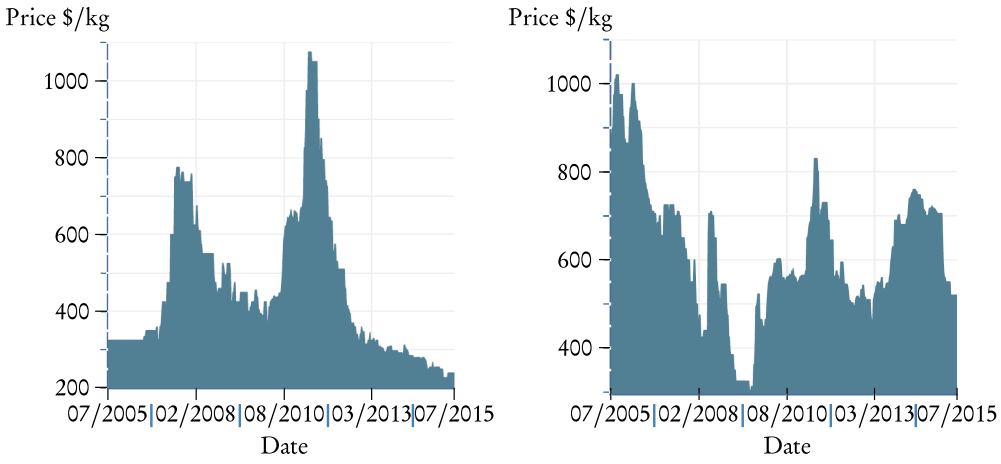

(a) – Gallium exchange rate.

(b) – Indium exchange rate.

Figure I.B.7 – Price per kg for gallium and indium over the past 10 years [50].

I.B.2.b The promising surface properties of Galinstan

Galinstan mainly consists of gallium. In the literature, a lot of studies dealing with the properties of liquid metals involve liquid Ga or other derived alloys (like eutectic GaIn). When exposed to ambient oxygen, the surface oxides primarily consist of gallium oxide Ga_2O_3, which thermodynamically prevails on other oxides [39], whatever the liquid metal considered. Consequently, most of the results concerning the surface properties of derived alloys of gallium can be applied to Galinstan [51].

At room conditions, on a time scale ranging from seconds to hundreds of seconds [41], pure Galinstan forms a thin oxide layer on its surface, with a typical thickness of a few nm [52], when suddenly exposed to ambient air. This oxide layer forms on Galinstan as long as the O_2 concentration in the surrounding atmosphere is greater

than 1 ppm [29], or when subjected to an oxygen dose of 1.8×10^4 Torr·s [52]. This oxide shell is amphoteric, and can be removed at pH<3, or pH>10 [51]. Despite its thinness, this oxide skin deeply alters the mechanical behaviour of, *e.g.*, a sessile droplet. A first effect of this oxide layer is its influence on the wettability of a given sample of Galinstan, *i.e.* on surface tension. As shown in Fig. I.B.8(a), the contact angle of a gallium sessile droplet immersed in an acid bath can be tuned by changing the HCl concentration of this bath. Whatever the acid concentration, the droplet configuration is hydrophobic, on the glass substrate. However, the droplet is less hydrophobic at lower than at higher acid concentrations, where pure liquid gallium is perfectly non-wetting. Thus, the surface oxide on Galinstan lowers the surface tension of the metal (see Fig. I.B.8(b)), very much like surfactants for aqueous fluids [29].

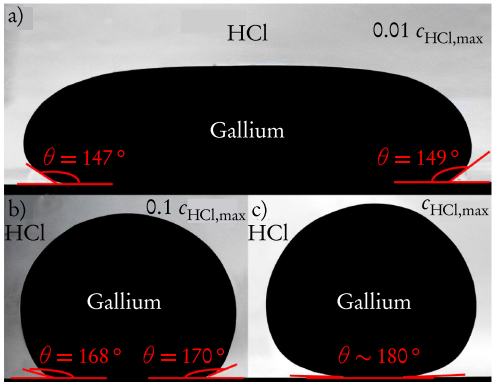

(a) – Gallium wettability on a glass surface, varying according to the HCl concentration of a surrounding acid bath [53] (θ=contact angle). a): $c_{HCl} = 0.01\ c_{HCl,max}$, gallium is "less" hydrophobic. b): $c_{HCl} = 0.1\ c_{HCl,max}$, gallium begins to bounce back to a spherical shape. c): $c_{HCl} = c_{HCl,max}$, maximum contact angle $\theta = 180°$, gallium is perfectly non-wetting.

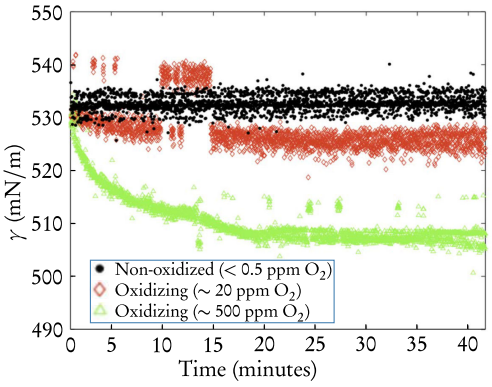

(b) – Effect of oxidation on the surface tension of Galinstan, according to the O_2 rate of oxygen [29].

Figure I.B.8 – Interfacial tension of a gradually oxidising Galinstan sample.

Furthermore, the oxide shell is very robust, being able to mechanically stabilize large deformations, leading to a kind of gel behaviour. As shown in Fig. I.B.8(a), a sessile droplet can be moulded into non-spherical shapes. The oxide skin can be removed by means of a hydrochloric acid bath, and the droplet recovers an equilibrium shape [51]. This behaviour has a consequence not only on surface tension, but also on the apparent bulk rheology of a Galinstan sample. Ga alloys are indeed Newtonian fluids, with a low bulk viscosity (see Tab. I.B.1). However, the oxide layer changes the apparent bulk viscosity; measurements carried out with a parallel-plate rheometer show that the apparent viscosity of an oxidised GaIn sample is dominated by a yield stress, at low shear rates. At higher shear rates, the oxide is broken, and the surface layer turns over, so that the bulk material becomes exposed to air and has a chance to

react with O_2. This creates more solid and resisting material to the rheometer plate, causing the increase of shear stress with time [53], emphasised in Fig. I.B.9(b).

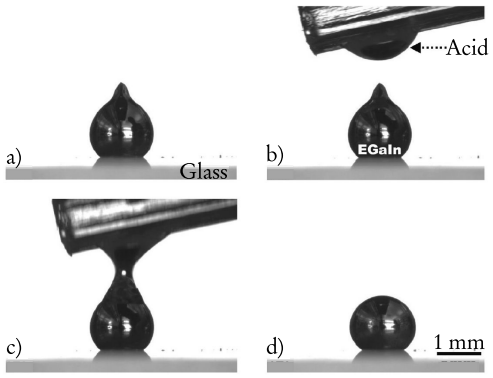

(a) – Gel behaviour of a GaIn droplet, varying according to the presence of an oxide skin on its surface [51]. a): non-equilibrium shape, b) and c): exposure to acid removes the oxide skin, d): equilibrium shape.

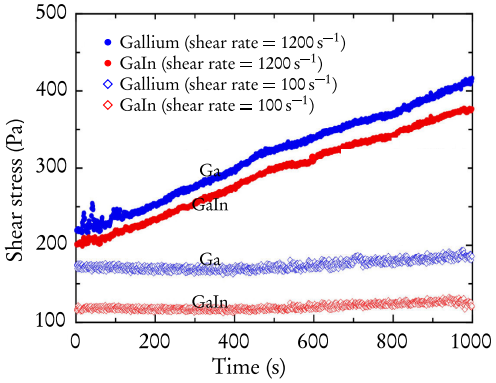

(b) – Oxidation of liquid metals exposed to air in rheometer measurements. Time evolution of shear stress with respect to time [53]. Open symbols (bottom): low shear rate, closed symbols (top): high shear rate.

Figure I.B.9 – Gel behaviour and varying apparent bulk viscosity of gradually oxidising Galinstan.

These original surface properties have led to numerous emerging applications in microfluidics, electronics, or optics (see [51] for an extensive review). Within the scope of this study, such properties make Galinstan the ideal candidate for investigating the MHD of a gradually oxidising liquid metal. As previously shown in Fig. I.B.6(a), Galinstan is the model fluid used in [5], where the interaction between bulk MHD and the oxidation state of a given interface has been highlighted. Consequently, Galinstan is the working fluid chosen in this thesis work to enhance the original coupling between MHD and surface rheology.

I.C Bridging the gap between MHD and surface rheology

In this chapter, the method that we shall adopt in this study to bridge the gap between MHD and surface rheology is unveiled, along with some determining outlines.

I.C.1 Overall approach

The fundamental issue of gradually changing MHD boundary conditions seems to have only been considered from an electrical point of view. In this study, our aim is to take the same kind of general approach for the boundary conditions, but this time from a mechanical point of view. Surface rheology accounts for the accurate description of interfacial transport, characterised by surface rheological parameters. One of them, *i.e.* surface tension γ, seems to be well-known, but the other two, *i.e.* surface viscosities η_S and $\varkappa_S$, seem totally unknown, as far as liquid metals are concerned.

We must therefore establish the theoretical foundations and draw some scaling laws in order to implement an experimental test-bench, allowing for the selective measurement of both surface viscosities, relative to a given interfacial oxidation. Besides, this experimental facility should ideally be designed so that the physical mechanisms of the coupling between MHD and surface rheology could be particularly highlighted. All these requirements lead us to the analytical, numerical and experimental investigation of an original device: the so-called annular MHD viscometer, derived from the promising layout of the classical deep-channel viscometer, emphasised above. The study of the annular MHD viscometer may give us access to the values of η_S and $\varkappa_S$ for the reference fluid, *i.e.* Galinstan. It can also give a first glimpse on stratified MHD flow patterns, influenced by varying interfacial boundary conditions.

Once these parameters estimated, we might use their values to feed other MHD flows concerned with interfacial issues. Stratified MHD flows are one of the asymptotic cases of MHD multiphase flows. The other asymptotic case corresponds to dispersed MHD flows. As a first-step towards the description of dispersed MHD flows, the MHD of a single gas bubble suspended in Galinstan with varying interfacial conditions should be worth of investigation. This particular layout would serve as a reference for more complicated dispersed MHD flow problems (*e.g.* MHD bubbly flows), and it is likely to emphasise insightful MHD effects due to the bubble dynamics.

I.C.2 Main assumptions

The full description of the physical coupling between MHD and surface rheology may reveal extremely complicated, potentially involving such different physical fields as electromagnetism, hydrodynamics, chemical physics…In order to take the first step towards MHD multiphase flows, we must simplify our approach by making physical approximations. The main assumptions of this work are justified hereafter.

First, we do not consider any dependence with respect to temperature: $\partial/\partial T = 0$, so that the *bulk* physical properties of a given medium are considered to be constant. All the physical processes described in this study, either thought or true experiments, are operated at room temperature $T = 20$ °C (if another constant temperature is not specified). The magneto-hydro-energetic (MHE) coupling is thus not investigated.

With respect to electromagnetic assumptions, we shall focus mainly on "dynamic" MHD, linked to external DC fields. "Frequency" MHD is induced by outer AC fields, which tend to have a strong influence on the interface shape, due to the electromagnetic pressure [6]. The scope of this study is to adopt the simplest approach on the MHD/surface rheology coupling. In this respect, frequency MHD is left aside from the reasoning, along with any kind of time-dependence in the electromagnetic equations, except in App. E, for a specific issue, which is not directly linked to the coupling between MHD and surface dynamics.

Concerning fluid dynamics, permanent regime is also assumed: consequently, $\partial/\partial t = 0$ throughout the whole study, as far as bulk equations are concerned. The other purely hydrodynamic assumptions are the following: we shall consistently assume that the flow under consideration is an incompressible and viscous Newtonian; the flow regime is always laminar, so that no turbulence issues need to be considered.

Finally, the most important approximations affects the modelling of the interfacial behaviour. The first issue deals with the shape of the interface: the geometry of the interface is always known *a priori*, which considerably simplifies our investigation. Indeed, we just need to impose a boundary condition upon normal velocity at the fluid interface, along with the tangential conditions, to close the problem formulation, and not the full normal stress boundary condition [20]. In practise, this leads us to leave γ aside from the analysis.

The second surface rheology issue is related to the interfacial transport of momentum: we assume that the interface flow can be modelled within a Newtonian approach. This is a very strong assumption: the "gel" behaviour, previously highlighted for Ga-alloys when exposed to air, seems to refute this hypothesis the very moment it is stated. It is true that the surface oxide imparts the metal with non-Newtonian rheological properties [51]. However, all the applications where such a visco-plastic behaviour is highlighted share a common point: all the metallic samples tested are initially totally oxidised. In parallel, some authors (see, *e.g.* [29]) have shown that this gel behaviour tends to disappear under controlled working conditions, and that Galinstan tends to behave like a true liquid. The Newtonian approach does not seem totally irrelevant in the light of these observations, and remains the simplest (but not simplistic) modelling of the interfacial transport of momentum.

The Newtonian approach requires the determination of surface parameters. As demonstrated, *e.g.*, by the Marangoni effect, the interfacial transport of surfactants (oxides in the case of liquid metals) may strongly affect the value of these parameters, resulting in surface gradients. In this study, these surface parameters are assumed to depend only on a given O_2 flux at a given surface, and do not vary over time and space.

First, fast thermodynamic equilibrium is expected (a few hundreds of seconds for Galinstan oxidation [41], at most). Concerning spatial invariance, this requires the uniform covering of the interface by metallic oxides. This approximation is equivalent to the following statement: surface chemical diffusion dominates surface convection, *i.e.* the surface Péclet number is very small, so that the surface concentration of metallic oxides is homogeneous. To our knowledge, there are no available data about the surface mass diffusivity of (gradually oxidising) liquid metals, at a liquid/gas interface. This assumption remains a strong hypothesis of this study, and should be confirmed (or denied) by future works. Nonetheless, would it reveal to be wrong, the results presented in this work could be considered as a description "at leading order". The interfacial gradients of surface parameters would induce spatial modulations around this leading order description. Finally, in this thesis work, such gradients are neglected: we consider the interface only from the mechanical point of view, and the interfacial mass transport is disregarded.

I.C.3 Outlines

To deal with the practical conditions of molten metals in metallurgy industry, we need to investigate surface mechanics separately from bulk flow, especially when the free surface is gradually oxidising. We must then introduce the fundamental physical phenomena and the corresponding mathematical descriptions at the root of both MHD and surface rheology. This review of fundamental MHD and surface rheology is carried out in Part II.

Once the physical modelling corresponding to each physics introduced, the mechanical coupling can be considered between a liquid surface and the underlying bulk, through the emergence of surface dilatational and shear viscosities. The original layout of the annular MHD viscometer is then analytically, numerically and experimentally investigated in Part III. The analytical and numerical results first allows for determining distinct experimental working conditions, that we shall use to implement the experimental test-bench, called the Madip experiment. The second objective of both analytical and numerical calculations is to test a wide range of values for MHD and surface rheology parameters, in order to enhance some original stratified MHD flow patterns resulting from the coupling between MHD and surface rheology. The results of Madip obtained so far are then discussed, highlighting the feasibility of accessing the values of surface viscosities. This part shall conclude the main matter of this thesis work.

In order to address the issues linked to MHD multiphase flows from both ends, a substantial work has been performed about the asymptotic study case of a single gas bubble immersed in Galinstan with a gradually oxidising liquid/gas interface. Un-

fortunately, by lack of time, the opportunity has not been given to present some numerical results concerning the MHD flow past a sphere undergoing varying interfacial dynamics. This is the reason why the "bubble MHD" problem is left aside from the main analysis. However, an insightful state-of-the-art of most significant achievements about the (electroconductive) flow past a gas bubble has been drawn, including a variety of (magneto)hydrodynamic effects, and the expected impact of surface dynamics. Some developments concerning the numerical implementation, and particularly the full interfacial boundary condition, have also been determined. Finally, this background approach constitutes a reference material for further prospects about the bubble MHD problem, and is consequently placed in App. D. It can be thought of as a first step towards the description of dispersed MHD flows.

Part II

Fundamentals

THIS *part gives an introduction on the physical background of both MHD and surface rheology. The equations of MHD and the associated approximations are introduced in the first chapter, along with the definitions of significant dimensionless groups. A distinction is made between hydrodynamic (linear momentum balance, or Navier-Stokes equations) and electromagnetic (induction equation) equations, in order to enhance the coupling terms in MHD,* i.e. *the electromotive current and the Lorentz force. The end of the first chapter addresses the notions of electromagnetic and dynamic boundary conditions that shall be used in this work.*

This review of MHD boundary conditions allows us to introduce surface rheology in the second chapter. Indeed, the interfacial transport of momentum at a given interface acts as a boundary condition of the MHD bulk flow. In our Newtonian approach of the interface dynamic behaviour, three parameters are required to model the relationship between surface stress and surface strain: surface tension, surface shear and surface dilatational viscosities. These three parameters are first phenomenologically introduced, along with a couple of notions about the definition of excess quantities across the interface. Afterwards, the equation governing the interfacial transport of momentum, i.e. *the jump of momentum balance (JMB), is produced, and the dimensionless groups characterising surface rheology are highlighted. It is shown that surface tension can be left aside from the analysis, so that only the surface viscosities are required to close the mathematical modelling. Finally, the global model for describing the coupling between MHD and interfacial dynamics is set up.*

II.A Introduction to magnetohydrodynamics

In this chapter, the focus is placed on the fundamental physical mechanisms involved in MHD processes. First, the electromagnetism and hydrodynamics equations are separately introduced. The characteristic dimensionless groups of MHD are then produced. Afterwards, the different electromagnetic and hydrodynamic boundary conditions used in this work are detailed. The coupling with surface rheology as a particular boundary condition is finally highlighted. For an extensive introduction to MHD, the reader may refer to MHD classical textbooks, for instance [4, 54].

II.A.1 Review of electromagnetism in an electroconductive fluid

II.A.1.a Maxwell's equations and Ohm's law in the quasi-static approximation

From the definition of the electric charge, fields and potentials are defined, which allow for the description of the interactions between electric charges. As stated in Sec. I.C.2, the bulk physical properties of the working fluid are assumed to be constant. With this approximation, the conservation of the electric charge, along with the definition of the electromagnetic fields, lead to four relationships called Maxwell's equations between the magnetic field $\vec{B}$, the electric field $\vec{E}$, the volume density of electric charge q and the electric current density $\vec{j}$:

$$\mathrm{div}\left(\vec{B}\right)=0, \quad (\mathrm{M}\Phi_0) \qquad \overrightarrow{\mathrm{curl}}\left(\vec{E}\right)=-\frac{\partial\vec{B}}{\partial t}, \qquad (\mathrm{MF}_0)$$

$$\mathrm{div}\left(\vec{E}\right)=\frac{q}{\epsilon}, \quad (\mathrm{MG}_0) \qquad \overrightarrow{\mathrm{curl}}\left(\vec{B}\right)=\mu\vec{j}+\mu\epsilon\frac{\partial\vec{E}}{\partial t}, \quad (\mathrm{MA}_0)$$

where ϵ and μ are the electric permittivity and the magnetic permeability of the working fluid, respectively. The electric current density is defined through a constitutive law called generalised Ohm's law for matter moving at velocity $\vec{v}$:

$$\vec{j}=q\vec{v}+\sigma\left(\vec{E}+\vec{v}\times\vec{B}\right),$$

where $q\vec{v}$ is the convective current, $\sigma\left(\vec{E}+\vec{v}\times\vec{B}\right)$ the conductive current, σ is the electrical conductivity of the fluid, and $\times$ is the mathematical cross product. Finally,

a conservation equation called continuity equation for electric current can be derived either from the conservation of electric charge, or from Eqs. (MG_0) and (MA_0):

$$\frac{\partial q}{\partial t} + \mathrm{div}\left(\vec{j}\right) = 0.$$

These equations are true in any medium (vacuum, insulator, conductor...). In the case of a non-relativistic electroconductive medium, they can be considerably simplified, by introducing the quasi-static or low-frequency approximation [54]. First, in generalised Ohm's law, the typical orders of magnitude of convection and conduction currents are investigated. Charge density is determined from Eq. (MG_0), so that the convective part of current densities $\vec{j}$ is of order:

$$\left\| q\vec{v} \right\| \sim \frac{\epsilon E V}{L},$$

where $\|\cdots\|$ is the Euclidean norm operator, E is a typical value of the electric field, V is a typical fluid velocity and L is a typical length scale. Besides, as $\vec{E}$ and $\vec{v} \times \vec{B}$ are of same order, an order of magnitude for the conduction current is σE, which yields:

$$\frac{\left\| q\vec{v} \right\|}{\left\| \sigma\vec{E} \right\|} \sim \tau_r \frac{V}{L},$$

where $\tau_r = \epsilon/\sigma$ is the typical relaxation time of electric charges. In the case of liquid metals or eutectic alloys, a typical value for τ_r is $10^{-17}, 10^{-18}$ s [4]. As a result, the convective current is fairly neglected all along this study. Now, concerning the displacement current $\epsilon \partial\vec{E}/\partial t$, Eq. ($MA_0$) provides:

$$\epsilon \left\| \frac{\partial \vec{E}}{\partial t} \right\| \sim \frac{\epsilon}{\tau_t} E,$$

where τ_t is the typical transit time of the electromagnetic field. According to Ohm's law, an order of magnitude of the electric current is given by:

$$\left\| \vec{j} \right\| \sim \sigma E,$$

Obviously, if $\tau_r/\tau_t \ll 1$, the displacement current can be omitted. Within the frame of the low-frequency assumption, this condition is certainly always fulfilled at laboratory scale, either in the case of AC electromagnetic fields with classical operating frequencies ($\tau_t \sim 10^{-9}$ s), or in the case of DC fields applied to a moving electroconductive medium ($\tau_t \sim 1 - 100$ s). As a result, the displacement current is consistently neglected in this entire work. Concerning continuity equation, substituting $\vec{j}$ according to Ohm's law, and considering $\tau_r \ll 1$ implies that $\partial q/\partial t$ can be omitted.

Consequently, assuming the low-frequency approximation, the final set of electromagnetic equations used for MHD problems is obtained, beginning with the continuity equation for electric current:

$$\mathrm{div}\left(\vec{j}\right) = 0, \tag{II.A.1}$$

meaning that the current lines must close up inside the electroconductive fluid, $\vec{j}$ being said solenoidal. Maxwell's equations write:

$$\mathrm{div}\left(\vec{B}\right)=0, \quad (\mathrm{M}\Phi) \qquad \overrightarrow{\mathrm{curl}}\left(\vec{B}\right)=\mu\vec{j}, \quad (\mathrm{MA}) \qquad \overrightarrow{\mathrm{curl}}\left(\vec{E}\right)=-\frac{\partial\vec{B}}{\partial t}. \quad (\mathrm{MF})$$

Note that q appears only in Maxwell-Gauss equation $\mathrm{div}(\vec{E})=q/\epsilon$, which is of no interest in MHD, and is not used henceforth. However, even if q is not required to solve for MHD problems, this *does not* mean that $\mathrm{div}(\vec{E})=0$; the equation is simply left aside [54]. Finally, generalised Ohm's law applied to moving matter writes:

$$\vec{j}=\sigma\left(\vec{E}+\vec{v}\times\vec{B}\right). \tag{II.A.2}$$

The fundamental equations of electromagnetism used in MHD are now established. From these equations, one single equation enhancing the coupling between the magnetic field $\vec{B}$ and the velocity field $\vec{v}$ can be obtained: the induction equation.

II.A.1.b The magnetic induction equation

Physical meaning

If we combine Eq. (MF) and the curl of Eqs. (MA) and (II.A.2), the electromagnetic problem is reduced to a single equation in $\vec{B}$, called the induction equation:

$$\frac{\partial\vec{B}}{\partial t}=\overrightarrow{\mathrm{curl}}\left(\vec{v}\times\vec{B}\right)+\frac{1}{\mu\sigma}\vec{\Delta}\vec{B}, \tag{II.A.3}$$

where $\vec{\Delta}$ is the vector laplacian operator. A formal analogy can be made with the equation of vorticity in classical hydrodynamics [4]. In the case of incompressible fluids, Eq. (II.A.3) writes:

$$\frac{\partial\vec{B}}{\partial t}+\left(\vec{v}\cdot\overrightarrow{\mathrm{grad}}\right)\vec{B}=\left(\vec{B}\cdot\overrightarrow{\mathrm{grad}}\right)\vec{v}+\frac{1}{\mu\sigma}\vec{\Delta}\vec{B}, \tag{II.A.4}$$

When grouped together, the two terms on the left represent the particular derivative $\mathrm{d}\vec{B}/\mathrm{d}t$, the term $(\vec{v}\cdot\overrightarrow{\mathrm{grad}})\vec{B}$ standing for the magnetic field convection term. The term $(\vec{B}\cdot\overrightarrow{\mathrm{grad}})\vec{v}$ represents the field production by stretching of the flux lines. The last term on the right represents the diffusion of the magnetic field within the fluid.

Normalised equation and dimensionless numbers

Let us define a typical length scale L, a typical time scale τ, a typical fluid velocity V, and a typical order of magnitude of the magnetic field B. The induction equation can be normalised, which leads to:

$$\mathrm{R}_\omega\frac{\partial\vec{B}^\star}{\partial t^\star}=\mathrm{Rm}\,\overrightarrow{\mathrm{curl}}^\star\left(\vec{v}^\star\times\vec{B}^\star\right)+\vec{\Delta}^\star\vec{B}^\star, \tag{II.A.5}$$

where $\vec{B}^\star = \vec{B}/B$, $t^\star = t/\tau$, and $\vec{v}^\star = \vec{v}/V$. In Eq. (II.A.5), two dimensionless numbers appear, the first of which being defined as:

$$\mathrm{R}_\omega = \frac{\text{field non-stationarity effects}}{\text{field diffusion effects}} = \frac{\mu\sigma L^2}{\tau}, \tag{II.A.6}$$

which is denominated the shielding parameter. The second dimensionless number resulting from Eq. (II.A.5) is the magnetic Reynolds number:

$$\mathrm{Rm} = \frac{\text{field advection effects}}{\text{field diffusion effects}} = \mu\sigma V L. \tag{II.A.7}$$

The two main classes of MHD problems can be deduced from Eq. (II.A.5), based on the physical meaning of the typical time scale τ. The first class deals with the problems where the transit time of the electromagnetic field is imposed by external conditions, *i.e.* the case of AC magnetic fields oscillating at typical pulsation $\omega = 1/\tau$, corresponding to AC MHD. The second class deals with the problems where the transit time of the electromagnetic field is the transit time of fluid particles $\tau = L/V$ in the domain, *i.e.* the case of DC MHD.

II.A.1.c AC electromagnetic fields

At laboratory scale, with typical velocities not exceeding a few cm·s^{-1}, let us assume that the pulsation ω of the oscillating magnetic field is such as $\mathrm{Rm} \ll \mathrm{R}_\omega$. In this case, the magnetic field is governed by a non-stationary diffusion equation:

$$\mathrm{R}_\omega \frac{\partial \vec{B}^\star}{\partial t^\star} = \vec{\Delta}^\star \vec{B}^\star, \tag{II.A.8}$$

where $\mathrm{R}_\omega = \mu\sigma\omega L^2$. Eq. (II.A.8) shall only be used in App. E, where a sudden decay of $\vec{B}$ is imposed in order to access the value of σ for a liquid metal sample. In the main matter of this thesis work, the focus is rather put on DC MHD, which is now introduced.

II.A.1.d DC electromagnetic fields and the low-Rm approximation

The induction equation and the low-Rm approximation

When the physical time-scale is $\tau = L/V$, the shielding parameter does not make sense and only the magnetic Reynolds number (to which R_ω is equal) is kept. Let us now consider the general case of an electroconductive flow subjected to a permanent uniform outer DC field $\vec{B}_0 = B_0\vec{e}_s$, $\vec{e}_s$ being the axis of the coordinate s along which the outer magnetic field is oriented. For this kind of MHD problems, it reveals particularly fruitful to define $\vec{B}$ as follows:

$$\vec{B} = \vec{B}_0 + \vec{b}, \tag{II.A.9}$$

i.e. as the superposition of the imposed uniform DC magnetic field $\vec{B}_0$ and of the varying magnetic induction $\vec{b}$, induced by fluid motion. As explained in Sec. I.C.2, we shall not consider any time dependence in dynamic MHD problems, so that $\partial\vec{b}/\partial t = 0$.

At laboratory scale, and at moderate velocity values, the magnetic Reynolds number is fairly assumed to be low (typical value: $\mathrm{Rm} \leq 10^{-2}$). According to Eq. (II.A.7), this means that the typical value of the induced magnetic field is much lower than the external magnetic field: $b \ll B_0$. The low-Rm approximation results in the fact that the electromotive current can be approximated as:

$$\vec{v} \times \vec{B} \sim \vec{v} \times \vec{B}_0, \tag{II.A.10}$$

a direct consequence of which is:

$$\overrightarrow{\mathrm{curl}}\left(\vec{v} \times \vec{B}\right) \sim B_0 \frac{\partial \vec{v}}{\partial s}. \tag{II.A.11}$$

Substituting Eq. (II.A.11) into Eq. (II.A.5) gives the following dimensionless induction equation at steady state:

$$\boxed{\vec{\Delta}^\star \vec{b}^\star + \mathrm{Rm}\frac{B_0}{b}\frac{\partial \vec{v}^\star}{\partial s^\star} = 0,} \tag{II.A.12}$$

where $\vec{b}^\star = \vec{b}/b$ and $s^\star = s/L$. Note that, even when $\mathrm{Rm} \ll 1$, the term multiplied by $B_0\mathrm{Rm}/b$ is not neglected ($B_0 \gg b$).

The induction equation: $\vec{j}$ formulation

In combination with Eq. (MF), the curl of Eq. (II.A.2) provides another equation, also called the "magnetic induction equation" in the literature [55], and that we shall preferentially refer to as the electric current formulation of the induction equation:

$$\overrightarrow{\mathrm{curl}}\left(\vec{j}\right) = \sigma \overrightarrow{\mathrm{curl}}\left(\vec{v} \times \vec{B}\right). \tag{II.A.13}$$

This equation can be normalised, within the low-Rm assumption, which yields:

$$\boxed{\overrightarrow{\mathrm{curl}}^\star\left(\vec{j}^\star\right) = \frac{\partial \vec{v}^\star}{\partial s^\star},} \tag{II.A.14}$$

where $\vec{j}^\star = \vec{j}/J$, and $J = \sigma V B_0$ according to Eq. (II.A.10).

Potential formulation

The magnetic induction equation constitutes the first classical approach in MHD. For certain applications, especially for numerical simulations, it reveals more convenient to develop a potential formulation. It is based on the definition of the electric potential ϕ and the magnetic vector potential $\vec{A}$:

$$\vec{E} = -\overrightarrow{\mathrm{grad}}(\phi), \vec{B} = \overrightarrow{\mathrm{curl}}\left(\vec{A}\right). \tag{II.A.15}$$

Ohm's law is then written:

$$\vec{j} = \sigma\left(-\overrightarrow{\text{grad}}(\phi) + \vec{v}\times\vec{B}\right). \tag{II.A.16}$$

Then, Ampère's law can be rewritten as:

$$\overrightarrow{\text{curl}}\left(\overrightarrow{\text{curl}}\left(\vec{A}\right)\right) - \mu\sigma\vec{v}\times\overrightarrow{\text{curl}}\left(\vec{A}\right) + \mu\sigma\overrightarrow{\text{grad}}(\phi) = 0, \tag{II.A.17}$$

and the continuity equation as:

$$\text{div}\left(\mu\sigma\vec{v}\times\overrightarrow{\text{curl}}\left(\vec{A}\right) - \mu\sigma\overrightarrow{\text{grad}}(\phi)\right) = 0, \tag{II.A.18}$$

completed by the Coulomb gauge to define uniquely $\vec{A}$, *i.e.* $\text{div}\left(\vec{A}\right) = 0$. If we substitute Eqs. (II.A.10) and (II.A.11) into Eqs. (II.A.17) and (II.A.18), this produces the following set of normalised equations (assuming the low-Rm approximation):

$$\overrightarrow{\text{curl}}^{\star}\left(\overrightarrow{\text{curl}}^{\star}\left(\vec{A}^{\star}\right)\right) + \frac{B_0\text{Rm}}{b}\left(\overrightarrow{\text{grad}}^{\star}(\phi^{\star}) - \vec{v}^{\star}\times\vec{e}_s\right) = 0, \tag{II.A.19}$$

$$\Delta^{\star}\phi^{\star} = \text{div}^{\star}\left(\vec{v}^{\star}\times\vec{e}_s\right), \tag{II.A.20}$$

where $\vec{A}^{\star} = \vec{A}/LB_0 = \vec{A}/A$, and $\phi^{\star} = \phi/\Phi$, with $\Phi = LVB_0$ according to Eq. (II.A.10). Note that Eq. (II.A.19) is only required when $\vec{B}$ must be known. If not, Eq. (II.A.20) is sufficient to determine ϕ, and then $\vec{j}$ through dimensionless Ohm's law:

$$\vec{j}^{\star} = -\overrightarrow{\text{grad}}(\phi^{\star}) + \vec{v}^{\star}\times\vec{e}_s, \tag{II.A.21}$$

where $\vec{j}^{\star} = \vec{j}/J$, and $J = \sigma VB_0$ according to Eq. (II.A.10).

What formulation for what problem?

The choice of a particular formulation strongly depends on the physical layout and on the related boundary conditions. For the analytical calculations, like those performed in Secs. III.B and App. D.3.a, the magnetic induction equation (II.A.12) is classically used [4, 34, 55, 56]. For the numerical simulations of Sec. III.C, the potential formulation based on Eqs. (II.A.19) and (II.A.20) is favoured [57, 58]. For future prospects concerning the "bubble MHD problem" (see App. D.4), this potential formulation should be also favoured.

The electromagnetic equations are now established. However, the MHD problem is not closed, the velocity field $\vec{v}^{\star}$ remaining unknown. This requires additional equations, as described hereafter.

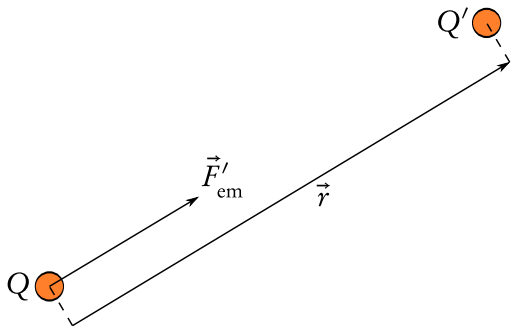

Figure II.A.1 – Electromagnetic interaction between two point charges.

II.A.2 Review of electroconductive fluid mechanics

II.A.2.a Electromagnetic force in the quasi-static approximation

Let two point charges Q and Q', subjected to an electromagnetic field, as described in Fig. II.A.1. The motion of Q is influenced by the electromagnetic force:

$$\vec{F}'_{\text{em}} = K\frac{QQ'}{r^2}\frac{\vec{r}}{\|\vec{r}\|} = Q\vec{E}',$$

where K is a constant, $\vec{r}$ is the vector pointing from Q to Q', and $\vec{E}'$ is the electric field generated by the charge Q', in the system of coordinates attached to Q'. The Lorentz transformation allows to express this force in the laboratory framework:

$$\vec{F}_{\text{em}} = Q\left(\vec{E} + \vec{u}\times\vec{B}\right),$$

where $\vec{u}$ is the velocity of the charge Q (the latter does not depend on the framework), in general absolutely different from the velocity field $\vec{v}$ of the fluid particle carrying it. $Q\vec{E}$ and $Q\vec{u}\times\vec{B}$ are the Coulomb and Lorentz parts of $\vec{F}_{\text{em}}$, respectively. If we sum now on a unit volume all the forces to which the charges present in this volume are subjected, this yields the following expression for the volume density of electromagnetic force $\vec{f}_{\text{em}}$:

$$\vec{f}_{\text{em}} = \sum Q\vec{E} + \sum Q\vec{u}\times\vec{B}.$$

This unit volume can always be taken as small as desired, so that $\vec{E}$ and $\vec{B}$ can be considered uniform. Therefore, with $q = \sum Q$ the volume density of electric charge, and $\vec{j} = \sum Q\vec{u}$ the volume density of electric current:

$$\vec{f}_{\text{em}} = q\vec{E} + \vec{j}\times\vec{B}.$$

Within the quasi-static approximation, the Coulomb force is negligible. The order of magnitude of the electric part of the body force is indeed:

$$\left\|q\vec{E}\right\| \sim \frac{\epsilon E^2}{L},$$

and for the magnetic part ($\vec{E}$ and $\vec{v}\times\vec{B}$ being of comparable order):

$$\left\|\vec{j}\times\vec{B}\right\| \sim \frac{\sigma E^2}{V}$$

Consequently, the electric and magnetic parts of $\vec{f}_{\mathrm{em}}$ are in ratio of order:

$$\frac{\left\|q\vec{E}\right\|}{\left\|\vec{j}\times\vec{B}\right\|} \sim \frac{\epsilon V}{\sigma L} = \frac{\tau_r}{\tau_t}.$$

Therefore, with $\tau_r/\tau_t \ll 1$ (see above), the volume density of electromagnetic force is reduced to the Lorentz force:

$$\vec{f}_{\mathrm{em}} = \vec{f}_{\mathrm{L}} = \vec{j}\times\vec{B}. \tag{II.A.22}$$

II.A.2.b Navier-Stokes equation

We shall consistently assume that every electroconductive flow under consideration all along this work is a permanent, incompressible, viscous Newtonian flow, as stated in Sec. I.C.2. Mass conservation and momentum conservation equations lead to the following set of equations:

$$\mathrm{div}\left(\vec{v}\right) = 0, \tag{II.A.23}$$

$$\rho\left(\vec{v}\cdot\overrightarrow{\mathrm{grad}}\right)\vec{v} = \overrightarrow{\mathrm{div}}\left(\overrightarrow{\overrightarrow{T}}\right) + \vec{f}_{\mathrm{L}} + \vec{f}, \tag{II.A.24}$$

which are, respectively, the continuity equation for fluid velocity, and the Navier-Stokes equations written in their most general form at steady state. Let us define

$$\overrightarrow{\overrightarrow{T}} = -\overline{p}\,\overrightarrow{\overrightarrow{I}} + \eta\left(\overrightarrow{\overrightarrow{\mathrm{grad}}}\vec{v} + \overrightarrow{\overrightarrow{\mathrm{grad}}}^{\top}\vec{v}\right), \tag{II.A.25}$$

where $\overrightarrow{\overrightarrow{I}}$ is the unit tensor, $\overrightarrow{\overrightarrow{\mathrm{grad}}}$ is the matrix gradient operator, $\overrightarrow{\overrightarrow{T}}$ is the bulk mechanical stress tensor, $^{\top}$ is the transpose operator, ρ and η are the bulk density and shear viscosity of the fluid, respectively, $\overline{p}$ is the pressure, and $\vec{f}$ represents non-electromagnetic volume forces (*e.g.* gravity). Navier-Stokes equations can be considerably simplified, by considering constant bulk physical properties, where only the Lorentz force $\vec{f}_{\mathrm{L}}$ is present, and where p is the pressure corrected by gravity:

$$\rho\left(\vec{v}\cdot\overrightarrow{\mathrm{grad}}\right)\vec{v} = -\overrightarrow{\mathrm{grad}}\,p + \eta\vec{\Delta}\vec{v} + \vec{j}\times\vec{B}. \tag{II.A.26}$$

II.A.2.c Dimensionless equations and the low-Rm approximation

The low-Rm assumption has a direct consequence on the mechanical equations, particularly on the Lorentz force expression. For a moving electroconductive fluid exposed to a strong outer DC magnetic field $B_0\vec{e}_s$, $\vec{f}_{\mathrm{L}}$ can indeed be approximated as:

$$\vec{f}_{\mathrm{L}} = \vec{j}\times\vec{B} \sim \vec{j}\times\vec{B}_0. \tag{II.A.27}$$

Consequently, Eq. (II.A.26) is scaled as such:

$$\left(\vec{v}^{\star}\cdot\overrightarrow{\text{grad}}^{\star}\right)\vec{v}^{\star}=-\overrightarrow{\text{grad}}^{\star}p^{\star}+\frac{1}{\text{Re}}\vec{\Delta}^{\star}\vec{v}^{\star}+\frac{\text{Ha}^2}{\text{Re}}\vec{j}^{\star}\times\vec{e}_s, \tag{II.A.28}$$

where $p^{\star}=p/\rho V^2$. The two dimensionless numbers appearing in the right-hand side of Eq. (II.A.28) are defined as:

$$\text{Re}=\frac{\text{Inertial effects}}{\text{Viscous effects}}=\frac{\rho V L}{\eta}, \tag{II.A.29}$$

that is the well-known (hydrodynamic) Reynolds number, and

$$\text{Ha}=\frac{\text{Electromagnetic effects}}{\text{Viscous effects}}=B_0 L\sqrt{\frac{\sigma}{\eta}}, \tag{II.A.30}$$

which is the Hartmann number. A third dimensionless number, the Stuart number, can be defined from Ha and Re:

$$\text{N}=\frac{\text{Electromagnetic effects}}{\text{Inertial effects}}=\frac{\text{Ha}^2}{\text{Re}}, \tag{II.A.31}$$

In this work, Eq. (II.A.28) (involving $\vec{j}^{\star}$) shall be used in Sec. III.C, App. D.3.a. For future prospects concerning the "bubble MHD problem" (see App. D.4), this formulation should be also favoured. Another formulation expressing the Lorentz force with respect to the induced magnetic field $\vec{b}^{\star}$ can be derived using Eq. (MA), and shall be used in Sec. III.B, where a $(\vec{v},\vec{B})$ formulation is implemented:

$$\left(\vec{v}^{\star}\cdot\overrightarrow{\text{grad}}^{\star}\right)\vec{v}^{\star}=-\overrightarrow{\text{grad}}^{\star}p^{\star}+\frac{1}{\text{Re}}\vec{\Delta}^{\star}\vec{v}^{\star}+\frac{\text{Ha}^2}{\text{ReRm}}\frac{b}{B_0}\overrightarrow{\text{curl}}^{\star}\left(\vec{b}^{\star}\right)\times\vec{e}_s. \tag{II.A.32}$$

II.A.3 Initial and boundary conditions

Initial conditions are required to define all the MHD variables at the initial instant for time-varying problems. In this study, initial conditions are not required to solve for the dynamic MHD problems emphasising the coupling between MHD and surface rheology in permanent regime. In this section, we shall describe the different kinds of MHD boundary conditions.

There are two types of boundary conditions (BCs) in MHD: mechanical BCs for $\vec{v}$, and electromagnetic BCs for $\vec{B}$ or $\vec{j}$, depending on the chosen formulation. These BCs are defined at the boundaries of the fluid domain under consideration. We shall distinguish three kinds of BCs in this work. First, the boundaries can be located at the interface between the liquid metal and a solid wall, and are referred to as “wall” BCs. They can also simply represent the boundaries of the computational domain,

e.g. BCs characterising the fluid at infinity for duct flows. In this case, they are denominated "inlet" or "outlet" BCs. Finally, they can be located at the interface between two different fluids, *e.g.* at a liquid/gas interface in this work. This interface can be assumed as totally free of "polluting species" (*i.e.* surfactants for aqueous solutions, or oxides in the case of liquid metals), leading to "free-surface" problems. More generally, the interface between two fluids may be more or less polluted, which contributes to generate surface dynamics more or less coupled with bulk dynamics. For a proper formulation of this last type of BCs, a balance is applied to an infinitesimal control volume straddling the interface. This point is particularly detailed in Sec. II.B, dedicated to fundamentals of steady surface rheology. In the following section, we focus on the description of dynamic and electromagnetic BCs for wall and inlet/outlet BCs.

II.A.3.a Wall boundary conditions

Dynamic BCs

At an impermeable, rigid, non-moving wall, the velocity is uniformly zero, due to viscosity effects. This is the no-slip BC, or Dirichlet BC for vanishing velocity:

$$\boxed{\vec{v}\big|_{\text{wall}} = \vec{0}.} \tag{II.A.33}$$

If the wall is now assumed to be moving along a tangential direction $\vec{t}$ at a given velocity v_t (as in Secs. III.B.1.a and III.B.2.c about a rotating floor BC), the no-slip and impermeability BCs are written:

$$\boxed{\vec{v}\cdot\vec{t}\,\Big|_{\text{moving wall}} = v_t, \quad \vec{v}\times\vec{t}\,\Big|_{\text{moving wall}} = \vec{0}.} \tag{II.A.34}$$

Electromagnetic BCs

Both $\vec{B}$ and $\vec{j}$ are solenoidal fields. Therefore, the normal component of both fields is continuous across a given interface. In this study, we shall only focus either on perfectly insulating walls or on liquid/gas interface. The condition for the electric current, used when a potential formulation is favoured, is quite straightforward. The electric current cannot penetrate into the wall, and thus the normal component of $\vec{j}$ vanishes at the wall:

$$\boxed{\vec{j}\cdot\vec{n}\big|_{\text{wall}} = 0,} \tag{II.A.35}$$

where $\vec{n}$ is the normal outer to the wall. If the induction equation is preferred, the previous condition with respect to $\vec{B}$ yields:

$$\overrightarrow{\text{curl}}\left(\vec{B}\right)\cdot\vec{n}\Big|_{\text{wall}} = 0.$$

As such, this condition is not usually a useful condition. In some cases, it is possible to specify more useful boundary conditions for $\vec{B}$. For instance, in the case of an electroconductive flow subjected to an outer DC field $B_0\vec{e}_s$, it is possible to write $\vec{B} = \vec{B}_0 + \vec{b}$ according to Eq. (II.A.9), where $\vec{b}$ is orthogonal to the direction of the outer field, in link with the low-Rm assumption. Now, following [33], let us suppose that, for some symmetry reasons, one of the component of $\vec{b}$, say the component b_t along a given $\vec{e}_t$ direction, can be expressed as a "current stream function" using (MA). Hence, the condition $\vec{j} \cdot \vec{n} = 0$ written at the liquid metal boundaries means, based on the definition of a stream function, that these boundaries constitute a streamline for $\vec{j}$, so that $b_t = \text{Cst}$ along these lines. Consequently, in this particular physical layout, it is possible to put at the liquid boundaries, with no loss of generality:

$$\boxed{b_t|_{\text{wall}} = 0.} \tag{II.A.36}$$

It is made the most of BC (II.A.36) in Sec. III.B.1.a about the annular MHD viscometer.

II.A.3.b Inlet/Outlet BCs

The inlet/outlet boundary conditions must address the critical issue of modelling the flow behaviour at infinity, without introducing non-physical artefacts due to necessary approximations. One typical application of such boundary conditions involves duct flows, where the focus is put on a particular section of the duct, as shown in Fig. II.A.2. In this work, the inlet/outlet BCs shall be mentioned in App. D.4, where the first approach towards the description of dispersed MHD flows is set up.

Dynamic BCs

The inlet boundary condition often expresses the velocity field of a fully established flow, like the Poiseuille flow for pure hydrodynamics. In MHD, a reference study about MHD duct flows with perfectly insulating walls is given in [33]. Contrary to the Hartmann flow detailed in Sec. I.B.1.a, where the walls perpendicular to the magnetic field are of infinite extension, the so-called Shercliff flow describes the MHD flow patterns confined into a rectangular duct. The influence of the confinement is taken into account through the side layers, whose normal is perpendicular to the outer magnetic field, that are called the *Shercliff layers*. Contrary to the Hartmann layers, the Shercliff layers play a more classical passive role of matching the core solution with the no-slip BC at the wall. The analytical solution corresponds to a fully developed MHD velocity profile, depending on the value of the Hartmann number (including the Poiseuille profile when $\text{Ha} = 0$). The explicit expression and some hints at the analytical calculation are given in App. C. The inlet velocity thus writes:

$$\boxed{\vec{v}|_{\text{inlet}} = \vec{v}_{\text{Sh}}.} \tag{II.A.37}$$

The outlet boundary condition is more challenging. The modelling of a duct portion is often justified by the presence of what we generally call an obstacle. This can

be a geometrical obstacle, but not only: thermal or chemical source or sink, electromagnetic obstacle…Obstacle means here something that may alter the flow between the inlet and the outlet of the duct section. The convection of resulting flow structures through the outlet of the pipe section must be eased without causing artificial flow distortions. Given these requirements, a zero-pressure, no viscous stress type of boundary condition is implemented at the outlet of duct flows:

$$p_{\text{outlet}} = 0, \quad \eta\left(\overrightarrow{\text{grad}}\vec{v} + \overrightarrow{\text{grad}}^{\top}\vec{v}\right)\cdot\vec{n}\Big|_{\text{outlet}} = 0, \tag{II.A.38}$$

where $\vec{n}$ is the normal outer to the outlet section. This boundary condition is physically equivalent to a boundary that is exiting into a large container. It is stable and admits total control of the pressure level along the entire boundary [59], provided some implementation precautions are taken (see App. D.4).

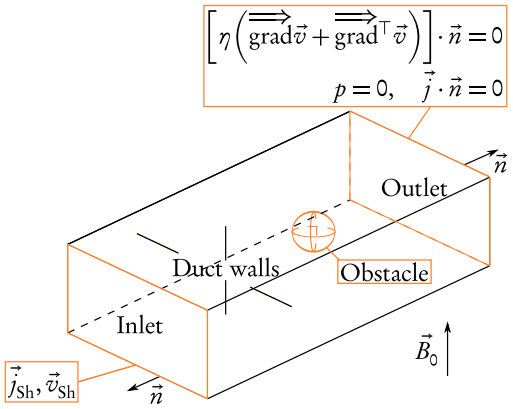

Figure II.A.2 – Inlet/outlet boundary conditions for a typical duct flow.

Electromagnetic BCs

Similarly to the mechanical inlet BC, the electromagnetic boundary condition at the inlet of the duct section must be consistent with the fully established Shercliff flow (in practise, the $\vec{j}\cdot\vec{n} = 0$ condition is still fulfilled, see App. C):

$$\vec{j}\Big|_{\text{inlet}} = \vec{j}_{\text{Sh}}. \tag{II.A.39}$$

At the outlet, it is usual to implement Eq. (II.A.35) for $\vec{j}$:

$$\vec{j}\cdot\vec{n}\Big|_{\text{outlet}} = 0. \tag{II.A.40}$$

As specified in the literature dedicated to MHD flows around obstacles (see, *e.g.* [57, 58]), this BC is exact only when averaged across the outlet. However, we apply it locally, which results in neglecting the currents normal to the outlet. These currents

being of the order 1/Ha, this approximation remains relevant as long as $\mathrm{Ha} \gg 1$, whatever the distance between the obstacle and the outlet cross-section. For small Ha values, a "buffer" region can be introduced, where the perturbations induced by the presence of the obstacle may freely expand, until they are totally damped. In this case, the Shercliff flow is physically representative of the flow patterns at the outlet, and Eq. (II.A.40) shall be implemented as the outlet electromagnetic BC.

II.A.3.c Liquid/gas interface

Special care must be taken to express the electric and mechanical influence of the oxide layer on core MHD. As such, it is at the heart of the coupling process between MHD and surface rheology. The following section clarifies the electromagnetic treatment that we shall adopt for the liquid/gas interface. The mechanical interfacial BC is entirely detailed in the following chapter, devoted to surface dynamics.

Oxide layer and electric current

The electromagnetic boundary conditions that must be written at a gradually oxidising liquid/gas interface are not trivial. Among others, the issue arises as to whether the oxide layer could question the relevance of a perfectly insulating boundary, by introducing conductivity gradients between the electroconductive fluid and the gas. To address this issue, let us consider a diffuse interface, and therefore a volume description of the gradually oxidising interface, as shown in Fig. II.A.3.

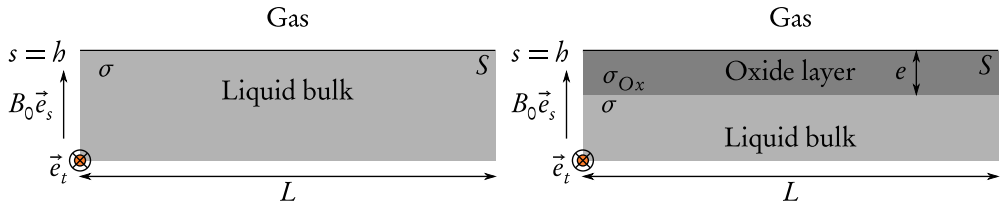

(a) – Pure interface. **(b)** – Oxidised interface.

Figure II.A.3 – Interface oxidation and electromagnetic BCs.

When it is pure, there is *a priori* no reason to distinguish it from the sub-phase. The gas-liquid interface S is located at a given altitude, say, $s = h$, and its electrical conductivity is supposed to be σ (see Fig. II.A.3(a)). When an oxide layer with thickness e is formed, and with a conductivity σ_{Ox} (see Fig. II.A.3(b)), an additional liquid-solid interface appears, between the liquid bulk and the solid interface. Classically, to take the influence of a wall with normal $\vec{e}_s$, thickness e, typical length L and conductivity $\sigma_{Ox} \neq \sigma$ into account, the condition at the fluid boundary is written as:

$$\vec{j} \cdot \vec{n}\Big|_{\text{wall}} = \vec{j}\Big|_{\text{wall}} \cdot \vec{n},$$

for the electric current and

$$b_t = \frac{e\sigma_{Ox}}{L\sigma} \frac{\partial b_t}{\partial s}\bigg|_{\text{wall}},$$

for the electric current stream function b_t [56]. As previously exposed in Sec. I.B.2.b, the oxide forms a thin layer that prevents the oxidation from diffusing further into the liquid sub-phase, and the thickness $e \sim$ a few nm [52]. These values are usually much smaller than the typical length value, ranging from $L \sim 10^{-3}$ m to 1 m. In practise, $\sigma_{\mathrm{Ox}} < 1\,\mathrm{S{\cdot}m^{-1}} \ll \sigma$ (see [60] for an evaluation of gallium oxide conductivity), and we assume that the electric current flowing through the oxide layer (proportional to σ_{Ox}) can be neglected compared to the current flowing in the liquid metal (proportional to σ). As such, the condition $e\sigma_{Ox}/L\sigma \ll 1$ is always fulfilled. Consequently, both Eqs. (II.A.35) and (II.A.36) (provided the previously mentioned prerequisites) are valid at a liquid/gas interface, as well as the assumption that the location of the interface remains fixed at $s = h$.

The electromagnetic boundary condition at a liquid/gas interface is thus considered equivalent to the classical electromagnetic boundary condition written at a non-conducting wall[1]. This approximation implies a significant modelling simplification: the impact of a gradually oxidising interface is therefore only considered from the mechanical point of view. Surface dynamics acts as a particular boundary condition for bulk MHD, through the surface velocity $\vec{v}_S$:

$$\boxed{\vec{v}|_{\text{interface}} = \vec{v}_S.} \tag{II.A.41}$$

This general formulation encompasses the wide range of fluid surface behaviours, from slip to no-slip conditions, by means of a momentum balance applied to an infinitesimal control volume straddling the interface. There are other existing boundary conditions available in the literature, used for describing fluid-fluid interfaces, the best-known being the mixed Navier slip BC:

$$\vec{v}_S + \beta \left.\frac{\partial \vec{v}}{\partial n}\right|_S = 0,$$

where β is referred to as the "slip length", though it could be rather thought of as a "slip depth". However, the determination of the coefficient β is often based on heuristic reasons, and leads to the vanishing of the tangential velocity component at the distance β outside the wall. As such, this method lacks somewhat of physical background, contrary to the approach based on the jump momentum balance, that we shall consistently adopt all along this thesis work. The governing physical phenomena and equations of surface rheology must now be introduced, in order to determine $\vec{v}_S$ and close the mathematical problem.

[1] Strictly speaking, this is an approximate description of the "true" micro-scale electromagnetic behaviour of the liquid/gas interface. Anticipating on Sec. II.B.1.b, one could actually formally define *in-excess* surface electromagnetic quantities, involving such parameters as, *e.g.*, an interfacial electrical conductivity σ_S. By definition, these surface-excess electromagnetic quantities would represent the amount of the corresponding quantity *assigned* to the interface, in order to model their strong variability across the interface. They do not correspond to the bulk quantities *valued* at the interface, in which case they would be simply called surface (and not surface-excess) quantities. Within the scope of this study, the choice is made to leave such considerations about surface-excess electromagnetism aside from the analysis, as an insightful outlook of the present thesis work. With this respect, the theoretical foundations introduced by Albano and Bedeaux [61] could be a relevant starting point.

II.B Introduction to surface rheology

Surface rheology is "the field of science that studies the response of mobile interfaces to deformation" [20]. This field is classically encountered in problems focusing on the interplay between the conventional 3-D hydrodynamics of a supporting sub-phase flow, and the 2-D dynamics of a so-called fluid surface, which acts as a boundary condition for the bulk flow. In the literature, this boundary condition is classically influenced by a (mono)layer of molecules called "surfactants" (detergents, lipids, proteins...), which introduces additional interfacial stresses and may experience interfacial transport. Interfacial (or surface) rheology describes the complex mechanisms governing this transport, and the influence upon the 2-D (and thus 3-D) flow.

In this study, the focus is placed upon the interface between a liquid metal and a gaseous phase. Here, the presence of metallic oxides over a bath of liquid metal is appraised as an original source of surface contamination. As previously emphasised in Sec. I.C.2, thermodynamic equilibrium is assumed all along this work, in link with a uniform coverage of the liquid metal/gas interface by the metallic oxides. Thus, there is no need to consider the surface transport of these metallic oxides. Besides, as already shown at the end of the previous chapter, surface electromagnetism is not taken into account, partly because of the low electrical conductivity and the thinness of the oxide layer. As a consequence, only the *surface dynamics* of the liquid/gas surface is investigated in the following text.

In this chapter, the fundamental physical mechanisms involved in surface dynamics are thus highlighted. First, the concept of 2-D “zero-thickness” interface is introduced. This concept results in the introduction of physical quantities characterising the interface, *i.e.* the rheological parameters, which are then phenomenologically described. Finally, the governing equations are given, along with the dimensionless groups characterising the interfacial transport of momentum.

II.B.1 From the microscale to the macroscale view of a fluid interface

II.B.1.a Guggenheim and Gibbs approaches

A fluid/fluid interface may be intuitively conceptualised as a very thin membrane, which separates two distinct media defined by their own bulk properties. This transition area, through which the properties of each fluid are subjected to sudden changes, may be described according to two different approaches, as described in Fig. II.B.1. The first approach, named Guggenheim approach, bears on a microscale description of the interface. The latter is seen as a diffuse area of interpenetration of the two adjacent sub-phases. The second approach, named Gibbs approach, is based on a macroscale

view of the interface. The latter is seen as a zero-thickness surface, strictly separating the two adjacent media [62].

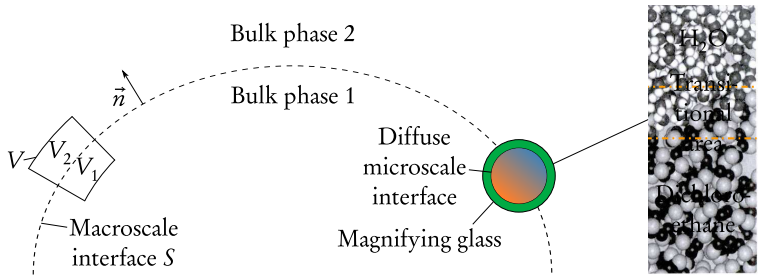

Figure II.B.1 – Gibbs (macroscale) and Guggenheim (microscale) view of a fluid interface [20]. Zoom: example of molecular dynamics simulation [63].

The Guggenheim approach does not require a particular modelling effort, the bulk variables being locally conserved everywhere. However, the strong gradients of physical properties limit the geometrical extent of this description, typically a few times the interface thickness. Such a limited spatial extent prevent us from modelling both the bulk and interfacial dynamics. In order to investigate the coupling between bulk MHD and surface rheology, the Gibbs approach is favoured in this work. This approach, compatible with continuum fluid mechanics at standard length scale ($\geq 1\,\mu$m), requires the introduction of surface properties, as it is now explained.

II.B.1.b In-excess surface quantities

Following [20], let $\boldsymbol{P}$ be a generic physical quantity. From the point of view of a macroscopic observer, the total amount Ψ_i of $\boldsymbol{P}$ contained within a control volume V_i (excluding the interface S) defined in phase i ($i = 1,2$, see Fig. II.B.1) can be expressed in terms of the generally discontinuous volumetric density field ψ_i (amount of the property $\boldsymbol{P}$ per unit volume):

$$\Psi_i = \iiint_{V_i} \psi_i \, \mathrm{d}V.$$

Besides, from the microscale point of view, a "true" field density ψ can be defined, fully continuous throughout the volume $V = V_1 \oplus V_2 \oplus S$ (where $\oplus$ stands for the mathematical union of geometrical subspaces). The true total amount Ψ of $\boldsymbol{P}$ in V writes with respect to the continuous volumetric density field ψ:

$$\Psi = \iiint_{V} \psi \, \mathrm{d}V.$$

In the vicinity of the interface S, differences between the densities ψ and ψ_i emerge, due to the large normal gradients of ψ in the transitional zone. In order to reconcile the usual (discontinuous) macroscale view of fluid interfaces with the true (continuous) microscale view, the residual difference:

$$\Psi_S = \Psi - \Psi_i$$

is assigned to the macroscale surface S as representing the total surface-excess amount of $\boldsymbol{P}$ in S. As shown in Fig. II.B.2, this leads to the definition of the surface-excess density field ψ_S, such as:

$$\Psi_S = \iint_S \psi_S \, \mathrm{d}S$$

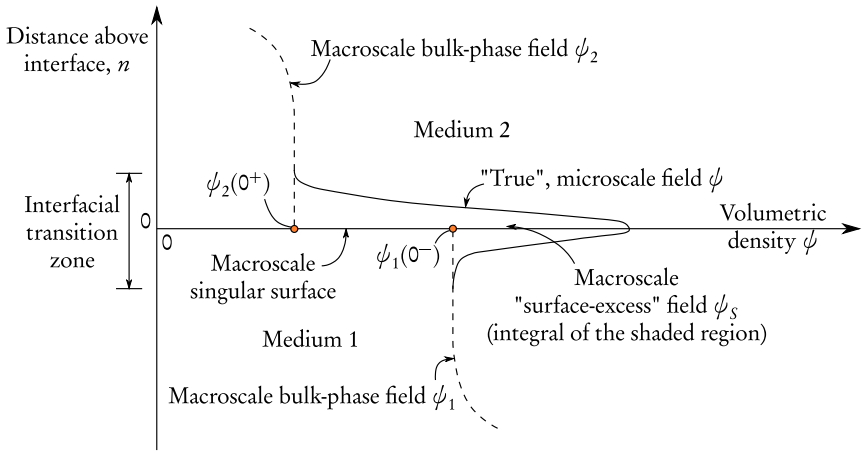

Figure II.B.2 – The macroscale bulk and surface excess fields, and the interfacial transition zone [20].

As pointed out in [20], ψ_S is *not* to be regarded as the actual amount of $\boldsymbol{P}$ per unit area at a given point of the interface (in which case it should only be qualified as a surface field, not surface-excess). ψ_S is the amount of $\boldsymbol{P}$ per unit area *assigned* to the interface, resulting from the discontinuous macroscale approach. However, velocity is a notable exception to this statement. Indeed, as the thermodynamic equilibrium is consistently assumed (see Sec. I.C.2), there is no mass-transfer through S. Thus, the bulk-phase velocity is always continuous across the interface. Consequently, the surface velocity $\vec{v}_S$ actually represents the "true" velocity at a given point of the interface.

It is obvious from Fig. II.B.2 that the definition of surface-excess quantities depends on the (arbitrary) choice of the location of the zero-thickness separating surface S. In the practical case of liquid metals, the gradually oxidising interfacial layer (representing the interfacial transition area) is certainly extremely thin (a few nm), but the interface must be positioned in this thinness. Let us consider the surface property $\boldsymbol{P} = \text{Mass}$, which leads to the definition of surface density ρ_S. To clear up the positioning ambiguity, in this thesis work, the location of the dividing surface is set such as $\rho_S = 0$, according to Gibbs convention. Surface density is then vanishingly small, and is not taken into account all along this study. Within the Gibbs approximation, the interface is considered as non-massive.

Now, apart from density fields, the previous analysis can be extended to density fluxes of a given surface property $\boldsymbol{P}$ across the fluid/fluid interface. This identification process lead to the definition of the surface-excess pressure dyadic (or surface stress tensor) for $\boldsymbol{P} = \text{Linear momentum}$. The modelling of this tensor, which implies the definition of the three remaining interfacial parameters of interest, *i.e.* surface tension and the two surface viscosities, is now introduced.

II.B.2 Interfacial transport of momentum

II.B.2.a The surface mechanical stress tensor

The Navier-Stokes equations (II.A.24) for a Newtonian incompressible fluid bring into play the bulk mechanical stress tensor, defined in Eq. (II.A.25). Similarly to bulk dynamics, and stemming from the previous analysis about in-excess surface quantities, a surface-excess mechanical stress tensor can be defined, within the Gibbs approach of a Newtonian interface [64]:

$$\overrightarrow{\overrightarrow{T_S}} = \left[\gamma + (\varkappa_S - \eta_S)\,\mathrm{div}_S\left(\vec{v}_S\right)\right]\overrightarrow{\overrightarrow{I_S}} + \eta_S\left[\left(\overrightarrow{\overrightarrow{\mathrm{grad}_S}}\,\vec{v}_S\right)\bullet\overrightarrow{\overrightarrow{I_S}} + \overrightarrow{\overrightarrow{I_S}}\bullet\left(\overrightarrow{\overrightarrow{\mathrm{grad}_S}}^{\top}\vec{v}_S\right)\right], \tag{II.B.1}$$

where $\overrightarrow{\overrightarrow{T_S}}$, $\overrightarrow{\overrightarrow{I_S}} = \overrightarrow{\overrightarrow{I}} - \vec{n}\otimes\vec{n}$ and $\overrightarrow{\overrightarrow{\mathrm{grad}_S}}$ are the surface-excess mechanical stress tensor, the surface projection (or identity) tensor and the surface (matrix) gradient operator, respectively; div_S is the surface divergence operator, $\vec{n}$ is the unitary vector normal to the interface, and $\bullet$ and $\otimes$ stand for the mathematical (ordinary) matrix product and tensor product, respectively. This linear expression for the surface mechanical stress tensor is called the Boussinesq-Scriven constitutive expression. This surface-excess stress tensor can then be written as the sum of the isotropic surface-excess tensor based on the surface tension γ, and the surface-excess viscous stress tensor based on the surface viscosities η_S and $\varkappa_S$. These three rheological parameters are now phenomenologically introduced.

For the sake of convenience, the "surface-excess" denomination will be replaced by the single term "surface", *e.g.*, the surface-excess mechanical stress tensor shall be consistently referred to as the surface mechanical stress tensor, or merely, the surface mechanical tensor. We remind that this (now implicit) notation does not correspond to the mechanical tensor valued at the interface, but assigned to it.

II.B.2.b Phenomenological approach of the basic properties of interfacial rheology

Interfacial tension

Let us (mentally) carry out the simple experiment consisting in stretching a film attached to an inert wall, as depicted in Fig. II.B.3. The external operator stretches the film by means of a rod, by applying the force $\vec{F}_{\mathrm{ext}}$ on the system. In doing so, he experiences a kind of opposite spring force, such as when he stops moving the rod, this opposite force $\vec{F}$ exactly cancels $\vec{F}_{\mathrm{ext}}$, and the rod reaches statical equilibrium (Fig. II.B.3(a)). When the rod is released, a mechanical relaxation of the film occurs, and the rod goes back to its initial equilibrium position, as a result of $\vec{F}$ (Fig. II.B.3(b)). Let L be the typical longitudinal extent of the film, and $\vec{e}_x$ the axis aligned with the rod displacement. It can be observed that the force $\vec{F}$ is proportional to L:

$$\vec{F} = \gamma L \vec{e}_x.$$

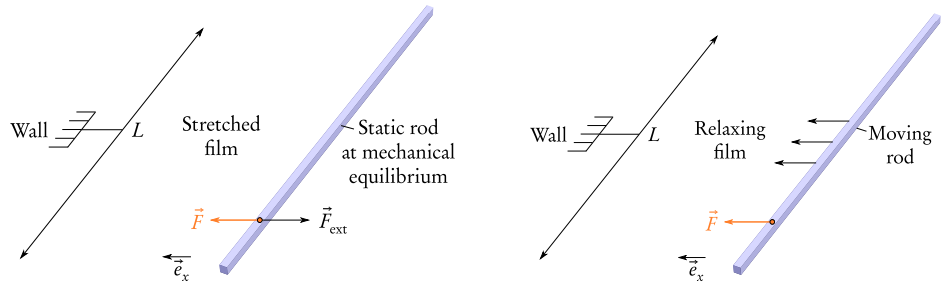

(a) – Stretched soap film at mechanical equilibrium.

(b) – Relaxing film, and motion induced by surface tension.

Figure II.B.3 – Highligthing interfacial tension effects through the example of a liquid film.

The coefficient γ that links $\vec{F}$ and L represents the interfacial tension of the film. The surface tension can then be interpreted as a force per unit length. Now, if the relaxed film moves along an elementary differential line $\mathrm{d}x\vec{e}_x$, then the elementary mechanical work δW due to this displacement is

$$\delta W = \gamma L \mathrm{d}x = \sigma \mathrm{d}S,$$

where $\mathrm{d}S$ is the differential area element generated by the elementary displacement $\mathrm{d}x$ of the line whose length is L, along the $\vec{e}_x$ direction. The quantity γ is thus homogeneous to an energy per unit surface, and can also be called surface energy. This last interpretation matches the thermodynamic description of γ: surface tension originates from short-range intermolecular interactions. These interactions statistically balance in the bulk, but near the interfacial region, a given elementary molecule will have less partners for molecular interactions, resulting in "surface molecules" with a higher energy than the interior molecules. Now, in order to minimise the energy state of the liquid, the number of surface molecules must be contained, leading to a minimal surface area. The interfacial tension γ corresponds to the additional surface energy that must be provided in order to create interfacial area [62].

The magnitude of interfacial tension strongly relies on the quantity of surfactants that are adsorbed at the interface. It diminishes significantly when surface-active materials accumulate at the interface. Indeed, the surfactants are preferentially located at the interface, where they minimise their energy state. The surface energy associated to a surfactant is inferior to the surface energy of a given sub-phase molecule: consequently, owing to the energetic interpretation of surface tension given above, the global surface energy associated to the interface, *i.e.* γ, diminishes. As previously enhanced in Sec. I.B.2.b, this behaviour has been confirmed for liquid metals, the oxides gradually covering the metal surface playing a role similar to surfactants.

Surface shear viscosity

Following [20], let us imagine a simple shear imposed upon a planar fluid surface. As described on the right-hand side of Fig. II.B.4, there are surface stresses acting upon the lineal boundaries of a two-dimensional differential surface fluid element $\Delta x \Delta y$.

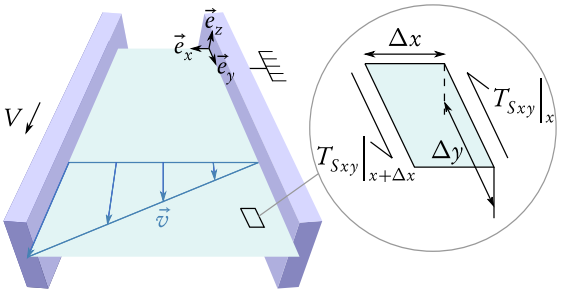

Figure II.B.4 – Surface shear imposed upon a planar fluid surface by the motion of the left-hand wall [20]. On the right: stresses acting upon a differential surface element.

These surface stresses are represented by the component T_{Sxy} of the surface mechanical tensor. In the absence of any external forces, the net force acting upon the surface element can be written as:

$$\left(T_{Sxy}\Big|_{x+\Delta x} - T_{Sxy}\Big|_{x} \right) \Delta y = 0.$$

If now, we divide the previous equation by the surface element $\Delta x \Delta y$, and that we allow this element to become vanishingly small, this yields:

$$\frac{\partial T_{Sxy}}{\partial x} = 0,$$

which stands for the balance of surface linear momentum for a highly-viscous insoluble monolayer subjected to a simple shearing. In order to close the modelling, a constitutive relation between the surface shear $\partial v_y/\partial x$ and the stress T_{Sxy} must be given. It is assumed that this relation consists of a simple proportionality (Newtonian approach), through the coefficient η_S, corresponding to a surface shear viscosity:

$$T_{Sxy} = \eta_S \frac{\partial v_y}{\partial x}.$$

Note that the origin of surface shear viscosity is similar to that of the bulk shear viscosity, in link with jumps of the molecules from one equilibrium position to another, by molecular diffusion [65]. Surface shear viscosity is negligible in the case of a surfactant-free interface, its magnitude increasing monotonically with adsorbed surfactant concentration, until an equilibrium state is reached [20]. As previously enhanced, there seems to be no available data in the literature concerning the evolution of η_S with respect to the level of oxidation of a metallic interface.

Surface dilatation viscosity

Following [20, 65], let us consider the uniform expansion at constant deformation rate of a circular, flat interface, whose surface area S is time-dependent (see Fig. II.B.5). The surface deformation α and the rate of surface deformation $\mathrm{d}\alpha/\mathrm{d}t$ are defined as:

$$\alpha = \frac{S(t) - S_0}{S_0}, \quad \frac{\mathrm{d}\alpha}{\mathrm{d}t} = \frac{1}{S}\frac{\mathrm{d}S}{\mathrm{d}t} = \mathrm{Cst} = A,$$

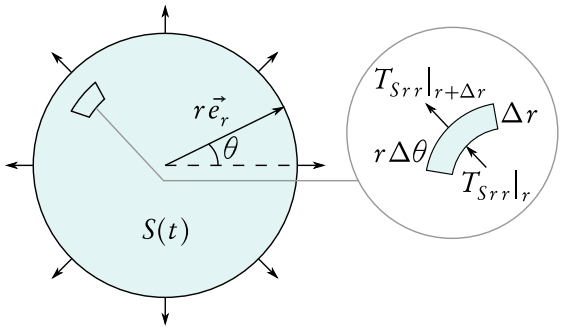

Figure II.B.5 – Uniform dilatation of a planar interface [20]. On the right: stresses acting upon a differential surface element.

where S_0 is the initial surface area. Besides, the balance of forces acting upon the elementary surface element $r\Delta\theta\Delta r$:

$$\left(T_{Srr}|_{r+\Delta r} - T_{Srr}|_r\right) r\Delta\theta = 0.$$

which leads to, when dividing by the vanishingly small elementary surface:

$$\frac{\mathrm{d}T_{Srr}}{\mathrm{d}r} = 0. \tag{II.B.2}$$

The dependence of the surface stress on α and A, *i.e.* the rheological constitutive equation, must now be given. Let us imagine that the force required to expand the highly viscous monolayer is instantaneously removed. Interfacial tension will then act to contract the interface, causing an elastic stress to change the area by a certain value. This surface deformation is related to rearrangement of the molecules, which perform Brownian motion and interact with each other. Let τ_{reaS} be the typical time of this rearrangement process, needed for the molecules to take their new positions upon deformation. When the surface shrinks with rate A, the characteristic time of surface deformation is $\tau_{\mathrm{defS}} = 1/A$. In a quasi-static process, $\tau_{\mathrm{defS}} \gg \tau_{\mathrm{reaS}}$, the molecules have time enough to reach their new equilibrium positions, so that the system is virtually at equilibrium during the entire process. The purely elastic process, directly linked to surface deformation, is only governed by surface tension.

However, in practical situations, the surface deformation is always performed with finite speed, so that $\tau_{\mathrm{defS}} \lesssim \tau_{\mathrm{reaS}}$: the rearrangement may lag behind the deformation. In order to maintain the speed A, an extra-stress must be exerted to force the molecules to go quickly to their new positions (the latter corresponding to α). This extra stress is a viscous stress, proportional to the deformation rate A. The proportionality coefficient is the surface dilatational viscosity $\varkappa_S$ [65]. The surface dilatational viscosity offers an additional dissipation mechanism to the interfacial contraction driven by interfacial tension. Consequently, the constitutive equation for T_{Srr} in the present case is:

$$T_{Srr} = \gamma + \varkappa_S A.$$

The experimental detection of $\varkappa_S$ is much more difficult than η_S, because of the coupling that arises in interfacial dilatational flows between interfacial dilatational viscous and elastic effects. The experimental layout of the annular MHD viscometer theoretically circumvents this difficulty, as explained in Part III. The rare available experimental data tend to show that $\varkappa_S$ and η_S have an identical qualitative behaviour; $\varkappa_S$ is negligible in the case of a pure (surfactant-free) surface, and tends to increase with the surface contamination, up to an equilibrium state [20]. To our knowledge, the determination of $\varkappa_S$ for liquid metals is an original approach.

Now that the basic rheological parameters have been phenomenologically introduced, let us go back to the modelling of the interfacial rheology, and particularly to the equations governing the interfacial transport of momentum.

II.B.2.c Governing equations of surface rheology

Jump momentum balance

Surface dynamics brings a new unknown into play, namely, in-plane surface velocity $\vec{v}_S$, through BC (II.A.41). This stands as the first term of the two-way coupling between the MHD bulk flow and surface equations. The latter can be derived from a momentum balance written on an elementary heterogeneous volume straddling the dividing interface of zero thickness, in accordance with the Gibbs approach (see [64]). As previously said, this allows us to circumvent the issue of the strong and often unknown variability of physical variables across a diffuse interface. In return, the surface-excess quantities, *i.e.* surface tension and surface viscosities, must be introduced to balance the jump in shear stress at the singular interface [20]. To model the relationship between surface stress and surface strain, the Boussinesq-Scriven constitutive law is used [66]. The jump momentum balance at the interface separating medium 1 from medium 2 writes generally:

$$\overrightarrow{\mathrm{div}}_S\left(\overline{\overline{T}}_S\right)+\vec{f}_S=\left[\!\left[\overline{\overline{T}}\cdot\vec{n}\right]\!\right], \tag{II.B.3}$$

where $\overrightarrow{\mathrm{div}}_S$ is the (vector) surface divergence operator, $\vec{f}_S$ is the surface excess force density vector, $\vec{n}$ is the normal vector pointing from medium 1 to medium 2, and $\cdot$ stands for the scalar product. The first term on the left-hand side of Eq. (II.B.3) represents the balance of surface stresses. $\vec{f}_S$ expresses the influence of body forces per unit surface acting on a surface element (*e.g.* electrostatic or magnetic surface forces). Note that, in this study, surface body forces are not taken into account, so that $\vec{f}_S$ shall be consistently dropped off the equations. Finally, the term on the right-hand side of Eq. (II.B.3) stands for the jump in stresses exerted on both sides of the interface by the adjacent phases, due to the discontinuity between them. It stands as the second coupling term of the aforementioned two-way coupling. The $[\![\cdots]\!]$ notation is equivalent to the jump operation $(\cdots_1-\cdots_2)|_S$. Note that the electromagnetic Maxwell stress tensor jump is neglected. The reason is given in [54]: media with "finite conductivity

preclude the occurrence of current sheets", leading to the continuity of the magnetic field across the interface, and the jump of the "Maxwell stress vanishes"[1].

Afterwards, Eq. (II.B.3) can be resolved into vectors normal (tangential) to (along) the interface. This yields:

$$\left[\!\left[\overrightarrow{\overrightarrow{T}}\cdot\vec{n}\right]\!\right]=\left[\!\left[\overrightarrow{\overrightarrow{T}}\cdot\vec{n}\right]\!\right]\bullet\left(\vec{n}\otimes\vec{n}\right)+\left[\!\left[\overrightarrow{\overrightarrow{T}}\cdot\vec{n}\right]\!\right]\bullet\overrightarrow{\overrightarrow{I_S}}. \tag{II.B.4}$$

The first term on the right-hand side of Eq. (II.B.4) is linked to the normal stress boundary condition, while the second term is linked to the tangential stress boundary conditions. Now, let us remind that in Sec. I.C.2, we have assumed that the geometrical configuration of the interface remains constant in time. As highlighted in [20], "specifying the interface shape prior to solution of the relevant is tantamount to specification of the normal velocity $\vec{v}\cdot\vec{n}$ at each point of the interface". In the case of a stratified interface between a liquid metal and a gaseous phase with no mass-transfer, this normal velocity is vanishingly small:

$$\boxed{\vec{v}\cdot\vec{n}\big|_S=0.} \tag{II.B.5}$$

In this case, imposing the normal stress as a BC overspecifies the problem. Either the geometry of the interface is known *a priori* and a boundary condition upon normal velocity at the fluid interface is imposed, or else the normal stress is imposed, the latter being in such circumstances responsible for the geometrical configuration of the fluid interface. Thus, we shall only focus on the tangential stress as a BC at the interface:

$$\boxed{\overrightarrow{\mathrm{div}}_S\left(\overrightarrow{\overrightarrow{T_S}}\right)\bullet\overrightarrow{\overrightarrow{I_S}}=\left[\!\left[\overrightarrow{\overrightarrow{T}}\cdot\vec{n}\right]\!\right]\bullet\overrightarrow{\overrightarrow{I_S}},} \tag{II.B.6}$$

where $\overrightarrow{\overrightarrow{T}}$ and $\overrightarrow{\overrightarrow{T_S}}$ are given in Eqs. (II.A.25) and (II.B.1), respectively. This very general form, sometimes referred to as the tangential component of the jump momentum balance, can be declined for a variety of reference layouts, see *e.g.* [20, 64] for a review.

Let us focus on the contribution of the interfacial tension to this tangential stress BC. As shown in Eq. (II.B.1):

$$\overrightarrow{\overrightarrow{T_S}}=\gamma\overrightarrow{\overrightarrow{I_S}}+\ldots$$

Thus, the specific contribution of γ to the tangential JMB is:

$$\overrightarrow{\mathrm{div}}_S\left(\gamma\overrightarrow{\overrightarrow{I_S}}\right)\bullet\overrightarrow{\overrightarrow{I_S}}=\left[\overrightarrow{\mathrm{grad}}_S(\gamma)\bullet\overrightarrow{\overrightarrow{I_S}}\right]\bullet\overrightarrow{\overrightarrow{I_S}}+\left[\gamma\overrightarrow{\mathrm{div}}_S\left(\overrightarrow{\overrightarrow{I_S}}\right)\right]\bullet\overrightarrow{\overrightarrow{I_S}}. \tag{II.B.7}$$

It can be shown that the $\overrightarrow{\mathrm{div}}_S(\overrightarrow{\overrightarrow{I_S}})$ term is only oriented along the normal direction. Consequently, the second term on the right-hand side of Eq. (II.B.7) vanishes. Furthermore, as stated in Sec. I.C.2, the hypothesis of a uniform coverage of the interface by metallic oxides leads us to neglect surface gradients of rheological parameters. The

[1] There is no reason to take the contribution due to electrostatics into account, because of the large typical size of systems under consideration.

first term on the right-hand side of Eq. (II.B.7), often known as the Marangoni effect, vanishes as well. Therefore, in combination with Eq. (II.B.5), surface tension can be fairly left aside from the analysis. This is the consequence of imposing *a priori* the geometrical shape of the interface, which bypasses the contribution of γ, and of neglecting the Marangoni effect (generated by surface tension gradients), which cancels the contribution of γ-gradients. Nonetheless, it was important to introduce γ among the other rheological parameters. For future prospects, one possible improvement to our modelling would be to loosen the constraint imposed by (II.B.5), which would imply the necessity of implementing the normal surface stress BC, where γ is present. Eqs. (II.B.1) and (II.B.3) supply the necessary theoretical material to address this future issue. Finally, only the surface viscosities η_S and $\varkappa_S$ are kept in the following parts.

II.B.2.d Scaling parameters

According to Eq. (II.B.1), the left-hand side of Eq. (II.B.6) scales as such:

$$\left\| \overrightarrow{\mathrm{div}_S}\left(\overrightarrow{\overrightarrow{T_S}}\right) \bullet \overrightarrow{\overrightarrow{I_S}} \right\| \sim \frac{\eta_S V}{L^2} \text{ and/or } \frac{\varkappa_S V}{L^2}, \tag{II.B.8}$$

depending on the relative weight of surface shear and surface dilatation. The scales L and V are the typical length and velocity, respectively. Now, according to (II.A.25), the right-hand side of Eq. (II.B.6) scales:

$$\left\| \left[\!\left[\overrightarrow{\overrightarrow{T}} \cdot \vec{n} \right]\!\right] \bullet \overrightarrow{\overrightarrow{I_S}} \right\| \sim \frac{\eta V}{L}. \tag{II.B.9}$$

From the balance (II.B.6), two rheological dimensionless numbers can be put forward:

$$\mathrm{Bo}_{\eta_S} = \frac{\eta_S}{\eta L}, \mathrm{Bo}_{\varkappa_S} = \frac{\varkappa_S}{\eta L}, \tag{II.B.10}$$

which are the surface shear and surface dilatational Boussinesq numbers, respectively. The $\mathrm{Bo}_{\eta S}$ number describes the balance between bulk and surface viscous shears, while $\mathrm{Bo}_{\varkappa_S}$ expresses the ratio between the dilatational stress along the interface and the bulk viscous shear. When $\mathrm{Bo}_{\eta_S}, \mathrm{Bo}_{\varkappa_S} \ll 1$, the surface flow is entirely controlled by the sub-phase shear, and the interface acts as a classical free surface in fluid dynamics. Conversely, if $\mathrm{Bo}_{\eta_S}, \mathrm{Bo}_{\varkappa_S} \gg 1$, the surface velocity profile is no longer coupled to the sub-phase flow, and it obeys to its own dynamics, governed by surface viscous shear and/or surface viscous dilatation.

Finally, the tangential stress BC (II.B.6) provides two differential equations along the directions tangential to the interface, and close the mathematical formulation of the overall coupling between MHD and surface rheology. The approximations exposed above have led us to bring only two rheological parameters into play, *i.e.* the two surface viscosities. Let us now introduce the dimensionless formulation of surface dynamics. This overall coupling process is summed up in the following chapter.

II.C Strong coupling

In this chapter, the overall coupling between subphase and surface flows is made evident in Fig. II.C.1. The coupling between electromagnetism and hydrodynamics is achieved by means of the electromotive current and the Lorentz force, with the Hartmann and Reynolds numbers as scaling parameters. Surface rheology provides the velocity boundary condition for solving bulk flow equations, through the surface velocity as a BC, while the MHD model for the bulk flow provides in turn the shear stress at the interface.

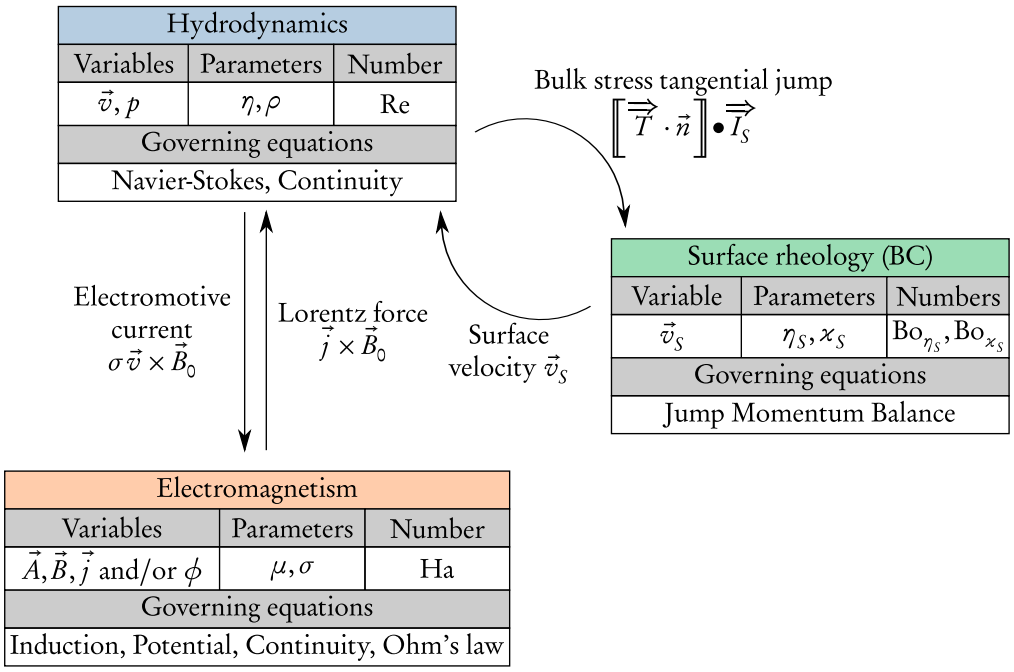

Figure II.C.1 – Overall mathematical coupling.

It can be noticed from Fig. II.C.1 that the coupling is set up between electromagnetism and fluid mechanics, or between surface rheology and hydrodynamics. However, no direct coupling between electromagnetism and surface rheology is introduced here. For future prospects, it could be worthwhile to investigate the possible arising of hypothetical quantities "surface-excess electromagnetic quantities" (*e.g.* surface electrical conductivity σ_S), and their respective contribution to a (weak/strong) coupling between surface rheology and electromagnetism (bottom right corner of Fig. II.C.1).

This chapter ends the fundamentals of MHD and surface rheology. We shall now apply these principles to a particular layout involving the coupling between surface rheology and a supporting stratified MHD flow: the annular MHD viscometer.

Part III

Surface rheology and stratified MHD flow: the annular MHD viscometer

In this part, which concludes the main matter of this thesis work, we put the focus on the following issues. First, our aim is to design and implement an experimental test-bench, in order to estimate the values of surface shear and dilatational viscosities, η_S and $\varkappa_S$, respectively. Moreover, the selected experimental design must allow for enhancing some original MHD flow patterns, in view of taking the first step towards the description of MHD stratified flows.

For this purpose, we investigate the promising features of the annular channel viscometer. First, the physical outlines of this particular layout are detailed: a state-of-the-art of the purely hydrodynamic annular viscometer is thus given, followed by the expected physical insight when an outer magnetic field is added. Afterwards, an analytical study of the annular MHD viscometer is performed, within the limit of ignoring inertial effects. The electrical activity of the Hartmann layers relative to surface viscous shearing is particularly highlighted. Then, inertial effects are brought into play, involving both surface viscous shear and surface viscous dilatation. The interaction between inertia, Lorentz force and surface dynamics is numerically investigated, leading to a variety of atypical MHD flow patterns. Analytical and numerical calculations allow us to propose scaling laws for implementing the experimental test-bench, called the Madip experiment. The latter is carried out in the final chapter: after introducing the experimental requirements, some technical developments are exposed, and first experimental observations are unveiled.

III.A Physical outlines of the annular MHD viscometer

In this chapter, the physical outlines of the annular MHD viscometer are discussed. First, a review about the hydrodynamic design is given. The motivations at the root of its historical development are exposed. Then, the typical experimental layout is introduced, and a distinction is made between the classical "deep-channel" design, and the more recent "shallow-channel" design. The typical flow patterns and the different achievements of the annular viscometer available in the literature are finally highlighted. Afterwards, an external DC magnetic field is added, and Galinstan is used as working fluid. The original layout of the annular MHD viscometer is thus obtained: its general description, expected physical insight and the underlying objectives are detailed.

III.A.1 The hydrodynamic annular viscometer: state-of-the-art

III.A.1.a Historical development and motivation

As mentioned in Sec. I.B.1.b about the historical development of surface rheology, in the early twentieth century, the rising concern about the influence of surface rheology in a variety of industrial applications (food and feed industry, for instance) led to the implementation of numerous experimental test-benches, in order to identify the different rheological parameters and their effects. The classical canal surface viscometer was first proposed in 1937 [67], and used surface pressure-driven interfacial flows. This early technique suffered from an inherent limitation, *i.e.* the difficulty of distinguishing between Marangoni and interfacial viscous effects. Other methods were proposed, all of them facing more or less the same issue. The first canal surface-viscometer that addressed this sensitivity issue is the annular *deep-channel* viscometer, developed by Mannheimer and Schechter in 1970 [31]. Later on, this reference solution has been derived by many authors for determining the rheological properties of a given fluid, covered by a monolayer of surfactants; see *e.g.* [68, 69, 70, 71, 72, 73].

The motivation at the root of this particular technique is to magnify interfacial viscous effects, and particularly those linked to surface viscous shear. Indeed, as further explained, the design of the annular channel viscometer is thought so that, typically, for surfactant-laden interfaces, the surface viscous stress due to in-plane shear dominates bulk viscous forces due to the jump of bulk stresses [20]. But surface viscous shear is not the only surface rheological parameter that may be identified by means of this technique. Quite recently, some authors have also discussed the feasibility of determining the surface dilatational viscosity by adapting the original layout [32]. Let

us now describe the two main designs of the annular viscometer: the classical "deep-channel" layout and the more recent "shallow-channel" configuration.

III.A.1.b Different experimental layouts and associated physical features

The deep-channel annular viscometer

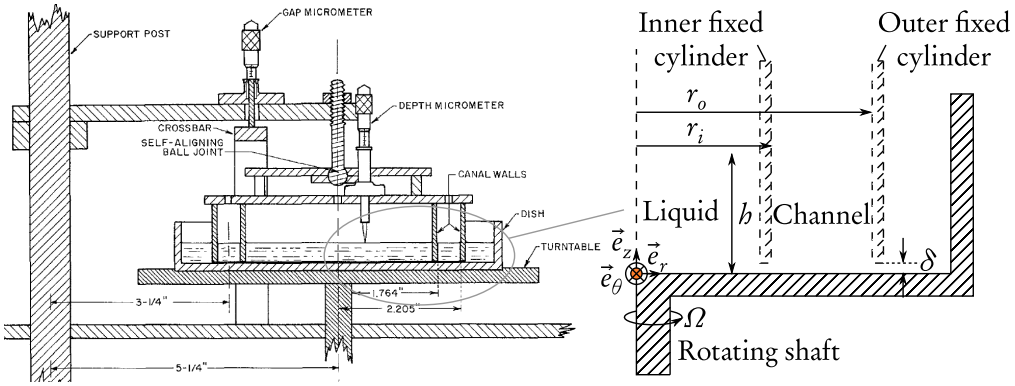

Figure III.A.1 – Schematic cross-section of the classical deep-channel surface viscometer [31].

A schematic view of the deep-channel surface viscometer is given in Fig. III.A.1. Its design consists of two concentric cylinders, lowered into a pool of liquid contained within a dish, to a depth at which the two cylinders nearly touch the bottom of the dish (δ is the gap between the rotating dish and the bottom of the channel walls). The inner and outer radii are r_i and r_o, respectively, and the height of the liquid cross-section of interest is h. The coordinate system used is the cylindrical system $\{O, \vec{e}_r, \vec{e}_\theta, \vec{e}_z\}$. The annular floor of the open channel rotates around the $\vec{e}_z$ axis with a varying angular speed Ω, while the two side walls are maintained fixed. The "deep-channel" denomination is linked to the fact that $r_o - r_i \lesssim h$.

Compared to the best-known Taylor-Couette layout, the vertical shear is particularly emphasized in the annular viscometer configuration. This means that strong velocity gradients are generated along the $\vec{e}_z$-axis, whereas these gradients preferentially develop along the $\vec{e}_r$-axis in the Taylor-Couette case. Anticipating what follows, it is shown later in Eqs. (III.C.14) and (III.C.15) that the coupling term between surface and subphase flows involves $\partial v_r/\partial z$ and $\partial v_\theta/\partial z$ terms, where v_r and v_θ are the radial component and the azimuthal component of velocity, respectively. Consequently, the resulting shearing is expected to be emphasised, and the impact of varying boundary conditions at the liquid surface on the overall flow may be more easily highlighted.

The shallow-channel annular viscometer

The shallow-channel layout is quite similar to the previous deep-channel configuration. The main difference lies in the fact that the height h is now reduced relative to the radial extent of the channel: $h < r_o - r_i$, the depth-to-width ratio is lower than unity. This derived version of the annular channel, proposed in [71, 72], has

a significant advantage over the classical layout. As mentioned earlier, the stronger the velocity gradients along $\vec{e}_z$ are, the easier it is to magnify the coupling terms between surface and subphase flows. When the value of h decreases, the liquid surface is brought down, closer to the rotating floor. In doing so, the jump momentum balance (JMB) written at the interface involves significant vertical bulk shear. The latter is expected to magnify particularly the interactions between bulk and surface dynamics, in the case of an interface gradually covered with surfactants.

Common bulk and surface effects

Both designs allow for a wide variety of hydrodynamic and rheological effects to be tested, beginning with bulk effects. The Reynolds number Re (introduced in Sec. II.A.2.c), based on the typical velocity $V = r_o\Omega$, can be defined as such:

$$\mathrm{Re} = \frac{\rho\Omega r_o^2}{\eta}. \tag{III.A.1}$$

Re governs the balance between inertial and viscous effects. Consequently, either inertial or viscous effects can be highlighted by simply changing the angular velocity Ω (see, *e.g.*, [69]). When the Reynolds number is small enough, the Stokes approximation can be made. Consequently, the only component of velocity is in the $\vec{e}_\theta$ direction, and is a function of r and z only [31]. On the contrary, for higher Re values (but not too high, so that the axisymmetric approximation remains true), due to centrifugal effects, a swirling flow is generated. A distinction is made between the (main) azimuthal flow v_θ, and the (secondary) meridian flow (v_r, v_z) (also referred to as overturning flow). Note that even if the velocity has three non-zero components, the physical problem cannot be (strictly speaking) qualified as three-dimensional in this case, since the independent variables in the entire description of the problem remain only two, r and z. The higher Re flow regime is thus qualified to be 2-D 1/2. Therefore, depending on the Re value, the purely hydrodynamic bulk flow shows promising features, switching from 2-D to 2-D 1/2 topology.

Obviously, the different hydrodynamic flow topologies play a significant role, as far as surface effects now are concerned. If the meridian flow vanishes, it can be shown that only the azimuthal component of JMB is involved. Consequently, the only relevant rheological parameter is surface shear viscosity η_S, the value of which may dramatically affect the main bulk flow [68]. On the contrary, if the inertial effects are significant, the radial component of JMB is brought into play. This means that the interface tends to stretch and that the surface dilatational viscosity $\varkappa_S$ can also affect the surface dynamics [69].

The surface viscosities greatly affect surface dynamics through the surface velocity profile $\vec{v}_S$. The latter is a key physical quantity, which corresponds to another decisive advantage of the annular surface viscometer: the single variable $\vec{v}_S$ potentially contains all the information about both the values of surface viscosities and the bulk dynamics. Provided that a relevant modelling of the flow is implemented, this considerably simplifies measurement issues, and reveals to be a distinct advantage when

working with such opaque fluid as liquid metals. We just need to characterise surface dynamics, which is facilitated by the easy access to the interface allowed by the experimental design. The latter point reveals also extremely interesting in view of controlling surface ageing (oxidation for liquid metals). Indeed, merely by controlling the O_2-rate of the surrounding atmosphere, it may be possible to "functionalise" the interface at will, monitoring its state of oxidation, leading to a variation in its rheological parameters, such as surface viscosities. This would result in a major change in the boundary condition at the liquid/gas interface.

Finally, depending on the value of the Re number, the bulk flow topologies may strongly impact surface dynamics, by bringing different rheological phenomena into play. Surface rheology may then modify in turn both the main and the secondary flows. Some typical flow patterns resulting from this interplay are introduced in the following section, in link with some significant achievements in the literature about the annular surface viscometer.

III.A.1.c Significant achievements and typical flow patterns highlighted in the literature

Stokes flow and surface viscous shearing

A reference study is carried out by Mannheimer and Schechter [31], and provides strong theoretical foundations about the coupling between bulk and surface hydrodynamics, for the deep-channel layout. In addition to the classical hydrodynamic assumptions exposed in Sec. I.C.2, the Stokes approximation is made. The angular speed Ω is indeed considered to be low enough so that the inertial effects can be neglected in the Navier-Stokes equations, and that only the main axisymmetric azimuthal flow $\vec{v}_\theta$ remains. As emphasised in Sec. III.A.1.b, only the surface shear viscosity is thus brought into play. The analytical study of the resulting boundary value problem leads to a solution based on hyperbolic series, referred to as:

$$v_{\theta \mathrm{MS}} = f\left(r, z, \mathrm{Bo}_{\eta_S \mathrm{MS}}\right), \tag{III.A.2}$$

where $\mathrm{Bo}_{\eta_S \mathrm{MS}}$ is the surface shear Boussinesq number (see Eq. (II.B.10)) defined as such:

$$\mathrm{Bo}_{\eta_S \mathrm{MS}} = \frac{\eta_S}{\eta (r_o - r_i)}. \tag{III.A.3}$$

The explicit expression and some hints at the analytical calculation are given in App. A. Surprisingly enough, Mannheimer and Schlechter do not use their solution to investigate the influence of surface viscous shear on bulk flow patterns. Rather, they expand their solution to liquid/liquid interfaces, and carry out experiments about surface flow characteristics of liquids with negligible surface viscosity (see Fig. III.A.2(a)), which is far from the scope of the present study. In this work, Eq. (III.A.2) will serve as an analytical benchmark of the modelling of the annular MHD viscometer, in the asymptotic case of a vanishing outer magnetic field, at low Reynolds number (see Sec. III.B.1.f).

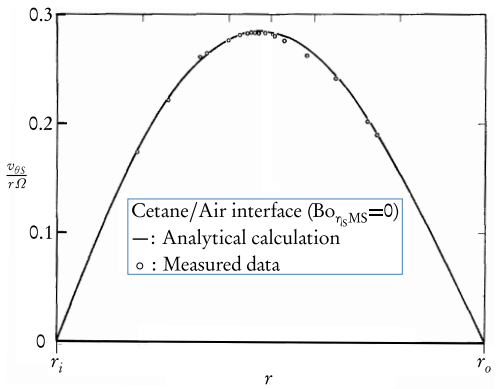

(a) – Comparison of the measured and calculated surface/floor velocity ratio, at different surface positions (Teflon tracers) [31].

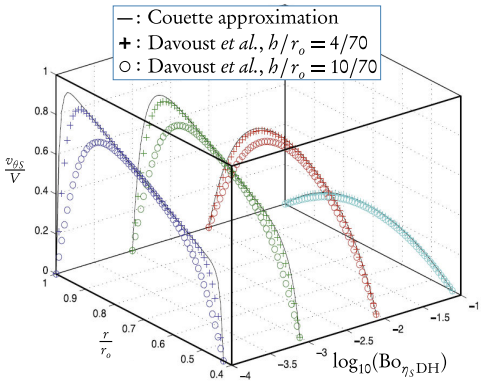

(b) – Surface velocity along the liquid surface, as predicted from Couette solution or from composite solution with different depth-to-width ratios [72].

Figure III.A.2 – Stokes flow and surface viscous shearing in the literature.

Concerning the shallow-channel layout, Davoust *et al.* have proposed an insightful discussion about the shearing of a stratified layer of amphiphilic molecules [72]. The (Stokes) shear flow within the annular channel is calculated by means of an asymptotic expansion, based on the small depth-to-width ratio $h/r_o \ll 1$. The calculation leads to an integral solution based on Bessel functions, referred to as:

$$v_{\theta \mathrm{Da}} = f\left(r, z, \frac{h}{r_o}, \mathrm{Bo}_{\eta_S \mathrm{Da}}\right), \tag{III.A.4}$$

where $\mathrm{Bo}_{\eta_S \mathrm{Da}}$ is the surface shear Boussinesq number, defined this time by:

$$\mathrm{Bo}_{\eta_S \mathrm{Da}} = \frac{\eta_S h}{\eta r_o^2}. \tag{III.A.5}$$

The explicit expression and some hints at the analytical calculation are given in App. B. Similarly to Mannheimer's solution, Eq. (III.A.4) will serve as an asymptotic benchmark in Sec. III.B.1.f. In [72], the authors use the composite solution to investigate both the impact of surface viscous shear and of the depth-to-width ratio on the surface flow. As shown in Fig. III.A.2(b), for a given ratio h/r_o, when surface viscosity decreases significantly (small $\mathrm{Bo}_{\eta_S \mathrm{Da}}$ numbers), surface velocity increases accordingly. This is to correlate with the growing impact of subphase viscous shearing at the liquid surface, which becomes preponderant over surface viscous shear, and tends to align the surface with the rotating floor. Conversely, for large $\mathrm{Bo}_{\eta_S \mathrm{Da}}$ numbers, the surface velocity decreases towards a Poiseuille-like parabolic profile, the surface viscous shear imposing here its own dynamics to interfacial motion. Finally, concerning the influence of the depth-to-width ratio at a given surface viscosity, the smaller this ratio is, the better the velocity profile approaches the classical Couette-like profile. Indeed, a smaller h/r_o value tends to reduce the impact of surface shear on surface dynamics,

for a given chemical state of the interface. The latter observation gives us a dimensioning criterion for the design of the experimental test-bench (see Sec. III.D.1). The depth-to-width ratio should be designed such as $h/r_o \in [1/15, 1/5]$, in order to enhance the coupling between bulk and surface dynamics. If this ratio is lower, surface viscous effects would be irremediably damped relative to bulk viscous effects, if it is higher, surface velocity would be too small to detect any measurable phenomena anyway (even with preponderant surface viscous effects).

Inertial effects and surface viscosities

As emphasised in Sec. III.A.1.b, when the Reynolds number is sufficiently high, a meridian flow due to centrifugal effects is enhanced, and the bulk flow switches from 2-D to 2-D 1/2 topology. In addition to surface viscous shearing, the liquid surface may experience surface dilatation, through the radial component of JMB. In the dedicated literature, the reference studies dealing with the interactions between inertia and surface rheology have been carried out by Hirsa and Lopez [32, 68, 74].

The first decisive result made evident by these authors deals with the feasibility of measuring the surface viscous dilatation $\varkappa_S$, by means of the annular viscometer [32]. By loosening the constraint of Stokes flow, they take advantage of the (axisymmetric) swirling flow for the determination of two ordinary differential equations in directly measurable quantities, *i.e.* surface velocity and its gradients. They also determine a scaling law on the value of the Reynolds number, so that the radial velocity v_{rS} along the surface becomes large enough compared with the azimuthal velocity $v_{\theta S}$. By means of a direct numerical simulation (DNS), they show that for $\mathrm{Re} \lesssim 200$, the Stokes assumption remains true, whereas for $\mathrm{Re} > 200$, the dynamical interactions between the primary and secondary flows become significant, as shown in Fig. III.A.3(a). Consequently, the authors recommend to test values of the Reynolds number up to 200 in order to isolate η_S within the Stokes flow approximation (see also Davoust *et al.* [73]), and then to increase Re up to 10^4, in order to magnify the coupling between inertial effects and surface rheology. This would allow access to the values of $\varkappa_S$, relative to the quantity of surfactants adsorbed at the interface. This scaling law based on Re shall be used in Sec. III.D.1.

Let us momently consider the issue linked to the maximum $\mathrm{Re} = 10^4$ value selected for the range of tested Re numbers. This relatively high value for the Reynolds number might question the assumption of an axisymmetric laminar flow, and more globally, the general approximation of neglecting turbulence, assumed in Sec. I.C.2. However, the Reynolds number defined in the present study by Eq. (III.A.1) (following *e.g.*[68, 69, 73]) is not really physically consistent, as its definition, only based on the outer radius of the annular channel, does not involve the aspect ratio h/r_o. Our definition clearly overestimates the local Reynolds number which remains to be estimated *a posteriori*. Therefore, even a value as large as $\mathrm{Re} = 10^4$ remains consistent here with the assumption of a laminar flow (see e.g. [75, 76] for considerations on the onset of non-axisymmetric instabilities and turbulence in similar layouts).

Another significant result about surface dynamics obtained by Hirsa *et al.* is detailed in [74]. They first show through DNS calculations and experimental measure-

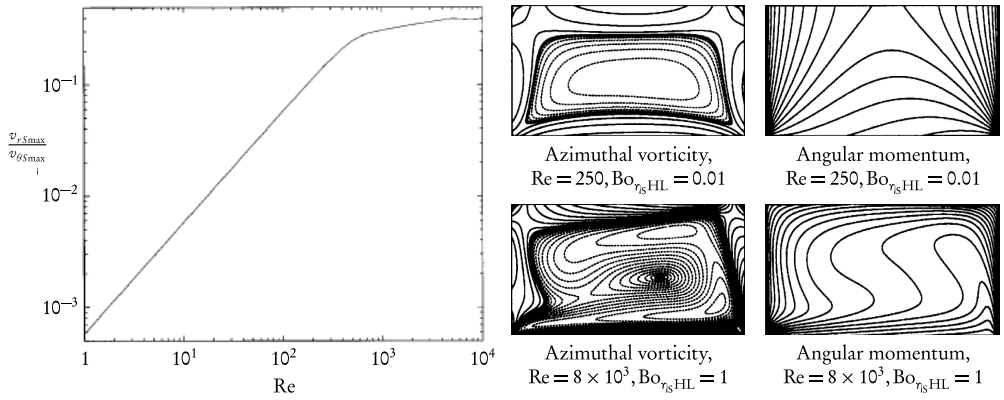

(a) – Computed radial/azimuthal velocity ratio with respect to the Reynolds number, at a surfactant-free interface [32].

(b) – Contours of bulk azimuthal vorticity ω and angular momentum α, depending on the Reynolds and surface shear Boussinesq numbers [68].

Figure III.A.3 – Inertial effects and surface viscosities in the literature.

ments that a uniform coverage of surfactants can occur for a suitable surfactant concentration, allowing to disregard the gradients in surface viscosities. Note that this point gives support to our own approximation made in Sec. I.C.2 about uniform oxidation of liquid metal surfaces. Moreover, they prove that when the surface exhibits an adequate amount of surfactants, the radial component of surface velocity is zero. Consequently, the JMB reduces to no-slip along the radial direction, regardless of the physicochemical state of the interface. The latter condition is equivalent to the following condition for the surface dilatational Boussinesq number (see Eq. (II.B.10)):

$$\mathrm{Bo}_{\varkappa_S\mathrm{HL}} \to \infty, \tag{III.A.6}$$

with

$$\mathrm{Bo}_{\varkappa_S\mathrm{HL}} = \frac{\varkappa_S}{\eta r_o}. \tag{III.A.7}$$

It shows that the respective evolutions of η_S and $\varkappa_S$ with respect to a chemical state of the interface are not necessarily quantitatively identical. Indeed, in this case, $\mathrm{Bo}_{\varkappa_S\mathrm{HL}}$ is very large, while the surface shear Boussinesq number:

$$\mathrm{Bo}_{r_S\mathrm{HL}} = \frac{\eta_S}{\eta r_o} \tag{III.A.8}$$

may range from very small to very large values. The latter point is crucial considering the extreme values for the two Boussinesq numbers that we shall test in this study. It is actually physically consistent to consider asymptotically small Bo_{r_S} and $\mathrm{Bo}_{\varkappa_S}$ numbers, because it corresponds to the classical case of a free surface, totally free of surfactants. However, it is *a priori* not as obvious as far as asymptotically large values are concerned. The previous observation gives us a scaling law that allows us to test such large values. As a consequence, in Secs. III.B and III.C, we select the following (arbitrarily set) asymptotic values: $\mathrm{Bo}_{r_S}, \mathrm{Bo}_{\varkappa_S} \in [10^{-4}, 10^4]$.

Finally, in the previous studies, Hirsa and co-workers mainly focus on surface flow patterns. Concerning bulk flow patterns, these authors investigate the interactions between surface viscous shear only (using condition (III.A.6)) and a supporting annular swirling flow in [68]. These interactions are highlighted in Fig. III.A.3(b), by displaying the contours of the azimuthal vorticity $\omega = \partial v_r/\partial z - \partial v_z/\partial r$, which governs the meridian flow, and the contours of the axial angular momentum $\alpha = r v_\theta$, which governs the main flow. The calculation predicts a secondary overturning flow due to inertial effects, intensifying with Re. As for the surface viscous shearing, the interface consistently evolves from free-surface when $\mathrm{Bo}_{\eta_{SHL}}$ is small (Fig. III.A.3(b), top) to no-slip boundary conditions when $\mathrm{Bo}_{\eta_{SHL}}$ reaches large values (Fig. III.A.3(b), bottom). Note that this study will serve as an asymptotic benchmark in Sec. III.C.2.a.

This state-of-the-art about the purely hydrodynamic annular channel flow patterns is now ended. Let us now add some electromagnetism in it, and put the focus on the original layout of the annular MHD viscometer.

III.A.2 The annular MHD viscometer: an original layout

III.A.2.a Description of the experimental layout

The annular MHD viscometer under consideration in this study is very similar to the shallow-channel surface viscometer described above. Indeed, the depth-to-width ratio h/r_o is low (typically between 1/15 and 1/5, see Sec. III.A.1.c), and the general layout is otherwise similar to Fig. III.A.1, with two main differences, though: now, an outer vertical DC magnetic field $\vec{B}_0 = B_0\vec{e}_z$ is imposed, and the channel is filled with an electroconductive fluid, *i.e.* Galinstan, as shown in Fig. III.A.4.

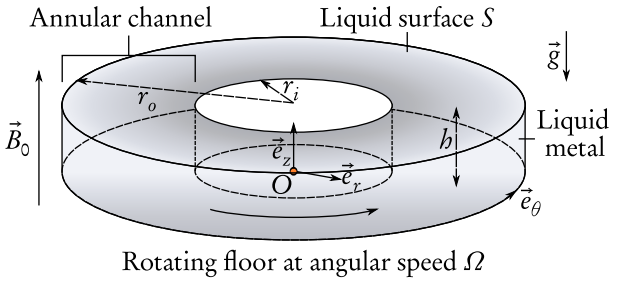

Figure III.A.4 – The annular MHD viscometer.

III.A.2.b Expected physical insight

The electroconductive rotating fluid subjected to the outer magnetic field $\vec{B}_0$ is crossed by motion-induced electric currents $\vec{j}$, and thus constitutes an annular open channel MHD flow. In addition to the numerous hydrodynamic advantages of the shallow-channel annular viscometer exposed in Sec. III.A.1.c, there are a couple of salient features that we can expect from the annular MHD viscometer layout, the first of which dealing with the relevance of promoting the velocity gradients along

the $\vec{e}_z$ direction. It has been shown that these gradients magnify the hydrodynamic coupling between bulk and surface dynamics: they also play a significant role considering the MHD coupling between the velocity field $\vec{v}$ and the magnetic induction $\vec{b}$. Anticipating what follows, it is indeed shown in Eq. (III.B.3) that the generating term for the azimuthal induction $b_\theta \vec{e}_\theta$ is $\partial v_\theta / \partial z$ as well. Favouring gradients along $\vec{e}_z$ thus magnifies the bulk MHD coupling, which in turn affects the coupling with surface dynamics.

The second expected salient feature is linked to the flow topology. It has been seen that the hydrodynamic flow may switch from 2-D to 2-D 1/2 topology, depending on the value of the Reynolds number. Let us imagine that the Reynolds number is high enough so that inertial effects lead to swirling flow patterns (it is mainly the case in practise, the low Re values being difficult to attain). When the electroconductive liquid is subjected to an outer magnetic field, electric current densities are induced. Once again, the (main) components (j_r, j_z) (due to the main azimuthal flow) are distinguished from the (secondary) component j_θ (due to the secondary meridian flow). The MHD bulk flow results from the competition between electromagnetic and inertial effects. Let us now mentally increase the value of B_0, in order to reach a "strong" outer magnetic field. By doing so, the experimental layout becomes comparable to Lehnert's experiment [3], mentioned in the general introduction of this work (see Fig. I.A.2(a)). As previously shown, this experiment was the first to point out the electromagnetic blocking of a supporting MHD flow. This blocking can be linked to the following outstanding MHD phenomenon: the outer magnetic field tends to align flow vorticity along its axis, when a high Hartmann number Ha (see Eq. (II.A.30)) is reached. This original effect, called the *two-dimensionality tendency* of magnetic induction, is now accurately described (see [4] for an extensive introduction to this phenomenon). Now, back to our MHD viscometer, we expect that this MHD 2-D tendency would tend to "freeze" the flow above the rotating floor, similar to what is observed by Lehnert. The secondary flow patterns would then be damped, in favour of the main MHD flow. Consequently, a strong outer magnetic field could bring the MHD flow back to a purely 2-D topology. This would result in a major impact on the coupling with surface dynamics, because only surface viscous shear would be brought into play. Apart from the original flow patterns expected, such a phenomenon would facilitate the selective measurement of η_S and/or $\varkappa_S$, by tuning the value of the outer magnetic field.

Actually, with respect to surface rheology, the final salient feature involves the interactions between the MHD bulk flow and the dynamics of the gradually oxidising interface. As highlighted in the general introduction, the unique properties of the Hartmann layers result in a major impact on the topology of the MHD core-flow (see Sec. I.B.1.a). By altering the interfacial BC, these Hartmann layers could be made electrically active or inactive, which would totally modify the electric circuit inside the fluid. Maybe, it would then be possible to determine atypical flow patterns, that we could link to identified values of surface viscosities, easing their experimental measurement. Finally, the use of a magnetic field could prove beneficial by allowing for greater control of the flow, thus introducing an updated method for measurement of the rheological properties of electroconductive fluids.

In the light of all the previous considerations, the physical insight provided by the annular MHD viscometer is expected to be significant. Let us conclude this chapter by exposing the main objectives and our overall approach to the physical problem.

III.A.2.c Objectives and overall approach

The annular MHD viscometer constitutes a liquid/gas stratified MHD flow. This is a basic study case in view of the description of different MHD two-phase flow regimes. Our first objective is thus to investigate the different flow patterns relative to determined values of the scaling parameters, *i.e.* the Reynolds, the Hartmann and the two Boussinesq numbers.

The second objective is a measurement one. First, thanks to an appropriate modelling, in combination with the development of an experimental set-up, measurement of the surface velocity would then give access to the bulk MHD. Second, we would be able to obtain information about the oxidised surface rheology, because it would be possible to determine the physical properties of liquid metal surfaces, for which only scarce information is available.

The overall physical approach that we shall adopt all along this study about the coupling between subphase and surface dynamics has been made evident in Sec. II.C. In order to address the resulting physical issues previously highlighted, we choose to implement the analytical/numerical/experimental triptych. First, a 2-D analytical investigation of the annular MHD viscometer is proposed in Sec. III.B.1, based on a $(\vec{v},\vec{B})$ formulation, within the approximations $\mathrm{Ha} \gg 1$ and $\mathrm{Ha} \gg \mathrm{Re}$. This analytical study shall be used as a benchmarking case for two numerical studies, the first of which being based on the same $(\vec{v},\vec{B})$ formulation, but with the $\mathrm{Ha} \gg 1$ constraint being loosened (see Sec. III.B.2). The scope of this study is then significantly extended in a 2-D 1/2 numerical calculation based on a potential formulation $(\vec{v},\vec{A},\phi)$, by loosening the constraint $\mathrm{Ha} \gg \mathrm{Re}$, hence taking account of the overturning MHD flow due to centrifugal effects (see Sec. III.C). The analytical and numerical results allow us to determine MHD scaling laws, used in the final chapter to design the experimental test-bench: the Madip experiment. The experimental results obtained so far, in link with the first experiments that we carried out, are finally unveiled in Sec. III.D.

III.B 2-D annular MHD flow and surface viscous shearing

In this chapter, the two-way coupling between the surface viscous shearing of the liquid surface (induced by a gradually oxidising interface) and the supporting 2-D annular MHD subphase flow is set, in the general layout of the annular MHD viscometer. First, using a matched asymptotic expansion based on the small parameter $1/\mathrm{Ha}$, we can express the surface velocity as a coupling variable in the jump momentum balance (JMB) at the liquid surface. By solving the latter through the determination of the Green's function, the whole flow is analytically calculated. Some salient flow patterns are then highlighted, with special emphasis on the Hartmann layers, along with scaling laws for dimensioning the experimental test-bench. Finally, these analytical results are compared to a 2-D numerical study based on the same $(\vec{v},\vec{B})$ formulation, but without the approximation $\mathrm{Ha}\gg 1$. To a certain extent, the following content has been published in [77].

III.B.1 2-D analytical study of the annular MHD viscometer

III.B.1.a Assumptions, notations, equations, boundary conditions and two-way coupling

Notations and assumptions

The system under consideration is the annular open-channel viscometer with a rectangular cross-section, subjected to a strong outer vertical magnetic field $B_0\vec{e}_z$, as depicted in Fig. III.A.4. The inner and outer radius are respectively r_i and r_o, and the height is h, with $h<r_i,r_o$ (indicative values: $r_i=3\,\mathrm{cm}$, $r_o=7\,\mathrm{cm}$ and $h=1\,\mathrm{cm}$). First, some general approximations (justified in Secs. I.C.2 and III.A) are made in order to simplify the physical approach. The annular flow considered is supposed to be a permanent, axisymmetric ($\partial/\partial\theta=0$), incompressible viscous Newtonian flow, with no temperature dependence, so that the bulk physical properties of the liquid metal considered (Galinstan) are considered to be constant (see Tab. I.B.1 for typical values). The interface is considered to be flat, with a capillary length $l_c=\sqrt{\gamma/\rho g}\ll(r_o-r_i)$, where g is the gravity and γ is the surface tension of Galinstan (indicative value: $\gamma=0.534\,\mathrm{N{\cdot}m^{-1}}$, see [29] and Sec. I.B.2.b). Concerning purely electromagnetic assumptions, the quasi-static and the low-Rm approximations are made (see Sec. II.A.1).

Further assumptions are made, concerning the parameters governing the bulk flow dynamics, *i.e.* the Reynolds and the Hartmann numbers, defined as such:

$$\mathrm{Re}=\frac{\rho\Omega r_o^2}{\eta} \tag{III.B.1}$$

for the Reynolds number, where Ω is the angular speed of the rotating floor (see Eq. (III.A.1)), and

$$\mathrm{Ha} = B_0 h \sqrt{\frac{\sigma}{\eta}} \tag{III.B.2}$$

for the Hartmann number. In this chapter, we suppose that Ω is small enough so that the inertial terms and the secondary flows in the Navier-Stokes equations are negligible, which proves to be true as long as the centrifugal force remains much smaller than the Lorentz force. If $\mathrm{Ha} \gg \mathrm{Re}$, then the inertial terms can be neglected. This is all the more justified within the following approximation, which consists in assuming that $\mathrm{Ha} \gg 1$. The Hartmann number is indeed considered to be large enough for a matched asymptotic expansion to be performed for the bulk flow, which is divided into 13 subdomains; all of these domains are displayed in Fig. III.B.1:

- C denotes the core flow;
- HT and HB are the Hartmann layers located along the rotating floor and the top of the bulk flow, respectively (the liquid surface being excluded), with a typical non-dimensional $O(\mathrm{Ha}^{-1})$ thickness when activated;
- SL and SR are the side layers or Shercliff layers located on the left and right walls of the channel, respectively, with typical $O(\mathrm{Ha}^{-1/2})$ thicknesses;
- ATL, ATR, ABL and ABR are the Hartmann layers adjacent to the side layers, at the top left, top right, bottom left and bottom right of the channel, respectively, with typical cross-sections of $O(\mathrm{Ha}^{-1}) \times O(\mathrm{Ha}^{-1/2})$;
- IC_1, IC_2, IC_3 and IC_4 are the corner regions with $O(\mathrm{Ha}^{-1}) \times O(\mathrm{Ha}^{-1})$ cross-sections.

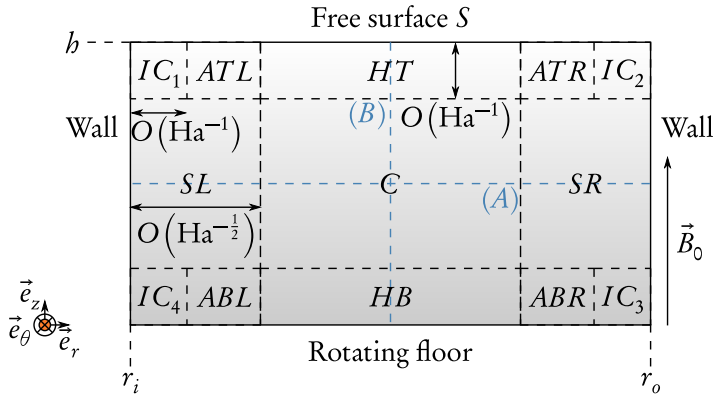

Figure III.B.1 – Subregions of the flow. (A) and (B) are cutting lines used for interpretation of the results.

As a consequence, the velocity $\vec{v}$ is considered to be only azimuthal, because of the negligible contributions of the secondary flows. Even when the magnetic Reynolds number is small, the outer magnetic field can be convected along the $\vec{e}_\theta$ direction inside the fluid. The quantities of interest for MHD can therefore be given as $\vec{v} = v_\theta(r,z)\vec{e}_\theta$ for the velocity field, $\vec{B} = b_\theta(r,z)\vec{e}_\theta + B_0\vec{e}_z$ for the magnetic induction and $\vec{j} = j_r(r,z)\vec{e}_r + j_z(r,z)\vec{e}_z$ for the electric current density inside the fluid.

Finally, the flow of the liquid surface S, with the bulk flow being excluded, is modelled using the tangential component of the JMB (see Sec. II.B.2.c), in which use is made of the surface shear viscosity, η_S. The latter is considered to depend only on the "rate of contamination" of the atmosphere, *i.e.* an O_2-rate, which implicitly requires thermodynamic equilibrium (see Sec. I.C.2). In particular, with the secondary flows being negligibly small, no radial dependence of η_S is taken into account.

Bulk flow

Using Eqs. (II.A.12) and (II.A.32), we can derive the following set of equations along the azimuthal component, based on a $\left(\vec{v},\vec{B}\right)$ formulation, that govern the MHD problem (see [34, 35] for further details about a similar physical layout):

$$\frac{\partial^2 b_\theta^*}{\partial r^{*2}}+\frac{1}{r^*}\frac{\partial b_\theta^*}{\partial r^*}-\frac{b_\theta^*}{r^{*2}}+\frac{\partial^2 b_\theta^*}{\partial z^{*2}}+\mathrm{Ha}\frac{\partial v_\theta^*}{\partial z^*}=0, \tag{III.B.3}$$

$$\frac{\partial^2 v_\theta^*}{\partial r^{*2}}+\frac{1}{r^*}\frac{\partial v_\theta^*}{\partial r^*}-\frac{v_\theta^*}{r^{*2}}+\frac{\partial^2 v_\theta^*}{\partial z^{*2}}+\mathrm{Ha}\frac{\partial b_\theta^*}{\partial z^*}=0. \tag{III.B.4}$$

The superscript * refers to the next dimensionless quantities: $r^*=r/h$, $z^*=z/h$, $v_\theta^*=v_\theta/\mathsf{V}$, $b_\theta^*=b_\theta/\mathsf{b}$, where $\mathsf{V}=h\Omega$ and $\mathsf{b}=\mu\mathsf{V}\sqrt{\sigma\eta}$. Note that V and b are no the "true" typical orders of magnitude of velocity and magnetic induction, which are V and b, but they are used in the first place for facilitating the analytical calculation (see Sec. III.B.1.f).

The boundary conditions with respect to $\vec{v}^\star$ are deduced from Eq. (II.A.33) for the no-slip BC at the motionless side-walls, Eq. (II.A.34) for the moving wall BC at the rotating floor, and Eq. (II.A.41) for the interfacial BC. Concerning $\vec{b}^\star$, it can be shown using (MA) that:

$$j_r=-\frac{\partial(b_\theta/\mu)}{\partial z},\quad j_z=\frac{1}{r}\frac{\partial(r\,(b_\theta/\mu))}{\partial r}.$$

Thus, b_θ/μ is actually a stream function for $\vec{j}$. The environment surrounding the fluid, *i.e.* the atmosphere above the free surface and the walls, is all considered to be insulating. Hence, the boundary conditions at the fluid boundaries are given by Eq. (II.A.36) (see the associated discussion of Sec. II.A.3.c for the interface). Finally, the whole set of BCs allowing to close the mathematical modelling of bulk dynamics is:

$$v_\theta^*(r^*=\frac{r_i}{h},z^*)=\ 0\ ,\qquad b_\theta^*(r^*=\frac{r_i}{h},z^*)=0, \tag{III.B.5}$$

$$v_\theta^*(r^*=\frac{r_o}{h},z^*)=\ 0\ ,\qquad b_\theta^*(r^*=\frac{r_o}{h},z^*)=0, \tag{III.B.6}$$

$$v_\theta^*\ (r^*,z^*=0)\ =\ r^*,\qquad b_\theta^*(r^*,z^*=0)\ \ =0, \tag{III.B.7}$$

$$b_\theta^*\ (r^*,z^*=1)\ =\ 0\ , \tag{III.B.8}$$

$$v_\theta^*\ (r^*,z^*=1)\ =v_{\theta S}^*(r^*). \tag{III.B.9}$$

Surface flow

The boundary condition (III.B.9) brings a new unknown into play, which is the surface velocity $v^{\star}_{\theta S}$. Within the Gibbs approximation (see Sec. II.B), and according to Eqs. (II.B.5) and (II.B.6), the dimensionless JMB can be written:

$$\mathrm{Bo}_{\eta_S}\left(\frac{\mathrm{d}^2 v^*_{\theta S}}{\mathrm{d}r^{*2}}+\frac{1}{r^*}\frac{\mathrm{d}v^*_{\theta S}}{\mathrm{d}r^*}-\frac{v^*_{\theta S}}{r^{*2}}\right)=\left.\frac{\partial v^*_\theta}{\partial z^*}\right|_{z^*=1}. \tag{III.B.10}$$

where the surface shear Boussinesq number, defined as such:

$$\mathrm{Bo}_{\eta_S}=\frac{\eta_S}{\eta h}, \tag{III.B.11}$$

describes the balance between bulk and surface viscous shearing. The following two Dirichlet end-point boundary conditions for surface velocity are deduced from the no-slip BCs at the side-walls:

$$v^*_{\theta S}\left(r^*=\frac{r_i}{h}\right)=0,\quad v^*_{\theta S}\left(r^*=\frac{r_o}{h}\right)=0. \tag{III.B.12}$$

III.B.1.b Two-way coupling

The overall coupling process between the sub-phase flow v^*_θ and the surface flow $v^*_{\theta S}$ is summarized in Fig. III.B.2. The roles of the surface velocity, $v^*_{\theta S}$, and the bulk shear stress estimated at the liquid surface, $\partial v^*_\theta/\partial z^*|_{z^*=1}$, as coupling variables between the bulk MHD and the surface rheology are particularly enhanced.

First, the two-way coupling between the surface and sub-phase flows is set. The bulk velocity v^*_θ and the magnetic induction b^*_θ are expressed with respect to the surface velocity $v^*_{\theta S}$ through a boundary condition involving the liquid surface, and thanks to a matched asymptotic method based on the Ha number. Then, the determination of the coupling term between the surface and bulk flows is implemented, leading to the solution of the JMB at the interface thanks to the calculation of a Green's function. The modelling of the gradually oxidised liquid surface is achieved by introducing the Bo_{η_S} number. Finally, the solution for the surface velocity is re-injected as a boundary condition of the MHD bulk flow for determination of the whole flow velocity and induction. The software selected to perform the calculation is the formal calculation software Maple 16®.

III.B.1.c An asymptotic solution: the classical MHD Couette flow

This section briefly gives the basic solution method, in the case where the side walls are considered to be infinitely far from each other, and the imposed velocity at the bottom of the flow is constant. In addition, the interface dynamics is reduced to the case where $\mathrm{Bo}_{\eta_S}\to\infty$, and as such, induces a no-slip condition at the top of the flow, which corresponds to a classical Couette flow.

The problem is now independent from r^*, and Eqs (III.B.3) and (III.B.4) degenerate into $\partial^2 b^*_\theta/\partial z^{*2}+\mathrm{Ha}\,\partial v^*_\theta/\partial z^*=0$ and $\partial^2 v^*_\theta/\partial z^{*2}+\mathrm{Ha}\,\partial b^*_\theta/\partial z^*=0$. Now, using

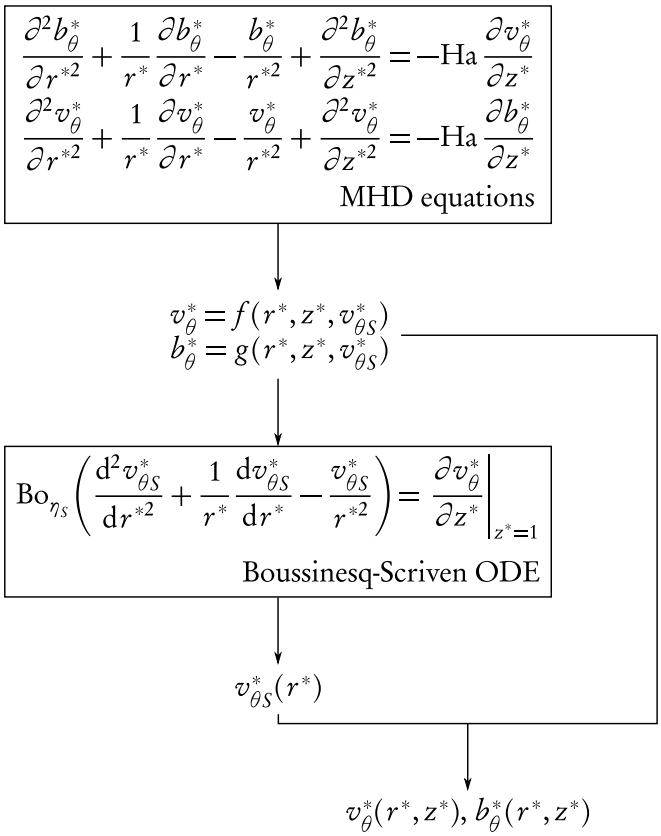

Figure III.B.2 – Two-way coupling between the bulk and surface flows.

the Elsasser variables as suggested in [4], $\psi_\pm^* = v_\theta^* \pm b_\theta^*$, the previous equations reduce to $\partial^2\psi_\pm^*/\partial z^{*2} \pm \mathrm{Ha}\partial\psi_\pm^*/\partial z^* = 0$ and are easily integrated. Taking the boundary conditions into account gives the following explicit solutions, by applying the reciprocal relations $v_\theta^* = 1/2\left(\psi_+^* + \psi_-^*\right)$ and $b_\theta^* = 1/2\left(\psi_+^* - \psi_-^*\right)$:

$$v_{\theta\mathrm{Co}}^*(z^*) = \frac{1}{2}\left(\frac{1}{\mathrm{e}^{-\mathrm{Ha}}-1}\left(\mathrm{e}^{-\mathrm{Ha}} - \mathrm{e}^{-\mathrm{Haz}^*}\right) + \frac{1}{\mathrm{e}^{\mathrm{Ha}}-1}\left(\mathrm{e}^{\mathrm{Ha}} - \mathrm{e}^{\mathrm{Haz}^*}\right)\right), \quad \text{(III.B.13)}$$

$$b_{\theta\mathrm{Co}}^*(z^*) = \frac{1}{2}\left(\frac{1}{\mathrm{e}^{-\mathrm{Ha}}-1}\left(\mathrm{e}^{-\mathrm{Ha}} - \mathrm{e}^{-\mathrm{Haz}^*}\right) - \frac{1}{\mathrm{e}^{\mathrm{Ha}}-1}\left(\mathrm{e}^{\mathrm{Ha}} - \mathrm{e}^{\mathrm{Haz}^*}\right)\right). \quad \text{(III.B.14)}$$

Eqs. (III.B.13) and (III.B.14) shall benchmark the analytic calculation in Sec. III.B.1.f. Note that, for comparison purposes, the typical velocity order of magnitude used for classical Couette MHD quantities when compared with the general case solved in this chapter (with radial dependence and an ageing interface) is the rotating floor velocity at the radial coordinates considered, *i.e.* $r\Omega$.

III.B.1.d Bulk flow at the leading order

As mentioned earlier, the strategy here consists of expressing the bulk quantities with respect to the surface velocity, using a matched asymptotic expansion based

on the small parameter 1/Ha (see *e.g.* [78, 79] for an extensive introduction to the matched asymptotic expansion method). This strategy, as adopted by numerous authors when tackling MHD problems, is particularly convenient here for two reasons: first, it allows for an accurate analysis of the interplay between the core flow and the Hartmann or Shercliff layers, as presented in Fig. III.B.1, and second, it allows for the introduction of the simplest possible dependence with respect to $v^*_{\theta S}$.

The core C and the Hartmann layers HB and HT

Following a classical approach in MHD [34], expansion of Eqs. (III.B.3) and (III.B.4) at leading order in Ha leads to:

$$\frac{\partial v^*_{\theta C}}{\partial z^*} = 0, \quad \frac{\partial b^*_{\theta C}}{\partial z^*} = 0,$$

for which the solutions are $b^*_{\theta C} = C_1(r^*)$ and $v^*_{\theta C} = C_2(r^*)$. C_1 and C_2 are two functions to be determined, thanks to the condition of matching to the boundary layer solutions. For this purpose, two new stretched variables are introduced for HB and HT, which are $z^*_{HB} = \mathrm{Ha} z^*$ and $z^*_{HT} = \mathrm{Ha}(1 - z^*)$, respectively, to describe more significant physical scales inside these boundary layers. Substituting these new variables into Eqs. (III.B.3) and (III.B.4) produces the following set of equations:

$$\begin{aligned}
\frac{\partial^2 v^*_{\theta HB(HT)}}{\partial z^{*2}_{HB(HT)}} + \frac{\partial b^*_{\theta HB(HT)}}{\partial z^*_{HB(HT)}} &= 0, \\
\frac{\partial^2 b^*_{\theta HB(HT)}}{\partial z^{*2}_{HB(HT)}} + \frac{\partial v^*_{\theta HB(HT)}}{\partial z^*_{HB(HT)}} &= 0.
\end{aligned}$$

The boundary conditions (III.B.7), (III.B.8) and (III.B.9) reduce to:

$$\begin{aligned}
v^*_{\theta HB(HT)}(r^*, z^*_{HB(HT)} = 0) &= r^* (\text{or } v^*_{\theta S}(r^*) \text{ for } (HT)), \\
b^*_{\theta HB(HT)}(r^*, z^*_{HB(HT)} = 0) &= 0,
\end{aligned}$$

and the matching condition to the core flow is written as:

$$\begin{aligned}
\lim_{z^*_{HB(HT)} \to \infty} v^*_{\theta HB(HT)} &= \lim_{z^* \to 0(1)} v^*_{\theta C}, \\
\lim_{z^*_{HB(HT)} \to \infty} b^*_{\theta HB(HT)} &= \lim_{z^* \to 0(1)} b^*_{\theta C}.
\end{aligned}$$

This leads to the following solutions:

$$
\begin{aligned}
v^*_{\theta C} &= \frac{1}{2}\Big(v^*_{\theta S}(r^*)+r^*\Big),\\
b^*_{\theta C} &= \frac{1}{2}\Big(v^*_{\theta S}(r^*)-r^*\Big),\\
v^*_{\theta HB} &= \frac{1}{2}\Big((r^*-v^*_{\theta S}(r^*))\mathrm{e}^{-z^*_{HB}}+v^*_{\theta S}(r^*)+r^*\Big),\\
b^*_{\theta HB} &= \frac{1}{2}\Big(v^*_{\theta S}(r^*)-r^*+(r^*-v^*_{\theta S}(r^*))\mathrm{e}^{-z^*_{HB}}\Big),\\
v^*_{\theta HT} &= \frac{1}{2}\Big((v^*_{\theta S}(r^*)-r^*)\mathrm{e}^{-z^*_{HT}}+v^*_{\theta S}(r^*)+r^*\Big)\\
b^*_{\theta HT} &= \frac{1}{2}\Big(v^*_{\theta S}(r^*)-r^*+(r^*-v^*_{\theta S}(r^*))\mathrm{e}^{-z^*_{HT}}\Big).
\end{aligned}
$$

Finally, a composite solution at the leading order, which is valid for the sub-domains C, HB and HT is given by:

$$v^*_{\theta CH} = v^*_{\theta HB}+v^*_{\theta HT}-v^*_{\theta C}, \tag{III.B.15}$$

$$b^*_{\theta CH} = b^*_{\theta HB}+b^*_{\theta HT}-b^*_{\theta C}. \tag{III.B.16}$$

The sub-domains ABL, ABR, ATL, and ATR, and the side layers SL and SR

Two new stretched coordinates are introduced: $r^*_{SL}=\sqrt{\mathrm{Ha}}(r^*-r_i/h)$, which is common to the ABL, ATL and SL sub-domains, and $r^*_{SR}=\sqrt{\mathrm{Ha}}(r_o/h-r^*)$, which is common to the ABR, ATR and SR sub-domains.

Let us first focus on the AB and AT sub-domains for which the relevant axial coordinates are denoted by z^*_{HB} and z^*_{HT}, respectively. Introducing these variables, along with r^*_{SL} or r^*_{SR}, into Eqs. (III.B.3) and (III.B.4), yields similar expressions to those obtained for the Hartmann layers HB and HT. The boundary conditions (III.B.7), (III.B.8) and (III.B.9) are written at the leading order as:

$$
\begin{gathered}
v^*_{\theta ABL}(r^*_{SL},z^*_{HB}=0)=r^*=\frac{r^*_{SL}}{\sqrt{\mathrm{Ha}}}+\frac{r_i}{h}\sim\frac{r_i}{h},\\
v^*_{\theta ATL}(r^*_{SL},z^*_{HT}=0)=v^*_{\theta S}(r^*)=v^*_{\theta S}\left(\frac{r^*_{SL}}{\sqrt{\mathrm{Ha}}}+\frac{r_i}{h}\right)\sim v^*_{\theta S}\left(\frac{r_i}{h}\right)=0,\\
b^*_{\theta ABL}(r^*_{SL},z^*_{HB}=0)=0,\\
b^*_{\theta ATL}(r^*_{SL},z^*_{HT}=0)=0.
\end{gathered}
$$

We now consider only the left part of the channel (with the reasoning being symmetrical). The solution can be expressed in the following form:

$$v^*_{\theta ABL}(r^*_{SL},z^*_{HB}) = C_3(r^*_{SL})\Big(\mathrm{e}^{-z^*_{HB}}-1\Big)+\frac{r_i}{h}, \tag{III.B.17}$$

$$b^*_{\theta ABL}(r^*_{SL},z^*_{HB}) = C_3(r^*_{SL})\Big(\mathrm{e}^{-z^*_{HB}}-1\Big)\,, \tag{III.B.18}$$

$$v^*_{\theta ATL}(r^*_{SL},z^*_{HT}) = C_4(r^*_{SL})\Big(\mathrm{e}^{-z^*_{HT}}-1\Big)\,, \tag{III.B.19}$$

$$b^*_{\theta ATL}(r^*_{SL},z^*_{HT}) = C_4(r^*_{SL})\Big(1-\mathrm{e}^{-z^*_{HT}}\Big)\,. \tag{III.B.20}$$

with C_3 and C_4 being determined by matching to the solution for the SL region.

Now, let us focus on the SL sub-domain, for which the relevant axial coordinate is z^*. Expansion of Eqs. (III.B.3) and (III.B.4) leads to the following set of typical diffusion equations:

$$\frac{\partial^2 v^*_{\theta SL}}{\partial r^{*2}_{SL}} + \frac{\partial b^*_{\theta SL}}{\partial z^*} = 0,$$
$$\frac{\partial^2 b^*_{\theta SL}}{\partial r^{*2}_{SL}} + \frac{\partial v^*_{\theta SL}}{\partial z^*} = 0,$$

which are completed by the boundary conditions (III.B.5):

$$v^*_{\theta SL}(r^*_{SL} = 0, z^*) = 0, \quad b^*_{\theta SL}(r^*_{SL} = 0, z^*) = 0,$$

with the additional condition of matching to the core solution:

$$\lim_{r^*_{SL}\to\infty} v^*_{\theta SL} = \lim_{r^*\to\frac{r_i}{h}} v^*_{\theta C} = \frac{1}{2}\frac{r_i}{h},$$
$$\lim_{r^*_{SL}\to\infty} b^*_{\theta SL} = \lim_{r^*\to\frac{r_i}{h}} b^*_{\theta C} = -\frac{1}{2}\frac{r_i}{h}.$$

From Eqs. (III.B.17), (III.B.18), (III.B.19) and (III.B.20), it is possible to build additional boundary conditions that allow us to close the system [34]. These equations lead to the following extra-BCs: $v^*_{\theta ABL} - b^*_{\theta ABL} = r_i/h$ and $v^*_{\theta ATL} + b^*_{\theta ATL} = 0$. Now, using the matching conditions between the regions ABL (or ATL) and SL, we obtain:

$$\lim_{z^*_{HB}\to\infty} (v^*_{\theta ABL} - b^*_{\theta ABL}) = \lim_{z^*\to 0} (v^*_{\theta SL} - b^*_{\theta SL}),$$
$$\lim_{z^*_{HT}\to\infty} (v^*_{\theta ATL} + b^*_{\theta ATL}) = \lim_{z^*\to 1} (v^*_{\theta SL} + b^*_{\theta SL}),$$

We also find the following extra conditions on $v^*_{\theta SL}$ and $b^*_{\theta SL}$:

$$[v^*_{\theta SL} - b^*_{\theta SL}](r^*_{SL}, z^* = 0) = \frac{r_i}{h}, \tag{III.B.21}$$
$$[v^*_{\theta SL} + b^*_{\theta SL}](r^*_{SL}, z^* = 1) = 0. \tag{III.B.22}$$

With the MHD system in the SL region being closed, the solution is as follows:

$$v^*_{\theta SL}(r^*_{SL}, z^*) = \frac{1}{2}\frac{r_i}{h}\mathrm{erf}\left(\frac{r^*_{SL}}{2\sqrt{z^*}}\right),$$
$$b^*_{\theta SL}(r^*_{SL}, z^*) = -\frac{1}{2}\frac{r_i}{h}\mathrm{erf}\left(\frac{r^*_{SL}}{2\sqrt{z^*}}\right).$$

Now, coming back to the ABL and ATL sub-domains, the expressions for the functions C_3 and C_4 in Eqs. (III.B.17), (III.B.18), (III.B.19) and (III.B.20) are found by invoking matching conditions (III.B.21) and (III.B.22). Thus, we obtain:

$$v^*_{\theta ABL}(r^*_{SL}, z^*_{HB}) = \frac{1}{2}\frac{r_i}{h}\left(1 + \mathrm{e}^{-z^*_{HB}}\right), \tag{III.B.23}$$

$$b^*_{\theta ABL}(r^*_{SL}, z^*_{HB}) = \frac{1}{2}\frac{r_i}{h}\left(\mathrm{e}^{-z^*_{HB}} - 1\right), \tag{III.B.24}$$

$$v^*_{\theta ATL}(r^*_{SL}, z^*_{HT}) = \frac{1}{2}\frac{r_i}{h}\mathrm{erf}\left(\frac{r^*_{SL}}{2}\right)\left(1 - \mathrm{e}^{-z^*_{HT}}\right), \tag{III.B.25}$$

$$b^*_{\theta ATL}(r^*_{SL}, z^*_{HT}) = \frac{1}{2}\frac{r_i}{h}\mathrm{erf}\left(\frac{r^*_{SL}}{2}\right)\left(\mathrm{e}^{-z^*_{HT}} - 1\right). \tag{III.B.26}$$

These solutions satisfy the matching conditions between the sub-domains ABL (or ATL) and HL (or HT), which shows the consistency of the asymptotic expansion so far. Finally, the composite solution that is valid in the sub-domains SL, ABL and ATL is given by:

$$v^*_{\theta SAL} = v^*_{\theta SL} + v^*_{\theta ABL} + v^*_{\theta ATL} - \lim_{z^*_{HB}\to\infty} v^*_{\theta ABL} - \lim_{z^*_{HT}\to\infty} v^*_{\theta ATL}, \tag{III.B.27}$$

$$b^*_{\theta SAL} = b^*_{\theta SL} + b^*_{\theta ABL} + b^*_{\theta ATL} - \lim_{z^*_{HB}\to\infty} b^*_{\theta ABL} - \lim_{z^*_{HT}\to\infty} b^*_{\theta ATL}. \tag{III.B.28}$$

Symmetrical reasoning for the right part would lead us to identical expressions for $v^*_{\theta SAR}$ and $b^*_{\theta SAR}$, by substituting for either r^*_{SL} by r^*_{SR} or r_i/h by r_o/h in the earlier expressions (III.B.23), (III.B.24), (III.B.25) and (III.B.26).

The corner regions IC_1, IC_2, IC_3 and IC_4

Using the explicit expressions for $v^*_{\theta SAL}$ and $b^*_{\theta SAL}$ that are given by Eqs. (III.B.27) and (III.B.28), we find that the condition $v^*_{\theta SAL} = b^*_{\theta SAL} = 0$ in $r^*_{SL} = 0$ is not respected. This is because of a singularity in the velocity boundary conditions, as emphasized by Eqs. (III.B.5) and (III.B.7).

The corner regions IC_1 and IC_2 need no further analysis for determination of the leading terms in each of the asymptotic expansions with regard to other subregions [80]. There are indeed no discontinuity boundary data near the interface (see the boundary conditions (III.B.5), (III.B.6) and (III.B.12)). However, regions IC_3 and IC_4 cannot be precisely described without further investigation, because a moving wall meets a stationary wall in these sub-regions.

Nevertheless, we have left these corner regions out of the reasoning, like many authors before us have done, *e.g.* [81], for several reasons:

- as previously stated, the typical cross-section of one of these regions is of the order $O(\mathrm{Ha}^{-1}) \times O(\mathrm{Ha}^{-1})$, which becomes very restricted if $\mathrm{Ha} \gg 1$. They can thus be neglected as specific side-effects.
- this issue has been addressed in the literature, for a similar bottom corner subregion called IC_4 [34]. One of the major differences between the latter work

and the present work is that the moving wall is fixed at a given radial position with a typical Taylor-Couette layout in the other study, which gives the boundary condition $v_\theta^* = \text{Cst}$ on this wall. In our case, the boundary condition for the velocity exhibits a radial dependence, $v_\theta^* = r^*$, along a rotating floor. This may explain why the method used in [34] seems much more complex to use for the corresponding corners in this work. Our efforts to simply match the solution for the outer regions with this method have not been successful.

- finally, by anticipating what follows, the solution for the sub-phase flow is calculated to deliver the JMB source term at the upper liquid surface; the ultimate aim of this is to find the surface velocity, $v_{\theta S}^*(r^*)$. This means that an analytical closed-form solution for v_θ^* with respect to $v_{\theta S}^*$ must be maintained; this condition is impossible to fulfill considering the complicated forms we might expect to find when taking account of corner singularities for the velocity along the rotating floor.

Overall composite solution at leading order

The global solution for the bulk variables v_θ^* and b_θ^* with respect to r^*, z^* and the surface velocity $v_{\theta S}^*$ is finally derived using Eqs. (III.B.15), (III.B.16), (III.B.27), (III.B.28) and the non-written equivalent of the latter for the right part, *i.e.* *SAR*. The matched expansion produces:

$$v_\theta^* = v_{\theta CH}^* + v_{\theta SAL}^* + v_{\theta SAR}^* - \lim_{r^* \to \frac{r_i}{b}} v_{\theta CH}^* - \lim_{r^* \to \frac{r_o}{b}} v_{\theta CH}^*, \tag{III.B.29}$$

$$b_\theta^* = b_{\theta CH}^* + b_{\theta SAL}^* + b_{\theta SAR}^* - \lim_{r^* \to \frac{r_i}{b}} b_{\theta CH}^* - \lim_{r^* \to \frac{r_o}{b}} b_{\theta CH}^*. \tag{III.B.30}$$

Now that the expression of the bulk quantities are determined with respect to the surface velocity, let us turn to the second step of the two-way coupling, *i.e.* the determination of the surface flow at leading order.

III.B.1.e Surface flow at the leading order

Explicit form of the JMB

First, by substituting Eq. (III.B.29) into (III.B.10), we can determine the second term of the two-way coupling, $\partial v_\theta^*/\partial z^*\big|_{z^*=1}$, in the JMB at the liquid surface:

$$\tilde{\text{Bo}}_{\eta_S}\left(\frac{\mathrm{d}^2 v_{\theta S}^*}{\mathrm{d}r^{*2}} + \frac{1}{r^*}\frac{\mathrm{d}v_{\theta S}^*}{\mathrm{d}r^*} - \frac{v_{\theta S}^*(r^*)}{r^{*2}}\right) - v_{\theta S}^*(r^*) = f(r^*), \tag{III.B.31}$$

with $\tilde{\text{Bo}}_{\eta_S}$, the modified surface shear Boussinesq number, defined as:

$$\tilde{\text{Bo}}_{\eta_S} = \frac{2\text{Bo}_{\eta_S}}{\text{Ha}\left(1 + \mathrm{e}^{-\text{Ha}}\right)}, \tag{III.B.32}$$

and which covers the competitive influences exerted by either the Hartmann number (and therefore the electromagnetic part) or by the surface shear Boussinesq number (and therefore the shear stress ratio) at the interface. The so-called forcing term, f, is defined as follows:

$$f(r^*) = -r^* - \frac{1}{2\sqrt{\pi \mathrm{Ha}}\left(1+\mathrm{e}^{-\mathrm{Ha}}\right)}\left[\frac{r_i}{h}\left(r^* - \frac{r_i}{h}\right)\mathrm{e}^{-\frac{\mathrm{Ha}}{4}\left(r^* - \frac{r_i}{h}\right)^2} + \frac{r_o}{h}\left(\frac{r_o}{h} - r^*\right)\mathrm{e}^{-\frac{\mathrm{Ha}}{4}\left(\frac{r_o}{h} - r^*\right)^2}\right] + \frac{1}{1+\mathrm{e}^{-\mathrm{Ha}}}\left[-\frac{r_i}{h}\mathrm{erf}\left(\frac{\sqrt{\mathrm{Ha}}}{2}\left(r^* - \frac{r_i}{h}\right)\right) - \frac{r_o}{h}\mathrm{erf}\left(\frac{\sqrt{\mathrm{Ha}}}{2}\left(\frac{r_o}{h} - r^*\right)\right) + \frac{r_i}{h} + \frac{r_o}{h}\right]. \tag{III.B.33}$$

Calculation of the Green function

The adjoint operator

As suggested by authors tackling a similar boundary value problem [72], it is worthwhile to introduce the Green's function $G(r|\xi)$, with ξ as the influence variable, associated with the differential operator $\mathfrak{J}$:

$$\mathfrak{J} \equiv \tilde{\mathrm{Bo}}_{\eta_S}\left(\frac{\mathrm{d}^2}{\mathrm{d}\xi^2} + \frac{1}{\xi}\frac{\mathrm{d}}{\mathrm{d}\xi} - \frac{1}{\xi^2}\right) - 1.$$

Eq. (III.B.31) can be intrinsically noted as:

$$\mathfrak{J} : v^*_{\theta S}(\xi) = f(\xi). \tag{III.B.34}$$

The Green function must be determined in order to solve for the surface flow. Let us start the calculation process by invoking the adjoint operator $\mathfrak{J}_*$ [82]. First, both sides of Eq. (III.B.34) are multiplied by $G(r^*|\xi)$, and integrated between $\frac{r_i}{h}$ and $\frac{r_o}{h}$:

$$\int_{\frac{r_i}{h}}^{\frac{r_o}{h}} G(r^*|\xi)\mathfrak{J} : v^*_{\theta S}(\xi)\,\mathrm{d}\xi = \int_{\frac{r_i}{h}}^{\frac{r_o}{h}} G(r^*|\xi) f(\xi)\,\mathrm{d}\xi. \tag{III.B.35}$$

Let us expand the right-hand side of Eq. (III.B.35):

$$\int_{\frac{r_i}{b}}^{\frac{r_o}{b}} G(r^*|\xi)\mathfrak{F} : v^*_{\theta S}(\xi)\,\mathrm{d}\xi \tag{III.B.36}$$

$$\begin{aligned}
&= \tilde{\mathrm{Bo}}_{\eta_S} \int_{\frac{r_i}{b}}^{\frac{r_o}{b}} G(r^*|\xi) \left[\left(\frac{\mathrm{d}^2 v^*_{\theta S}}{\mathrm{d}\xi^2} + \frac{1}{\xi}\frac{\mathrm{d}v^*_{\theta S}}{\mathrm{d}\xi} - \frac{1}{\tilde{\mathrm{Bo}}_{\eta_S}} \frac{v^*_{\theta S}}{\xi^2} \right) - v^*_{\theta S}(\xi) \right] \mathrm{d}\xi \\
&= \tilde{\mathrm{Bo}}_{\eta_S} \left(\int_{\frac{r_i}{b}}^{\frac{r_o}{b}} G(r^*|\xi) \frac{\mathrm{d}^2 v^*_{\theta S}}{\mathrm{d}\xi^2}\,\mathrm{d}\xi + \int_{\frac{r_i}{b}}^{\frac{r_o}{b}} G(r^*|\xi) \left[\frac{1}{\xi}\frac{\mathrm{d}v^*_{\theta S}}{\mathrm{d}\xi} - \frac{v^*_{\theta S}(\xi)}{\xi^2} \right] \mathrm{d}\xi \right. \\
&\quad \left. - \frac{1}{\tilde{\mathrm{Bo}}_{\eta_S}} \int_{\frac{r_i}{b}}^{\frac{r_o}{b}} G(r^*|\xi) v^*_{\theta S}(\xi)\,\mathrm{d}\xi \right) \\
&= \tilde{\mathrm{Bo}}_{\eta_S} \left(I_1 + I_2 - \frac{1}{\tilde{\mathrm{Bo}}_{\eta_S}} I_3 \right).
\end{aligned} \tag{III.B.37}$$

I_1 and I_2 are determined separately, using integration by parts. Let us calculate I_1:

$$\begin{aligned}
I_1 &= \int_{\frac{r_i}{b}}^{\frac{r_o}{b}} G(r^*|\xi) \frac{\mathrm{d}^2 v^*_{\theta S}}{\mathrm{d}\xi^2}\,\mathrm{d}\xi \\
&= \left[G(r^*|\xi) \frac{\mathrm{d}v^*_{\theta S}}{\mathrm{d}\xi} \right]_{\frac{r_i}{b}}^{\frac{r_o}{b}} - \int_{\frac{r_i}{b}}^{\frac{r_o}{b}} \frac{\partial G(r^*|\xi)}{\partial \xi} \frac{\mathrm{d}v^*_{\theta S}}{\mathrm{d}\xi}\,\mathrm{d}\xi \\
&= \left[G(r^*|\xi) \frac{\mathrm{d}v^*_{\theta S}}{\mathrm{d}\xi} - \frac{\partial G(r^*|\xi)}{\partial \xi} v^*_{\theta S}(\xi) \right]_{\frac{r_i}{b}}^{\frac{r_o}{b}} + \int_{\frac{r_i}{b}}^{\frac{r_o}{b}} \frac{\partial^2 G(r^*|\xi)}{\partial \xi^2} v^*_{\theta S}(\xi)\,\mathrm{d}\xi .
\end{aligned} \tag{III.B.38}$$

Then I_2:

$$\begin{aligned}
I_2 &= \int_{\frac{r_i}{b}}^{\frac{r_o}{b}} G(r^*|\xi) \left[\frac{1}{\xi}\frac{\mathrm{d}v^*_{\theta S}}{\mathrm{d}\xi} - \frac{v^*_{\theta S}(\xi)}{\xi^2} \right] \mathrm{d}\xi \\
&= \int_{\frac{r_i}{b}}^{\frac{r_o}{b}} G(r^*|\xi) \frac{\mathrm{d}}{\mathrm{d}\xi} \left(\frac{v^*_{\theta S}}{\xi} \right) \mathrm{d}\xi \\
&= \left[\frac{G(r^*|\xi)}{\xi} v^*_{\theta S}(\xi) \right]_{\frac{r_i}{b}}^{\frac{r_o}{b}} - \int_{\frac{r_i}{b}}^{\frac{r_o}{b}} \frac{1}{\xi} \frac{\partial G(r^*|\xi)}{\partial \xi} v^*_{\theta S}(\xi)\,\mathrm{d}\xi .
\end{aligned} \tag{III.B.39}$$

Substituting Eqs. III.B.38 and III.B.39 into III.B.37 yields:

$$\begin{aligned}
&\int_{\frac{r_i}{h}}^{\frac{r_o}{h}} G(r^*|\xi)\mathfrak{J} : v^*_{\theta S}(\xi)\,\mathrm{d}\xi = \tilde{\mathrm{Bo}}_{\eta_S}\left(I_1 + I_2 - \frac{1}{\tilde{\mathrm{Bo}}_{\eta_S}} I_3\right)\\
&= \tilde{\mathrm{Bo}}_{\eta_S}\left[G(r^*|\xi)\frac{\mathrm{d}v^*_{\theta S}}{\mathrm{d}\xi} - \frac{\partial G(r^*|\xi)}{\partial \xi} v^*_{\theta S}(\xi) + \frac{G(r^*|\xi)}{\xi} v^*_{\theta S}(\xi)\right]_{\frac{r_i}{h}}^{\frac{r_o}{h}}\\
&+ \int_{\frac{r_i}{h}}^{\frac{r_o}{h}} v^*_{\theta S}(\xi)\left[\tilde{\mathrm{Bo}}_{\eta_S}\left(\frac{\partial^2 G(r^*|\xi)}{\partial \xi^2} - \frac{1}{\xi}\frac{\partial G(r^*|\xi)}{\partial \xi}\right) - G(r^*|\xi)\right]\mathrm{d}\xi\\
&= \tilde{\mathrm{Bo}}_{\eta_S}\left[G(r^*|\xi)\frac{\mathrm{d}v^*_{\theta S}}{\mathrm{d}\xi} - \frac{\partial G(r^*|\xi)}{\partial \xi} v^*_{\theta S}(\xi) + \frac{G(r^*|\xi)}{\xi} v^*_{\theta S}(\xi)\right]_{\frac{r_i}{h}}^{\frac{r_o}{h}}\\
&+ \int_{\frac{r_i}{h}}^{\frac{r_o}{h}} v^*_{\theta S}(\xi)\mathfrak{J}_* : G(r^*|\xi)\,\mathrm{d}\xi,
\end{aligned} \tag{III.B.40}$$

where the adjoint operator $\mathfrak{J}^*$ is defined by:

$$\mathfrak{J}^* \equiv \tilde{\mathrm{Bo}}_{\eta_S}\left(\frac{\partial^2}{\partial \xi^2} - \frac{1}{\xi}\frac{\partial}{\partial \xi}\right) - 1. \tag{III.B.41}$$

Further definitions and conditions

Now the adjoint operator is known, the distribution theory allows us to link this operator to the Green function G [82], through the relation:

$$\mathfrak{J}_* : G(r^*|\xi) = \delta(\xi - r^*), \tag{III.B.42}$$

where $\delta(\xi - r^*)$ is the Dirac delta function. Let us then impose G to be $\mathscr{C}^1$ piecewise, and in addition to that, to be subjected to the following boundary conditions:

$$G\left(r^*|\frac{r_i}{h}\right) = 0 \quad \text{and} \quad G\left(r^*|\frac{r_o}{h}\right) = 0. \tag{III.B.43}$$

Using the surface velocity BCs of Eq. (III.B.12), and the BCs for G described just above, the term of Eq. (III.B.40) between the square brackets vanishes. Besides, the remaining integral can be expressed as such:

$$\int_{\frac{r_i}{h}}^{\frac{r_o}{h}} v^*_{\theta S}(\xi)\mathfrak{J}_* : G(r^*|\xi)\,\mathrm{d}\xi = \int_{\frac{r_i}{h}}^{\frac{r_o}{h}} v^*_{\theta S}(\xi)\delta(\xi - r^*)\,\mathrm{d}\xi = v^*_{\theta S}(r^*),$$

by using the Dirac distribution properties. Consequently, Eq. (III.B.40) reduce to:

$$\int_{\frac{r_i}{h}}^{\frac{r_o}{h}} G(r^*|\xi)\mathfrak{J} : v^*_{\theta S}(\xi)\,\mathrm{d}\xi = v^*_{\theta S}(r^*),$$

and coming back to Eq. (III.B.35):

$$v^*_{\theta S}(r^*) = \int_{\frac{r_i}{h}}^{\frac{r_o}{h}} G(r^*|\xi) f(\xi)\,\mathrm{d}\xi. \tag{III.B.44}$$

The Green function equation

The Ordinary Differential Equation – ODE – of G is given by Eq. (III.B.42):

$$\frac{\partial^2 G(r^*|\xi)}{\partial \xi^2} - \frac{1}{\xi}\frac{\partial G(r^*|\xi)}{\partial \xi} - \frac{1}{\tilde{\mathrm{Bo}}_{\eta_S}} G(r^*|\xi) = \frac{1}{\tilde{\mathrm{Bo}}_{\eta_S}} \delta(\xi - r^*). \tag{III.B.45}$$

Note that this equation is not directly solvable because of a non-homogeneous term caused by the Dirac distribution, which is the reason for the introduction of two sub-intervals, $[r_i/h, r^*[$ and $]r^*, r_o/h]$. The equation to solve become homogeneous on these two intervals:

$$\frac{\partial^2 G(r^*|\xi)}{\partial \xi^2} - \frac{1}{\xi}\frac{\partial G(r^*|\xi)}{\partial \xi} - \frac{1}{\tilde{\mathrm{Bo}}_{\eta_S}} G(r^*|\xi) = 0. \tag{III.B.46}$$

The two first BCs for G are given in Eq. (III.B.43):

$$G\left(r^*|\frac{r_i}{h}\right) = 0 \quad \text{and} \quad G\left(r^*|\frac{r_o}{h}\right) = 0. \tag{III.B.47}$$

As the interval is divided into two parts, two additional BCs must be found. The first one is given by the continuity of G in r^*:

$$\lim_{\xi \to r^{*-}} G(r^*|\xi) = \lim_{\xi \to r^{*+}} G(r^*|\xi). \tag{III.B.48}$$

The second one is deduced by multiplying Eq. (III.B.45) by ξ and integrating it between r^{*-} and r^{*+}:

$$\int_{r^{*-}}^{r^{*+}} \left[\xi \frac{\partial^2 G(r^*|\xi)}{\partial \xi^2} - \frac{\partial G(r^*|\xi)}{\partial \xi} - \frac{\xi}{\tilde{\mathrm{Bo}}_{\eta_S}} G(r^*|\xi) \right] \mathrm{d}\xi = \int_{r^{*-}}^{r^{*+}} \frac{\xi}{\tilde{\mathrm{Bo}}_{\eta_S}} \delta(\xi - r^*)\,\mathrm{d}\xi. \tag{III.B.49}$$

Let us expand the left-hand side of this equation:

$$\begin{aligned}
&\int_{r^{*-}}^{r^{*+}} \left[\xi \frac{\partial^2 G(r^*|\xi)}{\partial \xi^2} - \frac{\partial G(r^*|\xi)}{\partial \xi} - \frac{\xi}{\tilde{\mathrm{Bo}}_{\eta_S}} G(r^*|\xi) \right] \mathrm{d}\xi = \int_{r^{*-}}^{r^{*+}} \xi \frac{\partial^2 G(r^*|\xi)}{\partial \xi^2}\,\mathrm{d}\xi \\
&\quad - \int_{r^{*-}}^{r^{*+}} \frac{\partial G(r^*|\xi)}{\partial \xi}\,\mathrm{d}\xi - \int_{r^{*-}}^{r^{*+}} \frac{\xi}{\tilde{\mathrm{Bo}}_{\eta_S}} G(r^*|\xi)\,\mathrm{d}\xi \\
&= \left[\xi \frac{\partial G}{\partial \xi} \right]_{r^{*-}}^{r^{*+}} - 2\int_{r^{*-}}^{r^{*+}} \frac{\partial G(r^*|\xi)}{\partial \xi}\,\mathrm{d}\xi - \int_{r^{*-}}^{r^{*+}} \frac{\xi}{\tilde{\mathrm{Bo}}_{\eta_S}} G(r^*|\xi)\,\mathrm{d}\xi \\
&= \left[\xi \frac{\partial G}{\partial \xi} - 2G \right]_{r^{*-}}^{r^{*+}} - \int_{r^{*-}}^{r^{*+}} \frac{\xi}{\tilde{\mathrm{Bo}}_{\eta_S}} G(r^*|\xi)\,\mathrm{d}\xi.
\end{aligned}$$

The last remaining integral vanishes, by continuity of the bounded function ξG in r^*. By continuity of G, $[-2G]_{r^{*-}}^{r^{*+}} = 0$. Consequently, the left-hand side of Eq. (III.B.49) is written:

$$\int_{r^{*-}}^{r^{*+}} \left[\xi \frac{\partial^2 G(r^*|\xi)}{\partial \xi^2} - \frac{\partial G(r^*|\xi)}{\partial \xi} - \frac{\xi}{\tilde{\mathrm{Bo}}_{\eta_S}} G(r^*|\xi) \right] \mathrm{d}\xi = \left[\xi \frac{\partial G}{\partial \xi} \right]_{r^{*-}}^{r^{*+}}. \tag{III.B.50}$$

Concerning the right-hand side of Eq. (III.B.49), it is simply expressed:

$$\int_{r^{*-}}^{r^{*+}} \frac{\xi}{\tilde{\mathrm{Bo}}_{\eta_S}} \delta(\xi - r^*) \mathrm{d}\xi = \frac{r^*}{\tilde{\mathrm{Bo}}_{\eta_S}}.$$

Therefore, the final BC for G is written:

$$\left[\xi \frac{\partial G}{\partial \xi} \right]_{r^{*-}}^{r^{*+}} = \frac{r^*}{\tilde{\mathrm{Bo}}_{\eta_S}}. \tag{III.B.51}$$

General form of the solution

Introducing the change of variables $G(r^*|\xi) = \xi^\zeta y(r^*, \xi)$ into the homogeneous Eq. (III.B.46) leads to:

$$\xi^2 \frac{\partial^2 y}{\partial \xi^2} + (2\zeta - 1)\xi \frac{\partial y}{\partial \xi} + \left(\zeta(\zeta - 2) - \frac{\xi^2}{\tilde{\mathrm{Bo}}_{\eta_S}} \right) y(r^*, \xi) = 0.$$

Taking $\zeta = 1$, this equation transforms into a modified Bessel equation:

$$\xi^2 \frac{\partial^2 y}{\partial \xi^2} + \xi \frac{\partial y}{\partial \xi} - \left(1 + \left(\frac{\xi}{\sqrt{\tilde{\mathrm{Bo}}_{\eta_S}}} \right)^2 \right) y(r^*, \xi) = 0,$$

of which solutions are known:

$$y(r^*, \xi) = a(r^*) \mathscr{I}_1 \left(\frac{\xi}{\sqrt{\tilde{\mathrm{Bo}}_{\eta_S}}} \right) + b(r) \mathscr{K}_1 \left(\frac{\xi}{\sqrt{\tilde{\mathrm{Bo}}_{\eta_S}}} \right),$$

where $\mathscr{I}_1$ and $\mathscr{K}_1$ are the modified Bessel functions of the first and second kinds, respectively. A piecewise solution is given by:

$$G(r^*|\xi) = \begin{cases} A(r^*)\xi \mathscr{I}_1 \left(\frac{\xi}{\sqrt{\tilde{\mathrm{Bo}}_{\eta_S}}} \right) + B(r^*)\xi \mathscr{K}_1 \left(\frac{\xi}{\sqrt{\tilde{\mathrm{Bo}}_{\eta_S}}} \right) & \text{if } \xi \in \left[\frac{r_i}{h}, r^* \right[, \\ C(r^*)\xi \mathscr{I}_1 \left(\frac{\xi}{\sqrt{\tilde{\mathrm{Bo}}_{\eta_S}}} \right) + D(r^*)\xi \mathscr{K}_1 \left(\frac{\xi}{\sqrt{\tilde{\mathrm{Bo}}_{\eta_S}}} \right) & \text{if } \xi \in \left] r^*, \frac{r_o}{h} \right]. \end{cases} \tag{III.B.52}$$

Determination of the coefficients

The coefficients $A(r^*)$, $B(r^*)$, $C(r^*)$ and $D(r^*)$ remain to be found. First, the BCs defined in Eq. (III.B.47) lead to:

$$\frac{B(r^*)}{A(r^*)} = -\frac{\mathscr{I}_1\left(\frac{r_i}{h\sqrt{\tilde{\mathrm{Bo}}_{\eta_S}}}\right)}{\mathscr{K}_1\left(\frac{r_i}{h\sqrt{\tilde{\mathrm{Bo}}_{\eta_S}}}\right)}, \tag{III.B.53}$$

$$\frac{D(r^*)}{C(r^*)} = -\frac{\mathscr{I}_1\left(\frac{r_o}{h\sqrt{\tilde{\mathrm{Bo}}_{\eta_S}}}\right)}{\mathscr{K}_1\left(\frac{r_o}{h\sqrt{\tilde{\mathrm{Bo}}_{\eta_S}}}\right)}. \tag{III.B.54}$$

Now, Eq. (III.B.48) provides the additional relation:

$$(A(r^*)-C(r^*))\,\mathscr{I}_1\left(\frac{r^*}{\sqrt{\tilde{\mathrm{Bo}}_{\eta_S}}}\right) = (D(r^*)-B(r^*))\,\mathscr{K}_1\left(\frac{r^*}{\sqrt{\tilde{\mathrm{Bo}}_{\eta_S}}}\right). \tag{III.B.55}$$

Finally, using Eq. (III.B.52), it can be proved that:

$$\left.\frac{\partial G}{\partial \xi}\right|_{r^{*-}} = \frac{A(r^*)}{\sqrt{\tilde{\mathrm{Bo}}_{\eta_S}}} r^* \mathscr{I}_0\left(\frac{r^*}{\sqrt{\tilde{\mathrm{Bo}}_{\eta_S}}}\right) - \frac{B(r^*)}{\sqrt{\tilde{\mathrm{Bo}}_{\eta_S}}} r^* \mathscr{K}_0\left(\frac{r^*}{\sqrt{\tilde{\mathrm{Bo}}_{\eta_S}}}\right),$$

$$\left.\frac{\partial G}{\partial \xi}\right|_{r^{*+}} = \frac{C(r^*)}{\sqrt{\tilde{\mathrm{Bo}}_{\eta_S}}} r^* \mathscr{I}_0\left(\frac{r^*}{\sqrt{\tilde{\mathrm{Bo}}_{\eta_S}}}\right) - \frac{D(r^*)}{\sqrt{\tilde{\mathrm{Bo}}_{\eta_S}}} r^* \mathscr{K}_0\left(\frac{r^*}{\sqrt{\tilde{\mathrm{Bo}}_{\eta_S}}}\right).$$

As a consequence, the last condition (III.B.51) writes:

$$(C(r^*)-A(r^*))\,\mathscr{I}_0\left(\frac{r^*}{\sqrt{\tilde{\mathrm{Bo}}_{\eta_S}}}\right) - (D(r^*)-B(r^*))\,\mathscr{K}_0\left(\frac{r^*}{\sqrt{\tilde{\mathrm{Bo}}_{\eta_S}}}\right) = \frac{1}{r^*\sqrt{\tilde{\mathrm{Bo}}_{\eta_S}}}. \tag{III.B.56}$$

After further simplifications, bearing mainly on the properties of the Bessel functions, Eqs. (III.B.53), (III.B.54), (III.B.55) and (III.B.56) provides the following expression for the Green's function coefficients $A(r^*)$, $B(r^*)$, $C(r^*)$ and $D(r^*)$:

$$
\begin{aligned}
A(r^*) &= \frac{\mathscr{K}_1\left(\frac{r_i}{h\sqrt{\tilde{\mathrm{Bo}}_{\eta_S}}}\right)}{\tilde{\mathrm{Bo}}_{\eta_S}} \frac{\mathscr{I}_1\left(\frac{r^*}{\sqrt{\tilde{\mathrm{Bo}}_{\eta_S}}}\right)\mathscr{K}_1\left(\frac{r_o}{h\sqrt{\tilde{\mathrm{Bo}}_{\eta_S}}}\right) - \mathscr{I}_1\left(\frac{r_o}{h\sqrt{\tilde{\mathrm{Bo}}_{\eta_S}}}\right)\mathscr{K}_1\left(\frac{r^*}{\sqrt{\tilde{\mathrm{Bo}}_{\eta_S}}}\right)}{\mathscr{I}_1\left(\frac{r_o}{h\sqrt{\tilde{\mathrm{Bo}}_{\eta_S}}}\right)\mathscr{K}_1\left(\frac{r_i}{h\sqrt{\tilde{\mathrm{Bo}}_{\eta_S}}}\right) - \mathscr{I}_1\left(\frac{r_i}{h\sqrt{\tilde{\mathrm{Bo}}_{\eta_S}}}\right)\mathscr{K}_1\left(\frac{r_o}{h\sqrt{\tilde{\mathrm{Bo}}_{\eta_S}}}\right)}, \\
B(r^*) &= -\frac{\mathscr{I}_1\left(\frac{r_i}{h\sqrt{\tilde{\mathrm{Bo}}_{\eta_S}}}\right)}{\tilde{\mathrm{Bo}}_{\eta_S}} \frac{\mathscr{I}_1\left(\frac{r^*}{\sqrt{\tilde{\mathrm{Bo}}_{\eta_S}}}\right)\mathscr{K}_1\left(\frac{r_o}{h\sqrt{\tilde{\mathrm{Bo}}_{\eta_S}}}\right) - \mathscr{I}_1\left(\frac{r_o}{h\sqrt{\tilde{\mathrm{Bo}}_{\eta_S}}}\right)\mathscr{K}_1\left(\frac{r^*}{\sqrt{\tilde{\mathrm{Bo}}_{\eta_S}}}\right)}{\mathscr{I}_1\left(\frac{r_o}{h\sqrt{\tilde{\mathrm{Bo}}_{\eta_S}}}\right)\mathscr{K}_1\left(\frac{r_i}{h\sqrt{\tilde{\mathrm{Bo}}_{\eta_S}}}\right) - \mathscr{I}_1\left(\frac{r_i}{h\sqrt{\tilde{\mathrm{Bo}}_{\eta_S}}}\right)\mathscr{K}_1\left(\frac{r_o}{h\sqrt{\tilde{\mathrm{Bo}}_{\eta_S}}}\right)}, \\
C(r^*) &= \frac{\mathscr{K}_1\left(\frac{r_o}{h\sqrt{\tilde{\mathrm{Bo}}_{\eta_S}}}\right)}{\tilde{\mathrm{Bo}}_{\eta_S}} \frac{\mathscr{I}_1\left(\frac{r^*}{\sqrt{\tilde{\mathrm{Bo}}_{\eta_S}}}\right)\mathscr{K}_1\left(\frac{r_i}{h\sqrt{\tilde{\mathrm{Bo}}_{\eta_S}}}\right) - \mathscr{I}_1\left(\frac{r_i}{h\sqrt{\tilde{\mathrm{Bo}}_{\eta_S}}}\right)\mathscr{K}_1\left(\frac{r^*}{\sqrt{\tilde{\mathrm{Bo}}_{\eta_S}}}\right)}{\mathscr{I}_1\left(\frac{r_o}{h\sqrt{\tilde{\mathrm{Bo}}_{\eta_S}}}\right)\mathscr{K}_1\left(\frac{r_i}{h\sqrt{\tilde{\mathrm{Bo}}_{\eta_S}}}\right) - \mathscr{I}_1\left(\frac{r_i}{h\sqrt{\tilde{\mathrm{Bo}}_{\eta_S}}}\right)\mathscr{K}_1\left(\frac{r_o}{h\sqrt{\tilde{\mathrm{Bo}}_{\eta_S}}}\right)}, \\
D(r^*) &= -\frac{\mathscr{I}_1\left(\frac{r_o}{h\sqrt{\tilde{\mathrm{Bo}}_{\eta_S}}}\right)}{\tilde{\mathrm{Bo}}_{\eta_S}} \frac{\mathscr{I}_1\left(\frac{r^*}{\sqrt{\tilde{\mathrm{Bo}}_{\eta_S}}}\right)\mathscr{K}_1\left(\frac{r_i}{h\sqrt{\tilde{\mathrm{Bo}}_{\eta_S}}}\right) - \mathscr{I}_1\left(\frac{r_i}{h\sqrt{\tilde{\mathrm{Bo}}_{\eta_S}}}\right)\mathscr{K}_1\left(\frac{r^*}{\sqrt{\tilde{\mathrm{Bo}}_{\eta_S}}}\right)}{\mathscr{I}_1\left(\frac{r_o}{h\sqrt{\tilde{\mathrm{Bo}}_{\eta_S}}}\right)\mathscr{K}_1\left(\frac{r_i}{h\sqrt{\tilde{\mathrm{Bo}}_{\eta_S}}}\right) - \mathscr{I}_1\left(\frac{r_i}{h\sqrt{\tilde{\mathrm{Bo}}_{\eta_S}}}\right)\mathscr{K}_1\left(\frac{r_o}{h\sqrt{\tilde{\mathrm{Bo}}_{\eta_S}}}\right)}.
\end{aligned}
\tag{III.B.57}
$$

Solution for the surface velocity at the leading order

Finally, integrating Eq. (III.B.34) between r_i/h and r_o/h and using the Dirac distribution properties leads to:

$$
v^*_{\theta S}(r^*) = \int_{\frac{r_i}{h}}^{r^*} G(r^*|\xi) f(\xi)\,\mathrm{d}\xi + \int_{r^*}^{\frac{r_o}{h}} G(r^*|\xi) f(\xi)\,\mathrm{d}\xi, \tag{III.B.58}
$$

where $G(r^*|\xi)$ is given by Eq. (III.B.52) (with the coefficients defined in Eq. (III.B.57)), and $f(\xi)$ is provided by Eq. (III.B.33). The two integrals are numerically evaluated at each radial location, and deliver a curve fitting that comes from a set of discrete values obtained from Gauss integrations. Because numerical calculations arise at the very end of this analytical process, no loss of generality can be suspected. Then, Eq. (III.B.58) is injected in Eqs. (III.B.29) and (III.B.30), and the problem is mathematically solved.

III.B.1.f Results and interpretation

Relevant scaling

The choice of the height h as a scale-length allows for the determination of the corresponding MHD Eqs. (III.B.3) and (III.B.4), by avoiding the aspect ratios. However, the relevant typical length for the r variable is not h, but is in fact the outer radius r_o. For post-processing, a scaling analysis is thus needed to take the role of these aspect ratios into account, so that the magnitudes of the dimensionless quantities belong to $[0,1]$. All the new quantities that are drawn in the figures of Sec. III.B.1.f, as a result of this new scaling process, are superscripted *.

The definitions of these new non-dimensional quantities are as follows:

- the radial coordinate $r^\star = (h r^* - r_i)/(r_o - r_i) = (r - r_i)/(r_o - r_i)$;
- the axial coordinate $z^\star = z^* = z/h$;
- the velocity $v_\theta^\star = v_\theta/V = (h/r_o)v_\theta^* = (h/r_o)v_\theta/\mathsf{V}$, with $V = r_o\Omega = (r_o/h)\mathsf{V}$;
- the magnetic induction $b_\theta^\star = b_\theta/b = (h/r_o)B_\theta^* = (h/r_o)B_\theta/\mathsf{b}$, where we define $b = \mu V\sqrt{\sigma\eta} = (r_o/h)\mathsf{b}$;
- the electric current density: $\vec{j}^\star = \vec{j}/J = (h/r_o\mathrm{Ha})\vec{j}^* = (h/r_o\mathrm{Ha})\vec{j}/\mathsf{J}$, where we define $J = \sigma B_0 V = (r_o\mathrm{Ha}/h)\mathsf{B}/\mu h = (r_o\mathrm{Ha}/h)\mathsf{J}$;
- and eventually the Lorentz force density $\vec{f}_\mathrm{L}^\star = \vec{j}^\star \times \vec{e}_z = f_{\mathrm{L}\theta}^\star \vec{e}_\theta = -j_r^\star \vec{e}_\theta$.

The surface velocity

Fig. III.B.3 shows the dependence of $v_{\theta S}^\star$ with respect to $r^\star$, and to the Hartmann and Boussinesq numbers, Ha and Bo_{η_S}, respectively. For a given Ha number, a small

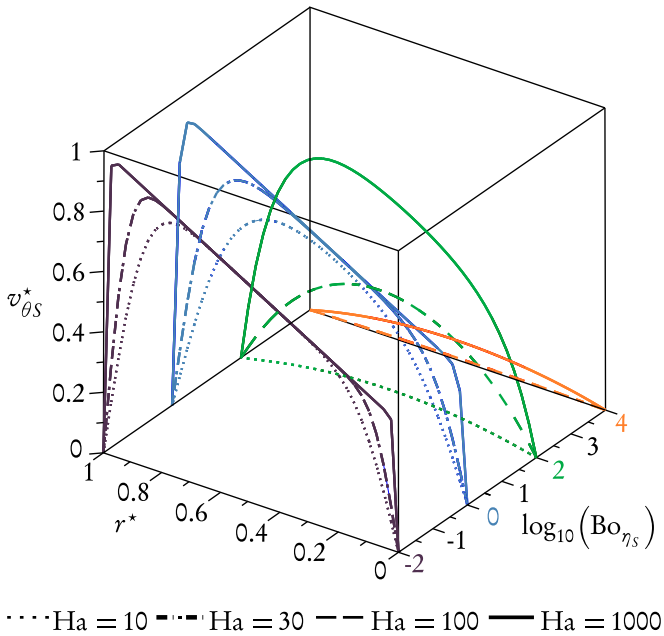

Figure III.B.3 – $v_{\theta S}^\star(r^\star)$ at various values of Ha and Bo_{η_S}.

value of the Bo_{η_S} number consistently involves a higher surface velocity with a profile along the annular gap that tends towards a Couette-like linear profile, apart from near the side walls, where matching to the Dirichlet conditions is fulfilled. This is essentially because in-plane viscous dissipation in the interface is reduced; meanwhile, the surface flow is entirely controlled by the sub-phase shear, which acts as an external body force for the liquid surface. One final consequence is that the linear momentum injected from the rotating floor is free to diffuse vertically up to the sliding interface. Conversely, when Bo_{η_S} is large, the surface velocity profile tends toward a Poiseuille-like parabolic profile with decreasing surface velocity. Then, the surface flow is no longer coupled to the sub-phase flow, and it obeys its own dynamics. Equation (III.B.10) reduces to a Laplace equation, and the two end-point Dirichlet boundary conditions impose a vanishing velocity all along the rigidified surface.

For a given Bo_{η_S} number, Fig. III.B.3 shows the higher Ha is, the higher surface velocity will be. Depending on the value used for Ha, either the linear or the parabolic velocity profile is recovered. This illustrates another mechanism: high magnetic induction tends to "freeze" the liquid metal similar to a rigid body motion (similarly to what is observed in the previously introduced Lehnert's experiment [3]). It favours the z component of the vorticity, $\omega_z = (1/r)\partial(r v_\theta)/\partial r$, so that v_θ depends only on r, and the same also applies for $v_{\theta S}$. This phenomenon can be mathematically illustrated as follows: Eq. (III.B.33) requires $\lim_{\mathrm{Ha}\to\infty} f(r^*) = -r^*$, which yields (using Eq. (III.B.31)) that $\lim_{\mathrm{Ha}\to\infty} v^*_{\theta S}(r^*) = r^*$. Also, it can be shown using Eq. (III.B.29) that $\lim_{\mathrm{Ha}\to\infty} v^*_\theta(r^*) = 1/2 \lim_{\mathrm{Ha}\to\infty}(v^*_{\theta S}(r^*) + r^*)$, leading to $\lim_{\mathrm{Ha}\to\infty} v^*_\theta(r^*) = r^*$. Therefore, when $\mathrm{Ha}\to\infty$, $v^*_\theta(r^*) = v^*_{\theta S}(r^*) = r^*$, the whole fluid may be indeed considered as a rotating rigid body.

In conclusion, on the surface velocity properties, it may be said that the well-known two-dimensionality tendency of the magnetic induction acts here in competition with the aforementioned damping due to strong surface viscous dissipation. With a very high Ha relative to Bo_{η_S}, the interface is almost perfectly aligned with the rotating floor because of the electromagnetic blocking, whereas a very high Bo_{η_S} prevents the momentum from diffusing throughout the bulk, which highlights the crucial role that the surface rheology may play in the MHD problem. These competitive effects are expected to be magnified in the analysis of the bulk quantities.

The bulk quantities

2-D Graphs for asymptotic cases

In this section, the 2-D graphs for both the velocities and the electromagnetic quantities are shown in two extreme cases, *i.e.*, in the case $\mathrm{Ha} = 30 \ll \mathrm{Bo}_{\eta_S} = 1000$ and in the case $\mathrm{Ha} = 50 \gg \mathrm{Bo}_{\eta_S} = 0.01$. These values correspond to the asymptotic values of the modified Boussinesq number that was defined in equation (III.B.32), *i.e.* $\tilde{\mathrm{Bo}}_{\eta_S} \gg 1$ and $\tilde{\mathrm{Bo}}_{\eta_S} \ll 1$. The first aim is to indicate two radically different MHD regimes, and then to verify how the overall flow topology can evolve. First, the results for the original variables $v^\star_\theta$ and $b^\star_\theta$ are summarized in Fig. III.B.4. The left-hand side corresponds to the $\tilde{\mathrm{Bo}}_{\eta_S} \ll 1$ case, while the right-hand side corresponds to the $\tilde{\mathrm{Bo}}_{\eta_S} \gg 1$ case.

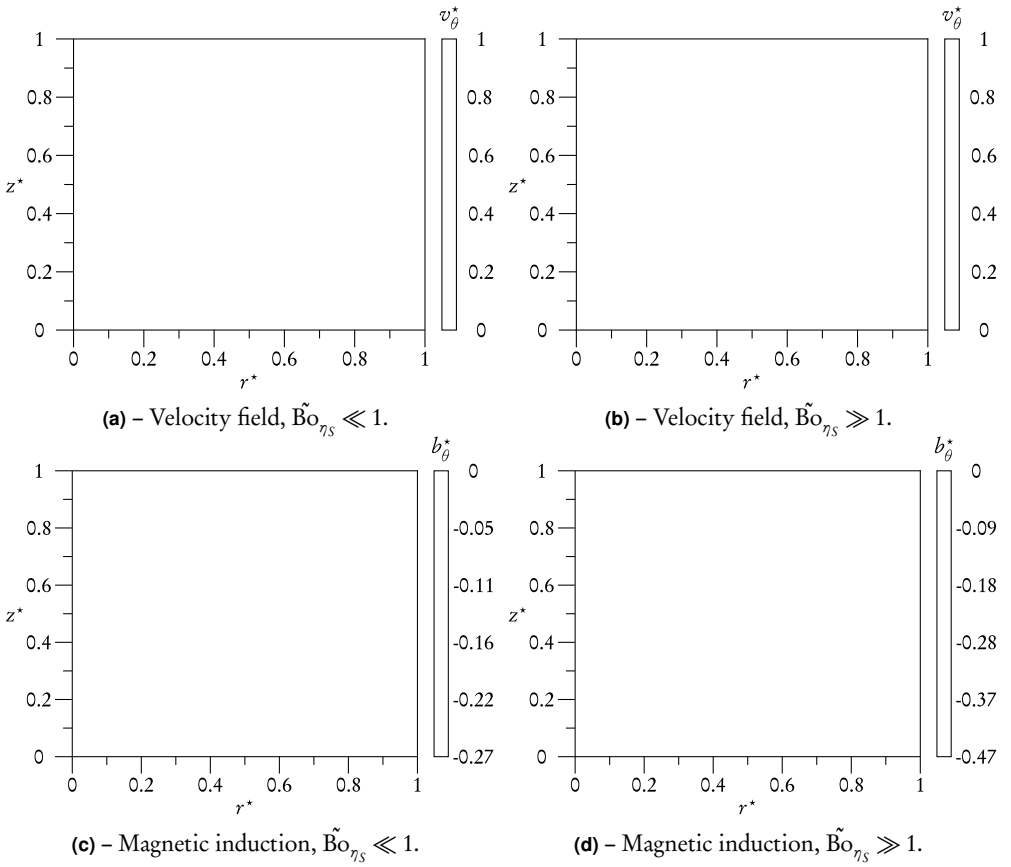

(a) – Velocity field, $\tilde{\mathrm{Bo}}_{\eta_S} \ll 1$.

(b) – Velocity field, $\tilde{\mathrm{Bo}}_{\eta_S} \gg 1$.

(c) – Magnetic induction, $\tilde{\mathrm{Bo}}_{\eta_S} \ll 1$.

(d) – Magnetic induction, $\tilde{\mathrm{Bo}}_{\eta_S} \gg 1$.

Figure III.B.4 – Velocity (top) and magnetic induction (bottom) for the two extreme cases $\tilde{\mathrm{Bo}}_{\eta_S} \ll 1$ (left-hand column) and $\tilde{\mathrm{Bo}}_{\eta_S} \gg 1$ (right-hand column).

When considering the velocity, the topology evolves from an exclusively radial dependence with velocity gradients that are perfectly aligned with $\vec{e}_r$ (apart from those near the side-walls) for $\mathrm{Ha} \gg \mathrm{Bo}_{\eta_S}$ in Fig. III.B.4(a), to a motionless configuration for $\mathrm{Ha} \ll \mathrm{Bo}_{\eta_S}$ in Fig. III.B.4(b), where the velocity is mainly concentrated near the bottom right corner. This behaviour is linked to significant physical phenomena. For Fig. III.B.4(a), the previously mentioned electromagnetic blocking is responsible for the dissipation of the secondary vortices, and for the fluid alignment with the rotating floor, as observed by Lehnert [3]. For Fig. III.B.4(a), the motionless topology is partly because of an inert interface for $\mathrm{Bo}_{\eta_S} \gg \mathrm{Ha}$, which imposes matching with a vanishing velocity at the interface, but other mechanisms are also brought into play, and are highlighted through analysis of the electromagnetic quantities. For this purpose, the results concerning the derived electromagnetic quantities, *i.e.* the electric current density and the Lorentz force density, are also displayed in Fig. III.B.5.

The magnetic induction and electric currents are obviously confined in the Shercliff layers when $\tilde{\mathrm{Bo}}_{\eta_S} \ll 1$, with two electrical loops near the side-walls, as shown in Figs. III.B.4(c) and III.B.5(a), with the core and the Hartmann layers making a negligible contribution. The topology is dramatically different for $\tilde{\mathrm{Bo}}_{\eta_S} \gg 1$, where the core

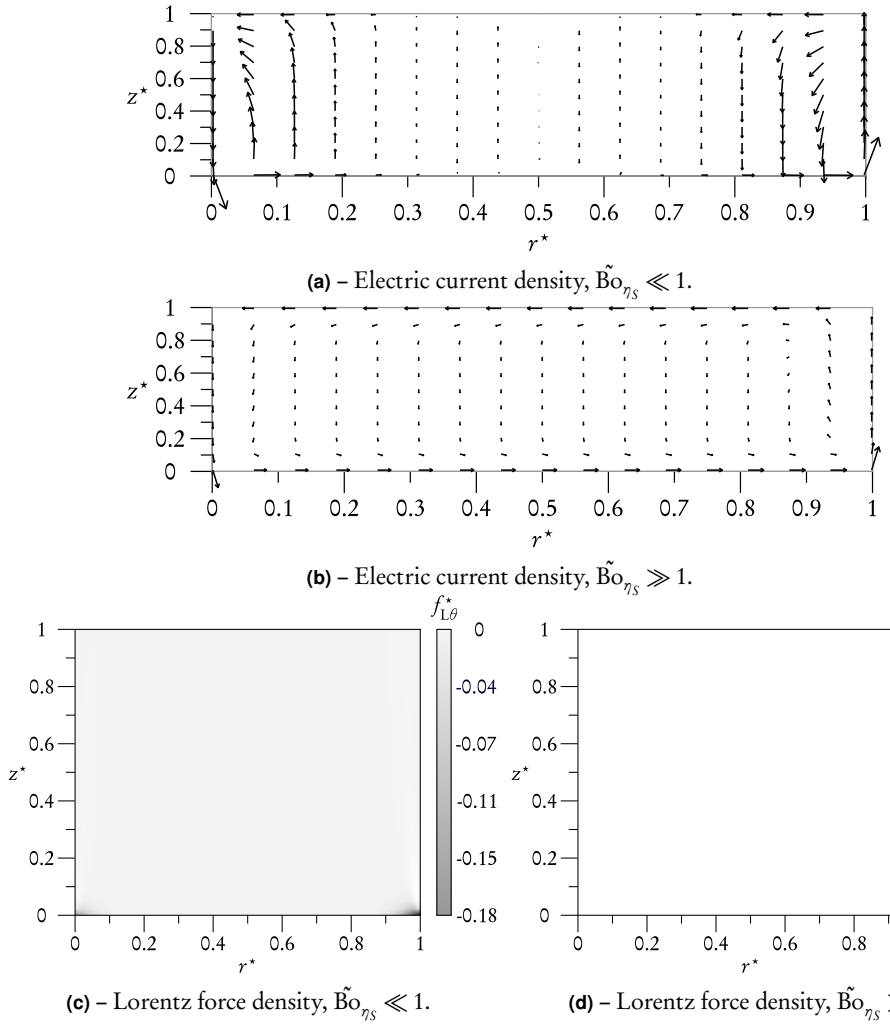

(a) – Electric current density, $\tilde{\mathrm{Bo}}_{\eta_S} \ll 1$.

(b) – Electric current density, $\tilde{\mathrm{Bo}}_{\eta_S} \gg 1$.

(c) – Lorentz force density, $\tilde{\mathrm{Bo}}_{\eta_S} \ll 1$.

(d) – Lorentz force density, $\tilde{\mathrm{Bo}}_{\eta_S} \gg 1$.

Figure III.B.5 – Electric current density (top, contours: $b_\theta^\star$ streamlines) and Lorentz force density (bottom) for the two extreme cases $\tilde{\mathrm{Bo}}_{\eta_S} \ll 1$ and $\tilde{\mathrm{Bo}}_{\eta_S} \gg 1$. For a given low velocity $\Omega = 0.25\,\mathrm{rpm}$, $J = 4.1 \times 10^2\,\mathrm{A{\cdot}m^{-2}}$ for $\mathrm{Ha} = 30$ and $6.8 \times 10^2\,\mathrm{A{\cdot}m^{-2}}$ for $\mathrm{Ha} = 50$. $\vec{j}^\star$ is log-scaled by the magnitude $\exp(\ln(\|\vec{j}^\star/\|\vec{j}^\star\|_{\max}))/(1+p))\|$, $p = 3$ for a) and $p = 1$ for b).

seems to be more involved, but the Hartmann layers in particular are now electrically active, with the setting of an "electric bridge" between the two side layers that is established through the Hartmann layers, as shown in Figs. III.B.4(d) and III.B.5(b). This is linked to the velocity topology mentioned earlier, with no particular gradients of $v_\theta^\star$ along the $\vec{e}_z$ axis in the case where $\mathrm{Ha} \gg \mathrm{Bo}_{\eta_S}$, other than near the side walls, whereas these gradients arise elsewhere and especially arise near the interface in the case where $\mathrm{Ha} \ll \mathrm{Bo}_{\eta_S}$. Depending on the prevailing regime, this means that the source term of $b_\theta^\star$ in Eq. (III.B.3) either exists or does not, which could explain the activation or non-activation behaviour of the Hartmann layers.

This is confirmed when analysing the graphs of the Lorentz force density. The presence of a strong radial component of the electric current density, in the $\tilde{\mathrm{Bo}}_{\eta_S} \gg 1$

case, in combination with the imposed magnetic field $B_0\vec{e}_z$, leads to the emergence of a Lorentz force density in the Hartmann layers, along the azimuthal direction (otherwise extremely confined, see Fig. III.B.5(c)). As deduced from Fig. III.B.5(d), this Lorentz force is negative at the bottom, and positive at the top of the channel cross-section. Consequently, this leads to an electromagnetic damping of the momentum injected from the rotating floor at the bottom, while it enhances momentum in the upper part of the channel. Both contributions lead to an homogenisation of the flow, which explains the overall flow patterns.

It is important to point out that the bottom Hartmann layer is only activated when the top layer is activated, whereas the "dynamic" configuration remains the same near the rotating floor. This is because of the current continuity equation, which yields $\mathrm{div}(\vec{j}^\star) = 0$ and causes the electric current to close up inside the fluid. When the Hartmann layer at the top is activated, the current then flows across the boundary layers, with the core contribution remaining quite small, and therefore closes up inside these layers.

Beyond this asymptotic analysis, which does not allow us to determine the flow topology quantitatively in conjunction with the values of Ha and Bo_{η_S}, a more refined analysis is now proposed, in order to draw some scaling laws with respect to the control parameters.

1-D Graphs for general analysis

The MHD quantities are plotted along the cutting lines (A) and (B) drawn in Fig. III.B.1, for numerous combinations of the Ha and Bo_{η_S} values. Line (A) is designed such that it allows the analysis of the Shercliff layers, and (B) allows the same for the Hartmann layers. The magnetic induction is not plotted here because the relevant information about the electromagnetic quantities is contained in the electric current density. The velocity $v_\theta^\star$ is plotted along the two cutting lines. With respect to the electric current, it depends on the layer being considered. Using $\mathrm{div}(\vec{j}^\star) = 0$, we can prove that with the stretched coordinate r_{SL}^* or r_{SR}^* inside the Shercliff layers (or alternatively z_{HB}^* or z_{HT}^* inside the Hartmann layers), the $\vec{e}_r$ component is several orders of magnitude lower than the $\vec{e}_z$ component inside the Shercliff layers; the opposite situation holds inside the Hartmann layers. Consequently, the choice is made to plot only $j_z^\star$ along (A), and to plot only $j_r^\star$ along (B).

The results are summarised in Fig. III.B.6. The left-hand side corresponds to the cutting line (A), while the right-hand side corresponds to the cutting line (B). Unlike the previous section where only the asymptotic cases were addressed, the analysis of the intermediate regimes allows us to depict the significant tendencies inside the core and the boundary layers, depending on two general cases: the evolution with respect to Ha for a given value of Bo_{η_S}, and the evolution with respect to Bo_{η_S} for a given value of Ha.

Let us begin with the first case, the Ha-dependence, for a given Bo_{η_S}, which corresponds to the curves (—), (···) and (— —). As shown in Fig. III.B.6(a), the velocity profiles are stretched along the $\vec{e}_z$ axis with increasing Ha, echoing the electromagnetic blocking phenomenon described earlier, which enhances the diffusion of the rotat-

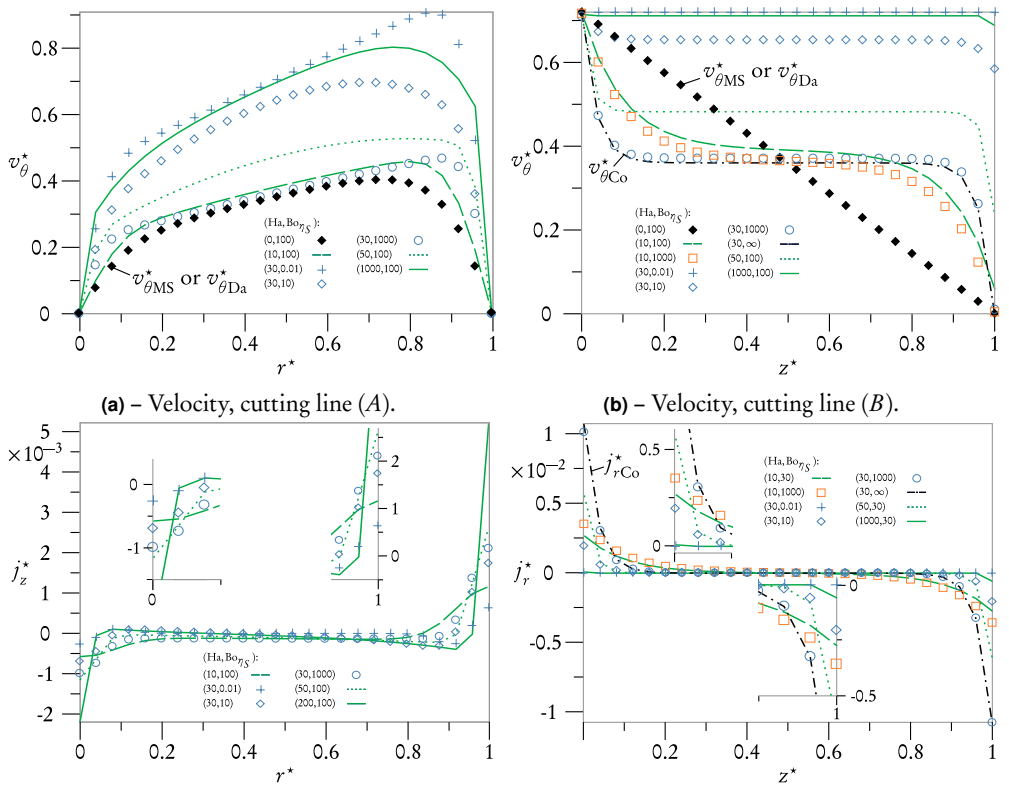

(a) – Velocity, cutting line (A).

(b) – Velocity, cutting line (B).

(c) – Axial electric current, cutting line (A).

(d) – Radial electric current, cutting line (B).

Figure III.B.6 – Velocity and electric current with respect to various (Ha, Bo$_{\eta_S}$) values, along cutting lines (A) (left-hand column) or (B) (right-hand column). MS, Da and Co refer to Mannheimer and Schechter (Eq. (III.A.2)), Davoust (Eq. (III.A.4)) or Couette asymptotic solutions (Eq. (III.B.13)), respectively. The electric current densities are normalised with respect to the maximum electric current $J_{\max} = 1.36 \times 10^4$ A·m^{-2} (reached for Ha $= 10^3$).

ing floor-induced momentum. Therefore, this leads to extension of the radial dependence, $v_\theta^\star = r^\star$, in the core (curve (—)). The strong gradients are located in the Shercliff layers, for which the typical thickness is closely linked to the Hartmann number through the order of magnitude $O(\mathrm{Ha}^{-1/2})$, and they match the no-slip conditions at the side walls. The velocities $v_{\theta\mathrm{MS}}^\star$ and $v_{\theta\mathrm{Da}}^\star$ (curve (◆)), derived by Mannheimer and Schechter [31] (see Eq. (III.A.2)) and Davoust *et.al.* [72] (see Eq. (III.A.4)), respectively, allow for benchmarking of the present results by giving an asymptotic reference (corresponding to Ha = 0), which was not accessible when using our matched asymptotic expansion based on a large Hartmann number.

The first question arising from the observation of curves (— —) and (◆), as shown in Fig. III.B.6(a), considers the fact that the velocity tends towards a damped although still linear relation between $v_\theta^\star$ and $r^\star$ with vanishing Ha, for the case $\mathrm{Bo}_{\eta_S} = 100$.

The same curves in Fig. III.B.6(b) illustrate even more conclusively the "freezing" of the liquid bulk due to the electromagnetic field; the topology along (B) evolves from independence with respect to $z^\star$ in curve (—), to strong gradients located within the Hartmann layers when Ha is weak in curve (— —). These layers become thicker

and thicker with decreasing Ha, with their typical thickness being $O(\mathrm{Ha}^{-1})$. The ideal case of a hydrodynamic vertical Couette flow with a fully linear dependence is recovered when $\mathrm{Ha}=0$ and $\mathrm{Bo}_{\eta_S} \gg 1$ (curve (◆), MS or Da solution). In any case, the value reached in $z^\star=1$ is $v^\star_{\theta S}$, which depends on the value of $\tilde{\mathrm{Bo}}_{\eta_S}$ (see Sec. III.B.1.f).

The main question arising from Fig. III.B.6(b) is the following: why does the velocity seem to decrease with increasing Ha in the bottom part of the flow, while the opposite tendency prevails at the top? This phenomenon can be seen when comparing curves (— —) and (···), and is shown even more dramatically when considering curves (○) and (□).

Similar questions arise for Fig. III.B.6(d), representing the radial component of the electric current $j^\star_r$ inside the core and the Hartmann layers. The reason why the electric current seems to be increasingly intense in curves (— —) or (···) with increasing Ha, until it reaches a certain onset value, from which it decreases to zero while Ha becomes very large (curve (—)), is not straightforward. Classically, increasing the Hartmann numbers should only increase the magnitudes of the electric currents inside the boundary layers. This is typically the case in the parallel layers with $j^\star_z$ shown in Fig. III.B.6(c). To answer all these questions, we must now address the second issue, which deals with the evolution of the topology with respect to Bo_{η_S}.

It is obvious in Fig. III.B.6(a) that for a given $\mathrm{Ha}=30$, corresponding to the three curves (+), (◇) and (○), the velocity along (A) evolves from the previously mentioned linear relation $v^\star_\theta = r^\star$ in the core when Bo_{η_S} is low because of the electromagnetic blocking, towards the motionless liquid bulk that is characterised by another linear profile, with the vertical Couette flow imposing a no-slip condition at the interface for large values of Bo_{η_S}. The first question is thus partly solved by the fact that high Bo_{η_S} values results into an inert interface, preventing the linear momentum from diffusing well vertically across the bulk.

Along line (B), in Fig. III.B.6(b), the same three curves show that when no surface shearing is present, the bulk velocity is totally independent of the axial coordinates, with the gradients being completely aligned with the $\vec{e}_r$ axis (see curve (+)). This gradually evolves into a configuration where the gradients are localized in the Hartmann layers, with the surface velocity vanishing, as shown in curves (◇) and (○). This reveals a significant phenomenon, which answers all of our questions as a whole: the value of the Boussinesq number drives the activation of the Hartmann layers.

To validate this statement, let us now focus on the electric current circuit by considering Fig. III.B.6(c) and III.B.6(d), and scrutinizing the same three curves (+), (◇) and (○). First, when shearing acts in the interface as shown in curve (○), a radial component of the electric current density $j^\star_r$ arises within the top and bottom Hartmann layers, because of velocity gradients that are induced in the vicinity of the interface, whereas it progressively vanishes with decreasing Bo_{η_S}, as shown in Fig. III.B.6(d). This is not as obvious as far as the Shercliff layers are concerned, as shown in Fig. III.B.6(c). The Boussinesq number indeed seems to control the magnitude of $j^\star_z$, which increases a little with Bo_{η_S}, but the gain is not as dramatic. The reason for this is that, independently from the activation of the Hartmann layers, the velocity gradients always exist in the Shercliff layers, because of the inert side walls. This results in an electric current $j^\star_z$ even when Bo_{η_S} is very low (see curve (+)).

Nevertheless, this activation is responsible for all the phenomena evoked above, because it is the source of a $\vec{e}_\theta$-component of the Lorentz force acting in the Hartmann layers, $-j_r^\star \vec{e}_\theta$. This means that when j_r is positive, it acts as a braking force, whereas when j_r is negative, it acts as a driving force for the flow. Consequently, as we can deduce from Fig. III.B.6(d), the Lorentz force, which become more intense with increasing Ha, prevents the diffusion of the momentum from the rotating floor inside the bulk, damping the flow in the bottom part of the channel, whereas it enhances the momentum diffusion in the top part. This tendency to make the velocity profile uniform can be observed in Fig. III.B.6(b) with curves (○) and (□). The onset point at which the electric current starts to vanish with increasing Ha corresponds to a sufficiently low $\tilde{\mathrm{Bo}}_{\eta_S}$ number, that suppresses the shearing and aligns the surface motion with the bulk dynamics, thus deactivating the Hartmann layers, and therefore switching off the electric currents within them. Otherwise, the classical increase of the electric current order of magnitude with Ha is permitted.

One final remark about this evolution with respect to Bo_{η_S} is that the latter does not control the thicknesses of the boundary layers for a given Hartmann number, which remains consistent with the definition of these boundary layers, for which the typical length is only linked to Ha. In addition, the relevance of these results is tested by comparing the case where the Boussinesq number is very high, *i.e.* curve (○), to that of the classical MHD Couette flow defined in Eqs. (III.B.13) and (III.B.14), where the interface is considered to be a rigid wall, *i.e.* $\mathrm{Bo}_{\eta_S} \to \infty$ (curve (— · —)). The agreement between these two curves for either the velocity in Fig. III.B.6(b) or the electric current density in Fig. III.B.6(d) is quite satisfying. Finally, for a given Ha number, one can notice that the calculation is directly at an end in Eq. (III.B.31), and the surface velocity is explicitly given by Eq. (III.B.33), if the asymptotic inviscid interface limit $\mathrm{Bo}_{\eta_S} = 0$ is taken, before the additional difficulty of assuming a viscous interface. The results thus obtained are compared to those calculated when the viscous interface is indeed assumed, in the limit $\mathrm{Bo}_{\eta_S} \to 0$. The reason why these results are not displayed in Fig. III.B.5 is that the two curves would be perfectly superimposed for low enough Bo_{η_S} (typically $\mathrm{Bo}_{\eta_S} = 0.01$).

Consequently, we are reasonably confident about the diagnosis that the Boussinesq number indeed drives the activation of the Hartmann layers, and consequently drives the magnitude of both velocity and electric currents in both the core and boundary layers, although to a lesser extent in the Shercliff layers. As for the Hartmann number, it controls the typical thicknesses of these boundary layers, along with the magnitudes of both the dynamic and electrical quantities, but the evolutions of these quantities are not classical. This is due to the balance between these two numbers, which illustrates two competitive phenomena: on the one hand, the MHD tendency towards two-dimensionality, on the other hand, the interface shearing. Their competitive effects are determined by the new dimensionless number introduced in this work, *i.e.* the modified Boussinesq number $\hat{\mathrm{Bo}}_{\eta_S}$. In order to confirm these fundamental conclusions, let us implement now a 2-D numerical study focusing also on the coupling between surface viscous shear and bulk MHD, that we shall benchmark with the previous analytical results.

III.B.2 2-D numerical study of the annular MHD viscometer

III.B.2.a Motivation for a numerical approach

The previous analytical results derive from a matched asymptotic expansion based on the vanishing parameter 1/Ha. Strictly speaking, these results are mathematically true when $\mathrm{Ha} \to \infty$. However, in order to keep some significant physical insight, a large range of values for Ha has been tested and interpreted, resulting in different MHD topologies. The interpretations stemming from this analysis must therefore be benchmarked to check how far they are relevant when Ha is only considered high enough (and not infinite). Consequently, there is a need for a method that circumvents the infinite Ha issue, even if the model must still conform to the assumption that the inertial terms are neglected. This benchmark must also take the corner regions into account, that were ignored in the analytical reasoning. In the light of all these issues, the choice of a 2-D numerical model proves relevant. The software selected to perform the calculation is the finite-element method (FEM) Comsol® software.

III.B.2.b The choice of a FEM software: why Comsol?

The present work is essentially multiphysics, involving such different fields as fluid mechanics, electromagnetism and surface rheology. As far as a numerical study is required, the software used has to address the issue of multi-modelling. Comsol Multiphysics is one among the worldwide references in multiphysics simulations, proposing various physical modules: AC/DC for electromagnetic and/or electric problems, CFD for computational fluid dynamics (including chemical species transport, fluid flow: single-phase or two-phase…), plasma, electro-chemistry, etc. It also includes a lot of mathematical models, allowing for the development of customised weak forms of a given physical problem, in the case it is not satisfyingly addressed in one of the aforementioned modules.

As said before, Comsol is a FEM software. The finite-element method consists in transferring a physical problem into its variational or "weak" form in the considered domain. This weak form is generally equivalent to the minimisation of energy principle. The spatial domain is divided into a mesh, consisting of different points (the nodes). The approximate problem is then written in a mathematical sub-space with finite dimension n, and the sub-domain corresponding to each mesh element is described by so-called "test" functions w, with order n, constituting a basis for the space coordinates. The approximate solution is thus a function determined by its values at the mesh nodes (linked themselves to the expression of the test functions w at these points).

This method is widely used to discretise the Maxwell equations in electromagnetism. However, the discrete approximation is not *a priori* conservative, because contrary to the finite-volume method (FVM), the governing equations are not integrated in the form of conservative laws. Therefore, particular care is required to ensure a conservative solution, as well as strong asymptotic cases to validate the numerical

results. Nonetheless, such attention is not needed in the present case, the continuity equations $\mathrm{div}(\vec{v}) = \mathrm{div}(\vec{j}) = 0$ being always fulfilled in the 2-D axisymmetric case.

III.B.2.c Problem formulation and implementation in Comsol

Physical layout and approximations

The physical layout is completely identical to the system described in the analytical part, based on the rectangular cross-section of the annular MHD viscometer. This layout is reminded in Fig. III.B.7, along with the boundary conditions. We make exactly the same approximations as in the previous section, with the following notable exception: it is only assumed in this section that $\mathrm{Ha} \gg \mathrm{Re}$, and not that $\mathrm{Ha} \gg 1$, which was required in the previous analytical section for implementing the matched asymptotic expansion.

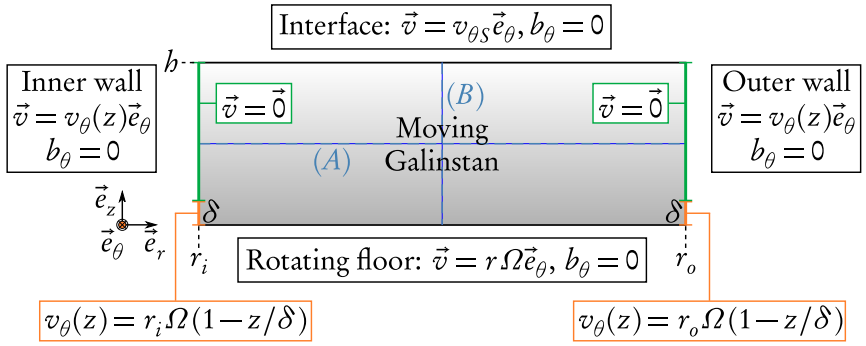

Figure III.B.7 – Geometry and boundary conditions of the channel crossed-section used for 2-D numerical computation.

Governing equations and boundary conditions

From strong to weak forms

Like in the analytical study, the two unknowns are the dimensionless azimuthal magnetic induction $b_\theta^\star$ and velocity $v_\theta^\star$. As previously explained, they are governed by the azimuthal projection of induction equation and of Navier-Stokes equation, given in their dimensionless strong forms by Eqs. (III.B.3) and (III.B.4). These equations are completed with the BCs (III.B.5), (III.B.6), (III.B.7) and (III.B.8), (III.B.9). The latter BC involves the coupling variable $v_{\theta S}^\star$, which links the bulk dynamics with surface rheology. This variable is ruled by the Boussinesq-Scriven ordinary differential equation (ODE) (III.B.10).

Eqs. (III.B.3) and (III.B.4) are Poisson's partial differential equations, whose weak form determination is a classical mathematical problem. By the way, it is directly implemented in adequate mathematical modules called "coefficient form PDE" in Comsol; hence, these weak forms are not detailed here (see. [59] for further details). The (motionless and rotating) wall boundary conditions are defined in subsequent nodes.

The treatment of the JMB at the interface, though, is worth further investigation, because it is not directly available in Comsol. Indeed, the BC (III.B.10) is taken into account through the module "weak form boundary", which requires the weak form calculation. Let us first remind the strong form of the JMB:

$$\mathrm{Bo}_{\eta_S}\frac{\mathrm{d}}{\mathrm{d}r^*}\left(\frac{1}{r^*}\frac{\mathrm{d}}{\mathrm{d}r^*}\left(r^* v^*_{\theta S}\right)\right)-\left.\frac{\partial v^*_\theta}{\partial z^*}\right|_{z^*=1}=0.$$

This strong form is then multiplied by the test functions w and integrated along the interface:

$$\int_{\frac{r_i}{h}}^{\frac{r_o}{h}} w(r^*)\left(\mathrm{Bo}_{\eta_S}\frac{\mathrm{d}}{\mathrm{d}r^*}\left(\frac{1}{r^*}\frac{\mathrm{d}}{\mathrm{d}r^*}\left(r^* v^*_{\theta S}\right)\right)-\left.\frac{\partial v^*_\theta}{\partial z^*}\right|_{z^*=1}\right)\mathrm{d}r^*=0. \tag{III.B.59}$$

Now, let us focus on the weak contribution due to the left-hand term of the integrand, *i.e.* the one linked to the surface viscous shearing. This term is integrated by parts, in order to lower the order of derivatives. This yields, assuming $w(r_i/h)=w(r_o/h)=0$:

$$\int_{\frac{r_i}{h}}^{\frac{r_o}{h}} \mathrm{Bo}_{\eta_S} w(r^*)\frac{\mathrm{d}}{\mathrm{d}r^*}\left(\frac{1}{r^*}\frac{\mathrm{d}}{\mathrm{d}r^*}\left(r^* v^*_{\theta S}\right)\right)\mathrm{d}r^*=\underbrace{\left[\frac{\mathrm{Bo}_{\eta_S} w(r^*)}{r^*}\frac{\mathrm{d}}{\mathrm{d}r^*}\left(r^* v^*_{\theta S}\right)\right]_{\frac{r_i}{h}}^{\frac{r_o}{h}}}_{0}$$

$$-\int_{\frac{r_i}{h}}^{\frac{r_o}{h}}\frac{\mathrm{Bo}_{\eta_S}}{r^\star}\frac{\mathrm{d}w}{\mathrm{d}r^*}\frac{\mathrm{d}}{\mathrm{d}r^*}\left(r^* v^*_{\theta S}\right)\mathrm{d}r^*=-\int_{\frac{r_i}{h}}^{\frac{r_o}{h}}\mathrm{Bo}_{\eta_S}\frac{\mathrm{d}w}{\mathrm{d}r^*}\left(\frac{\mathrm{d}v_{\theta S}}{\mathrm{d}r^*}+\frac{v_{\theta S}}{r^*}\right)\mathrm{d}r^*.$$

The right-hand term of Eq. (III.B.59) does not require further simplification, since it is the (bulk) source term, that we can directly use without further investigation. Eq. (III.B.59) must remain true whatever the considered test function w. As a consequence, the weak formulation of the azimuthal component of the JMB at the liquid surface, that we shall implement in the weak form boundary module, is written:

$$\mathrm{Bo}_{\eta_S}\frac{\mathrm{d}w}{\mathrm{d}r^*}\left(\frac{\mathrm{d}v_{\theta S}}{\mathrm{d}r^*}+\frac{v_{\theta S}}{r^*}\right)+w(r^*)\left.\frac{\partial v^*_\theta}{\partial z^*}\right|_{z^*=1}=0. \tag{III.B.60}$$

Numerical treatment of boundary data discontinuity at the bottom corners

At the inner and outer side-walls, a no-slip boundary condition is normally imposed for velocity. However, there is a boundary discontinuity between the inner or outer (motionless) side-walls and the rotating floor. This discontinuity may lead to non-physical numerical artefacts, which could propagate from the corner and thus alter the core-flow patterns. In order to circumvent these difficulties, two matching functions are introduced for the azimuthal component of velocity, as shown in Fig. III.B.7. These functions apply along segments of typical length $\delta \ll r_i, r_o$ (indicative value: $\delta = 2.5\times10^{-4}$ m) at the inner and outer walls of the annular channel

cross-section. With these matching functions, a Couette-like profile for velocity is classically assumed at the matching segments [83], which leads to:

$$v_\theta(r=r_i,z)=\begin{cases} r_i\Omega\left(1-\frac{z}{\delta}\right) & \text{if } z\in[0,\delta], \\ 0 & \text{if } z\in\,]\delta,h], \end{cases} \tag{III.B.61}$$

for the inner wall and to

$$v_\theta(r=r_o,z)=\begin{cases} r_o\Omega\left(1-\frac{z}{\delta}\right) & \text{if } z\in[0,\delta], \\ 0 & \text{if } z\in\,]\delta,h], \end{cases} \tag{III.B.62}$$

for the outer wall. Thus, velocity is imposed such that lubrication conditions in the gaps are taken into account, the continuity of v_θ being warranted at the matching points $z=\delta$ at both walls. These lubrication conditions are not simply a numerical technique. They stem from the true experimental layout, where this gap concretely exists between a rotating dish (rotating floor) and an inert cover (side walls), as described in Fig. III.B.8.

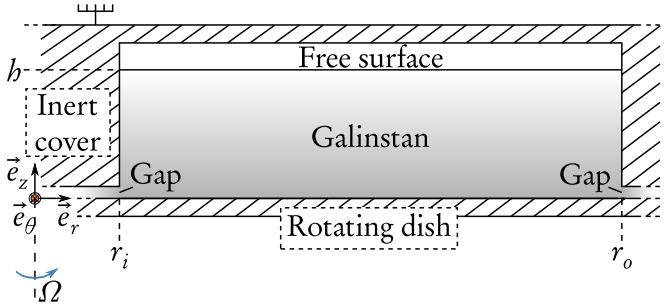

Figure III.B.8 – Lubrication gaps between the rotating floor and the motionless side-walls, with respect to the experimental layout (see *e.g.* Mannheimer *et al.* [31]).

Numerical implementation

The discretisation of the physical problem is performed on the basis of quadratic Lagrange elements. With respect to numerical methods, due to the basic layout of the computational domain, a fully-coupled approach is implemented, based on the full Jacobian matrix as one entity. This approach is based on the Newton-Raphson method, which linearises the problem based on the current solution, at each iteration. A linear stationary direct solver is implemented to solve the linearised problem, *i.e.* the multifrontal massively parallel sparse direct solver (MUMPS), based on lower-upper (LU) factorization (see [84] for further details).

Finally, the implemented mesh is displayed in Fig. III.B.9. It consists of 18 036 elements, mainly triangular, with mesh refinement on the Galinstan domain. A specific rectangular boundary layer mesh is set up at the boundaries of the fluid domain. Typically, the relative thickness of the first layer is set so as to be much lower than the reciprocal of the Hartmann number, which monitors the thickness of the physical boundary layers.

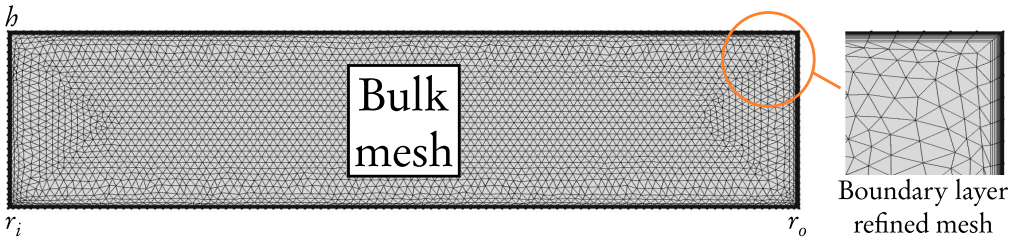

Figure III.B.9 – Mesh used for the 2-D numerical computation (18 036 elements). Inset: zoom on the boundary layer mesh.

III.B.2.d Numerical results

Agreement with the matched asymptotic expansion

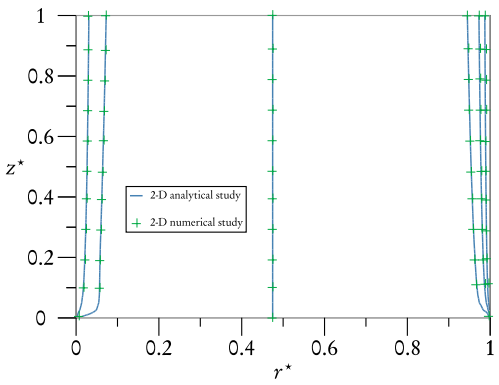

(a) – Azimuthal velocity contours, $\mathrm{Ha} = 50$, $\mathrm{Bo}_{\eta_S} = 0.01$.

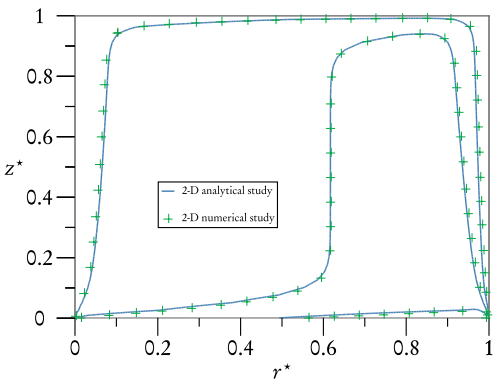

(b) – Azimuthal velocity contours, $\mathrm{Ha} = 30$, $\mathrm{Bo}_{\eta_S} = 1000$.

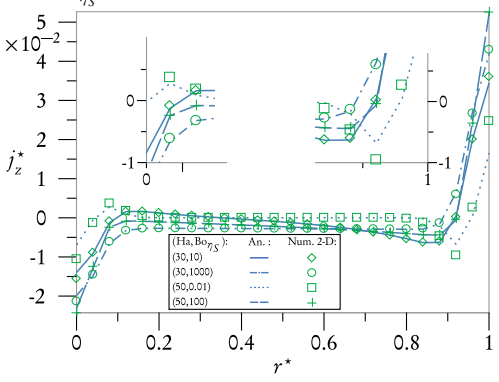

(c) – Vertical electric current along cutting line (A) (Core and Shercliff layers).

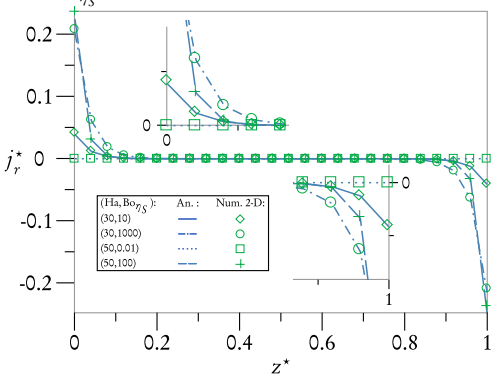

(d) – Radial electric current along cutting line (B) (Core and Hartmann layers).

Figure III.B.10 – Comparison between 2-D analytical and numerical results for velocity (top) and electric currents (bottom), with respect to various $(\mathrm{Ha}, \mathrm{Bo}_{\eta_S})$ values. The electric current densities are normalised with respect to the maximum electric current $J_{\max} = 6.8 \times 10^2\ \mathrm{A{\cdot}m^{-2}}$ reached in all cases, *i.e.* for $\mathrm{Ha} = 50$.

In this section, the 2-D numerical results are benchmarked with the analytical results described in Sec. III.B.1. Some results about the velocity field and electric currents are shown in Fig. III.B.10. The general agreement between analytical and numerical results is satisfying, particularly for velocity, where the contours resulting from the two different approaches are superimposed, either for $\mathrm{Ha} \gg \mathrm{Bo}_{\eta_S}$ (Fig. III.B.10(a)) or $\mathrm{Ha} \ll \mathrm{Bo}_{\eta_S}$ (Fig. III.B.10(b)). Now, concerning the electric current densities, a little discrepancy can be noted for the axial electric current flowing in the Shercliff layers (Fig. III.B.10(c)), for the curves corresponding to the case $\mathrm{Ha} \gg \mathrm{Bo}_{\eta_S}$ (for instance, curves (□) and (···)). However, the general agreement is quite satisfying for various $(\mathrm{Ha}, \mathrm{Bo}_{\eta_S})$ values, especially for the radial electric current flowing in the Hartmann layers (see Fig. III.B.10(d)), where the different curves are qualitatively and quantitatively the same.

The boudary data discontinuity

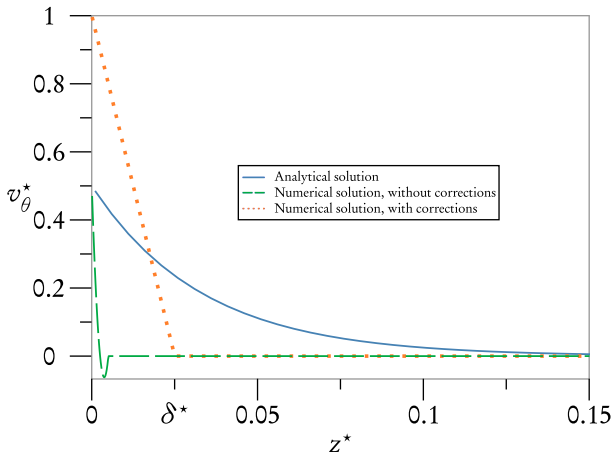

Figure III.B.11 – Comparison of the analytical and numerical results about right-wall velocity for $(\mathrm{Ha}, \mathrm{Bo}_{\eta_S}) = (30, 10)$.

The consequences of the numerical treatment of the boundary data discontinuity at the bottom corners are analysed in this section. The velocity profile at the right wall is shown in Fig. III.B.11, for the cases corresponding to the analytical calculation, the numerical simulation without the "matching lines" (see above) and the numerical simulation with the matching lines. The analytical results predict an exponential decay of the velocity $v_\theta^\star$ over a wide range of $r^\star$ values. The numerical result without corrections shows a non-physical negative peak value near the wall, and then rapidly matches the zero-value. With respect to the corrected numerical results, a linear decay is observed from the true $v_\theta^\star = 1$ value in $z^\star = 0$ (corresponding to the maximum velocity at the end of the rotating floor) to a vanishing velocity in $z^\star = \delta^\star = \delta/h$ (in link with a true experimental layout, see Fig. III.B.8). The velocity is in this case confined to the lubrication gap area, which shows the relevance of our numerical treatment.

Lower Ha limit of the agreement between matched asymptotic expansion and numerical simulation

As previously said, the analytical calculation is based on the assumption $\mathrm{Ha} \gg 1$, allowing for the matched asymptotic expansion to be performed. This stringent condition does not apply to the numerical simulation, as long as the inertial effects can be neglected. This is therefore interesting to determine the critical Ha value at the onset of which the two methods show a significant discrepancy. For this purpose, $v_\theta^\star$ and $j_z^\star$ profiles along the cutting line (A) are displayed in Fig. III.B.12 for several small Ha numbers, at a fixed $\mathrm{Bo}_{\eta_S} = 1$ value.

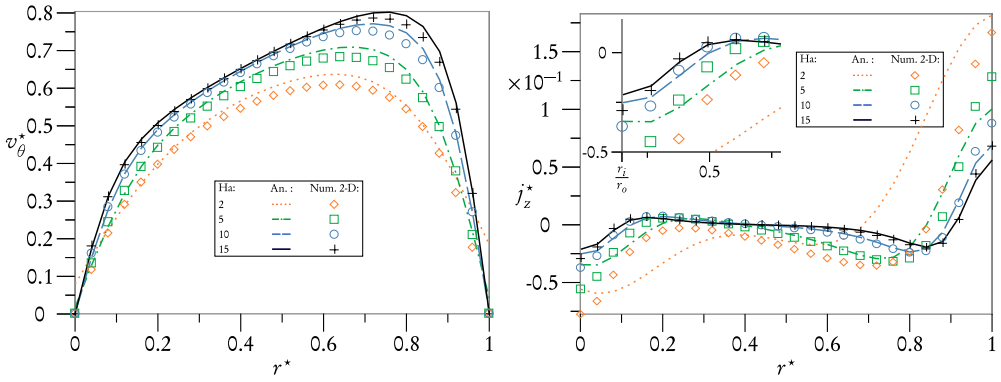

(a) – Azimuthal velocity along (A) for various Ha values ($\mathrm{Bo}_{\eta_S} = 1$).

(b) – Vertical electric current along (A) for various Ha values ($\mathrm{Bo}_{\eta_S} = 1$).

Figure III.B.12 – Comparison between 2-D analytical and numerical results for velocity and axial electric current density, along the cutting line (A), with respect to various Ha values ($\mathrm{Bo}_{\eta_S} = 1$).

Concerning velocity, the discrepancy is hardly noticeable (Fig. III.B.12(a)). A major difference consists of a non-vanishing velocity at the side walls for a very low $\mathrm{Ha} = 2$ value (curves (···) and (◇)). This non-physical result (the side-walls being motionless in this area) is explained by the fact that in the analytical study, the so-called inner corner regions have been left out of the reasoning. The typical cross-section of such regions is $O(\mathrm{Ha}^{-1}) \times O(\mathrm{Ha}^{-1})$, which means that their influence on the flow is all the stronger with lower Ha values ($\mathrm{Ha} = 2$ here).

The discrepancy is more obviously observed in Fig. III.B.12(b), concerning the electric current density $j_z^\star$. For $\mathrm{Ha} = 2$ (curves (···) and (◇)) or $\mathrm{Ha} = 5$ (curves (— · —) and (□)), the results significantly differ from each other, whereas for $\mathrm{Ha} = 10$ (curves (— —) and (○)) or $\mathrm{Ha} = 15$ (curves (—) and (+)), the agreement is quite satisfying. As a consequence, the value $\mathrm{Ha} = 10$ can be proposed as a threshold value above which the matched asymptotic expansion proves relevant.

III.B.3 Conclusion: what about inertia?

Based on both an original analytical investigation and a numerical simulation, the coupling mechanisms between the rheology of a liquid surface and a supporting

MHD bulk flow have been successfully investigated in this chapter. The competitive effects of surface viscous shearing and electromagnetism have been highlighted: surface rheology is indeed found to monitor the generation of the Hartmann layers, leading therefore to a major change in the topology of the electrical circuit, which dramatically affects the overall MHD core flow. The comparison between the analytical and numerical results show a good agreement, and allows for the value $\mathrm{Ha} = 10$ to be selected as the threshold value for the relevance of the matched asymptotic expansion. This first part has also pointed out the need for the Hartmann number to reach values as high as $\mathrm{Ha} = 100$, in order to magnify the coupling effects. This scaling law is used as a dimensioning criterion for the experimental test-bench in Sec. III.D.1.

So far, the inertial effects have been disregarded, through the following assumption: $\mathrm{Ha} \gg \mathrm{Re}$. In the following chapter, this constraint is loosened, not only to bring viscous dilatation into play, but also to establish scaling laws about the angular velocity of the rotating floor, with the aim of achieving the design of Madip.

III.C 2-D $^1/_2$ topology of the MHD viscometer: inertia and surface dilatation

In this chapter, the general coupling between both surface viscous shear and dilatation of the liquid surface and the supporting 2-D $^1/_2$ annular MHD subphase flow is set, by taking the inertial effects into account. First, we focus on the purely hydrodynamic interplay between the main azimuthal flow (induced by a rotating floor) and the secondary overturning flow (generated by centrifugation), coupled with the surface rheology of the gradually oxidising interface. Afterwards, the flow is subjected to an outer vertical magnetic field, and the focus is put on the competition between centrifugation and electromagnetic effects. This competition, in link with surface dynamics, leads to a variety of atypical MHD flow patterns, allowing us to determine distinct experimental working conditions for the Madip experiment. To a certain extent, the following content has been published in [85].

III.C.1 Physical modelling and numerical implementation

III.C.1.a Outlines

Significant physical issues in link with the 2-D $^1/_2$ topology

The previous chapter focused on the analytical and numerical investigations of the 2-D flow topology of the annular MHD viscometer. These benchmarking studies are based on the assumption $\mathrm{Ha} \gg \mathrm{Re}$. This allowed us to ignore the inertial effects, and to highlight the competitive effects between surface viscous shearing and a strong transverse uniform magnetic field. Typically, it has been shown that surface rheology actually monitors the electrical activation of Hartmann layers.

For the present chapter, no particular assumptions have been made concerning the values of Re and Ha (except that $\mathrm{Re} \leq 10^4$ in order to avoid turbulence issues, see Sec. III.A.1.c). Consequently, a swirling flow occurs when $\mathrm{Ha} < \mathrm{Re}$, leading to inertial centrifugal effects (see Sec. III.A.1.b). As highlighted in Sec. III.A.2.b, depending on the relative values of Ha and Re, the flow switches from 2-D to 2-D $^1/_2$ topology, which significantly affects surface rheology. As a consequence, a new rheological parameter is brought into play at the interface, linked to surface viscous dilatation, which might affect core flow. Furthermore, interacting with the outer magnetic field, the centrifugal effects generate an original MHD flow, which in turn competes with surface rheology. Their coupling is now investigated.

Depending on the externally applied magnetic field and on the imposed angular speed, the model could be used to determine distinct experimental working conditions by establishing scaling laws on the values of the Reynolds and the Hartmann numbers, beyond the goal of highlighting the physical mechanisms of this coupling.

Numerical approach

In this chapter, we need to show how the addition of inertial effects may impact the annular MHD flow patterns. The resulting overturning flow is generated by the non-linear terms in the Navier-Stokes equations, in which viscous and electromagnetic terms must be kept as well, in order to investigate the switch from 2-D to 2-D 1/2 flow topology. The difficulty to solve analytically for the full set of Navier-Stokes equations leads us to choose a discretised formulation, *i.e.* a numerical approach. For the same reasons as those exposed in Sec. III.B.2.b, we decide to implement the modelling in the Comsol multiphysics FEM software. Unlike the previous modellings, we choose to adopt a potential formulation in this chapter, which reveals more convenient to handle the different physical quantities. Besides, it is interesting to compare the results given by two different approaches on the same physical problem, for the sake of multiple benchmarking.

As it happens, this numerical simulation is systematically benchmarked with various asymptotic cases. For the classical annular viscometer layout (with no applied magnetic field), the first benchmark takes inertia and surface viscous shearing into account [68]. The purely hydrodynamic results are then extrapolated to the case where surface viscous dilatation significantly affects the bulk flow. Then, the outer magnetic field is added, and the numerical results are benchmarked with the supporting 2-D analytical study [77], which highlights the interactions between surface viscous shearing, electromagnetism, and creeping flow. Once this benchmarking case has been secured, a scaling law is defined to emphasize the interactions between the MHD bulk flow (with inertial effects) and surface rheology (including both surface shearing and dilatation). Their most salient features are then displayed and discussed.

III.C.1.b Notations and assumptions

The hydrodynamic, electromagnetic and rheological assumptions are essentially the same as those exposed in Sec. III.B.1.a for the purely 2-D case. The only (but important) difference is that in this chapter, Re is increased up to the value $\mathrm{Re} \leq 10^4$ in order to study inertial effects, so that the criterion $\mathrm{Ha} \gg \mathrm{Re}$ is invalidated. Furthermore, the flow of the liquid surface is still modelled through the JMB, but the latter now involves two rheological parameters: not only surface shear viscosity, η_S, but also surface dilatational viscosity, $\varkappa_S$.

A distinction is made between the (main) azimuthal flow v_θ, and the (secondary) meridian flow (v_r, v_z) (also referred to as overturning flow). When the electroconductive liquid is subjected to an outer magnetic field, electric current densities are induced. Once again, the (main) components (j_r, j_z) (due to the main azimuthal flow) are distinguished from the (secondary) component j_θ (due to the secondary meridian flow)

leading to a so-called 2-D 1/2 flow topology. Note that despite the generation of the overturning flow, the axisymmetric assumption still holds.

III.C.1.c Geometry, governing equations, boundary conditions

Geometry

For symmetry reasons, we can only focus on a cross-section of the annular channel. Note that the out-of plane components of MHD quantities must be solved, due to the swirling flow. The geometry of the numerical problem, along with the conditions implemented at the boundaries of the calculation domains, are given in Fig. III.C.1.

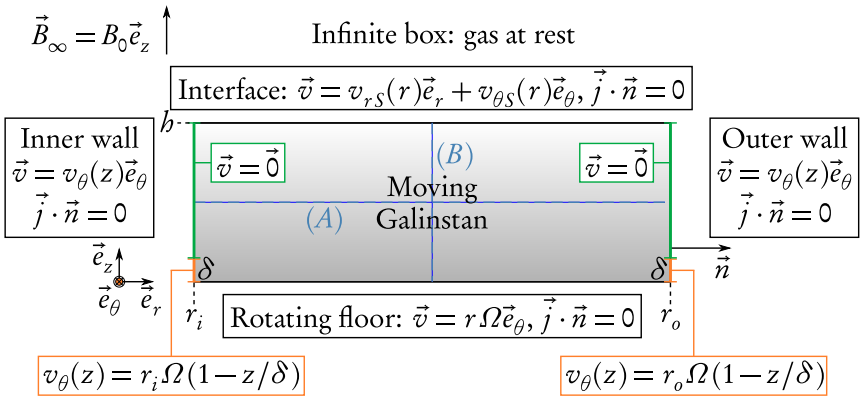

Figure III.C.1 – Geometry and boundary conditions of the channel crossed-section used for 2-D ½ numerical computation.

Bulk flow

Electromagnetism

As previously said, a potential formulation is used to describe the electromagnetic part of the problem. The basic equations are derived in Sec. II.A.1.d (see Eqs. (II.A.17) and (II.A.18)), and are recalled here; the Maxwell-Ampère equation writes

$$\overrightarrow{\mathrm{curl}}\left(\overrightarrow{\mathrm{curl}}\left(\vec{A}\right)\right) - \mu\sigma\vec{v}\times\overrightarrow{\mathrm{curl}}\left(\vec{A}\right) + \mu\sigma\overrightarrow{\mathrm{grad}}(\phi) = \vec{0}, \tag{III.C.1}$$

and the continuity equation

$$\mathrm{div}\left(\mu\sigma\vec{v}\times\overrightarrow{\mathrm{curl}}\left(\vec{A}\right) - \mu\sigma\overrightarrow{\mathrm{grad}}(\phi)\right) = 0, \tag{III.C.2}$$

where $\vec{A}$ is the magnetic vector potential, and ϕ is the electric potential. These two equations are completed by generalised Ohm's law:

$$\vec{j} = -\sigma\left(\overrightarrow{\mathrm{grad}}(\phi) + \vec{v}\times\vec{B}_0\right), \tag{III.C.3}$$

and the Coulomb gauge, to define uniquely $\vec{A}$, *i.e.* $\mathrm{div}\left(\vec{A}\right)=0$.

As shown in Fig. III.C.1, the electromagnetic boundary conditions first consist of an externally applied constant axial magnetic field, imposed through an "infinite" box surrounding the fluid area: $\vec{B}_\infty = B_0\vec{e}_z$. As unveiled in Sec. II.A.3.a, the assumption $\mathrm{Rm} \ll 1$ yields: $B_z\vec{e}_z \sim B_0\vec{e}_z$, throughout the entire computational domain. The result is, in terms of the magnetic vector potential:

$$\frac{1}{r}\frac{\partial r A_\theta}{\partial r} = B_0. \tag{III.C.4}$$

The second electromagnetic boundary condition is the electrical insulation at the fluid boundaries (side-walls, rotating floor, and liquid/gas interface), detailed in Sec. II.A.3.a: $\vec{j}\cdot\vec{n}\Big|_{\text{fluid walls}} = 0$. Using Eq. (III.C.3), it writes with respect to electric potential:

$$\sigma\left(-\overrightarrow{\mathrm{grad}}(\phi)+\vec{v}\times\vec{B}_0\right)\Big|_{\text{fluid walls}}\cdot\vec{n}=0, \tag{III.C.5}$$

where $\vec{n}$ is the unit normal vector at the considered boundary – see Fig. III.C.1.

Fluid mechanics

A primitive pressure-velocity formulation is used, based on the complete set of Navier-Stokes equations, previously given in Eq. (II.A.26) (see Sec. II.A.2.b for further details) and reminded here. The governing equations are

$$\mathrm{div}\left(\vec{v}\right)=0, \tag{III.C.6}$$

for the continuity equation and

$$\rho\left(\vec{v}\cdot\overrightarrow{\mathrm{grad}}\right)\vec{v} = -\overrightarrow{\mathrm{grad}}\,p+\eta\vec{\Delta}\vec{v}+\vec{f}_\mathrm{L}, \tag{III.C.7}$$

for the Navier-Stokes equations. The coupling term $\vec{f}_\mathrm{L}$ is the Lorentz force, defined as $\vec{f}_\mathrm{L}=\vec{j}\times\vec{B}_0$ within the low-Rm approximation, which can be explicitly written as follows, using Eq. (III.C.3):

$$\vec{j}=\sigma\left(-\overrightarrow{\mathrm{grad}}(\phi)+\vec{v}\times\vec{B}_0\right)=\sigma\begin{bmatrix}-\frac{\partial\phi}{\partial r}+v_\theta B_0\\ -v_r B_0\\ -\frac{\partial\phi}{\partial z}\end{bmatrix}, \tag{III.C.8}$$

$$\vec{f}_\mathrm{L}=\vec{j}\times\vec{B}_0=\sigma\begin{bmatrix}-v_r B_0^2\\ B_0\left(\frac{\partial\phi}{\partial r}-v_\theta B_0\right)\\ 0\end{bmatrix}. \tag{III.C.9}$$

Let us now examine the hydrodynamic boundary conditions shown in Fig. III.C.1, starting with the no-slip boundary condition at the motionless side-walls:

$$\vec{v}(r=r_i,z)=\vec{v}(r=r_o,z)=\vec{0}. \tag{III.C.10}$$

At the inner and outer side-walls, in order to circumvent the boundary data discontinuity issue, we adopt the same approach based on lubrication gaps as in Sec. III.B.2.c, resulting in the following BCs along the provided matching segments:

$$\vec{v}(r=r_i,z)=v_\theta(r=r_i,z)\vec{e}_\theta=\begin{cases} r_i\Omega\left(1-\frac{z}{\delta}\right)\vec{e}_\theta & \text{if } z\in[0,\delta], \\ \vec{0} & \text{if } z\in]\delta,h], \end{cases} \tag{III.C.11}$$

for the inner wall and

$$\vec{v}(r=r_o,z)=v_\theta(r=r_o,z)\vec{e}_\theta=\begin{cases} r_o\Omega\left(1-\frac{z}{\delta}\right)\vec{e}_\theta & \text{if } z\in[0,\delta], \\ \vec{0} & \text{if } z\in]\delta,h], \end{cases} \tag{III.C.12}$$

for the outer wall. The last remaining velocity boundary conditions at the liquid gas/interface are given by the surface rheology equations, governing surface velocity $\vec{v}_S$ dynamics – see Eq. (III.C.14) and (III.C.15):

$$\vec{v}(r,z=h)=\vec{v}_S(r)=v_{rS}(r)\vec{e}_r+v_{\theta S}(r)\vec{e}_\theta. \tag{III.C.13}$$

Dimensionless quantities

As mentioned above, when normalising MHD equations, two scaling parameters emerge, *i.e.* $\mathrm{Ha}=B_0h\sqrt{\sigma/\eta}$ and $\mathrm{Re}=\rho\Omega r_o^2/\eta$. A third one can be used instead of Re, *i.e.* the Stuart Number or interaction parameter: $\mathrm{N}=\mathrm{Ha}^2/\mathrm{Re}$ (see Eq. (II.A.31)). Classically in MHD, a (Ha, N) formulation is favoured, where N governs the actual competition between inertial and electromagnetic effects. However, in this work, Ha and Re are preferred for the following reasons. First, some results are displayed for a purely hydrodynamic flow, meaning that $\mathrm{N}=0$, regardless of the value of the Reynolds number. Moreover, the Couette-like layout of the problem, with an imposed velocity at the rotating floor, makes us tend towards the (Ha, Re) description, since the boundary condition at the bottom of the channel is directly linked to Re through the angular speed Ω. Consequently, by monitoring the Reynolds number, different dynamic configurations are described.

Echoing Sec. III.B.1.f, the bulk dimensionless quantities of interest, superscripted *, are then defined as follows:

- the radial coordinate $r^\star=(r-r_i)/(r_o-r_i)$;
- the axial coordinate $z^\star=z/h$;
- the velocity $\vec{v}^\star=\vec{v}/V$, where $V=r_o\Omega$. The azimuthal component $v_\theta^\star$, and the meridian components $(v_r^\star,v_z^\star)$ allow for analysis of the main and secondary MHD bulk flows, respectively;
- the electric current densities: $\vec{j}^\star=\vec{j}/J$, where $J=\sigma B_0V$. The meridian components $(j_r^\star,j_z^\star)$, and the azimuthal component $j_\theta^\star$ allow for analysis of the main and secondary MHD bulk flows, respectively;
- and the Lorentz force: $\vec{f}_\mathrm{L}^\star=\vec{f}_\mathrm{L}/f_\mathrm{L}$, where $f_\mathrm{L}=\sigma B_0^2V$. The radial component $F_r^\star$, and the azimuthal component $F_\theta^\star$ allow for analysis of the main and secondary MHD bulk flows, respectively.

Surface flow

Surface rheology

The boundary condition (III.C.13) brings a new unknown into play, namely in-plane surface velocity $\vec{v}_S$. Contrary to the previous chapter, where only the azimuthal component of the JMB was brought into play, the surface dynamics are now governed by the two following components of the JMB (see Eq. (II.B.6)), in link with the swirling flow generated by inertial effects:

$$(\eta_S + \varkappa_S)\left(\frac{\mathrm{d}^2 v_{rS}}{\mathrm{d}r^2} + \frac{1}{r}\frac{\mathrm{d}v_{rS}}{\mathrm{d}r} - \frac{v_{rS}}{r^2}\right) = \eta \left.\frac{\partial v_r}{\partial z}\right|_{z=h}, \tag{III.C.14}$$

$$\eta_S\left(\frac{\mathrm{d}^2 v_{\theta S}}{\mathrm{d}r^2} + \frac{1}{r}\frac{\mathrm{d}v_{\theta S}}{\mathrm{d}r} - \frac{v_{\theta S}}{r^2}\right) = \eta \left.\frac{\partial v_\theta}{\partial z}\right|_{z=h}. \tag{III.C.15}$$

We remind that the left-hand term of Eq. (III.C.14) represents a combination of surface viscous shear and surface viscous dilatation along the liquid surface, while only the surface viscous shear is present in Eq. (III.C.15), where η_S and $\varkappa_S$ are the surface shear and dilatation viscosities, respectively. The right-hand terms of both equations are the liquid shears vertically imposed from the supporting subphase flow.

Finally, to solve for the JMB, the following Dirichlet end-point boundary conditions for surface flow are required:

$$v_{rS}(r = r_i) = v_{rS}(r = r_o) = v_{\theta S}(r = r_i) = v_{\theta S}(r = r_o) = 0. \tag{III.C.16}$$

Dimensionless quantities

As detailed in Sec. II.B.2.d, normalising Eqs. (III.C.14) and (III.C.15) leads to the definition of two rheological scaling parameters:

$$\mathrm{Bo}_{\eta_S} = \frac{\eta_S}{\eta h}, \mathrm{Bo}_{\varkappa_S} = \frac{\varkappa_S}{\eta h}, \tag{III.C.17}$$

where Bo_{η_S} and $\mathrm{Bo}_{\varkappa_S}$ are the surface shear and surface dilatational Boussinesq numbers, respectively. It should be noted that, compared to the previous chapter, $\mathrm{Bo}_{\varkappa_S}$ is a new feature emerging due to the inertial effects.

Finally, the dimensionless quantities of interest for surface dynamics consist only of surface velocity: $\vec{v}_S^\star = \vec{v}_S/V$; $v_{rS}^\star$ and $v_{\theta S}^\star$ allow for analysis of the main and secondary surface flows, respectively.

Numerical implementation

Similarly to the 2-D numerical simulation introduced in Sec. III.B.2, the governing equations are discretised in Comsol. Concerning classical electromagnetic and hydrodynamic equations, this discretisation is performed through the so-called "magnetic and electric fields" and "laminar flow" Comsol modules. With respect to surface dynamics, Eqs. (III.C.14) and (III.C.15) are discretised along the interface by calculating their respective weak forms, following the aforementioned method in Sec.III.B.2.c.

With respect to numerical methods, the non-linear physical problem is linearised by using once again the Newton-Raphson method, in combination with the linear stationary direct solver MUMPS, based on LU factorisation. Finally, the implemented mesh is displayed in Fig. III.C.2(a). It consists of 27 524 elements, mainly triangular, with mesh refinement on the Galinstan domain. As shown in Fig. III.C.2(b), a specific rectangular boundary layer mesh is set up at the boundaries of the fluid domain, and a large-extent box is defined in order to take BC (III.C.4) into account. Typically, the relative thickness of the first layer is set so as to be much lower than the reciprocal of the Hartmann and Reynolds numbers, which both monitor the thickness of the physical boundary layers.

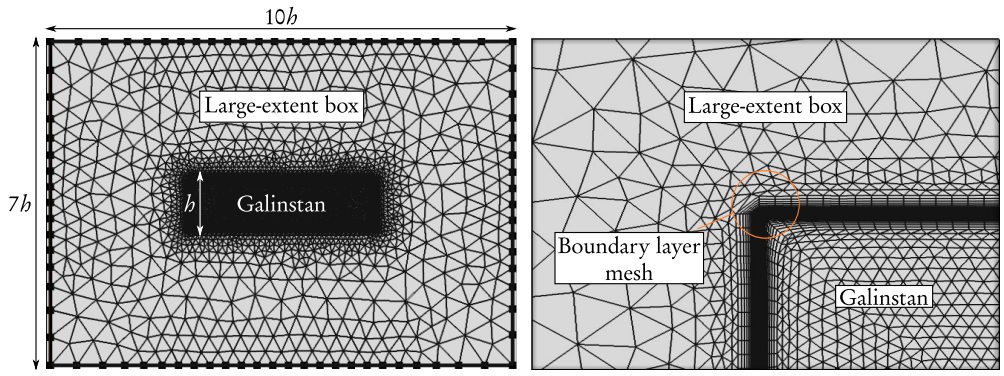

(a) – Global view. **(b)** – Zoom on the boundary layer mesh.

Figure III.C.2 – Mesh used for the 2-D 1/2 numerical computation (27 524 elements).

III.C.2 Results and interpretations

III.C.2.a The annular hydrodynamic viscometer $(\mathrm{Ha} = 0)$

In this section, the interaction between the purely hydrodynamic subphase flow and the surface rheology is analysed. Let us first validate the 2-D 1/2 numerical modelling with a benchmarking asymptotic study.

The deep-channel viscometer benchmark: inertia and surface viscous shearing

The first selected benchmark is the DNS of the classical deep-channel annular viscometer (with no outer magnetic field, *i.e.* $\mathrm{Ha} = 0$), performed by Hirsa *et al.* [68], previously introduced in Sec. III.A.1.c. In this case, only the hydrodynamic issue is brought into focus, taking inertia into account, but considering that the interfacial condition along the radial direction (Eq. (III.C.14) of the present study) reduces to no-slip, which is similar to the condition $\mathrm{Bo}_{\varkappa_S} \to \infty$ (see Eq. (III.A.6)). As a result, the role of surface viscous shearing alone is enhanced, through the parameter Bo_{η_S}.

In this part, relevant quantities must be temporarily redefined to fit with Hirsa *et al.* notations and typical values, and are subscripted $_{\mathrm{HL}}$ (corresponding to Hirsa

layout). Thus, the height and the inner and outer radii of the channel are noted h_{HL}, $r_{i\mathrm{HL}}$ and $r_{o\mathrm{HL}}$, respectively. The surface shear Boussinesq number used in this part is $\mathrm{Bo}_{\eta_S\mathrm{HL}} = \eta_S/\eta r_{o\mathrm{HL}}$, defined in Eq. (III.A.7). The definitions of the other relevant physical quantities are unchanged (particularly the Reynolds number Re).

Some results obtained for the same geometrical layout as Hirsa *et al.* are then shown in Fig. III.C.3. The quantities displayed are:

- the contours of azimuthal vorticity $\omega^\star = \partial v_r^\star/\partial z^\star - \partial v_z^\star/\partial r^\star$, that governs the meridian flow, in Fig. III.C.3(a), for different $\mathrm{Bo}_{\eta_S\mathrm{HL}}$ and Re values;
- the contours of axial angular momentum $\alpha^\star = r^\star v_\theta^\star$, in Fig. III.C.3(b), for different $\mathrm{Bo}_{\eta_S\mathrm{HL}}$ and Re values;
- surface azimuthal velocity $v_{\theta S}^\star$ in Fig. III.C.3(c) and III.C.3(d), for $\mathrm{Bo}_{\eta_S\mathrm{HL}} = 0.01$ or 10, respectively, and various Re values.

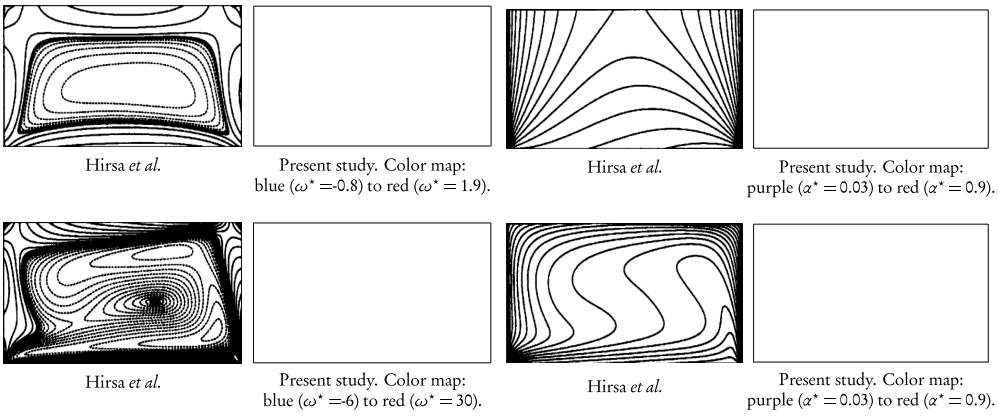

(a) – Azimuthal vorticity: $\mathrm{Re} = 250$, $\mathrm{Bo}_{\eta_S\mathrm{HL}} = 0.01$ (top), $\mathrm{Re} = 8000$, $\mathrm{Bo}_{\eta_S\mathrm{HL}} = 1$ (bottom).

(b) – Angular momentum: $\mathrm{Re} = 250$, $\mathrm{Bo}_{\eta_S\mathrm{HL}} = 0.01$ (top), $\mathrm{Re} = 8000$, $\mathrm{Bo}_{\eta_S\mathrm{HL}} = 1$ (bottom).

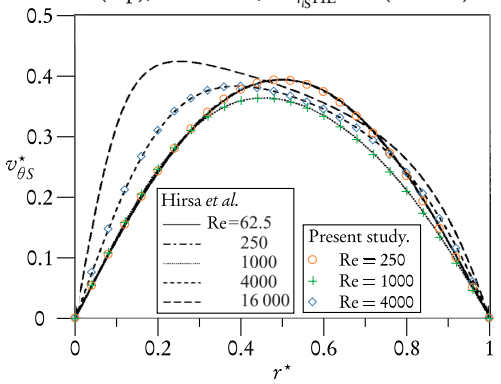

(c) – Surface azimuthal velocity: $\mathrm{Bo}_{\eta_S\mathrm{HL}} = 0.01$, various Re.

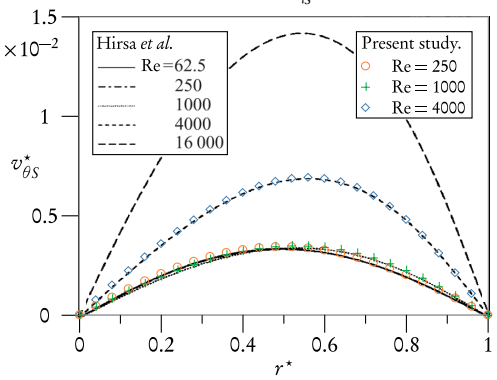

(d) – Surface azimuthal velocity: $\mathrm{Bo}_{\eta_S\mathrm{HL}} = 10$, various Re.

Figure III.C.3 – Numerical benchmark for the purely hydrodynamic 2-D ½ flow [68].

The agreement between both studies is quite satisfying. Both models predict a secondary overturning flow due to inertial effects, intensifying with Re. At low Reynolds numbers, the angular momentum diffuses from the rotating floor into the

liquid metal (see Fig. III.C.3(b), top). For higher Re, an Ekman layer appears near the rotating floor, concentrating the vortex lines. Due to the outer wall, this layer is turned vertically into a jet-like flow, and then turned inwards at the interface, advecting fluid with large angular momentum radially inwards. This results in a spin-up of the fluid interface increasingly closer to the inner wall (see Fig. III.C.3(b), bottom, and Fig. III.C.3(c)).

With respect to the impact of surface viscous shearing, it can be seen in Fig. III.C.3(b) that if $\mathrm{Bo}_{\eta_{S\mathrm{HL}}}$ is small (top), the vortex lines are normal to the liquid surface, and if it is large (bottom), then the lines are tangential to the liquid/gas interface, evolving consistently from a free surface (Neumann) to no-slip (Dirichlet) boundary conditions. Consequently, the azimuthal velocity $v^\star_{\theta S}$ decreases as $\mathrm{Bo}_{\eta_{S\mathrm{HL}}}$ increases, as seen when comparing Figs. III.C.3(c) and III.C.3(d). In the case where $\mathrm{Bo}_{\eta_{S\mathrm{HL}}}$ is large enough, the interface is only governed by surface viscous shearing, and the vertical bulk shear taken at the vicinity of the interface does not affect it. This leads to a vanishing Poiseuille-like velocity profile along the interface, as shown in Fig. III.C.3(d).

The shallow annular channel: inertia, surface viscous shearing and dilatation

Now that the relevance of hydrodynamic numerical simulation is proved, let us return to the geometrical layout of the shallow annular channel. In this section, the interaction between inertia and surface rheology is particularly emphasised for bulk flow, while the previous benchmark mainly focused on surface phenomena. The results are displayed in Fig. III.C.4.

Influence of Bo_{η_S}

The way in which surface viscous shearing affects the purely hydrodynamic flow through Bo_{η_S} is investigated in this section, by comparing Fig. III.C.4(a) and III.C.4(b) ($\mathrm{Bo}_{\varkappa_S}$ is set negligibly small: $\mathrm{Bo}_{\varkappa_S} = 10^{-4}$). For the azimuthal flow $v^\star_\theta$, velocity profile evolution with respect to Bo_{η_S} is similar to the previous benchmark, with slight changes due to the difference in geometrical layouts between the deep and the shallow channel viscometer.

With respect to the overturning flow $(v^\star_r, v^\star_z)$, an increase in Bo_{η_S} leads to flow homogenisation, as shown in Fig. III.C.4(b). When $\mathrm{Bo}_{\eta_S} = 10^{-4}$, *i.e.* in the case where the liquid surface acts similarly to a free surface, the main vortex governing the overturning flow is mainly located in the outer part of the channel. When $\mathrm{Bo}_{\eta_S} = 10^4$, this vortex expands radially inwards throughout the whole cross-section of the channel. This difference can be accounted for by the nature of the interface boundary condition. When the latter is similar to a free surface, the momentum injected from the rotating floor is dissipated in the bulk and at the sliding interface, with a significant surface radial velocity (see Fig. III.C.4(a)). When the liquid surface is rigid (vanishing surface velocity, see Fig. III.C.4(b)), it no longer participates in viscous damping of the injected momentum. Bulk viscous damping is therefore enhanced, leading to expansion of the main vortex inside the subphase flow.

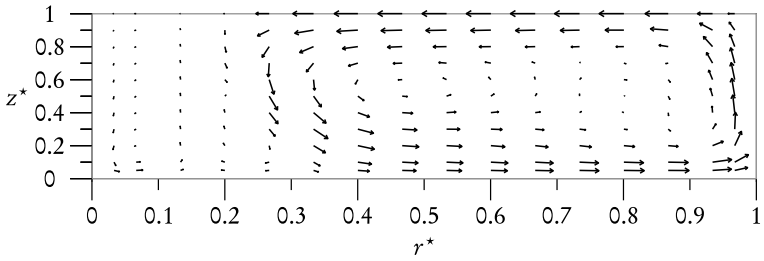

(a) – Main (contours: $v_\theta^\star$) and secondary (arrows: $(v_r^\star, v_z^\star)$) flows, $\mathrm{Re} = 10^4$, $\mathrm{Bo}_{\eta_S} = 10^{-4}$, $\mathrm{Bo}_{\varkappa_S} = 10^{-4}$.

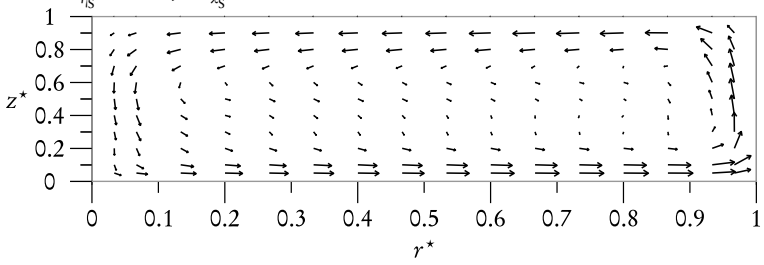

(b) – Main (contours: $v_\theta^\star$) and secondary (arrows: $(v_r^\star, v_z^\star)$) flows, $\mathrm{Re} = 10^4$, $\mathrm{Bo}_{\eta_S} = 10^4$, $\mathrm{Bo}_{\varkappa_S} = 10^{-4}$.

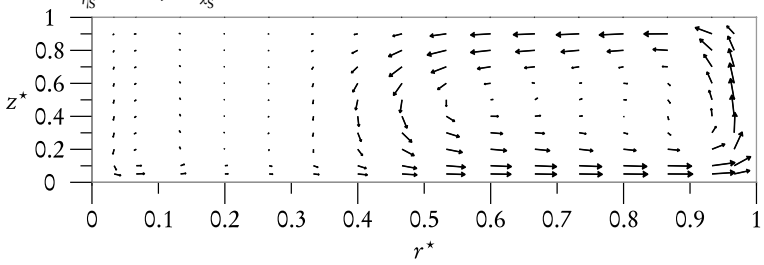

(c) – Main (contours: $v_\theta^\star$) and secondary (arrows: $(v_r^\star, v_z^\star)$) flows, $\mathrm{Re} = 10^4$, $\mathrm{Bo}_{\eta_S} = 10^4$, $\mathrm{Bo}_{\varkappa_S} = 10^4$.

Figure III.C.4 – Bo_{η_S} and $\mathrm{Bo}_{\varkappa_S}$ impact on the velocity field for the classical annular viscometer layout ($\mathrm{Ha} = 0$). The meridian flow $(v_r^\star, v_z^\star)$ is log-scaled by the magnitude $\exp\left(\left(\ln\left(\|(v_r^\star, v_z^\star)\|/\|(v_r^\star, v_z^\star)\|_{\max}\right)\right)/(1+p)\right)$; $p = 0.5$ for a), b), c).

Note that when Re varies at fixed Bo_{η_S}, overturning flow magnitude increases with Re, and the main vortex governing the secondary flow is enlarged. Momentum is then increasingly confined within the Ekman layers, similarly to what is observed the previous benchmark for the main flow. However, the qualitative impact of Bo_{η_S} on the meridian flow remains identical irrespective of Re.

Influence of $\mathrm{Bo}_{\varkappa_S}$

The way in which surface viscous dilatation affects the purely hydrodynamic flow through $\mathrm{Bo}_{\varkappa_S}$ is now investigated, by comparing Figs. III.C.4(a) and III.C.4(c) (Bo_{η_S} is set negligibly small: $\mathrm{Bo}_{\eta_S} = 10^{-4}$). Concerning the azimuthal flow, an increase in $\mathrm{Bo}_{\varkappa_S}$ does not lead to a significant change in the velocity profile $v_\theta^\star$. It seems only that the main flow is less efficiently advected by the secondary flow.

This observation is confirmed by turning to the analysis of the meridian flow $(v_r^\star, v_z^\star)$. Contrary to what is observed for Bo_{η_S}, in this case the main vortex governing the secondary flow decreases when $\mathrm{Bo}_{\varkappa_S}$ increases in Fig. III.C.4(c). This phenomenon is quite unexpected, because for the secondary flow, the boundary condition at the liquid surface along the radial direction is the same both in the case of an infinite value for both Bo_{η_S} and $\mathrm{Bo}_{\varkappa_S}$, *i.e.* a vanishing $v_{rS}^\star$ (where the interface is similar to a non-sliding wall, see Eq. (III.C.14)). However, as Bo_{η_S} also governs the azimuthal boundary condition for the main flow, when the surface viscous shear is very high, the main azimuthal flow must also match with a vanishing $v_{\theta S}^\star$ (see Eq. (III.C.15)). Consequently, there is a complete deflection of momentum at the interface, favoring expansion of the main overturning vortex as mentioned above (Fig. III.C.4(b)). For surface dilatation, even when $\mathrm{Bo}_{\varkappa_S}$ greatly increases, it has no direct consequence on the boundary condition $v_{\theta S}^\star$ for the main flow. Therefore, for $\mathrm{Bo}_{\varkappa_S} = 10^4$, the overturning flow must match with a vanishing value of $v_{rS}^\star$, whereas the main flow remains unchanged at the vicinity of the interface (with a fixed $\mathrm{Bo}_{\eta_S} = 10^{-4}$). This favours damping of the main vortex governing the secondary flow near the interface observed in Fig. III.C.4(c). Note that, as it is the case for Bo_{η_S}, changing the value of Re does not affect the qualitative impact of $\mathrm{Bo}_{\varkappa_S}$ on the (secondary) centrifugal flow.

III.C.2.b The annular MHD viscometer $(\mathrm{Ha} \neq 0)$

The purely hydrodynamic 2-D 1/2 flow has been fully investigated; let us now add an outer magnetic field and turn to the annular MHD viscometer layout. For this purpose, the electroconductive flow is now subjected to an outer magnetic field $B_0\vec{e}_z$. This time, the interaction between the MHD subphase flow and the surface rheology is investigated. We shall begin with a benchmarking asymptotic study to validate 2-D 1/2 MHD numerical calculations.

MHD, no inertia and surface viscous shearing

The second benchmark is constituted by the analytical and numerical study of the 2-D annular MHD flow, performed in Sec. III.B, within the limit of ignoring inertial effects when $\mathrm{Ha} \gg \mathrm{Re}$. Some results are shown in Fig. III.C.5. Note that cutting lines (A) and (B) are defined in Fig. III.C.1, and allow for analysis of the MHD core flow and the Shercliff or the Hartmann layers, respectively. In addition to this first benchmark, the solutions derived by Mannheimer and Schechter [31] (see Eq. (III.A.2)) and Davoust *et.al.* [72] (see Eq. (III.A.4)) are displayed, to test the relevance of the 2-D 1/2 modelling in the asymptotic limit $\mathrm{Ha} \to 0$ (see Fig. III.C.5(c)).

The general agreement between all studies is once again quite satisfying. They predict radically different topologies for the MHD flows, depending on the relative values of Ha and Bo_{η_S}. When $\mathrm{Ha} \gg \mathrm{Bo}_{\eta_S}$, the 2-D tendency with exclusively radial velocity gradients (except near the side-walls) is recovered, as seen in Fig. III.C.5(a) (see Sec. III.B.1.f for further details). In this case, the electric current density is essentially confined to the Shercliff layers, with two electric loops closing up near the side-walls (see Figs. III.C.5(d) and III.C.5(e), in the case $(\mathrm{Ha}, \mathrm{Bo}_{\eta_S}) = (50, 0.01)$). Now,

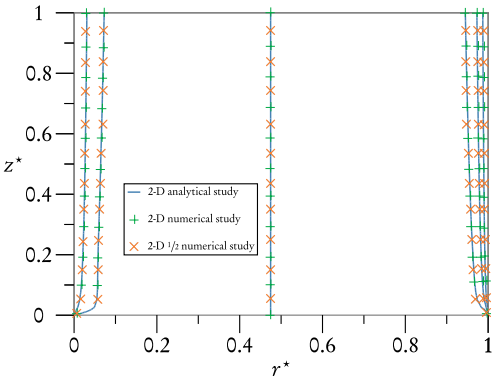

(a) – Azimuthal velocity contours: Ha = 50, $\mathrm{Bo}_{r_{IS}}$ = 0.01.

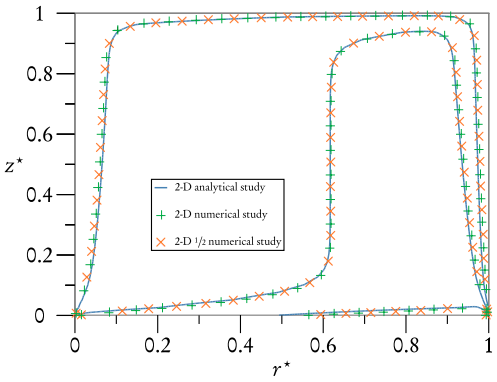

(b) – Azimuthal velocity contours: Ha = 30, $\mathrm{Bo}_{r_{IS}}$ = 0.01.

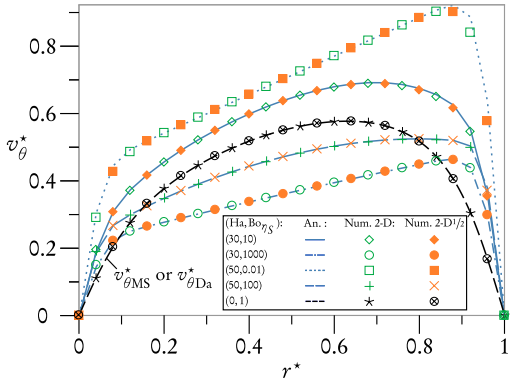

(c) – Azimuthal velocity along cutting line (A) (Core and Shercliff layers). MS and Da refer to Eqs. (III.A.2) and (III.A.4), respectively.

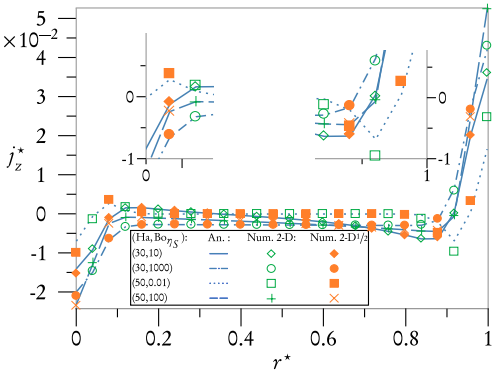

(d) – Vertical electric current along cutting line (A) (Core and Shercliff layers).

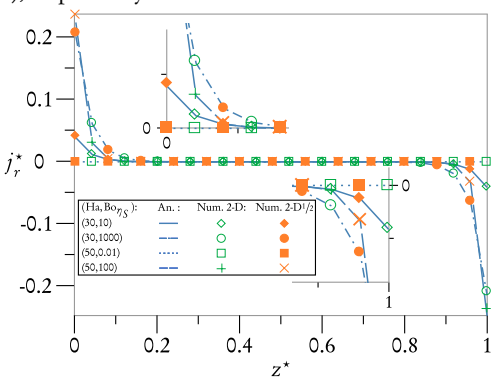

(e) – Radial electric current along cutting line (B) (Core and Hartmann layers).

Figure III.C.5 – Comparison between 2-D ½ modelling and 2-D analytical and numerical results for velocity (top) and electric currents (bottom), either for purely hydrodynamic creeping flow (Ha = 0: c), curves ---, ∗, ⊗), or for Ha ≫ Re (no inertia: other curves), with respect to various $(\mathrm{Ha}, \mathrm{Bo}_{\eta_S})$ values. The electric current densities are normalised with respect to the maximum electric current $J_{\max} = 6.8 \times 10^2$ A·m^{-2} reached in all cases, *i.e.* for Ha = 50.

when $\mathrm{Ha} \ll \mathrm{Bo}_{\eta_S}$, the three modellings consistently lead to the homogeneous "motionless" topology already investigated in Sec. III.B.1.f (Fig. III.C.5(b)). Due to strong velocity gradients near the liquid/gas surface, and to current continuity, electric current densities are now found to flow within the top and bottom Hartmann layers, which are therefore electrically active, as seen in Fig. III.C.5(e).

Scaling laws for inertial MHD and surface rheology interaction

2-D 1/2 numerical simulations, the reliability of which is demonstrated from the previous asymptotic cases, can now be confidently extrapolated to conditions including MHD of an annular swirling flow, coupled with surface rheology. For this purpose, a scaling law is required to determine the relevant values of Ha and Re, for which the interactions between the (main and secondary) subphase MHD and surface flows are the most insightful. We choose the following criterion, based on the ratio of surface velocities for each (Re, Ha) pair:

$$\left| \frac{v^\star_{rS}}{v^\star_{\theta S}} \right|_{\max} \geq 0.01. \tag{III.C.18}$$

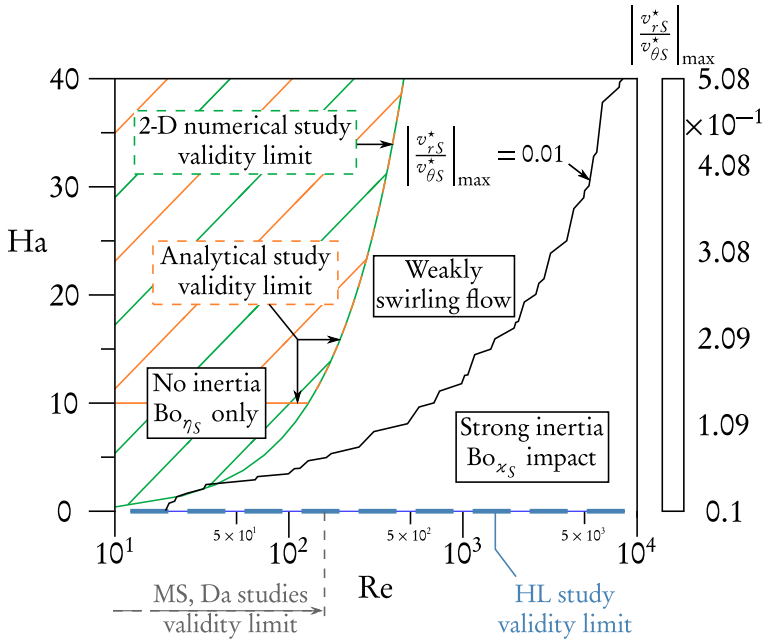

Figure III.C.6. Scaling law for determining the most insightful working conditions, in view of overall coupling between MHD with inertia and surface rheology with both surface shear and dilatation. Here, $\mathrm{Bo}_{\eta_S} = \mathrm{Bo}_{\varkappa_S} = 10^{-4}$. MS, Da and Co refer to Mannheimer and Schechter, Davoust, or Hirsa and Lopez asymptotic solutions (see Sec. III.A.1.c), respectively.

The choice of this particular limit is explained in Fig. III.C.6, which represents the magnitude of this ratio compared with the values of (Re, Ha) pairs, for a classical free surface BC ($\mathrm{Bo}_{\eta_S} = \mathrm{Bo}_{\varkappa_S} = 10^{-4}$). In this figure, three main areas can be distinguished:

first, the hatched one represents the area where inertia can be ignored. In this part, which includes both 2-D analytical and numerical studies, the impact of surface viscous shear only can be investigated. The validity limit of this area stems from the criterion taken from [36] (about MHD secondary flows at high Ha numbers), stating that inertial effects can be ignored as soon as:

$$\frac{h^3 \mathrm{Re}^2}{(r_o - r_i)\, r_o^2 \mathrm{Ha}^2 \sqrt{\mathrm{Ha}}} < 1. \tag{III.C.19}$$

This criterion is indeed better adapted to the annular channel layout than the generic criterion $\mathrm{N} = \mathrm{Ha}^2/\mathrm{Re} \gg 1$. As previously shown, the results of the matched asymptotic expansion and of the numerical simulations (within the limit of ignoring inertial effects) are in fair agreement as soon as $\mathrm{Ha} \geq 10$.

The second area is referred to as "weakly swirling flow". In this transitional zone, inertia can no longer be ignored. However, the overturning flow is not strong enough to stretch significantly the interface, and the magnitude of the ratio $|v^\star_{rS}/v^\star_{\theta S}|_{\max}$ continues to be very small. Therefore, surface dilatation impact on bulk MHD is likely to be negligible, and this "weakly swirling flow" area is left apart from the analysis.

The color-mapped area represents the working conditions for which the ratio $|v^\star_{rS}/v^\star_{\theta S}|_{\max} \geq 0.01$. Note that the purely hydrodynamic study by Mannheimer and Schechter [31] or Davoust *et al.* [72] (for low Reynolds values), and Hirsa *et al.* [68] (for higher Reynolds values) are also indicated as the abscissa axis $\mathrm{Ha} = 0$. In this part, surface radial velocity tends to become the same order of magnitude as the surface azimuthal velocity. As a result, surface viscous dilatation can become significant, and may strongly interact with bulk flow through the $\mathrm{Bo}_{\varkappa_S}$ number, in addition to surface viscous shear.

The goal of this study is to highlight the secondary MHD flow due to inertia, and emphasise the coupling between bulk MHD and surface viscous shear and dilatation. To maximise the most salient interactions, we choose the working conditions matching with the third area. Fig. III.C.6 gives us the relevant scaling laws, *i.e.* for $\mathrm{Re} \leq 10^4$, in the following results, the value of the Hartmann number does not exceed the threshold value $\mathrm{Ha} = 10$.

MHD, inertia, and surface viscous shear

In this section, the influence of surface viscous shearing only (through Bo_{η_S}) on main and secondary MHD bulk flows is investigated, in order to complete the analytical analysis [77]. For this purpose, the surface dilatation Boussinesq number is set to be negligibly small: $\mathrm{Bo}_{\varkappa_S} = 10^{-4}$.

Main MHD bulk flow

In this part, there is no need to produce any specific graph either for $v^\star_\theta$ or for $(j^\star_r, j^\star_z)$ (note that an overall view of MHD flow patterns is shown in Fig. III.C.8). Depending on the relative values of Ha and Re, the qualitative effects of surface viscous

shearing on the velocity and electric current density profiles are essentially the same as in the two previously detailed benchmarking asymptotic cases. For instance, when $\mathrm{Re} = 10^3$ and $\mathrm{Ha} = 5$, if $\mathrm{Bo}_{\eta_S} \ll \mathrm{Ha}$, then the fluid flow tends towards a rigid body motion (though not really pronounced as Ha is not large enough) where the electric current densities are confined within the (thick) Shercliff layers. If $\mathrm{Bo}_{\eta_S} \gg \mathrm{Ha}$, an electromagnetic damping of the flow is also observed (again not so marked), and the Hartmann layers become electrically active, as described in Sec. III.B.1.f. When the Reynolds number is increased (for instance $\mathrm{Re} = 10^4$), the velocity profile evolution with respect to Bo_{η_S} is similar to Sec. III.C.2.a. The influence of Ha is less significant, as the flow is almost purely hydrodynamic.

Secondary MHD bulk flow

Let us now analyse the overturning MHD flow, beginning with the meridian velocities $(v_r^\star, v_z^\star)$, for which no specific figures are displayed (see Fig. III.C.9 for an overall view of MHD flow patterns). The outer magnetic field does not yield a significant qualitative difference with respect to the purely hydrodynamic case (Sec. III.C.2.a), regarding the Bo_{η_S} impact. Thus, for given $(\mathrm{Re}, \mathrm{Bo}_{\eta_S})$ values, an increase in Ha actually affects both the meridian velocities magnitude and topology. The main vortex governing the meridian flow is increasingly diminished, due to MHD tendency towards two-dimensionality. However, for given (Re, Ha) values, increasing Bo_{η_S} still leads to the stretching of the overturning flow, as observed previously in the case of Figs. III.C.4(a) and III.C.4(b). Consequently, the most salient phenomena qualitatively remain the same irrespective of the Re and Ha values.

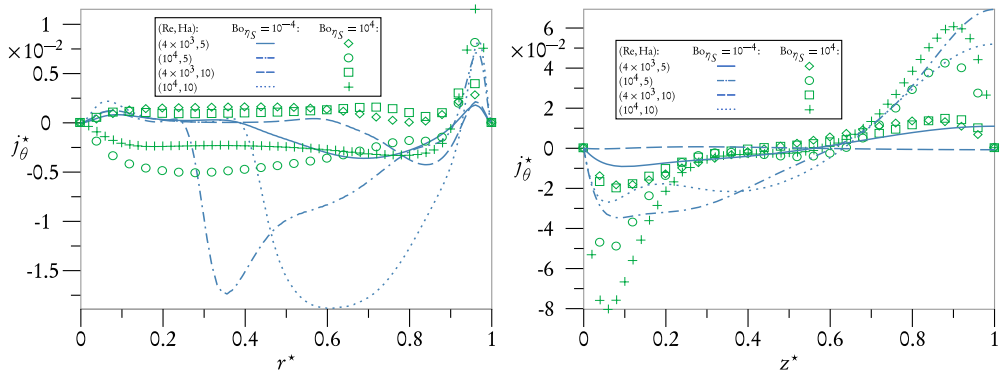

(a) – Azimuthal electric current, Cutting line (A). **(b)** – Azimuthal electric current, Cutting line (B).

Figure III.C.7 – Azimuthal electric current density $j_\theta^\star$, along cutting lines (A) for a) and B for b), for various Re, Ha and Bo_{η_S} values. $j_\theta^\star$ is normalized by $J_{\max} = 3.96 \times 10^3\ \mathrm{A{\cdot}m^{-2}}$, *i.e.* the maximum electric current reached in all cases, for the highest $(\mathrm{Re}, \mathrm{Ha}) = (10^4, 10)$ values.

However, this is very different when the azimuthal electric current $j_\theta^\star$ is considered. The typical order of magnitude for electric current densities is in fact $J = \sigma B_0 V$ (we remind that V is the order of magnitude of the main flow velocity $v_\theta^\star$, directly imposed through the rotating floor). Consequently, an increase in Ha or Re leads to higher orders of magnitude for the meridian electric current densities $(j_r^\star, j_z^\star)$ (linked

to the main MHD flow). However, as $j_\theta = -\sigma v_r B_0$ (see Eq. (III.C.8)), there is competition between the electromagnetic and inertial effects concerning the secondary flow: when Ha (and therefore B_0) is increased, the radial velocity v_r is damped due to the MHD tendency towards two-dimensionality. Fig. III.C.7 shows the evolution of $j_\theta^\star$ with respect to different $(\mathrm{Re}, \mathrm{Ha}, \mathrm{Bo}_{\eta_S})$ triplets, along cutting lines (A) and (B).

For given $(\mathrm{Ha}, \mathrm{Bo}_{\eta_S})$ values, an increase in Re causes a significant increase of $j_\theta^\star$ along (A) and (B), directly linked to the expansion and strengthening of the centrifugal flow highlighted in Sec. III.C.2.a (see for instance curves (—) and (— · —), or (□) and (+)).

For given $(\mathrm{Re}, \mathrm{Bo}_{\eta_S})$ values, a variation of Ha results in many evolutions for $j_\theta^\star$, from which no general principle can be deduced. It appears clear in Fig. III.C.7(b) that along (B), an increase in Ha leads to a drop of $j_\theta^\star$ magnitude for low Bo_{η_S} values (see for instance blue curves (—) and (— —)), whereas for high Bo_{η_S} values (green symbols, for instance (◇) and (□)), $j_\theta^\star$ increases with Ha. This seems to be globally the contrary in Fig. III.C.7(b), along cutting line (A). This complex interaction expresses the aforementioned competition between electromagnetic and inertial effects, which have opposite influence on the evolution of $j_\theta^\star$.

As already said, for given $(\mathrm{Re}, \mathrm{Ha})$ values, an increase in Bo_{η_S} helps to expand the main vortex governing the secondary flow. Consequently, along (A), the curves are flattened with high Bo_{η_S} values, because $j_\theta^\star$ is proportional to $-v_r^\star$ (Fig. III.C.7(b)). Concerning (B), for $\mathrm{Re} = 4 \times 10^3$, $\mathrm{Ha} = 10$ and $\mathrm{Bo}_{\eta_S} = 10^{-4}$ (Fig. III.C.7(b)), the main vortex closes up without including the vertical cutting line, leading to a vanishing $j_\theta^\star$ due to vanishing $v_r^\star$ (curve (— —)). At higher $\mathrm{Bo}_{\eta_S} = 10^4$, expansion of the main vortex leads to the emergence of $j_\theta^\star$ along (B) (curve (□)). The overturning shape of the centrifugal flow is consistently found, for the latter case as well as for other $(\mathrm{Re}, \mathrm{Ha})$ values. This centrifugal profile is increasingly symmetric with respect to the $z^\star = 0.5$ axis with increasing Bo_{η_S}, with the asymptotic value $\mathrm{Bo}_{\eta_S} = 10^4$ imposing a vanishing $j_\theta^\star$ at the liquid surface (see for instance curves (— · —) and (+)).

We shall now make one final comment about this part, concerning the role played by the Shercliff or Hartmann boundary layers. In the benchmarking case of Sec. III.B linked to the main MHD flow, the influence of these layers is significantly affected by the surface viscous shear. In turn, they dramatically impact bulk MHD. For the secondary MHD flow analyzed in this section, this crucial role of these layers has not been found. This can be accounted for by the nature of the secondary MHD flow: $j_\theta^\star$ is indeed purely electromotive, being only linked to radial velocity. Consequently, it naturally closes within the MHD core all around the channel with no need for Hartmann or Shercliff boundary layers. The fact that there is no requirement for any electric fields leads to a "passive" interplay between $j_\theta^\star$ and the meridian flow $(v_r^\star, v_z^\star)$.

Overall MHD flow patterns

To conclude this section about the impact of surface viscous shearing on bulk MHD, let us display some figures allowing an overview of the overall MHD bulk flow. Let us begin with the electric current densities $\vec{j}^\star$ in Fig. III.C.8, for a given $\mathrm{Ha} = 5$.

Depending on the values of $(\mathrm{Re}, \mathrm{Bo}_{\eta_S})$, very interesting features appear. At low Re, the main electric loops are located near the side walls in the Shercliff layers for

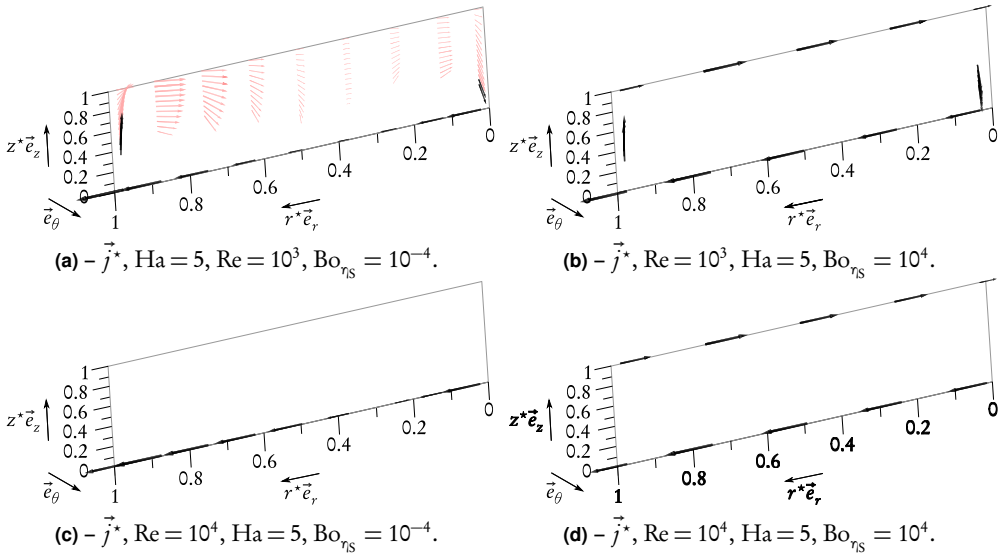

(a) – $\vec{j}^{\star}$, $\mathrm{Ha} = 5$, $\mathrm{Re} = 10^3$, $\mathrm{Bo}_{\eta_S} = 10^{-4}$.

(b) – $\vec{j}^{\star}$, $\mathrm{Re} = 10^3$, $\mathrm{Ha} = 5$, $\mathrm{Bo}_{\eta_S} = 10^{4}$.

(c) – $\vec{j}^{\star}$, $\mathrm{Re} = 10^4$, $\mathrm{Ha} = 5$, $\mathrm{Bo}_{\eta_S} = 10^{-4}$.

(d) – $\vec{j}^{\star}$, $\mathrm{Re} = 10^4$, $\mathrm{Ha} = 5$, $\mathrm{Bo}_{\eta_S} = 10^{4}$.

Figure III.C.8 – $\vec{j}^{\star}$ for $\mathrm{Ha} = 5$. $\vec{j}^{\star}$ is log-scaled by the magnitude $\exp((\ln(\|\vec{j}^{\star}\|/\|\vec{j}^{\star}\|_{\max}))/(1+p))$; $p = 1.5$ for a), b), c), and 2 for d). Black (greyscale: darkest) arrows are essentially meridian, while beige (greyscale: lightest) and blue (greyscale: intermediate) arrows correspond to significantly ($|j_{\theta}^{\star}|/\|\vec{j}^{\star}\| \geq 0.01$) positive and negative azimuthal components, respectively.

low Bo_{η_S} values (see Fig. III.C.8(a)). An increase in Bo_{η_S} magnifies the role of the Hartmann layers (see Fig. III.C.8(b)). The impact of the overturning flow can be already seen, with quite significant azimuthal perturbation throughout the cross-section (increasing as Bo_{η_S} increases). This effect is even more dramatic for very high Re numbers. When $\mathrm{Bo}_{\eta_S} = 10^{-4}$, the azimuthal component $j_{\theta}^{\star}$ is very strong, although the helical pattern of current densities is not well-structured, because the main vortex governing the secondary flow is still not expanded (Fig. III.C.8(c)). For $\mathrm{Bo}_{\eta_S} = 10^{4}$, this expansion takes place throughout the entire cross-section, and the current density closes up into a kind of well-developed helical pattern in the core flow (Fig. III.C.8(d)). Since the secondary flow is radially inwards along the surface, the electric current loops are counter-clockwise when the channel is seen from above. Along the rotating floor, the electric current loops are found to be clockwise. This is the reason why the electric current is so twisted at the mid-height of the cavity.

In order to refine the analysis of the overall MHD flow patterns, Fig. III.C.9 displays the velocity field $\vec{v}^{\star}$, along with the distribution of the Lorentz force density $\vec{f}_{\mathrm{L}}^{\star}$, with respect to several $(\mathrm{Re}, \mathrm{Ha}, \mathrm{Bo}_{\eta_S})$ values. At a given relatively low Re value, if $\mathrm{Bo}_{\eta_S} \ll \mathrm{Ha}$, the MHD tendency towards two-dimensioning is consistently highlighted by Figs. III.C.9(a) and III.C.9(b), the Lorentz force being essentially confined within the Shercliff layers. If $\mathrm{Bo}_{\eta_S} \gg \mathrm{Ha}$ (Figs. III.C.9(c) and III.C.9(d)) the previously observed electromagnetic damping of the flow is recovered (again not so marked), with a (damping) negative Lorentz force at the bottom, and a (driving) positive Lorentz force at the top, due to the electric current flowing in the active Hartmann layers. Finally, when the Reynolds number is increased (for instance $\mathrm{Re} = 10^4$, in Figs. III.C.9(e) and III.C.9(f)), the azimuthal velocity profile evolution with respect to Bo_{η_S} shows an

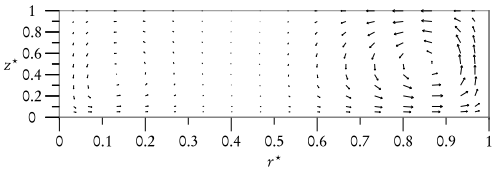

(a) – $\vec{v}^\star$, $\mathrm{Re}=10^3$, $\mathrm{Ha}=5$, $\mathrm{Bo}_{\eta_S}=10^{-4}$. Contours: $v_\theta^\star$, arrows: $(v_r^\star, v_z^\star)$.

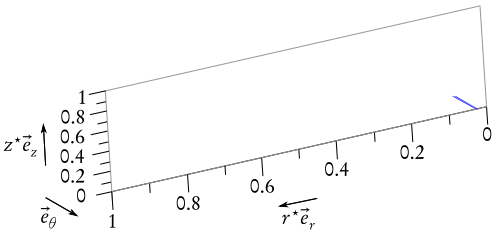

(b) – $\vec{f}_{\mathrm{L}}^\star$, $\mathrm{Re}=10^3$, $\mathrm{Ha}=5$, $\mathrm{Bo}_{\eta_S}=10^4$.

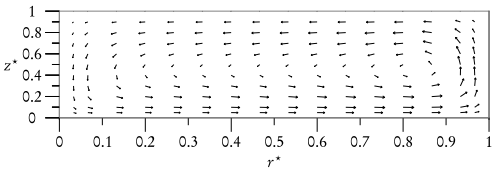

(c) – $\vec{v}^\star$, $\mathrm{Re}=10^3$, $\mathrm{Ha}=5$, $\mathrm{Bo}_{\eta_S}=10^4$. Contours: $v_\theta^\star$, arrows: $(v_r^\star, v_z^\star)$.

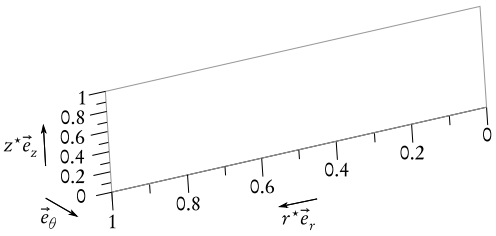

(d) – $\vec{f}_{\mathrm{L}}^\star$, $\mathrm{Re}=10^3$, $\mathrm{Ha}=5$, $\mathrm{Bo}_{\eta_S}=10^4$.

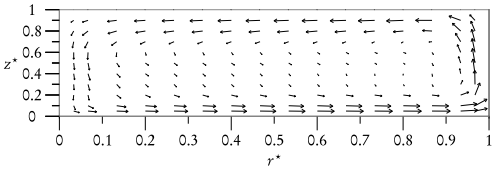

(e) – $\vec{v}^\star$, $\mathrm{Re}=10^4$, $\mathrm{Ha}=5$, $\mathrm{Bo}_{\eta_S}=10^4$. Contours: $v_\theta^\star$, arrows: $(v_r^\star, v_z^\star)$.

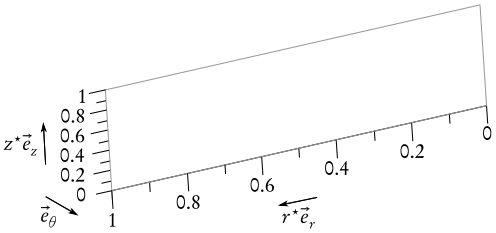

(f) – $\vec{f}_{\mathrm{L}}^\star$, $\mathrm{Re}=10^4$, $\mathrm{Ha}=5$, $\mathrm{Bo}_{\eta_S}=10^4$.

Figure III.C.9 – Bo_{η_S} impact on $\vec{v}^\star$ (left part) and $\vec{f}_{\mathrm{L}}^\star$ (right part), for $\mathrm{Ha}=5$. $(v_r^\star, v_z^\star)$ is log-scaled by the magnitude $\exp((\ln(\|(v_r^\star, v_z^\star)\|/\|(v_r^\star, v_z^\star)\|_{\max}))/(1+p))$; for a), c), e): $p=0.5$. $\vec{f}_{\mathrm{L}}^\star$ is log-scaled by the magnitude $\exp((\ln(\|f^\star\|/\|f^\star\|_{\max}))/(1+p))$; $p=1.5$ for b), d), and f). Concerning $\vec{f}_{\mathrm{L}}^\star$, black (greyscale: darkest) arrows are essentially meridian, while beige (greyscale: lightest) and blue (greyscale: intermediate) arrows correspond to significantly $(|f_{\mathrm{L}\theta}^\star|/\|\vec{f}_{\mathrm{L}}^\star\| \geq 0.01)$ positive and negative azimuthal components, respectively.

efficient advection of the main flow by the secondary flow. Momentum is then increasingly confined within the Ekman layers, resulting into the well-developed helical pattern in the core flow for the Lorentz force. This atypical flow pattern is due to a significant Lorentz force radial component, in link with strong centrifugal effects. Increasing Ha does not provide any interesting new features, concerning the qualitative impact of Bo_{η_S} on the MHD flow patterns.

MHD, inertia, and surface viscous dilatation

Following analysis of the impact of surface viscous shear on the overall MHD bulk flow, we shall now investigate the interactions between surface viscous dilatation and the subphase flow. As we focus only on the parameter $\mathrm{Bo}_{\varkappa_S}$, the surface shear Boussi-

nesq number is set to be negligibly small in this section: $\mathrm{Bo}_{\eta_S} = 10^{-4}$.

Main MHD bulk flow

With respect to surface viscous dilatation effects, when an outer magnetic field is applied, some interesting new features appear depending on the Ha value. Concerning azimuthal velocity $v_\theta^\star$, the results are shown in Fig. III.C.10, for the particular values $\mathrm{Re} = 10^4, \mathrm{Ha} = 10, \mathrm{Bo}_{\varkappa_S} = 10^4$ (contours). These results can be compared to the

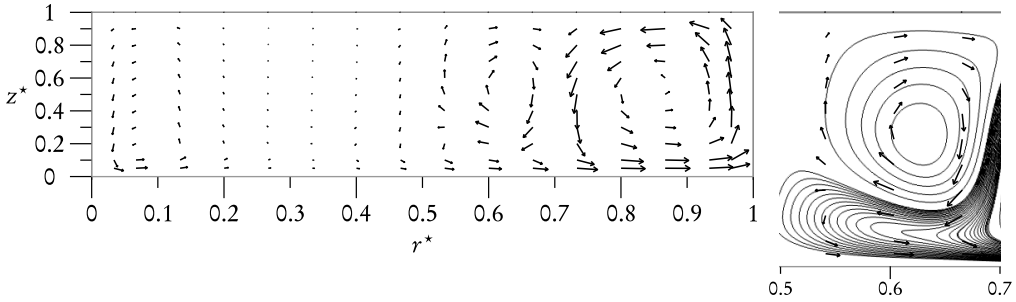

(a) – Counter-rotating vortex due to the influence of surface viscous dilatation.

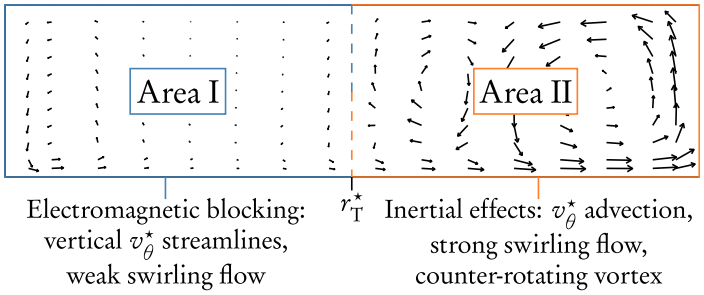

(b) – Distinct flow areas.

Figure III.C.10. $\mathrm{Bo}_{\varkappa_S}$ impact on the velocity field for the annular MHD viscometer: main (contours: $v_\theta^\star$) and secondary (arrows: $(v_r^\star, v_z^\star)$) flows, $\mathrm{Re} = 10^4, \mathrm{Ha} = 10, \mathrm{Bo}_{\varkappa_S} = 10^4$. $(v_r^\star, v_z^\star)$ is log-scaled by the magnitude $\exp((\ln(\|(v_r^\star, v_z^\star)\|/\|(v_r^\star, v_z^\star)\|_{\max}))/(1+p))$, where $p = 1$. For a); inset: streamlines of the counter-rotating vortex. For b); $r_\mathrm{T}^\star$ corresponds to the transitional radius between the two separate flow areas.

purely hydrodynamic case ($\mathrm{Ha} = 0$) of Fig. III.C.4(c). Contrary to the latter, the cross-section can be divided into two sub areas in this case, as shown in Fig. III.C.10(b). For the inner part of the cross section, where the velocity magnitude is lower, the inertial effects are weak compared to the electromagnetic effects. Consequently, the electromagnetic blocking previously observed predominates in this area. For the outer part, inertia is preponderant, and the advection of $v_\theta^\star$ by the overturning flow is strong, as in Sec. III.C.2.a. In between, a transitional area is found, governed by the balance between inertial and electromagnetic effects.

With respect to meridian electric current densities, there is no need to display some specific figures (an overall view for $\vec{j}^\star$ is shown in Fig. III.C.13). For given (Re, Ha) values, an increase in $\mathrm{Bo}_{\varkappa_S}$ does not affect the electric circuit: the current densities remain confined within the Shercliff layers. Contrary to Bo_{η_S}, an increase in $\mathrm{Bo}_{\varkappa_S}$ does not lead to the electrical activation of the Hartmann layers, which considerably

restricts the impact on the main MHD flow.

Secondary MHD bulk flow

The interaction between surface dilatation and the meridian flow is now investigated, by focusing on the quantities $(v_r^\star, v_z^\star)$ and $j_\theta^\star$. We shall begin with the meridian velocities, for $\mathrm{Re} = 10^4, \mathrm{Ha} = 10, \mathrm{Bo}_{\varkappa_S} = 10^4$ (arrows), in Fig. III.C.10. The first obvious impact of the outer magnetic field, when compared to the purely hydrodynamic case of Fig. III.C.4(c), is the decay of the main vortex governing the secondary flow. This vortex is increasingly confined to the outer part of the cross-section either with increasing Ha, due to MHD tendency towards two-dimensionality, or with increasing $\mathrm{Bo}_{\varkappa_S}$, as observed in Fig. III.C.4(c) for the purely hydrodynamic case.

Moreover, depending on the $(\mathrm{Re}, \mathrm{Ha}, \mathrm{Bo}_{\varkappa_S})$ values, the emergence of new flow patterns is observed. In the transitional area mentioned above, a counter-rotating vortex appears. Such a complex overturning flow pattern greatly depends on the values of the three parameters $(\mathrm{Re}, \mathrm{Ha}, \mathrm{Bo}_{\varkappa_S})$: it is not observed with $\mathrm{Re} = 10^3$, or $\mathrm{Ha} = 5$, or $\mathrm{Bo}_{\varkappa_S} = 10^{-4}$. Thus, contrary to the Bo_{η_S} counterpart, the meridian velocities $(v_r^\star, v_z^\star)$ may exhibit different flow patterns depending on the value of the Ha number.

The emergence of this new vortex seems to stem from a purely hydrodynamic phenomenon. There are several hints endorsing this assumption. First, the radial Lorentz force in this area is found to be always oriented in the opposite direction to the velocity field, due to the Lenz principle. The purely electromotive azimuthal component of the electric current density $j_\theta^\star$ only results in electromagnetic braking of this counter-rotating flow, and as such, cannot generate this new vortex.

Besides, the emergence of this new vortex seems to be directly related to the profile of the curl of the centrifugal force, $\partial v_\theta^{\star 2}/\partial z^\star$, in area II, as shown in Fig. III.C.11. When $\mathrm{Bo}_{\varkappa_S} = 10^{-4}$, this term is everywhere positive, giving rise to the single main vortex ruling the swirling flow. When $\mathrm{Bo}_{\varkappa_S} = 10^4$, this term is oscillating, and the changes of sign are strongly linked to the emergence of counter-rotating vortices.

Finally, a purely hydrodynamic ($\mathrm{Ha} = 0$) calculation has been performed, by keeping only Area II for the calculation domain. The inner wall boundary condition is modified as such: the velocity profile at $r^\star = r_{\mathrm{I}}^\star$ resulting from previous MHD calculations is imposed at this fluid boundary. Despite some quantitative differences (due to the lack of Lorentz force for instance), the qualitative aspect of the flow patterns observed in Fig. III.C.10(b) is consistently found in this hydrodynamic calculation. The resulting flow topology could be phenomenologically related to the hydrodynamic instabilities (due for instance to inflection points in the velocity profiles) appearing for confined flows in rotor/stator configuration [76]. However, the study of the mechanisms explaining the emergence of such instabilities is far from the scope of this work, and the previous hypothesis is left for future prospects.

Whatever it be, it is assuredly the coincidence of the values of the three dimensionless parameters $(\mathrm{Re}, \mathrm{Ha}, \mathrm{Bo}_{\varkappa_S})$ that leads to this original flow pattern: sufficiently high Ha and $\mathrm{Bo}_{\varkappa_S}$ values enhance electromagnetic blocking of the flow in the inner part of the channel (by damping the main vortex governing the secondary flow, thus promoting the rigid-body motion), whereas a high Re number allows inertial effects to

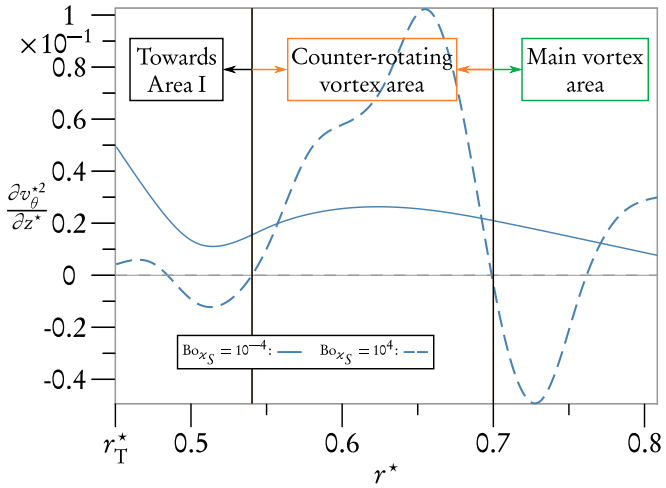

Figure III.C.11. The curl of the centrifugal force in Area II, along cutting line (A). $r_\mathrm{T}^\star$ corresponds to the transitional radial position of Fig. III.C.10(b).

predominate in the outer part of the cross-section. The geometrical configuration of the flow is therefore greatly modified, with the centrifugal flow concentrated against the outer wall, leading to the hydrodynamic development of this new counter-rotating vortex. Note that this new flow pattern is not found in the corresponding part concerning the Bo_{η_S} effect: for the same $\mathrm{Re} = 10^4, \mathrm{Ha} = 10$ values, an increase in Bo_{η_S} leads to the damping of the main azimuthal flow, through the electrical activation of the Hartmann layers, and to stretching of the secondary flow. Flow topology is significantly different from that observed here for the $\mathrm{Bo}_{\varkappa_S}$ effect, and as such, does not lead to the emergence of the counter-rotating flow.

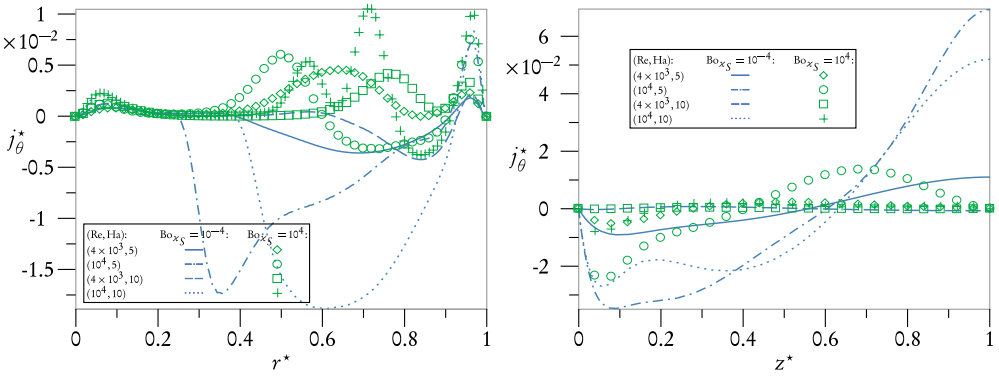

(a) – Azimuthal electric current, Cutting line (A). **(b)** – Azimuthal electric current, Cutting line (B).

Figure III.C.12 – Azimuthal electric current density $j_\theta^\star$, along cutting lines (A) for a) and B for b), for various Re, Ha and $\mathrm{Bo}_{\varkappa_S}$ values. $j_\theta^\star$ is normalized by $J_{\max} = 3.96 \times 10^3\ \mathrm{A{\cdot}m^{-2}}$, *i.e.* the maximum electric current reached in all cases, for the highest $(\mathrm{Re}, \mathrm{Ha}) = (10^4, 10)$ values.

We shall now examine the evolution of $j_\theta^\star$, along the cutting lines (A) and (B), in Fig. III.C.12. As explained in the part about Bo_{η_S} influence, it is worthwhile investigating the dependence of $j_\theta^\star$ not only with respect to $\mathrm{Bo}_{\varkappa_S}$, but also to Re and Ha. For

given (Ha, $Bo_{\varkappa_S}$), the impact of varying Re is the same as for Bo_{η_S}, *i.e.* $j_\theta^\star$ increases with Re because of the expansion of the overturning flow (*e.g.* curves (——) and (···), or (◇) and (○)).

A change in the Ha value leads to complex evolutions along (*A*) and (*B*), similar to the Bo_{η_S} effect, related to the competition between inertial and electromagnetic effects. However, there is a major difference between surface dilatation and shear. For $Bo_{\varkappa_S}$, along a given cutting line, the impact of increasing Ha remains qualitatively the same at low or at high $Bo_{\varkappa_S}$ values, whereas it depends on Bo_{η_S} values for the previous case. The effect is nonetheless the opposite between the two cutting lines. For instance, along (*A*), the magnitude of $j_\theta^\star$ globally increases with Ha both at low (see curves (——) and (···)) and at high (see curves (+) and (○)) $Bo_{\varkappa_S}$ values. Along (*B*), the magnitude of $j_\theta^\star$ is lower when there is an increase in Ha, whatever the value of $Bo_{\varkappa_S}$ (same curves).

Finally, for given (Re, Ha) values, along (*A*) (Fig. III.C.12(a)), an increase in the value of $Bo_{\varkappa_S}$ does not lead to flattening of the profiles previously observed with Bo_{η_S} (Fig. III.C.7(a)). Rather, at high $Bo_{\varkappa_S}$ values (green symbols), $j_\theta^\star$ oscillates around the $j_\theta^\star = 0$ axis, where the amplitude and the number of peaks are maximum for the following particular values: $(Re, Ha, Bo_{\varkappa_S}) = (10^4, 10, 10^4)$ (curve (+)). These oscillations are linked to the emergence of the counter-rotating vortex for high $Bo_{\varkappa_S}$ values ($j_\theta^\star$ is proportional to $-v_r^\star$). Note that near the inner wall, the curves for low (blue lines) and high (green symbols) $Bo_{\varkappa_S}$ values are superimposed. This is because an increase in $Bo_{\varkappa_S}$ does not lead to a significant change for the overturning flow in this part of the channel cross-section. Along (*B*), and contrary to what is noticed for the Bo_{η_S} effect (Fig. III.C.7(b)), the overturning profile is not recovered with an increase in $Bo_{\varkappa_S}$ (Fig. III.C.12(b)). Rather, the curves are increasingly flattened, due to the progressive damping of the main vortex governing the secondary flow. Consequently, the cutting line (*B*) is no longer included in the area where $v_r^\star$ is still significant.

As for the Bo_{η_S} counterpart, the interaction between the Shercliff or Hartmann layers and surface dilatation (through $Bo_{\varkappa_S}$) does not provide any insights into the swirling flow topology.

Overall MHD flow patterns

To complete this section on the impact of surface viscous dilatation on bulk MHD, we shall now display some results allowing an overview of the overall MHD bulk flow, beginning with the electric current densities in Fig. III.C.13. Contrary to the Bo_{η_S} impact, it has been previously shown that the flow pattern qualitatively depends on the value of the Ha number as well as on Re and $Bo_{\varkappa_S}$ (with the emergence of the counter-rotating vortex). Therefore, the $Bo_{\varkappa_S}$ impact is analyzed for Ha = 5 (left part) and for Ha = 10 (right part).

Let us begin with the $Bo_{\varkappa_S}$ influence over the electric current densities. For this purpose, the left parts of Fig. III.C.8 (corresponding to the case $Bo_{\varkappa_S} = 10^{-4}$ for given (Re, Ha, Bo_{η_S}) values) and of Fig. III.C.13 ($Bo_{\varkappa_S} = 10^4$ for the same (Re, Ha, Bo_{η_S}) values) are compared. As expected from the previous results, for a given Ha = 5, the increase in $Bo_{\varkappa_S}$ does not result in an obvious impact (Figs. III.C.8(a) and III.C.13(a),

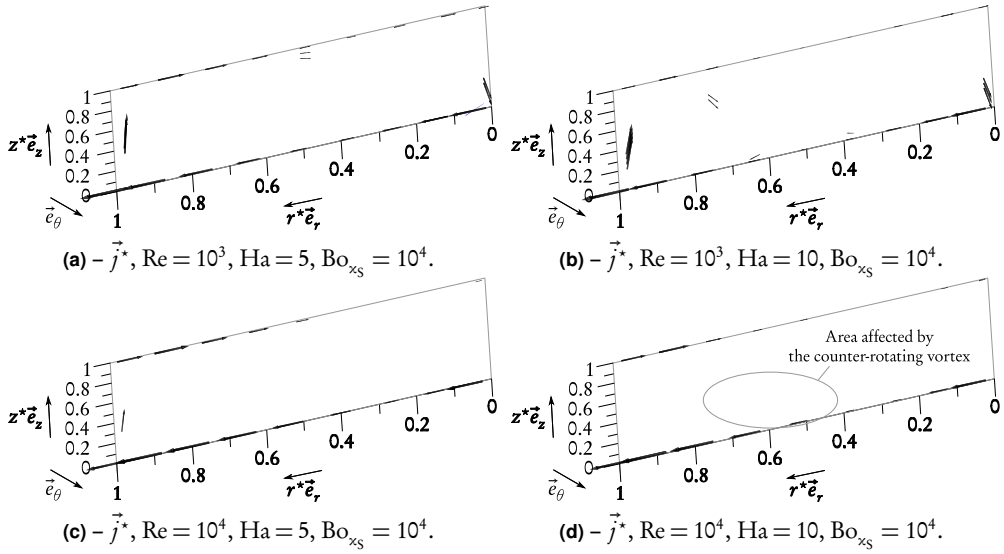

Figure III.C.13 – $\vec{j}^\star$ for Ha = 5 (left part), or Ha = 10 (right part). $\vec{j}^\star$ is log-scaled by the magnitude $\exp((\ln(\|\vec{j}^\star\|/\|\vec{j}^\star\|_{\max}))/(1+p))$; $p = 2$ for a), b), and 1.5 for c), d). Black (greyscale: darkest) arrows are essentially meridian, while beige (greyscale: lightest) and blue (greyscale: intermediate) arrows correspond to significantly ($|j^\star_\theta|/\|\vec{j}^\star\| \geq 0.01$) positive and negative azimuthal components, respectively.

Figs. III.C.8(c) and III.C.13(c)), irrespective of Re value (Re = 10^3 for a), Re = 10^4 for c)). The main difference occurs at the liquid surface, where $\vec{j}$ becomes purely radial for Bo$_{\varkappa_S}$ = 10^4.

To highlight some interesting new features linked to a high Bo$_{\varkappa_S}$ value, the Ha number is increased to 10 (Fig. III.C.13, right part). When Re = 10^3, the electric current densities are essentially confined inside the Shercliff layers (Fig. III.C.13(b)), similarly to what is observed in the benchmarking case of Sec. III.B for a low Bo$_{\eta_S} = 10^{-4}$. For a higher Re = 10^4, the new patterns previously observed for the secondary flow are recovered. The helical pattern for $\vec{j}^\star$, previously observed in the core for the Bo$_{\eta_S}$ effect (Fig. III.C.8(d)), is recovered in Fig. III.C.13(d). However, the electric current is mostly located near the outer wall, with the inner half of the flow being current-free, due to the confinement of the main vortex governing the secondary flow for a high Bo$_{\varkappa_S}$. Besides, $\vec{j}$ is significantly perturbed by the emergence of the counter-rotating vortex. This vortex induces radially outwards (at the top) and radially inwards (near the bottom) flows, whereas along the rotating floor, the flow must remain radially outwards (see inset in Fig. III.C.10(a)). Consequently, the electric current densities are twisted at two locations, essentially because their azimuthal orientation is governed by the radial component of the meridian flow: a first twist is observed in the middle of the secondary vortex, while a second twist is observed near the rotating floor. Such an original pattern is a typical example of how surface dilatation may affect the MHD bulk flow.

Finally, Fig. III.C.9 links the velocity field topology to the distribution of Lorentz force density, with respect to several (Re, Ha, Bo$_{\varkappa_S}$) values. First of all, Figs. III.C.9(a)

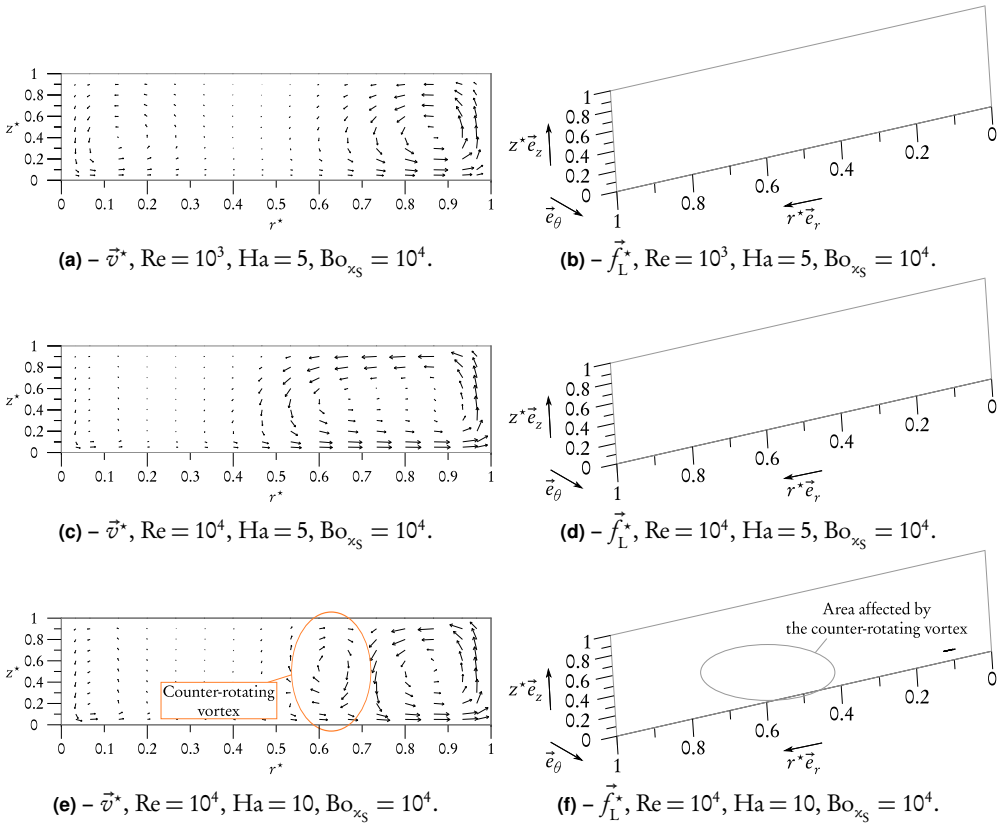

(a) – $\vec{v}^\star$, $\mathrm{Re} = 10^3$, $\mathrm{Ha} = 5$, $\mathrm{Bo}_{\varkappa_S} = 10^4$.

(b) – $\vec{f}_L^\star$, $\mathrm{Re} = 10^3$, $\mathrm{Ha} = 5$, $\mathrm{Bo}_{\varkappa_S} = 10^4$.

(c) – $\vec{v}^\star$, $\mathrm{Re} = 10^4$, $\mathrm{Ha} = 5$, $\mathrm{Bo}_{\varkappa_S} = 10^4$.

(d) – $\vec{f}_L^\star$, $\mathrm{Re} = 10^4$, $\mathrm{Ha} = 5$, $\mathrm{Bo}_{\varkappa_S} = 10^4$.

(e) – $\vec{v}^\star$, $\mathrm{Re} = 10^4$, $\mathrm{Ha} = 10$, $\mathrm{Bo}_{\varkappa_S} = 10^4$.

(f) – $\vec{f}_L^\star$, $\mathrm{Re} = 10^4$, $\mathrm{Ha} = 10$, $\mathrm{Bo}_{\varkappa_S} = 10^4$.

Figure III.C.14 – $\mathrm{Bo}_{\varkappa_S}$ impact on $\vec{v}^\star$ (left part) and $\vec{f}_L^\star$ (right part). $(v_r^\star, v_z^\star)$ is log-scaled by the magnitude $\exp((\ln(\|(v_r^\star, v_z^\star)\|/\|(v_r^\star, v_z^\star)\|_{\max}))/(1+p))$, where $p = 0.5$ for a), c), $p = 1$ for e). $\vec{f}_L^\star$ is log-scaled by the magnitude $\exp((\ln(\|\vec{f}^\star\|/\|\vec{f}^\star\|_{\max}))/(1+p))$; $p = 1.5$ for b), d), and f). Concerning $\vec{f}_L^\star$, black (greyscale: darkest) arrows are essentially meridian, while beige (greyscale: lightest) and blue (greyscale: intermediate) arrows correspond to significantly $(|f_{L\theta}^\star|/\|\vec{f}_L^\star\| \geq 0.01)$ positive and negative azimuthal components.

and III.C.14(a) for velocity (respectively III.C.9(b) and III.C.14(b) for Lorentz force) are compared to analyse surface dilatation impact on the main MHD flow. An increase in $\mathrm{Bo}_{\varkappa_S}$ does not seem to alter significantly the main MHD flow for these (Re, Ha) values, the azimuthal components of both velocity and Lorentz force remaining quite unchanged. As previously enhanced in Sec. III.C.2.a, the main flow is less efficiently advected by the secondary flow, the main vortex governing the secondary flow slightly decreases when $\mathrm{Bo}_{\varkappa_S}$ increases.

Now, when the (Re, Ha) values are increased, we have shown that some interesting new features appear. When Re increases at fixed $(\mathrm{Ha}, \mathrm{Bo}_{\varkappa_S})$, the magnitude of the overturning flow increases with Re, and the main vortex governing the secondary flow is enlarged (Fig. III.C.14(c)), favouring main flow advection, as seen in Sec. III.C.2.a. The Hartmann layers remaining electrically inactive, the Lorentz force is essentially electromotive, following the variations of $v_r^\star$ (Fig. III.C.14(d)). However, contrary to the previous section about the impact of Bo_{η_S}, an increase in Ha really modifies the qualitative influence of $\mathrm{Bo}_{\varkappa_S}$ on the swirling flow. As previously shown in Fig. III.C.10,

two distinct areas can be distinguished, with preponderant inertia in the outer part, and preponderant electromagnetic blocking for the inner part (Fig. III.C.14(e)). The emergence of the counter-rotating vortex imposes a sudden change of sign along the radial direction to the mainly electromotive Lorentz force density (Fig. III.C.14(f)).

III.C.3 Conclusion and final scaling laws towards the experimental test-bench

In addition to the 2-D study performed in Sec. III.B, this 2-D ½ numerical modelling shows how a change in the mechanical properties of a fluid interface can greatly influence a MHD core flow. Moreover, it has been proved that shear and dilatational viscosities of the surface do not generate the same changes. On the one hand, viscous shearing of the interface actively modifies the main annular flow by means of the Hartmann layers, which become electrically active. A damping is clearly demonstrated, as is also a 2-D MHD tendency. On the other hand, the dilatational viscosity of the interface is only responsible for damping the meridian flow driven by centrifugation, with a new pattern if inertia and electromagnetic blocking are both significant.

In parallel, the relevant working conditions highlighting the competitive effects of inertia, electromagnetism and surface rheology have been identified, and particularly the relative values of the Hartmann and Reynolds numbers allowing for either magnifying or extinguishing inertial effects. These scaling laws are used in the next chapter for the design of Madip.

One concluding remark relates to the activity of the electrical boundary layers. Given the relatively low Ha values required for development of the swirling flow, the influence of the Hartmann layers is in any case reduced. However, regarding the possible influence of surface viscous dilatation on the main and secondary flows, the Shercliff layers and, in particular, the Hartmann layers do not especially become electrically active throughout the many configurations tested in this paper. Consequently, their impact on the core flow is not as dramatic as when a strong surface viscous shear is applied, the latter case promoting damping of the main azimuthal flow through electrical activation of the Hartmann layers.

III.D MHD and surface viscosities: Madip, first experimental investigations

In this chapter, the experimental developments for the characterisation of the interfacial properties of a gradually oxidising liquid metal MHD flow are introduced. The scaling laws stemming from the previous analytical and numerical results are first reminded. Using these scaling laws as dimensioning criteria, some significant instrumental and technical developments are derived, in link with the design of the experimental test-bench: Madip (for *Magnétohydrodynamique diphasique*, in French). Finally, the first experimental results are reported, unveiling significant physical features along with some *in situ* observations of the surface rheological behaviour of Galinstan, from which we can deduce some salient prospects for future tests.

III.D.1 Scaling laws for dimensioning the experimental set-up

In order to design the experimental test-bench, distinct operating conditions have been determined, through scaling laws. Some of the latter have been deduced from the state-of-the-art of existing works, like in Sec. I.B.2.b about the necessity to monitor the ambient atmosphere within one-ppm accuracy, and Sec. III.A, about the geometrical dimensioning of the "shallow channel" of the annular viscometer. In the latter, it has also been shown that monitoring the surface velocity $\vec{v}_S$ alone would give access both to bulk dynamics and surface viscosities. Other scaling laws have been determined about the parameters governing bulk MHD, *i.e.* the Hartmann and the Reynolds numbers, by carrying out analytical and numerical investigations in Secs. III.B and III.C. From now on, we shall use these scaling laws as the main dimensioning criteria for the experimental test-bench. These criteria are gathered in Tab. III.D.1, along with the technical solutions proposed to address the related experimental requirements. Note that other dimensioning issues, of secondary interest, are tackled in the following section, about the instrumentation and technical developments involved in Madip.

III.D.2 Instrumentation and technical developments

In this section, a general overview of the experimental test-bench is first given. The different working areas and the corresponding experimental issues are then detailed.

Quantity	Criterion	Experimental requirements	Technical solution
r_i, r_o, h, δ	$\frac{h}{r_o} < 1$, $\frac{\delta}{r_o} \ll 1$	Small, controlled aspect ratios and vertical gaps	µm-accuracy manufacturing and implementation of the shallow annular channel
$\vec{v}_S$	Measurable	Monitor surface dynamics, in order to access bulk dynamics/ surface properties	Imaging surface dynamics of tracers, flow calculation by particle tracking velocimetry (PTV)
Bo_{η_S}, $\mathrm{Bo}_{\varkappa_S}$	Wide range of values	Monitor the O_2 rate of ambient atmosphere	Confinement of the viscometer in a glass container filled with Ar/O_2 controlled mixtures
Re	$\mathrm{Re} \in [10, 10^4]$	Accurate control of the angular speed Ω (esp. at low velocities)	Compact piezomotor
Ha	$\mathrm{Ha} \in [0, \max]$	Supply/ monitor a (strong) vertical uniform (at flow scale) DC field $\vec{B}_0$, compatible with confinement	DC Electromagnet, $B_{0\max} = 0.45\,\mathrm{T}$

Table III.D.1 – Dimensioning criteria.

III.D.2.a Overview of the experimental set-up

A general overview of the Madip experiment, drawn by using the computer-aided design (CAD) Catia® software, is shown in Fig. III.D.1. Five distinct working areas are distinguished, *i.e.* the viscometer itself, the gas circuit, the electromagnet, the optical test-bench and the provided instrumentation. Note that a photograph of the real experimental layout is given in Fig. III.D.2. Let us now detail each working area, and highlight some technical issues of interest.

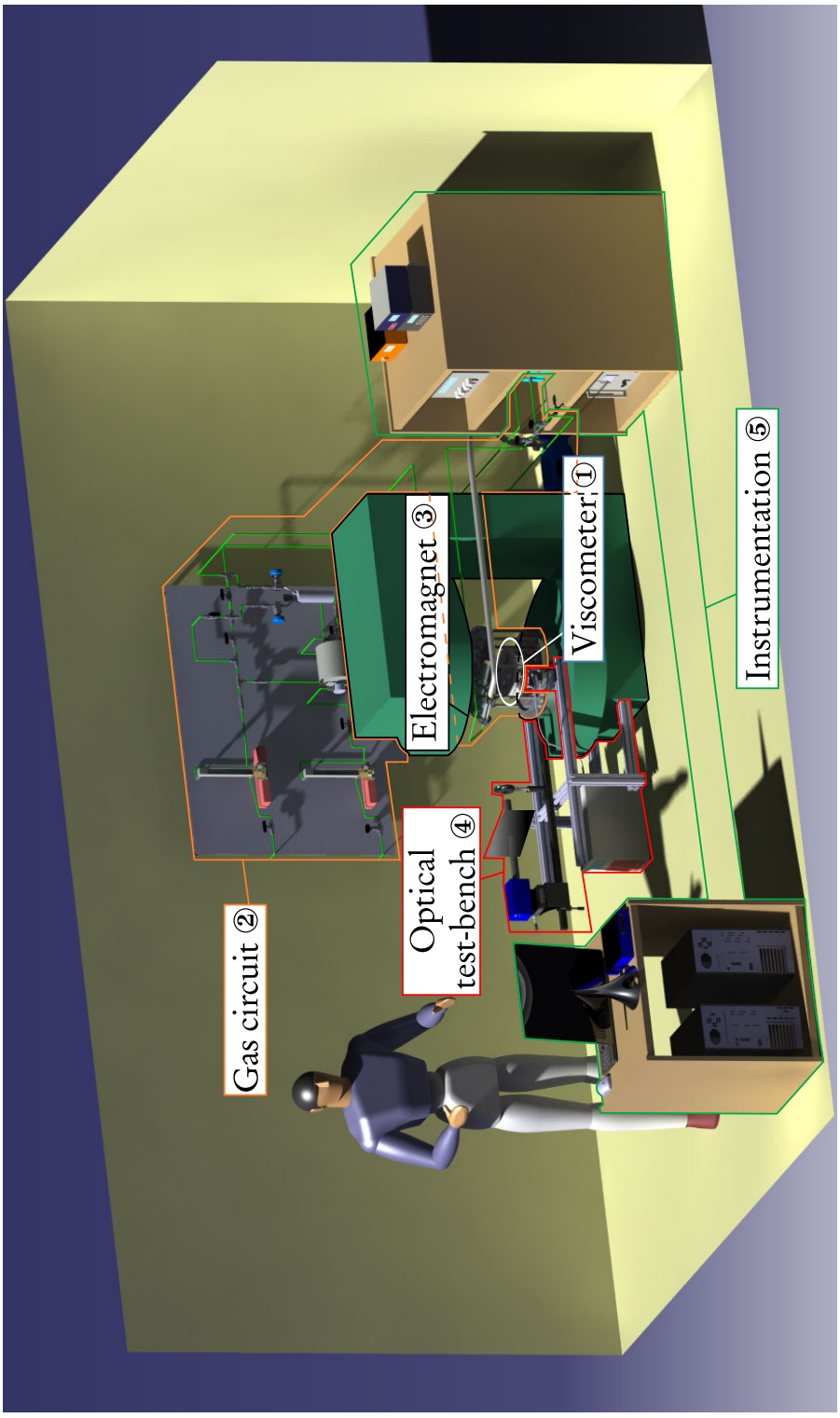

Figure III.D.1 – General overview of the Madip experiment with five distinct working areas. Note that the electromagnet power supply is not represented, for it would mask a large part of the test-bench. The human operator is 1.73 m tall.

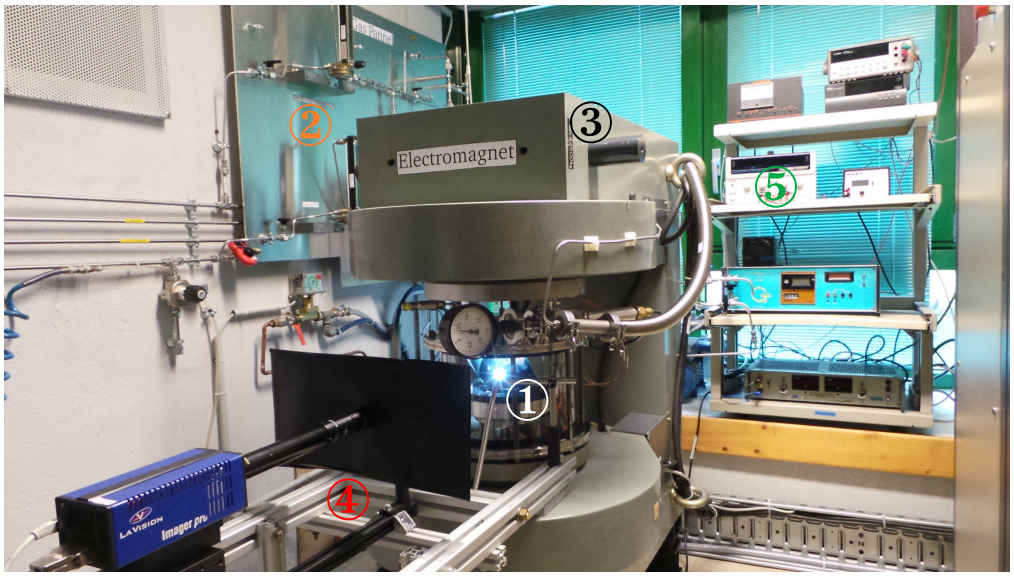

Figure III.D.2 – Photograph of the real experimental test-bench, with the 5 distinct working areas. Note that the electromagnet power supply and the computer workstation are not represented.

III.D.2.b Area ①: the annular viscometer

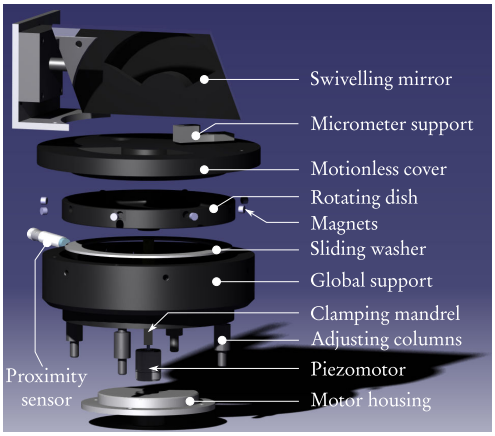

(a) – CAD view of the annular viscometer.

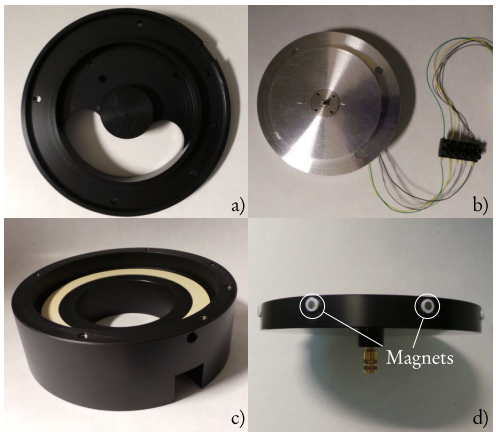

(b) – Photograph of some elements of the annular viscometer. a): cover, b): piezomotor, c): Global support, d): rotating assembly.

Figure III.D.3 – Working area ①: the annular channel viscometer.

The first working area consists of the annular viscometer assembly, as displayed in the CAD views of Figs. III.D.3(a) and III.D.4. The main body is constituted by polyoxymethylene (POM) pieces, for the global support, the rotating dish (rotating floor) and the motionless cover (inert side-walls), the latter two defining the annular channel, of which radial dimensions r_i, r_o are equal to 2.5 cm and 6.5 cm, respectively. There

are numerous advantages of using POM as a reference material: this material is a black resin, preventing from any undesired reflection light. Besides, it is chemically neutral and compatible with Galinstan, and can be machined with a μm accuracy, because of its good mechanical properties.

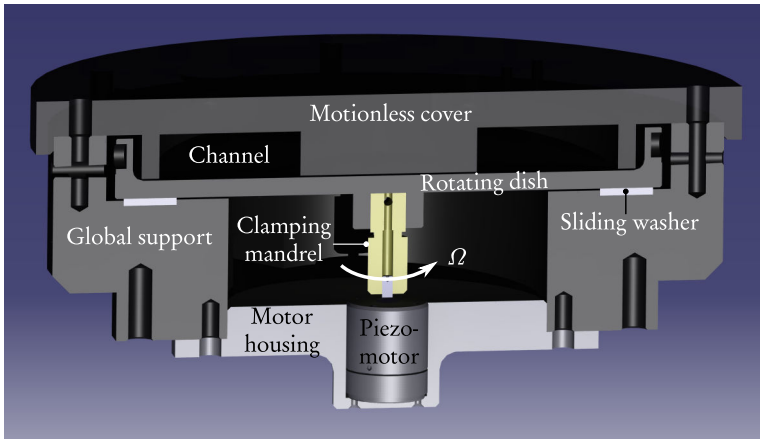

Figure III.D.4 – Cross-sectional CAD view of the annular channel and the motor block.

A motor is required in order to rotate the dish which will contain Galinstan. There are several requirements to achieve, the first of which being the compatibility with the high electromagnetic field environment: the motor must not interfere with or be damaged by the outer magnetic field delivered by the electromagnet. This motor must also be vacuum-compatible, and accurate rather than fast, the range for the values of the Reynolds number corresponding to an angular speed $\Omega \in \sim [10^{-1}, 10^{1}]$ rpm. Finally, because of the limited extent of the electromagnet gap, and because of the confinement reactor (see hereafter), the motor must be extremely compact. All these requirements have considerably restricted our choice, and led us to choose a piezomotor designed by Faulhaber® . It is very accurate at low velocities (angular resolution of 0.2 μrad), however its maximum angular speed allows us to reach only the maximum value $\mathrm{Re} = 5 \times 10^{3}$. According to Fig. III.C.6, this value is still high enough to magnify inertial effects, and potentially identify surface dilatation. The original flow patterns highlighted in Sec. III.C.2.b for $\mathrm{Re} = 10^{4}$, in link with the counter-rotating vortex, will be more difficult to observe, though.

As shown in Figs. III.D.3(a) and III.D.3(b)d), little magnets are implanted all along the circumference of the rotating dish, at regular intervals. These magnets are strong enough to trigger the proximity sensor screwed into the support, and thus give access to the angular speed of the rotating dish. Note that their short-range influence do not interfere with the magnetic field imposed by the electromagnet in the annular channel (negligible perturbation of $\pm 3 \times 10^{-4}$ T, measured with a gaussmeter).

Finally, the motor is clamped to the rotating dish, and adjusted inside a provided housing, screwed into the global support. A sliding washer is introduced between the rotating dish and the support, to avoid friction. The condition of centring the whole system is fulfilled by means of a μm accuracy machining, avoiding eccentricity due to off-centring. Note that the horizontality of the rotating floor is controlled by

means of a ultra-accurate spirit level: the level variation is thus restricted to 30 μm at dish scale. The cover is then μm-adjusted and screwed onto the support. During this step, the lubrication gap δ between the rotating floor and the vertical side-walls is fixed at $\delta \sim 5 \times 10^2$ μm, by means of a depth micrometer adapted onto the cover (see Sec. III.D.3.e for another *in situ* application of this micrometer). A swivelling mirror designed for surface flow imaging is eventually screwed onto the cover.

III.D.2.c Area ②: the gas circuit

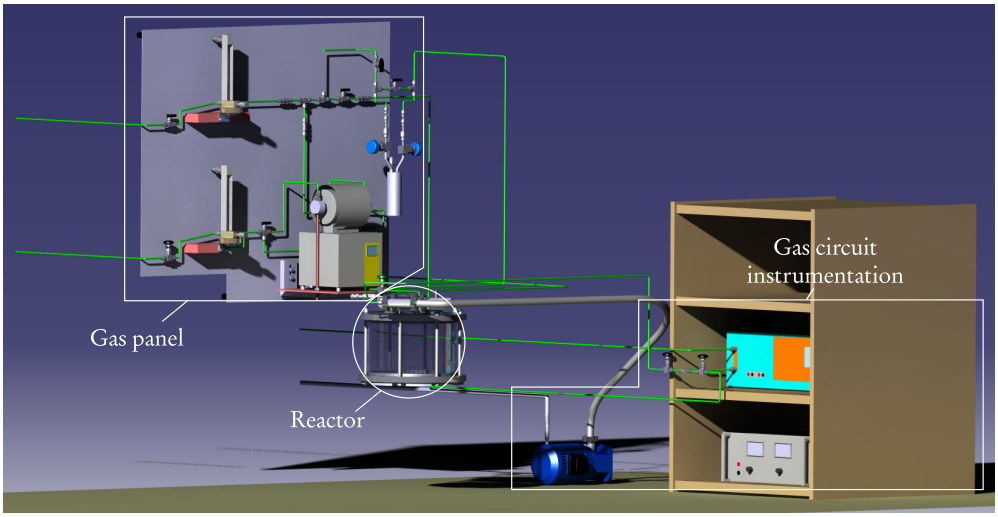

Figure III.D.5 – Working area ②: CAD view of the gas circuit of Madip.

The second working area is the gas circuit of Madip, a general CAD view of which is given in Fig. III.D.5. It is made up of three distinct parts, that we shall separately describe, *i.e.* the gas panel, the chemical reactor and the associated instrumentation.

Gas panel

A general view of the gas panel of Madip is given in Fig. III.D.6. The aim of this panel is to supply the working atmosphere to the chemical reactor, and to allow the transfer of Galinstan in controlled conditions, *i.e.* at given flow rates and purity.

For this purpose, two gas lines are implemented. The first line at the bottom of the panel is linked to an Ar bottle, and consists of a flowmeter and a tubular oven, inside which an O_2 "scavenger" is placed. The latter consists of a partially reduced zirconia pellet, stabilised with yttrium, and has a special affinity with O_2. Indeed, when heated at 800 °C, this pellet traps almost every O_2 molecule present in the gas flowing across the tubular oven. Note that we do not provide any reference here, because this remains quite a confidential issue, developed in partnership with Dr. Jonathan Deseure from the LEPMI laboratory in Grenoble. As a consequence, this first gas line provides a very pure working argon gas (measurements have been performed with O_2 impurities below 10^{-6} ppm, *i.e.* far below 1 ppm, the rate at which the oxidation of Galinstan

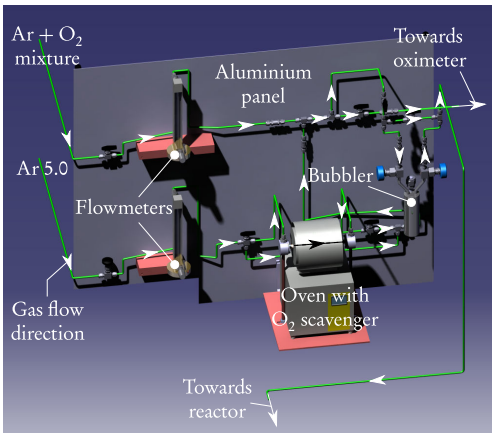

(a) – CAD view of the gas panel.

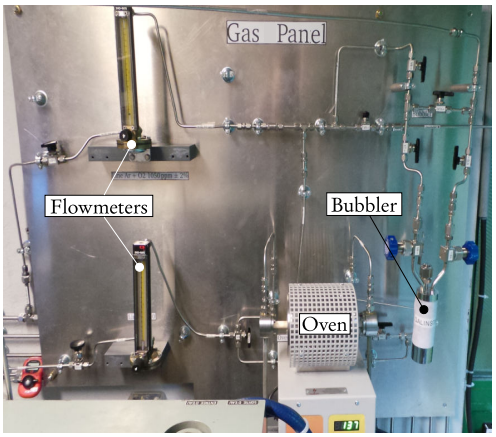

(b) – Photograph of the gas panel of Madip.

Figure III.D.6 – The gas panel of Madip.

is expected to start). The second line at the top is connected to a bottle filled with a mixture of argon and oxygen, and allows for a controlled pollution in O_2 of the working atmosphere, leading to a controlled oxidation of the liquid metal sample.

These two lines then join, either to reach the bubbler area or to bypass it and reach the oximeter. The reason of this bypass is to control the working gas prior to use it inside the reactor or the bubbler. The latter may be described as a stainless steel airproof can, which contains the alloy and allows for its transfer inside the chemical reactor in very pure conditions (see Sec. III.D.3.c for further details about its use).

The chemical reactor

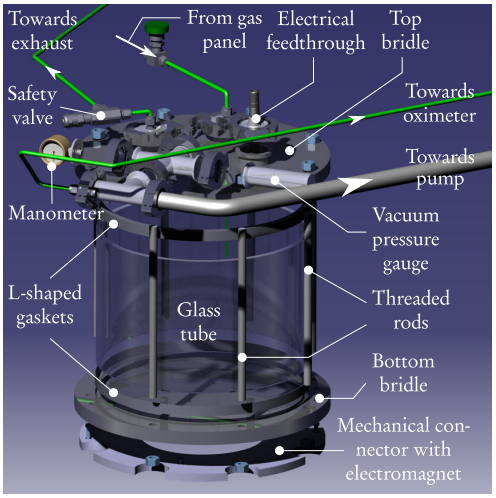

(a) – CAD view of the chemical reactor. Electrical connections are not displayed.

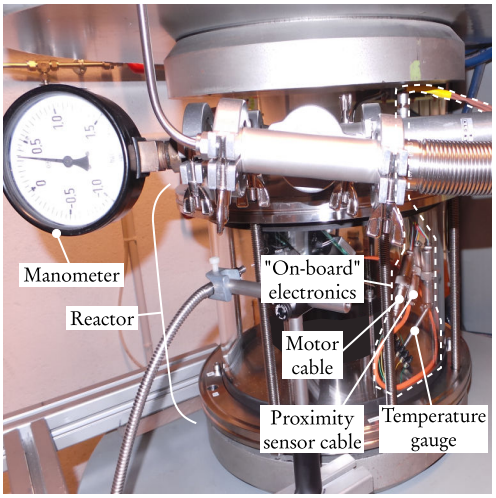

(b) – Photograph of the chemical reactor, highlighting the "on-board" electronics.

Figure III.D.7 – The chemical reactor of Madip.

A detailed view of the chemical reactor of Madip is displayed in Fig. III.D.7. The reactor design plays a significant role:

- it must ensure the perfect confinement of the annular viscometer, contain the working gas coming from the gas panel, allow for the flowing of Galinstan inside the rotating dish under controlled pressure conditions;
- it must permit the air-proof implementation of what we call the "on-board" electronics, consisting of a temperature gauge Pt 100, the motor power supply and command cables, and the proximity sensor wires (see Fig. III.D.7(b));
- finally, it must be compact enough to enter in the electromagnet gap. Obviously, it must not contain ferromagnetic materials.

The confinement issue is addressed by means of a glass tube clasped between two stainless steel bridles, connected by stainless steel threaded rods, the airtightness being secured by two L-shaped fluoropolymer gaskets, as shown in Fig. III.D.7(a). This assembly is mechanically connected to the electromagnet pole by means of a provided polycarbonate piece. Gas feedthroughs are made across the top bridle. The inlet feedthrough allows for the transfer of gas and Galinstan from the gas pannel. The outlet feedthrough allows for the vacuum pumping and for the analysis of the working atmosphere with the oximeter. The working pressure can be measured either with a manometer, or, for vacuum pressure, with a vacuum pressure gauge. A safety valve is set, in case of accidental overpressure.

Gas circuit instrumentation

The instrumentation devoted to the gas circuit is shown in Fig. III.D.8, and it consists of a rotary pump allowing to reach a primary vacuum, and of the oximeter system for measuring the O_2 rate of the working atmosphere.

Let us briefly focus on the oximeter, which plays a role of prime interest. The oximeter is basically an electrochemical gauge. It bears on the properties of a galvanic cell $\{M, O_2(p_{ref})\}$ / solid oxide electrolyte / $M, O_2(p_m)\}$, where M is an electronic conductor, the solid oxide electrolyte is an oxide ceramic, p_{ref} is a reference (known) O_2 partial pressure, and p_m is the O_2 partial pressure to determine [86]. The voltage at the terminals of the cell can be expressed by the Nernst's law:

$$e = \frac{RT}{4F} \ln\left(\frac{p_m}{p_{ref}}\right), \tag{III.D.1}$$

where e is the electromotive force of the cell, R is the gas constant, F is the Faraday constant and T is the temperature of the cell. Thus, the knowledge of p_{ref} and T, and the measurement of e give access to the O_2-rate of the working atmosphere, far below 1-ppm accuracy, *i.e.* far below the rate at which the oxidation of Galinstan begins [86]. The particular oximeter used in Madip is a prototype developed in Grenoble, and has been kindly loaned by Dr. J. Deseure, from the LEPMI laboratory.

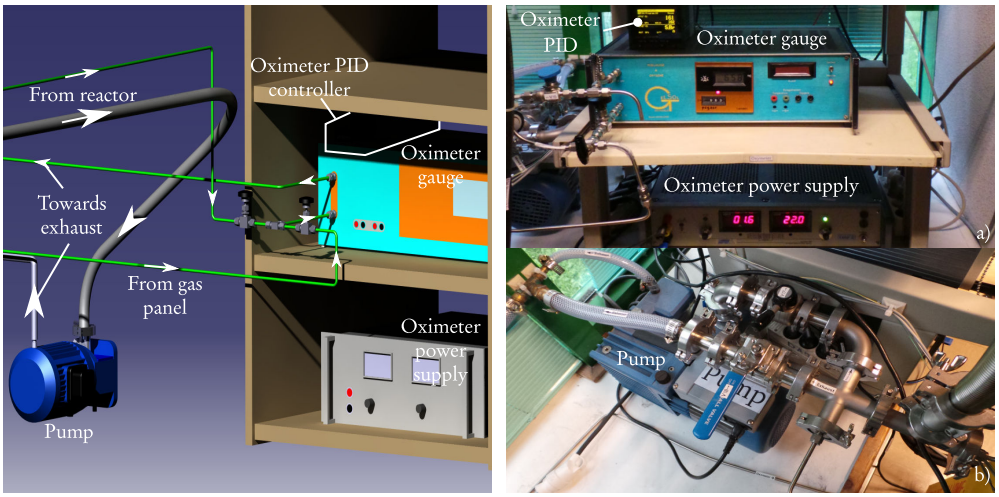

(a) – CAD view of the gas circuit instrumentation, *i.e.* the oximeter and the pump.

(b) – Photograph of the gas circuit instrumentation. a): oximeter, b): pump.

Figure III.D.8 – Instrumentation devoted to the gas circuit of Madip.

III.D.2.d Area ③: the electromagnet

The third working area is the electromagnet system. As shown in Fig. III.D.9(a), it is composed of an electromagnet power supply, which delivers a high-intensity DC electric current. This current is concentrated in the yoke, which constitutes the magnetic circuit with the poles of the electromagnet. The particular design of the assembly allows for reaching a strong DC magnetic field in the air gap between the two poles: $B_{0\max} = 0.45\,\mathrm{T}$, at the location of the annular channel. The verticality and homogeneity of this field has been characterised with a gaussmeter, of which orientation and position have been controlled with a spatial grid made of polystyrene. As seen in Fig. III.D.9(b), the verticality and homogeneity of the magnetic field in the area where the annular channel is located is quite satisfying, both being achieved within one percent accuracy. Finally, a dedicated measuring cell on the electrical cabinet is used in coordination with the gaussmeter to link the control voltage with the value of the imposed magnetic field between the poles.

III.D.2.e Area ④: the optical test bench

The fourth working area of Madip is the optical test-bench. A general view is given in Fig. III.D.10. It consists of a LaVision® high-resolution camera, coupled with an Optem® magnifying lens. The lens is able to magnify as small areal elements as $1\,\mathrm{mm}^2$, which might reveal interesting for future prospects about monitoring oxidation transients. In this work, we use a "normal" zoom, corresponding to the extension of the annular channel. The camera system is fixed to a 2-D translation table, allowing for an accurate determination of the focal plane. A cover, adapted at the end of the lens, prevents from any undesirable reflections. The assembly is screwed onto an optical rail, attached to aluminium profiles, that are directly and only con-

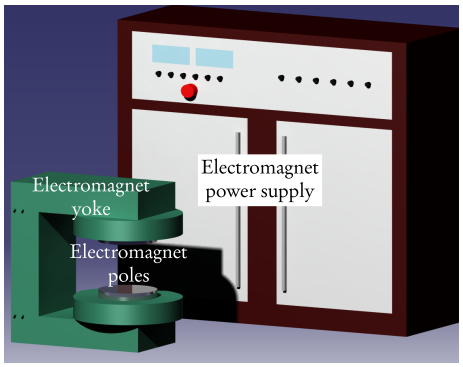

(a) – CAD view of the electromagnet yoke and power supply of Madip.

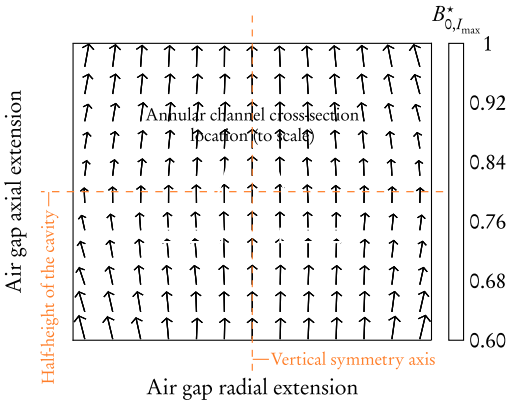

(b) – Electromagnet calibration in a cross-section between the poles. Arrows: orientation of $\vec{B}_0$, color scale: magnitude of $\vec{B}_0$ relative to its maximum value (reached at the pole), for the maximum DC current.

Figure III.D.9 – Working area ③: the electromagnet of Madip.

nected with the DC electromagnet. As such, any small vibrations of the machine are not likely to influence the imaging process (the camera following these vibrations). A Hamamatsu® light source, based on a mercury-xenon lamp, provides the necessary illumination through an optical fibre cable. Two polarisers are used to set the suitable contrast, and emphasise the difference of polarisation between pure Galinstan and oxide patches. Finally, it is important to point out another significant role played by the aluminium profiles, in link with the mounting or dismantling of the reactor. Indeed, it is physically impossible to work directly in the electromagnet gap, the available space being not sufficient enough to adapt the viscometer and then the reactor *in situ*. As a consequence, the assembly or disassembly is shifted onto these profiles, and then brought back between the electromagnet poles.

III.D.2.f Area ⑤: instrumentation

Finally, the instrumentation used in Madip constitutes the fifth working area. As shown in Fig. III.D.11, it consists of a vacuum pressure gauge, a mVmeter for displaying the O_2 partial pressure from the oximeter, the Piezomotor control box and power supply, the proximity sensor power supply, and a monitoring unit which collects all relevant physical data, *i.e.* the values of the angular speed, the outer magnetic field and the temperature inside the reactor. A camera control unit drives the camera frame-grabber, and two computers are used for monitoring and imaging. Note that the instrumentation is only used for monitoring purpose, and not for automatic processing: Madip is a "manual-control" experiment.

Now that the implementation of the Madip experiment has been described, let us turn to the experimental protocol that we shall follow in order to carry out measurement campaigns.

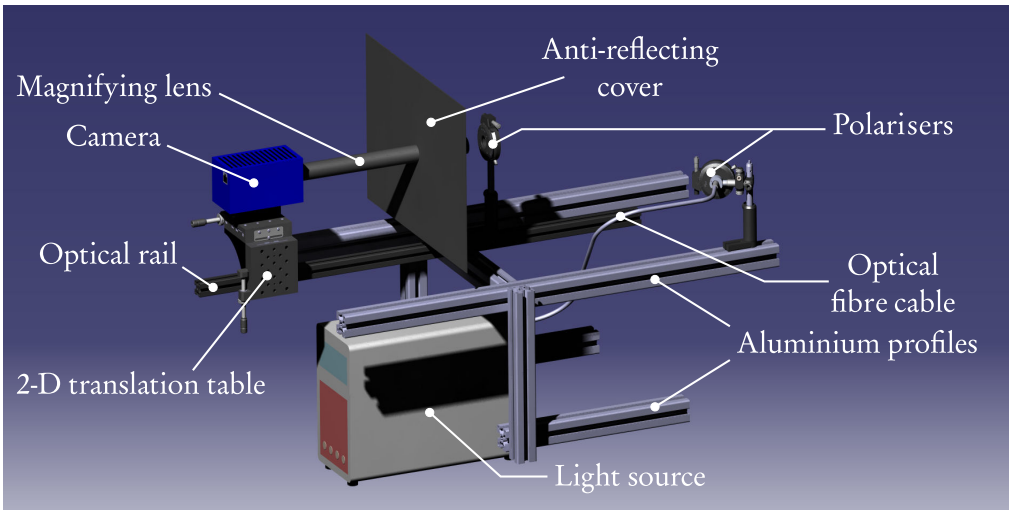

(a) – CAD view of the optical test-bench.

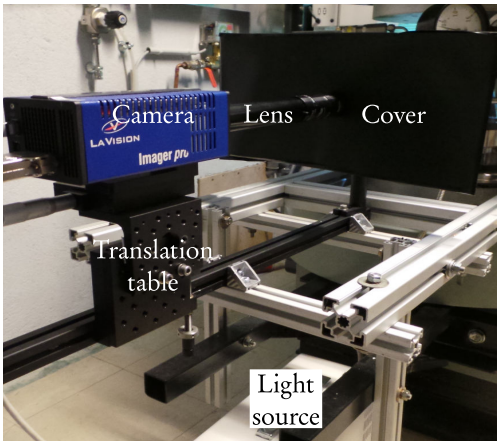

(b) – Photograph of the optical test-bench: before the cover.

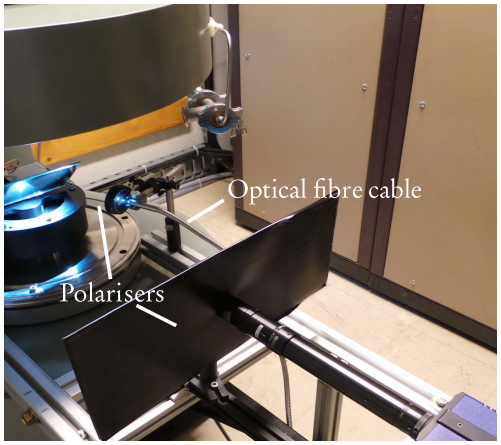

(c) – Photograph of the optical test-bench: behind the cover.

Figure III.D.10 – Working area ④: the optical test-bench of Madip.

III.D.3 Experimental protocol

III.D.3.a Preparing the alloy

In this section, the instructions for the preparation of the eutectic alloy Galinstan $Ga_{67\%}-In_{20.5\%}-Sn_{12.5\%}$ (weight fractions) in controlled conditions are described. First, the samples of gallium, indium and tin are mechanically abraded, and weighed on a 10^{-2} g precision balance. Then, each component is carefully cleaned by chemical means in ultrasonic bath with ethanol and placed into sealed plastic bags.

Ideally, Galinstan should be melted in very pure conditions, so that no oxidation process occurs. For this purpose, a glove-box filled with ultra-pure argon (O_2-rate < 0.5 ppm) is used. The different metallic samples are transferred into this glove-box (see Fig. III.D.12(a)). The working atmosphere is monitored with an oximeter similar

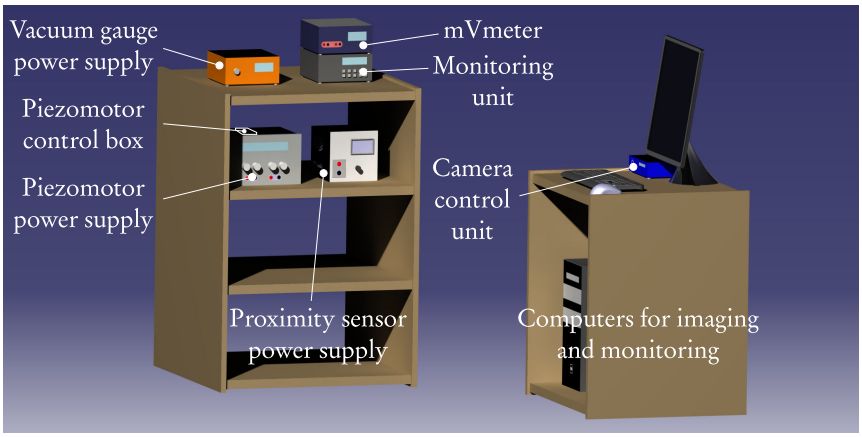

Figure III.D.11 – Working area ⑤: Cad view of the processing and monitoring instrumentation of Madip.

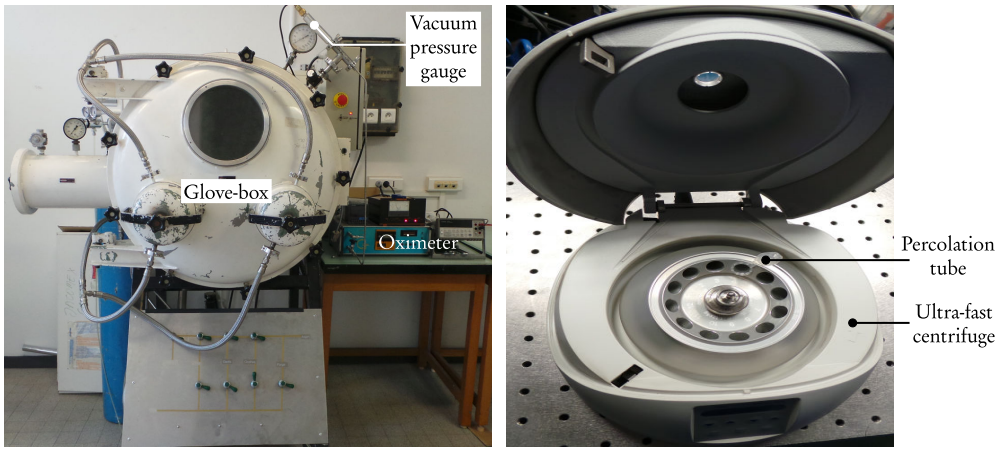

(a) – Glove-box used for preparing the alloy. **(b)** – Centrifuge used for preparing the tracers.

Figure III.D.12 – Glove-box and ultra-fast centrifuge used for preparing the alloy and the tracers.

to the one used in Madip. Once the adequate conditions are fulfilled, the different samples are melted on a hot-plate, the alloy being mechanically stirred with a glass stirrer during the melting. Once at room temperature, a two-stage filtration process is performed, across two stainless steel 50 μm and then 20 μm filters. When all the slag is removed, the free surface of Galinstan is mirror-like; the pure Galinstan is then poured into the bubbler, which is hermetically sealed. The bubbler and polluted materials are finally removed from the glove box, and transferred to the Madip experiment or to waste treatment, respectively.

III.D.3.b Preparing the tracers for PTV

As described above, we shall use tracers to get access to surface dynamics. Tracers made of polyethylene are chosen, because of their chemical neutrality with a variety of liquid metals, including Galinstan [49]. The average size of these spherical tracers

is about 200 μm. The cleaning procedure of these tracers is as follows: they are immersed into percolation tubes filled with ultra-pure ethanol solution, and placed into an ultra-fast centrifuge (rotation speed; 1.5×10^4 tr·min^{-1}, see Fig. III.D.12(b)). During centrifugation, ethanol percolates across the polyethylene spheres. These spheres are then introduced inside the viscometer, just before the chemical reactor is closed.

III.D.3.c Flushing out the gas circuit

The purpose of this step is to prepare the gas circuit for the experimental campaign. Our first objective is to work under very pure conditions inside the chemical reactor. To this end, vacuum/argon sweeping cycles are repeated. Vacuum pumping is first performed throughout the whole gas circuit, for O_2 desorption. When primary vacuum is reached ($p < 10^{-2}$ mbar), the pump is isolated, and the gas bottom line is open. Argon sweeping flushes the residual O_2 molecules out.

After several pumping/sweeping cycles, the O_2-rate inside the reactor is monitored by means of the oximeter. If the O_2-rate of the gas is lower than 10 ppm, the gas circuit is ready for the final purifying step. The reactor is isolated form the gas panel, and the tubular oven containing the O_2 scavenger is switched on. Note that the scavenger is not used prior to these repeated cycles, because it would get instantly oxidised (and so unusable) if the O_2-rate is originally too high. The bypass circuit is used to monitor the O_2-rate. Meanwhile, the atmosphere inside the reactor is pumped once again, until primary vacuum. Once the O_2-rate of the gas flowing through the oven is lower than 0.5 ppm, pumping is stopped, and the reactor is filled with ultra-pure argon. When it is in slight overpressure, the reactor is isolated. The O_2-rate of the gas inside the reactor is controlled with the oximeter, and if it is lower than 0.5 ppm, the reactor is ready for Galinstan introduction.

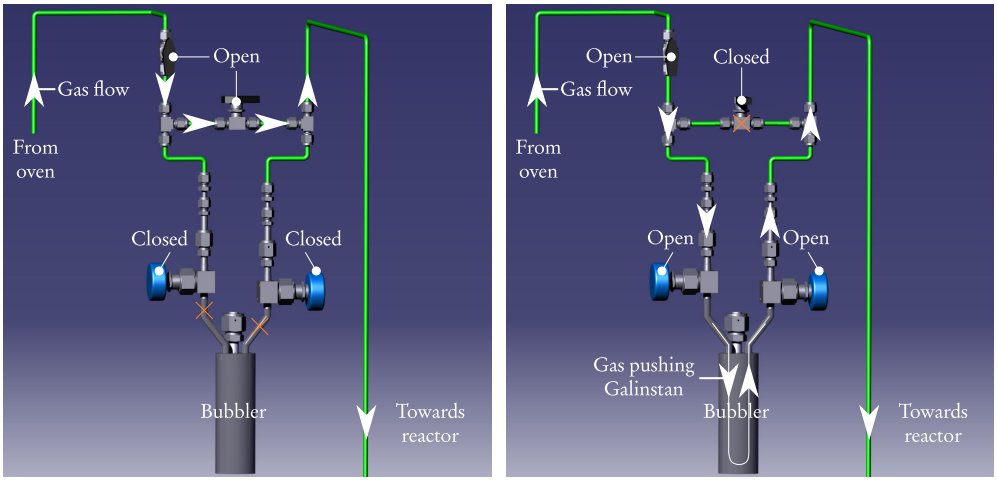

(a) – Cad view of the bubbler configuration for flushing the gas circuit out.

(b) – Cad view of the bubbler configuration transfer Galinstan inside the chemical reactor.

Figure III.D.13 – Bubbler system configurations for argon sweeping and transferring Galinstan.

During the previous step, the bubbler system is set as described in Fig. III.D.13(a), this configuration allowing for the repeated pumping/sweeping cycles. However, in order to introduce Galinstan inside the rotating dish, the configuration of the gates is changed as shown in Fig. III.D.13(b), so that the pressure drop between the upstream (coming from the oven) and the downstream (inside the reactor) ultra-pure argon is enough to push Galinstan towards the reactor. A visual control of the level of Galinstan allows for pouring the adequate volume of liquid metal inside the dish. Madip is now ready for the measurement campaigns.

III.D.3.d The principles of "live" measurement campaigns: chemical steps, imaging, and data acquisition

Each measurement campaign corresponds to a well-defined "chemical step". Indeed, the first measurement campaign is performed on the purest interface possible, corresponding to the lowest O_2-rate. Once the measurements performed for this initial step, the liquid metal surface is gradually oxidised by means of the $Ar + O_2$ mixtures flowing in the top gas line. The O_2-rate x of these mixtures is first controlled with the oximeter, using the bubbler bypass. The reactor is then filled with the $Ar + O_2$ mixture, at a given constant flow rate Q (measured with the flowmeter), during a known time interval Δt (measured with a chronometer). As such, we can relate each chemical step to a given quantity of oxygen injected inside the reactor.

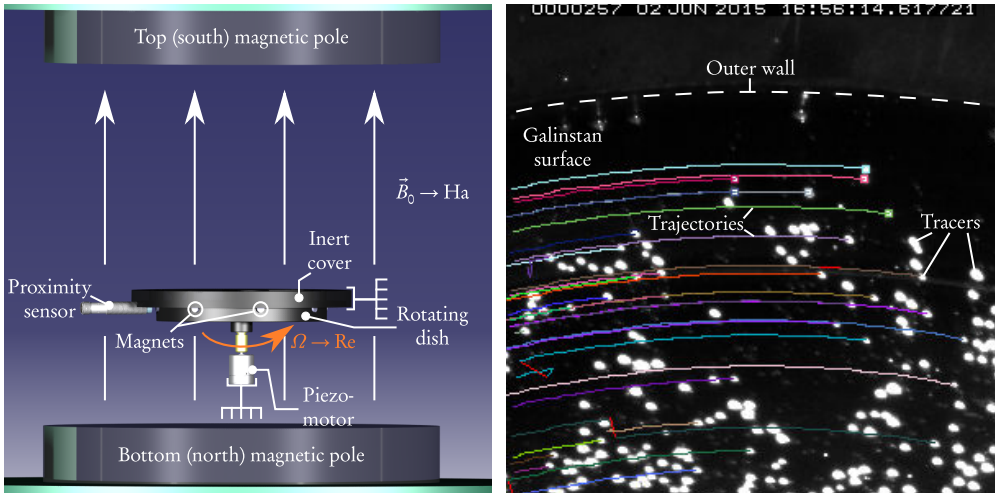

(a) – Cad view of the rotating dish and outer magnetic field in the electromagnet air gap.

(b) – Tracer trajectories as calculated by ImageJ.

Figure III.D.14 – Operating annular MHD viscometer and PTV technique.

For each chemical step, the measurement campaign remains the same. The governing parameters are the Re (through the rotating floor) and the Ha (through the electromagnet) numbers, as depicted in Fig. III.D.14(a). We choose to test different combinations in the following ranges for (Re, Ha) couples: $\mathrm{Re} \in [250, 5000]$, and $\mathrm{Ha} \in [0, 180]$. In link with the previous analytical and numerical investigations, these

values are likely to emphasise a variety of original MHD flow patterns, and to give access to the values of surface viscosities. For this purpose, for a given (Re, Ha) pair, the surface dynamics is imaged by means of the optical test-bench connected with the imaging computer. The resulting image sequence is post-treated by means of the ImageJ software (open-source), and especially the plug-in entitled "particle detector and tracker". As shown in Fig. III.D.14(b), this extension allows for the determination of tracers trajectories in Cartesian coordinates (for further details, the feature point detection and tracking algorithm at the root of the PTV technique are described in [87]). By means of a spatial calibration, these trajectories give access to the real velocities of the tracers at the liquid surface, which are expressed in the cylindrical system of coordinates. These Lagrangian profiles are then averaged and identified to the Eulerian velocity profiles of the supporting fluid, which reveals quite straightforward with an axisymmetric flow at steady state. The resulting radial and azimuthal surface velocity profiles are finally compared to those obtained with the modellings. Note that the large curvature radius of the glass containment allows us to neglect optical distortion (the so-called "barrel effect" being negligible).

Apart from imaging, there is a certain quantity of data to collect in order to trace back to the surface viscosities. Obviously, the angular speed of the rotating floor Ω and the outer magnetic field B_0 must be stored. It is also interesting to know the operating temperature T. The control voltage corresponding to each Ω, B_0, T value is monitored through a monitoring Fluke® unit, which collects the voltage measured respectively by the proximity sensor, the measurement cell on the electrical cabinet and the Pt 100 probe, and the data are exported to the monitoring PC. Finally, for each chemical step, the quantities x, Q and Δt are carefully stored. Each data set is then linked to the corresponding image sequence.

III.D.3.e Subsequent measurement: the height of liquid metal

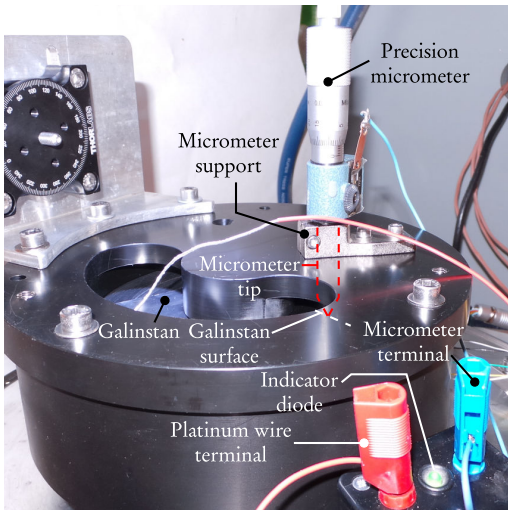

Figure III.D.15 – Measurement of the liquid metal height in the annular channel.

When the liquid surface of Galistan is totally oxidised, the "live" measurement campaigns are finished. However, one parameter remains to be determined in order to establish a comparison with the benchmarking modellings, *i.e.* the height h of liquid metal above the rotating dish.

Once the reactor is totally dismantled, a precision micrometer is adapted on the cover of the annular viscometer. As shown in Fig. III.D.15, this micrometer is connected at one of the terminals of a battery, equipped with an indicator diode. The other terminal is connected to a platinum wire, immersed into Galinstan. The micrometer is gradually lowered, and when the tip touches the liquid metal surface, the electric circuit is closed, and the diode lights on. The value indicated on the micrometer is then compared to a reference level (taken during the lubrication gaps adjustment, see Sec. III.D.2.b), which gives access to h, and concludes the measurement campaigns.

III.D.4 First experimental campaigns: qualitative/quantitative results

In the previous sections, the technical developments and the "ideal" protocol used to carry out the Madip experiment have been introduced. However, the "real" protocol (corresponding to the results exposed in this section) differs slightly from the original one. As the experimental test-bench has been designed and assembled from scratch, a long time was required to implement the different working areas described above, especially the different equipments constituting the gas circuit. Moreover, the preparation of Galinstan in very pure conditions (see Sec. III.D.3) also turned out to be a long process, particularly because of the glove-box adaptation, so that it can fit with our purity standards.

Along with classical experimental issues, these problems explain the fact that only a couple of qualitative and quantitative results can be unveiled in this section. On the one hand, we have performed a first campaign of measurements involving hydrochloric acid (HCl), in order to test a pure interface condition. On the other hand, once the gas circuit finally implemented, an intermediate state of oxidation has been reached inside the reactor. The first corresponding *in situ* measurements are investigated, with promising results and observations. Note that all the following results are obtained at room temperature $T = 25 \pm 1$ °C (as measured with the Pt 100 probe).

III.D.4.a HCl experiment: an attempt to reproduce a pure interface

As previously said, the gas circuit of Madip has been long to implement. Before its full operability, we have carried out the following benchmarking experiment. As described in Fig. III.D.16, a thin layer of highly concentrated HCl is used to prevent the liquid metal surface from any oxidation process (typical values for the different heights: $h = 9.86 \times 10^{-3}$ m, $h_{\mathrm{HCl}} = 2.64 \times 10^{-3}$ m). Note that the Galinstan used for the experiment is previously washed in a separate acid bath, which totally reduces the oxide skin. The experimental protocol remains globally the same (except for the parts concerning the gas circuit): the dish is rotated at different velocities, and the outer magnetic field is varied. The density of the tracers used is set so that they deposit upon

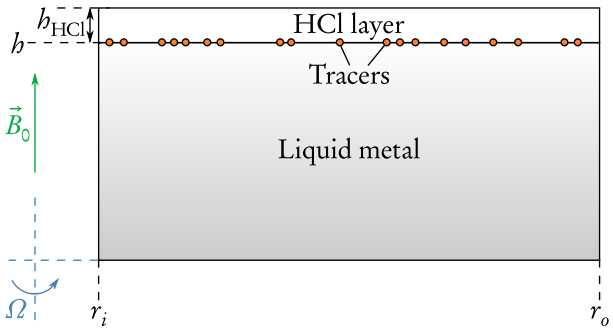

Figure III.D.16 – Experimental layout with the HCl layer.

the liquid metal surface, enabling direct imaging of the liquid metal surface dynamics. The radial and azimuthal surface velocity profiles, recovered after post-treatment with the PTV module, are then compared to the modelling predictions. Finally, the layer of acid is removed, and the liquid metal surface is totally oxidised. Some important qualitative remarks are then made with respect to the latter asymptotic case, corresponding to an interface totally covered with oxides.

Experimental issues

It is first important to point out that, contrary to the case of a liquid metal/gas interface, the frictions due to the acid layer cannot strictly be ignored. Indeed, the dynamic viscosity of the HCl solution used ($c = 2.33\,\text{mol}\cdot\text{L}^{-1}$) is $\eta_{\text{HCl}} = 1.14\eta_{\text{wat}}$ [88]. However, in the asymptotic case of a very pure interface due to an in-excess HCl layer, we make the assumption that these frictions do not impact the interface BC, which reduces to $\partial v_r/\partial z = 0$ along $\vec{e}_r$ and $\partial v_\theta/\partial z = 0$ along $\vec{e}_\theta$ (see Eqs. (III.C.14) and (III.C.15)). As such, the shear stress in the HCl layer is assumed to be vanishingly small, which requires that the HCl/gas interface is totally free from surfactants.

Another interesting point deals with the relevancy of using the HCl layer as a mean of exploring various oxidation regimes of the interface. Indeed, by means of different Red-Ox equilibria, it could be possible to describe different chemical steps, rather than using the gas circuit. However, in this study, we did not favour this option. In fact, we only use highly concentrated HCl to describe the asymptotic case of a pure interface, for the following reasons:

- it would cause a considerable complication of the modelling (such as modelling the mass transport in the acid layer, for instance, or managing the stoichiometric equilibrium of the Red-ox reaction),
- HCl evaporation makes the determination of the stoichiometry difficult, and raises some safety issues,
- the approach based on the use of a gas circuit is designed for a very accurate control of the quantity of O2 injected, and should theoretically allow for a good reproducibility,
- to fit with practical conditions met in the industry, where the acid layer is never present at the interface between the liquid metal and the gaseous phase.

Finally, before any comment about the experimental results, let us briefly discuss about the sources of experimental errors. They principally concern the estimation of the radial positions and of the surface velocities. Concerning the radial positions (horizontal error bars), the initial calibration step is accurate to within 100 μm. The particle tracking algorithm is accurate to within 0.5 px [87]. With respect to surface velocities (vertical error bars), given the focus and the time step of the camera, the measurement of surface velocities are accurate to within 0.5 mm·s^{-1}. Consequently, the higher the Reynolds number is, the more the velocity measurements are accurate. One solution to reduce the error bars is to increase the lens focus, in order to zoom on an area of interest, so that very slow motion can be accurately measured. However, this would considerably complicate the imaging process, because we would no longer have access to the whole extent of the annular channel. Because the aim of the following campaign of measurements is to give a first glance at the technical feasibility of Madip, we leave subsequent developments about the relevant optical settings for future prospects. In this work, due to lack of time, the focus is then only set such as the radial extent of the annular channel is captured.

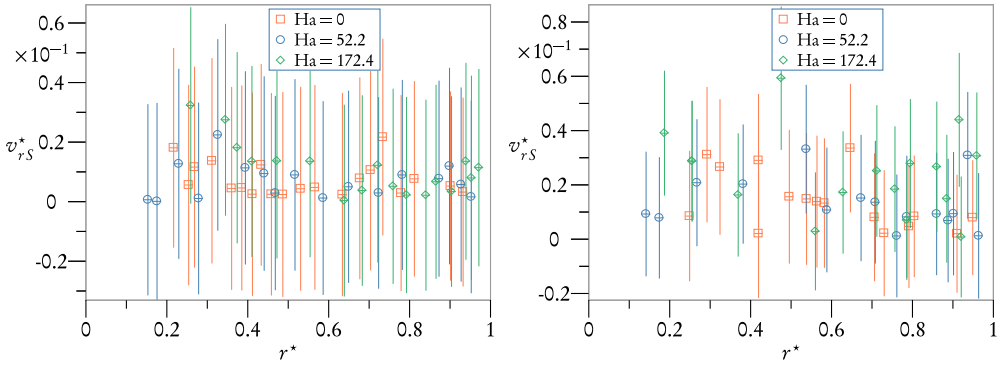

(a) – $v^\star_{rS}$ data points for Re = 2659. **(b)** – $v^\star_{rS}$ data points for Re = 4109.

Figure III.D.17 – Experimental $v^\star_{rS}$ data points and associated errors, with respect to various (Re, Ha).

The analysis of radial velocity profiles illustrates this experimental limitation. As previously explained, the piezomotor used to rotate the dish containing galinstan cannot reach Re values much higher than Re = 5000. As shown in Fig. III.D.17, such a limitation proves to be quite dramatic for radial velocity measurements, whatever the (Re, Ha) values tested. The experimental error is indeed of the order of magnitude of the measured velocities. Even in this case corresponding to a pure interface, for which the surface velocities are expected to reach their maximum values, $v^\star_{rS}$ cannot be accurately measured. We can deduce from these graphs that the determination of surface dilatational viscosity (brought into play by the radial component of the JMB) requires a modification of the imaging process. In this work, we choose to keep on with the same optical configuration, and to focus on the azimuthal velocity profiles.

Azimuthal velocity profiles

As shown in Fig. III.D.18, the order of magnitude of the surface azimuthal velocity $v^\star_{\theta S}$ is sufficiently large to circumvent the previous accuracy issues. Except near the inner wall, where a lack of tracers can be noticed, we are able to access the values of $v^\star_{\theta S}$ all along the interface. The experimental data are compared with the 2-D 1/2 numerical predictions of Sec. III.C, in the case of a pure interface, *i.e.* for $\mathrm{Bo}_{\eta_S} = 0$.

There is undoubtedly a noticeable discrepancy between the predicted and experimental values. This difference could be accounted for by the dynamic interaction between the HCl layer and galinstan, that we have assumed to be negligible. Another possibility is that the tracers do not exactly follow the liquid metal/HCl dynamics. However, despite these quantitative differences, let us focus on the qualitative aspects. The selected (Re, Ha) pairs allow for investigating the cases $N \gg 1$ (negligible inertial effects), $N \sim 1$ and $N \ll 1$ (negligible electromagnetic effects). For $\mathrm{Re} = 2159$ and $\mathrm{Re} = 4109$, both predictions and experimental measurements show that for $\mathrm{Ha} = 0$ ($N = 0$: curves (□)), the decay of $v^\star_{\theta S}$ is much faster than in the cases $\mathrm{Ha} = 52.2$ and $\mathrm{Ha} = 172.4$ (curves (○): $N \sim 1$, and (◇): $N \gg 1$), where almost linear profiles are observed. These significant observations testify first from the electromagnetic blocking of the flow when increasing Ha, while the advection of $v^\star_{\theta S}$ is guessed for $\mathrm{Ha} = 0$ (obviously, the inflection points are quantitatively different). Furthermore, the blocking seems globally more efficient at higher Ha numbers, when comparing (○) and (◇) for both $\mathrm{Re} = 2159$ and $\mathrm{Re} = 4109$. This interpretation is in agreement with one significant physical feature emphasised in Sec. III.B, *i.e.* the tendency towards two-dimensionality with increasing Ha.

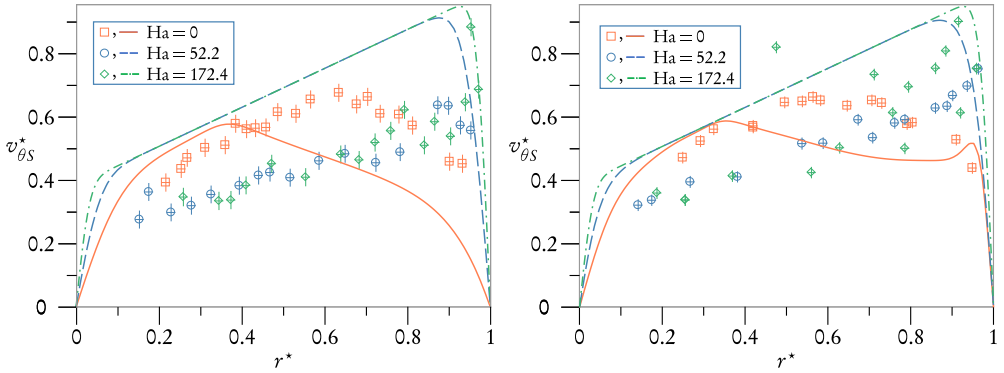

(a) – $v^\star_{\theta S}$ ($\mathrm{Re} = 2659$). Lines: 2-D 1/2 numerical results ($\mathrm{Bo}_{\eta_S} = 0$), symbols: exp. data.

(b) – $v^\star_{\theta S}$ ($\mathrm{Re} = 4109$). Lines: 2-D 1/2 numerical results ($\mathrm{Bo}_{\eta_S} = 0$), symbols: exp. data.

Figure III.D.18 – $v^\star_{\theta S}$ profiles: experimental data and numerical predictions, for various (Re, Ha).

The case of a totally oxidised interface

In order to precise the qualitative observations given above, after the measurements involving the HCl layer, the latter is removed, and the liquid metal surface is exposed to ambient air. After a while, the metal surface appears totally oxidised. Then

the angular speed and the outer magnetic field are varied. The reason why no graphs are produced in this section is simple: whatever the (Re, Ha) values, the oxide skin remains inert. The velocity of the tracers at the interface is indeed zero; but the dish containing Galinstan is actually rotating, as indicated by the proximity sensor.

Although the latter observation does not provide any quantitative information, it is qualitatively extremely important. If both radial and azimuthal surface velocities are vanishingly small, irrespective of the (Re, Ha) values, we can reasonably suppose (thanks to the analytical and numerical calculations) that at least the surface viscous shear is high enough to damp any surface flow. Moreover, even if the surface remains motionless, some salient features can be deduced when increasing Ha. Indeed, for a given Re, a sub-surface flow motion can be guessed from small "ripples" deflection occurring beneath the oxide membrane. This deflection are phenomenologically comparable with the observations of Zhang *et al.*, previously highlighted in Fig. I.B.6. In their study, these authors have observed an intense swirling motion of Galinstan *beneath* the closed oxide layer *at rest* [5] (for a completely different experimental layout, though). Consequently, it really seems like the outer magnetic field tends to align the sub-phase dynamics on the rotating floor, which confirms the occurrence of the electromagnetic blocking.

We can be even more precise: if the surface remains motionless despite the electromagnetic blocking of the sub-phase, this means that the surface shear Boussinesq number of a totally oxidised Galinstan surface is at least equal to the maximum Ha value, according to Eq. (III.B.32):

$$\mathrm{Bo}_{\eta_{S,\mathrm{full\_ox}}} > \mathrm{Ha}_{\mathrm{max}} = 172.4,$$

so that

$$\eta_{S,\mathrm{full\_ox}} > 3.6 \times 10^{-3}\,\mathrm{kg{\cdot}s^{-1}}. \tag{III.D.2}$$

To our knowledge, this is the first time that such an estimation of the surface viscous shear of an oxidised liquid metal/gas interface is given. It also confirms our initial assumption about the ability of liquid metal surfaces to have a wide range of possible values for Bo_{η_S}.

To conclude with the HCl experiment, let us remind that a qualitative agreement between the predictions and the experimental measurements has been found, though only for the azimuthal velocity. Some significant physical phenomena like the electromagnetic blocking or the capacity of the interface to evolve from a slip to a no-slip boundary condition. However, only asymptotic cases have been investigated so far, with a significant quantitative discrepancy between the model and the experiment. In order to describe intermediate oxidation states, and ultimately get access to the values of Bo_{η_S} (and potentially $\mathrm{Bo}_{\varkappa_S}$) for a gradually oxidising interface, let us turn to the next measurement campaign, involving the whole experimental set-up.

III.D.4.b Reactor experiment: partial oxidation

Experimental issues

As previously enhanced, the implementation of the gas circuit aims at purifying and monitoring the working atmosphere, and at introducing Galinstan in ultra-pure conditions. The ultimate objective is to perform different chemical steps, so that the gradual oxidation of the liquid metal surface can be related to a quantity of O_2 injected inside the reactor.

For various reasons, only partial results can be presented here. First, the implementation of the gas circuit has been achieved with a significant delay. In addition to the long process of alloy preparation, due to lack of time, we had only the opportunity to carry out two experimental campaigns. This restriction is linked to the reduced bubbler capacity (roughly 150 mL of Galinstan). Unfortunately, the first experimental campaign came to a sudden end. The purification process perfectly worked, as well as the introduction of Galinstan in controlled conditions: the liquid surface was mirror-like; but at the very beginning of measurements, the clamping mandrel came loose, and the rotating dish decoupled from the motor shaft.

The second experimental campaign revealed more fruitful, and the corresponding results are presented hereafter (height of liquid metal: $h = 6.5 \times 10^{-3}$ m). However, during this campaign, we faced an unexpected issue: the Galinstan surface was this time already partially oxidised, despite all the precautions taken during the transfer. We suspect a long-term sealing problem with the bubbler: the first campaign previously mentioned, where the purification step was successful, was actually carried out just after the alloy preparation. The second campaign occurred one month later, leaving perhaps enough time for Galinstan oxidation inside the bubbler. As it is shown in Fig. III.D.19, all the inner part of the liquid metal surface exhibit oxide patches, which saturates the camera sensor. Such a radially inwards packing along the liquid surface could originate from centrifugation, which would lead to the emergence of a circular Reynolds ridge, similarly to [71]. Anyway, this unexpected oxidation has two main consequences:

- as the surface is already oxidised, it is not worthwhile to monitor the O_2-rate inside the reactor. It is actually impossible to relate the initial oxidation state of the interface to a well-defined O_2 flux. Consequently, we shall only work in ultra-pure gas conditions inside the reactor, to prevent from further oxidation of the Galinstan surface;
- this surface oxidation corresponds to an intermediate oxidation state, because when the dish is rotated, a surface motion can be observed. If the oxidation was total, as highlighted in the previous section, the velocity at the oxidised surface would be vanishingly small. As it is not the case here, we are able to measure surface velocity profiles all along the interface. We can use the oxide patches as tracers for the outer half, the saturation of the CCD sensor being limited in this area. However, the saturation occurring in the inner half of the channel prevents us from imaging correctly the tracers dynamics, and thus from drawing the velocity profiles in this inner area.

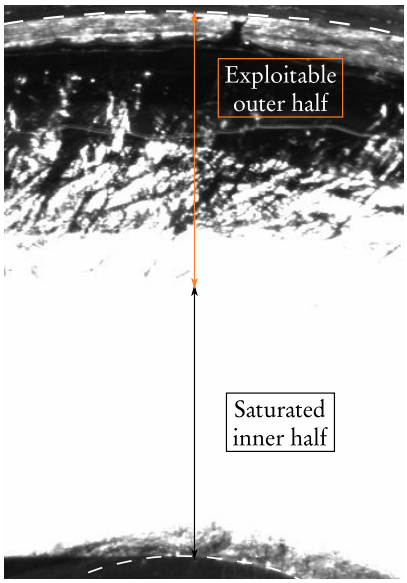

Figure III.D.19 – Picture of the partially oxidised liquid metal surface.

Nevertheless, despite these two limitations, some salient features can still be deduced from these partial measurements. We shall prove that it is possible to give an estimation of the surface viscous shear corresponding to this intermediate state of oxidation, by focusing on the $v^{\star}_{\theta S}$ profiles (the radial velocity profiles being left aside from the analysis, for the same reasons as those exposed in Sec. III.D.4.a).

Azimuthal velocity profiles: the first estimation of Bo_{η_S}

In this section, we aim at giving a first order of magnitude of the surface viscous shear through Bo_{η_S}. Consequently, we choose to focus on the working conditions favouring the identification of the surface viscous shear, *i.e.* when $\mathrm{Ha}^2 \gg \mathrm{Re}$, corresponding to the theoretical approach of Sec. III.B.1. Despite these precautions, at small Re values, for instance $\mathrm{Re} = 245$, the azimuthal velocity profiles suffer from the same lack of accuracy as the radial profiles.

Let us make now an assessment on the basis of our initial objectives. We remind that the ultimate aim of the Madip experiment is to determine the surface shear and dilatational viscosities, with respect to a given oxidation rate of the liquid metal/gas interface. In the light of the aforementioned restrictions, we will not be able to address neither the surface dilatation nor the O_2-rate dependence issues. The first results in view of accessing the surface viscous shear are not exploitable at low Re. However, for higher Re values, for instance $\mathrm{Re} = 1351$ and $\mathrm{Re} = 4494$, the order of magnitude of the surface azimuthal velocity seems sufficiently large to avoid this accuracy issue. Let us see now if we can deduce at least some hints at the values of the surface viscous shear, corresponding to this particular (though unknown) oxidation state.

Our approach consists in focusing on the following (Re, Ha) pairs: $\mathrm{Re} = 1351$ and $\mathrm{Ha} = \{52.2, 104.4, 172.4\}$; or $\mathrm{Re} = 4494$ and $\mathrm{Ha} = \{104.4, 172.4\}$. We fit the N

experimental data points with the predicted profiles (for the same (Re, Ha) values), obtained from the analytical modelling exposed in Sec. III.B. By means of the last mean square method, we are then able to trace back to the (fitting) value of Bo_{η_S}. The different values obtained with respect to the corresponding (Re, Ha) pairs, along with the mean absolute error ϵ:

$$\epsilon = \sum_{n=1}^{N} \left| \frac{v^\star_{\theta S,\mathrm{model}}\left(r^\star = r^\star_n, \mathrm{Bo}_{\eta_{S,\mathrm{fit}}}\right) - v^\star_{\theta S,\mathrm{exp}}\left(r^\star = r^\star_n\right)}{N} \right|,$$

and the corresponding η_S values are displayed in Tab. III.D.2. The resulting graphs for $\mathrm{Re} = 1351$ and $\mathrm{Re} = 4494$ are displayed in Figs. III.D.20 and III.D.21, respectively.

(Re, Ha)	Bo_{η_S}	η_S [kg·s^{-1}]	ϵ [%]
(1351, 52.2)	0.2	2.8×10^{-6}	1.7
(1351, 104.4)	1.0	1.4×10^{-5}	1.5
(1351, 172.4)	1.8	2.5×10^{-5}	1.4
(4494, 104.4)	1.4	1.9×10^{-5}	1.5
(4494, 172.4)	0.7	9.7×10^{-6}	3.6
Average values			
	1.0	1.4×10^{-5}	1.9

Table III.D.2 – Fitting values of Bo_{η_S} with respect to different (Re, Ha) pairs, in the case of a partially oxidised liquid metal surface.

Obviously, the lack of experimental data in the inner part is detrimental to our analysis. Nevertheless, the agreement between the theoretical predictions and experimental measurements seems both qualitatively and quantitatively satisfying. First, for $\mathrm{Re} = 1351$, the values predicted for Bo_{η_S} vary between 0.2 and 1.8. Ideally, the predicted value should remain the same, whatever the Ha value. However, given the wide range of possible values for Bo_{η_S} previously highlighted (virtually from 0 to at least 200), and given the accuracy of the velocity measurements, these variations remain quite satisfyingly restricted. Besides, in Fig. III.D.21(c), the experimental measurements confirm the modelling predictions, in the fact that the $v^\star_{\theta S}$ profiles are almost the same, irrespective of the Ha value. This clearly shows that for the selected (Re, Ha) pairs, the surface flow is already perfectly aligned with the sub-phase flow, explaining the identical linear profiles.

For higher Reynolds, for instance $\mathrm{Re} = 4494$, the latter point differs somewhat. Indeed, in Fig. III.D.21(c), both experimental data and associated analytical fittings show a slight difference between $v^\star_{\theta S}$ profiles for $\mathrm{Ha} = 104.4$ and $\mathrm{Ha} = 172.4$. Contrary to the case where $\mathrm{Re} = 1351$, here the alignment of the interface dynamics with respect

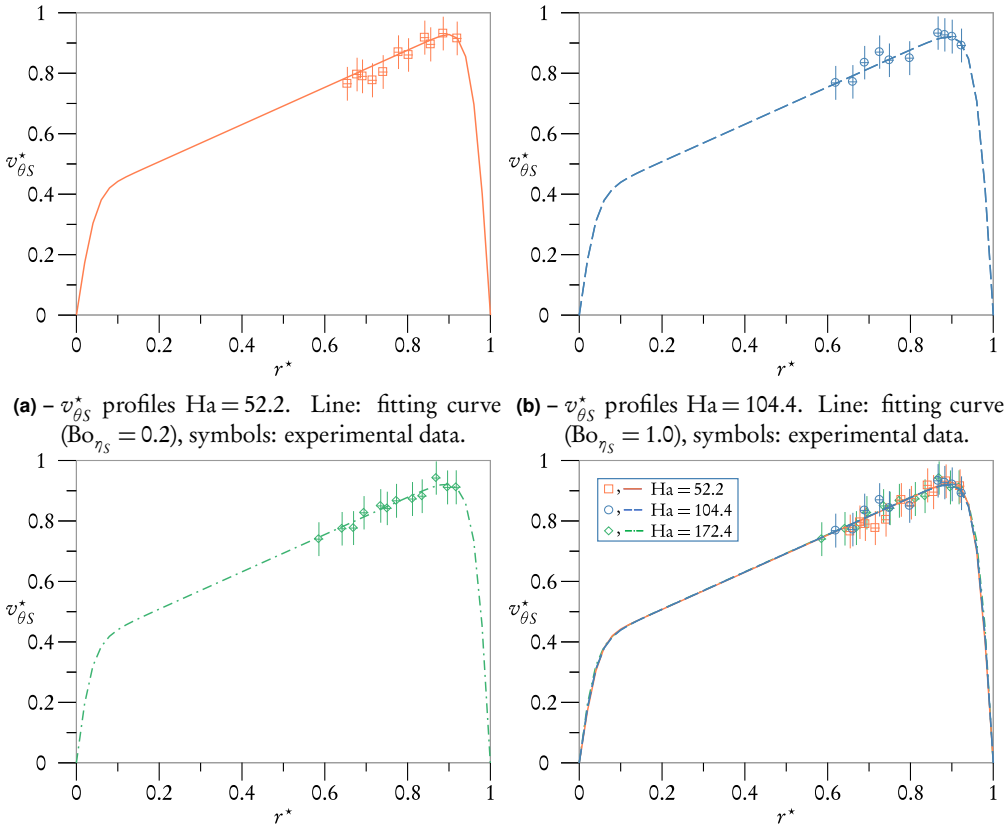

(a) – $v^\star_{\theta S}$ profiles Ha = 52.2. Line: fitting curve ($\mathrm{Bo}_{\eta_S} = 0.2$), symbols: experimental data.

(b) – $v^\star_{\theta S}$ profiles Ha = 104.4. Line: fitting curve ($\mathrm{Bo}_{\eta_S} = 1.0$), symbols: experimental data.

(c) – $v^\star_{\theta S}$ profiles Ha = 172.4. Line: fitting curve ($\mathrm{Bo}_{\eta_S} = 1.8$), symbols: experimental data.

(d) – $v^\star_{\theta S}$ profiles for the different Ha values. Lines: fitting curves, symbols: experimental data.

Figure III.D.20 – Experimental $v^\star_{\theta S}$ profiles and associated curve fittings, for Re = 1351 and various Ha.

to the bulk dynamics improves with increasing Ha. The reason is certainly that, even if we select (Re, Ha) pairs such as the criterion given in Eq. (III.C.19) is fulfilled, the higher the ratio $\mathrm{Ha}^2/\mathrm{Re}$ is, the more the diffusion of momentum from the rotating floor is eased. Consequently, for the same Ha value, the interface is more rapidly blocked when Re = 1351. Now, concerning the Bo_{η_S} values, they vary between 0.7 and 1.4. These values are comparable with those found for Re = 1351. These relative independence with respect to Re and Ha makes us confident about the following statement; the surface viscous shear of the oxidised Galinstan/gas interface can be estimated as:

$$\eta_{S,\mathrm{partial\_ox}} \sim 1.4 \times 10^{-5}\,\mathrm{kg{\cdot}s^{-1}}. \tag{III.D.3}$$

To our knowledge, this is the first time that such a value of the surface shear viscosity of a partially oxidised liquid metal/gas interface is given.

As a conclusion of this experimental part, we remind that the first measurement campaigns have shown very promising features. The HCl experiment, corresponding to the asymptotic case of a very pure interface, and the reactor campaign, corresponding to a partially oxidised interface, have highlighted some salient phenomena, both

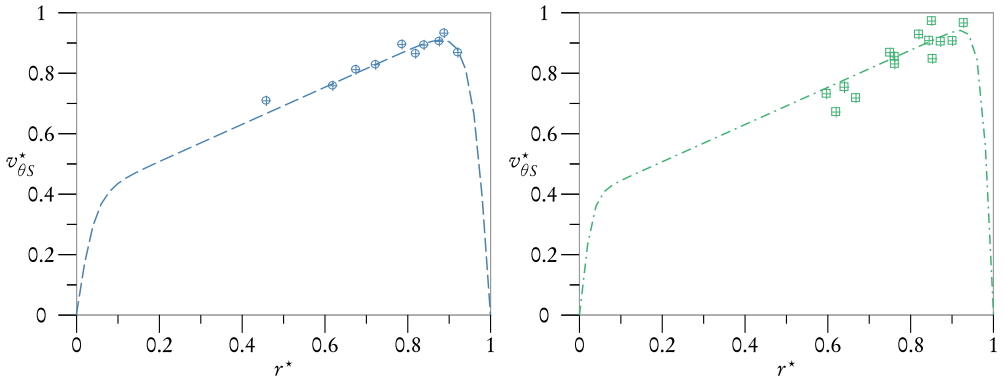

(a) – $v^\star_{\theta S}$ profiles Ha = 104.4. Line: fitting curve ($\mathrm{Bo}_{\eta_S} = 1.4$), symbols: experimental data.

(b) – $v^\star_{\theta S}$ profiles Ha = 172.4. Line: fitting curve ($\mathrm{Bo}_{\eta_S} = 0.7$), symbols: experimental data.

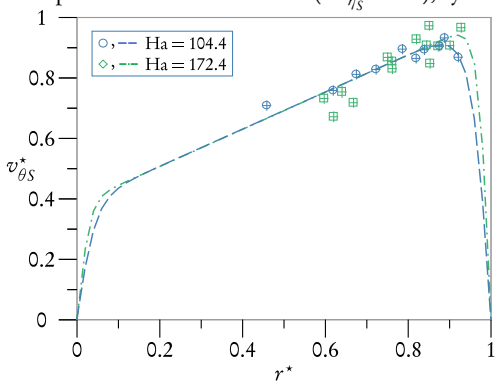

(c) – $v^\star_{\theta S}$ profiles for the different Ha values. Lines: fitting curves, symbols: experimental data.

Figure III.D.21 – Experimental $v^\star_{\theta S}$ profiles and associated curve fittings, for Re = 4494 and various Ha.

from qualitative and quantitative point of views. Of course, the measurements for Bo_{η_S} must be completed, the optical bench must be modified to estimate $\mathrm{Bo}_{\varkappa_S}$, and different chemical steps must be performed. But at least, despite these limitations, the experimental feasibility and relevancy of the annular MHD viscometer has been demonstrated, allowing us for giving first estimations of the surface viscous shear of a liquid metal surface, which constitutes totally original data.

Conclusion

Summary and outlook

The main concern of this thesis work has been to determine whether the alteration of a liquid metal/gas interface, due to oxidation processes, may significantly affect a supporting permanent MHD flow, or not. In the light of the major achievements previously highlighted, a positive answer can be given to this fundamental question. The original coupling between MHD and the surface rheology of a liquid metal/gas interface has been investigated through a variety of theoretical, numerical and experimental developments, particularly within the framework of the annular MHD viscometer. The most salient features of this threefold approach are now summarised.

In the general introduction of this thesis work (see Part I), the fundamental and industrial concerns about the modelling of MHD multiphase flows have been highlighted. Particularly, the need for an accurate description of the influence of interfacial properties on bulk MHD has allowed us to draw a common thread, valid for both stratified and dispersed topologies. It has been shown that the progressive contamination of the liquid/gas interface results in a varying mechanical interfacial behaviour. Besides, it has been highlighted that the coupling between this mechanically changing surface condition and a supporting MHD core-flow constitutes an original boundary-value problem, the fundamental MHD issue of varying boundary conditions being classically only considered from an electrical point of view. In order to magnify this atypical coupling, it has been suggested to investigate the surface rheology of such electroconductive fluids as liquid metals, undergoing gradual oxidation processes, and flowing under the influence of an outer magnetic field. By the way, Galinstan has been selected as the model system in order to magnify this coupling, because of its promising MHD, physicochemical and surface properties.

As such, this thesis work aims at bridging the gap between MHD and surface rheology, two physical fields usually distinct. This is the reason why the theoretical foundations pertaining to each field have been first separately introduced in Part II. Concerning single-phase MHD, the focus has been put on the different formulations of the coupling between electromagnetism and fluid mechanics, and a distinction has been made between the $(\vec{v},\vec{b})$ approach based on the magnetic induction equation, and the $(\vec{v},\vec{A},\phi)$ potential formulation. With respect to surface rheology, the concept of in-excess surface quantities has been particularly emphasised, leading to the introduction of surface shear and surface dilatational viscosities. The overall coupling between bulk MHD and surface dynamics has then been set up, by considering the latter as a particular boundary condition for the supporting MHD flow.

In Part III, which constitutes the main part of this thesis work, the choice has been made to focus on a particular physical layout: the annular MHD viscometer.

The associated physical features have been first introduced in Chap. III.A. It has been shown that depending on the Reynolds number value, the purely hydrodynamic bulk flow already exhibited promising features, switching from 2-D to 2-D 1/2 topology by simply tuning on the value of the angular velocity, changing thus the rotating floor condition. A brief state-of-the-art of existing achievements, involving the coupling between the hydrodynamic annular flow and the surface rheology of fluid/fluid interfaces gradually covered by surfactants, has been drawn. It has highlighted the feasibility of characterising experimentally the surface viscosities by means of the annular viscometer. Eventually, it has been shown how the addition of the outer magnetic field could arouse original stratified MHD flow patterns, particularly through the electrical (in)activation of the Hartmann layers, depending on the interfacial oxidation rate.

In Chap. III.B.1.a, the coupling mechanism between surface rheology and the supporting annular MHD bulk flow has been investigated, within the approximation of a strong outer DC magnetic field. Using a matched asymptotic expansion based on the small parameter 1/Ha, the surface velocity has been expressed as a coupling variable between the 2-D MHD flow, described by a $(\vec{v}, \vec{b})$ formulation, and the jump momentum balance, which only brings surface shear into play. The competitive effects of these phenomena have been highlighted through a new modified Boussinesq number $\tilde{\mathrm{Bo}}_{\eta_S}$, representing the balance between surface viscous shearing and the Lorentz force. It has been shown that surface rheology monitored the generation of the Hartmann layers, and therefore the activation of the electric circuit, dramatically affecting the velocity field in the MHD core. These original MHD flow patterns have been consistently found in a supporting 2-D numerical study. The MHD tendency towards two-dimensionality has also been emphasised, enabling selective measurements of surface viscous shear by extinguishing recirculating flow patterns due to centrifugation.

The latter inertial effects have been investigated in Chap. III.C. Magnifying centrifugal effects by increasing the angular velocity of the rotating floor generates an overturning flow, which has been proved to generate surface shear as well as surface dilatation. Depending on the relative values of the Reynolds, Hartmann and Boussinesq numbers, atypical MHD flow patterns arise. In particular, it has been stressed that surface dilatational viscosity does not generate the same changes as its shearing counterpart. Dilatational viscosity is indeed only responsible for damping the meridian flow driven by centrifugation, with the emergence of an original counter-rotating pattern if inertia and electromagnetic blocking are both significant. Unlike surface shear, surface dilatation is not found to play a significant role concerning the electrical activation of the Hartmann layers, whose impact on the core flow is consequently less dramatic. This 2-D 1/2 numerical investigation has also allowed us to complete the determination of distinct experimental conditions, for characterising the surface rheology of a gradually oxidising liquid metal surface.

These scaling laws have been used in the final chapter III.D, to design the Madip experiment. The different working areas of Madip have been detailed. The focus has particularly been put on the design of the gas circuit, in order to transfer Galinstan in the annular channel and monitor its oxidation in controlled conditions. Preliminary experimental campaigns have been performed, involving the use of a HCl layer

to mimic the behaviour of a clean interface. Despite quantitative discrepancies with the theoretical and numerical predictions, a qualitative agreement has been found for azimuthal surface velocity profiles, highlighting such fundamental phenomena as the electromagnetic blocking occurring at high Ha, or a significant advection at high Re. When removing the HCl layer, a motionless surface has been observed, with subsurface flow motion, endorsing our initial guess about the possibility of an oxidised surface to reach high surface shear values. Finally, an experimental campaign using the full gas circuit, including the chemical reactor and the ultra-pure gas circuit, has been carried out. Unfortunately, the Galinstan sample was partially oxidised from the beginning. Nevertheless, the opportunity was given to characterise this intermediate state of oxidation. Due to experimental limitations, the radial velocity profiles have not been investigated. However, concerning the exploitable azimuthal velocity profiles, a qualitative and quantitative agreement has been found with respect to the theoretical predictions, when considering the higher Ha cases. These partial results have allowed us to give (for the first time) an estimation of the surface shear viscosity of a partially oxidised liquid metal/gas interface.

As far as future prospects are concerned, several areas of improvement can be proposed. In the short-term, the Madip experiment should be slightly adapted to carry out new experimental campaigns. First, concerning oxidation issues, the bubbler should be tested, and replaced if a sealing problem is detected. An additional purification stage, involving a "buffer" HCl solution, could be included in series at the bubbler outlet, so that Galinstan is initially cleaned from any oxide patches at its surface. Then, the different "chemical steps" could be performed, and the selective measurement of surface shear at high Ha could be related to a given O2-rate of the surrounding atmosphere. Furthermore, if the optical resolution issue is addressed, so that the radial velocity profiles become measurable, it could be possible to trace back to the value of surface dilatation. Thus, the focus should be first put on experimental issues, so that Madip can supply reliable and reproducible experimental data about the surface viscosities of Galinstan.

In the mid-term, it could be possible to improve the modelling of surface dynamics at a gradually oxidising interface, by questioning some of the initial assumptions made in this thesis work. Particularly, still considering an interface whose shape is known, gradients of surface properties could be taken into account in the description of the tangential jump momentum balance, including surface tension gradients (Marangoni effect) and gradients of surface viscosities. These surface gradients could be added in the modelling of the annular MHD viscometer, to go beyond the "leading-order" analysis, and get more accurate measurements of surface viscosities. The relevance of the Newtonian approach for describing the surface dynamics of Galinstan could also be questioned. If the oxide skin behaviour tends to impart the metal with non-Newtonian rheological properties, another approach based on nonlinear viscous models or Bingham plastic models described in [20] could be investigated.

The experimental data could be then used to feed other MHD problems involving liquid metal/gas interface. The annular channel viscometer is indeed a typical MHD stratified flow. In order to address the issues linked to MHD multiphase flows from

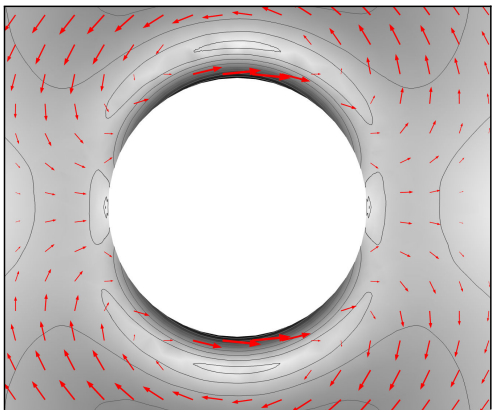

(a) – Current patterns for bubble MHD [89].

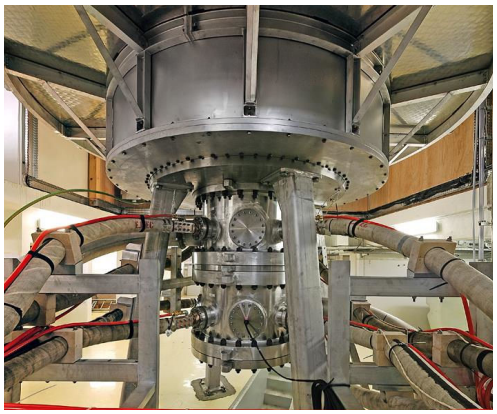

(b) – LnCMI hybrid magnet (45 T targeted) [90].

Figure Concl. 1 – Future prospects.

both ends, a typical MHD dispersed flow could be investigated. A background step towards the description of MHD bubbly flows could be the asymptotic study case of a single spherical gas bubble immersed in Galinstan with a gradually oxidising liquid/gas interface. To this end, a substantial preparatory work is introduced in App. D, unveiling some physical features of the "bubble MHD problem" (Fig. Concl. 1(a)).

One long-term outlook concerns the modelling of "surface electromagnetism". There is *a priori* no reason that the strong gradients of electromagnetic quantities near the oxide layer could not lead to the definition of surface-excess electromagnetic quantities (such as surface conductivity). New theoretical foundations should be introduced, possibly deriving from those proposed by Albano and Bedeaux [61]. At least, the effect of oxidation on the apparent bulk electrical conductivity of a liquid metal sample could be characterised. A possible starting point is given in App. E.

Another long-term modelling issue involves the shape of the liquid/gas interface. The interface shape, up to now *a priori* given, could be indeed released from this constraint. Thus, the normal stress boundary condition of the jump momentum balance should be imposed, in order to define the geometrical configuration of the fluid interface. By the way, a numerical approach should be certainly systematically favoured, and classical numerical methods of detection (VOF, level-set…) could be used. In the case of FEM simulations concerning the "deforming bubble MHD problem", the mathematical developments of App. D.4.b could be reused to implement the weak form of the overall jump momentum balance at the bubble surface.

Finally, the annular channel viscometer could be adapted to operate not only with liquid metals, but also with far less conducting fluids such as strong electrolytes, with typical electrical conductivity $\sigma \sim 10^2\,\mathrm{S{\cdot}m^{-1}}$. In similitude with Madip, this means that the imposed outer magnetic field should be roughly one hundred times as strong as it is in the case of liquid metals, requiring the generation of a few dozen Tesla DC fields. A cooperation with the *laboratoire national des champs magnétiques intenses* (LnCMI) in Grenoble could reveal fruitful (Fig. Concl. 1(b)), in order to broaden the research spectrum about the coupling between surface rheology and bulk MHD.

Appendices

Appendix A. Mannheimer and Schechter's modelling of the annular channel viscometer

In this appendix, the theoretical analysis of the annular channel viscometer performed by Mannheimer and Schechter is introduced [31], in link with the typical layout shown in Fig. III.A.1. Within the approximation $\mathrm{Re} \ll 1$, the governing equations are the axisymmetric Stokes equations for the azimuthal velocity v_θ:

$$\frac{\partial^2 v_\theta}{\partial r^2} + \frac{1}{r}\frac{\partial v_\theta}{\partial r} - \frac{v_\theta}{r^2} + \frac{\partial^2 v_\theta}{\partial z^2} = 0,$$

completed with the following no-slip boundary conditions at the inner wall (r_i) and outer wall (r_o):

$$v_\theta(r_o, z) = v_\theta(r_i, z) = 0,$$

along with the rotating floor BC in $z = 0$:

$$v_\theta(r, 0) = r\Omega.$$

The last BC is the azimuthal component of the JMB:

$$\eta_s\left(\frac{\mathrm{d}^2 v_{\theta S}}{\mathrm{d}r^2} + \frac{1}{r}\frac{\mathrm{d}v_{\theta S}}{\mathrm{d}r} - \frac{v_{\theta S}}{r^2}\right) = \eta \left.\frac{\partial v_\theta(r,z)}{\partial z}\right|_{z=h}.$$

An analysis of this boundary value problem results in the following series solutions for the surface velocity $v_{\theta S}$ along the interface and the bulk velocity field v_θ ($V = r_o\Omega$):

$$\frac{v_{\theta,S}}{V} = \frac{2}{\frac{r_o}{e}}\sum_{i=1}^{\infty}\left\{\frac{\left[\left(\frac{r_o}{e}\right)^2\psi_0\left(\frac{r_o}{e}\beta_i\right) - \left(\frac{r_i}{e}\right)^2\psi_0\left(\frac{r_i}{e}\beta_i\right)\right]}{\beta_i\left[\left(\frac{r_i}{e}\right)^2\psi_0^2\left(\frac{r_i}{e}\beta_i\right) - \left(\frac{r_o}{e}\right)^2\psi_0^2\left(\frac{r_o}{e}\beta_i\right)\right]}\right.$$
$$\left.\cdot\frac{\psi_1\left(\frac{r}{e}\beta_i\right)}{\left[\cosh\left(\beta_i\frac{h}{e}\right) + \beta_i\frac{\eta_s}{\eta e}\sinh\left(\beta_i\frac{h}{e}\right)\right]}\right\},$$

$$\frac{v_\theta}{V} = \sum_{i=1}^{\infty}\left(A_i\sinh\left(\frac{\beta_i z}{e}\right) + B_i\cosh\left(\frac{\beta_i z}{e}\right)\right)\psi_1\left(\frac{\beta_i r}{e}\right),$$

for $r \in [r_i, r_o]$ and $z \in [0, h]$, where

$$A_i = \frac{-B_i\left(\frac{\beta_i \eta_s}{\eta e}\cosh\left(\frac{\beta_i h}{e}\right) + \sinh\left(\frac{\beta_i h}{e}\right)\right)}{\frac{\beta_i \eta_S}{\eta e}\sinh\left(\frac{\beta_i h}{e}\right) + \cosh\left(\frac{\beta_i h}{e}\right)},$$

and

$$B_i = \frac{2}{\frac{r_o}{e}} \frac{\left(\frac{r_o}{e}\right)^2 \psi_0\left(\frac{\beta_i r_o}{e}\right) - \left(\frac{r_i}{e}\right)^2 \psi_0\left(\frac{\beta_i r_i}{e}\right)}{\beta_i\left(\left(\frac{r_i}{e}\right)^2 \psi_0^2\left(\frac{\beta_i r_i}{e}\right) - \left(\frac{r_o}{e}\right)^2 \psi_0^2\left(\frac{\beta_i r_o}{e}\right)\right)},$$

with

$$\psi_1\left(\frac{r}{e}\beta_i\right) = \mathscr{J}_1\left(\frac{r}{e}\beta_i\right)\mathscr{Y}_1\left(\frac{r_i}{e}\beta_i\right) - \mathscr{J}_1\left(\frac{r_i}{e}\beta_i\right)\mathscr{Y}_1\left(\frac{r}{e}\beta_i\right),$$

and

$$\psi_0\left(\frac{r}{e}\beta_i\right) = \mathscr{J}_0\left(\frac{r}{e}\beta_i\right)\mathscr{Y}_1\left(\frac{r_i}{e}\beta_i\right) - \mathscr{J}_1\left(\frac{r_i}{e}\beta_i\right)\mathscr{Y}_0\left(\frac{r}{e}\beta_i\right).$$

The quantities $\mathscr{J}$ and $\mathscr{Y}$ are Bessel functions of the first and second kind, the subscripts denoting their orders. Here β_i is the ith root of the relation:

$$\mathscr{J}_1\left(\frac{r_o}{e}\beta_i\right)\mathscr{Y}_1\left(\frac{r_i}{e}\beta_i\right) - \mathscr{J}_1\left(\frac{r_i}{e}\beta_i\right)\mathscr{Y}_1\left(\frac{r_o}{e}\beta_i\right).$$

Appendix B. Davoust and Huang's modelling of the annular channel viscometer

In this appendix, the theoretical analysis of the deep-channel annular channel viscometer performed by Davoust and Huang is detailed [72], in link with the typical layout shown in Fig. III.A.1, but for a shallow-channel configuration (*i.e.* $h < r_o - r_i$). Assuming $\mathrm{Re} \ll 1$, the governing equations are the axisymmetric Stokes equations for the azimuthal component of velocity v_θ:

$$\frac{\partial^2 v_\theta}{\partial r^2} + \frac{1}{r}\frac{\partial v_\theta}{\partial r} - \frac{v_\theta}{r^2} + \frac{\partial^2 v_\theta}{\partial z^2} = 0,$$

completed with the following no-slip boundary conditions at the inner wall (r_i) and outer wall (r_o):

$$v_\theta(r_o, z) = v_\theta(r_i, z) = 0,$$

along with the rotating floor BC in $z = 0$:

$$v_\theta(r, 0) = r\Omega,$$

The last BC is the azimuthal component of the JMB:

$$\eta_s \left(\frac{\mathrm{d}^2 v_{\theta S}}{\mathrm{d}r^2} + \frac{1}{r}\frac{\mathrm{d}v_{\theta S}}{\mathrm{d}r} - \frac{v_{\theta S}}{r^2} \right) = \eta \left. \frac{\partial v_\theta(r,z)}{\partial z} \right|_{z=h}.$$

A scaling analysis leads to the definition of the following dimensionless quantities: $r^\star = r/r_o$, $z^\star = r/h$, $v_\theta^\star = v_\theta/r_o\Omega$, and the (surface shear) Boussinesq number, defined as $\mathrm{Bo} = \eta_S h/\eta r_o^2$. Now, within the lubrication approximation $h/(r_o - r_i) \ll 1$, a matched asymptotic expansion is performed, based on the small value of the aspect ratio $\chi = h/r_o$. This leads to the following solution at leading order for the dimensionless bulk azimuthal velocity:

$$v_\theta^\star(r^\star, z^\star) = \left(v_{\theta S}^\star(r^\star) - r^\star\right) z^\star - 2\sum_{n=1}^{\infty} \frac{\sin(n\pi z^\star)}{n\pi} \left(\mathrm{e}^{-n\pi\frac{1-r^\star}{\chi}} + \frac{r_i}{r_o}\mathrm{e}^{-n\pi\frac{r^\star - \frac{r_i}{r_o}}{\chi}} \right),$$

where the surface velocity writes

$$v_{\theta S}^\star(r^\star) = \int_{\frac{r_i}{r_o}}^{r^\star} G(r^\star|\xi) f(\xi)\,\mathrm{d}\xi + \int_{r^\star}^{1} G(r^\star|\xi) f(\xi)\,\mathrm{d}\xi,$$

where the forcing function f is defined as:

$$f(r^\star) = -r^\star + 2\frac{\mathrm{e}^{-\pi\frac{1-r^\star}{\chi}}}{1+\mathrm{e}^{-\pi\frac{1-r^\star}{\chi}}} + 2\frac{r_i}{r_o}\frac{\mathrm{e}^{-\pi\frac{r^\star-\frac{r_i}{r_o}}{\chi}}}{1+\mathrm{e}^{-\pi\frac{r^\star-\frac{r_i}{r_o}}{\chi}}},$$

and where G is the following piecewise Green function:

$$G(r^\star|\xi) = \begin{cases} A(r^\star)\xi\mathscr{I}_1\left(\frac{\xi}{\sqrt{\mathrm{Bo}}}\right) + B(r^\star)\xi\mathscr{K}_1\left(\frac{\xi}{\sqrt{\mathrm{Bo}}}\right) & \text{if } \xi \in \left[\frac{r_i}{r_o}, r^\star\right[, \\ C(r^\star)\xi\mathscr{I}_1\left(\frac{\xi}{\sqrt{\mathrm{Bo}}}\right) + D(r^\star)\xi\mathscr{K}_1\left(\frac{\xi}{\sqrt{\mathrm{Bo}}}\right) & \text{if } \xi \in]r^\star, 1]. \end{cases}$$

The coefficients $A(r^\star)$, $B(r^\star)$, $C(r^\star)$ and $D(r^\star)$ are given by:

$$A(r^\star) = \frac{\mathscr{K}_1\left(\frac{r_i}{r_o\sqrt{\mathrm{Bo}}}\right)}{\mathrm{Bo}} \frac{\mathscr{I}_1\left(\frac{r^\star}{\sqrt{\mathrm{Bo}}}\right)\mathscr{K}_1\left(\frac{1}{\sqrt{\mathrm{Bo}}}\right) - \mathscr{I}_1\left(\frac{1}{\sqrt{\mathrm{Bo}}}\right)\mathscr{K}_1\left(\frac{r^\star}{\sqrt{\mathrm{Bo}}}\right)}{\mathscr{I}_1\left(\frac{1}{\sqrt{\mathrm{Bo}}}\right)\mathscr{K}_1\left(\frac{r_i}{r_o\sqrt{\mathrm{Bo}}}\right) - \mathscr{I}_1\left(\frac{r_i}{r_o\sqrt{\mathrm{Bo}}}\right)\mathscr{K}_1\left(\frac{1}{\sqrt{\mathrm{Bo}}}\right)},$$

$$B(r^\star) = -\frac{\mathscr{I}_1\left(\frac{r_i}{r_o\sqrt{\mathrm{Bo}}}\right)}{\mathrm{Bo}} \frac{\mathscr{I}_1\left(\frac{r^\star}{\sqrt{\mathrm{Bo}}}\right)\mathscr{K}_1\left(\frac{1}{\sqrt{\mathrm{Bo}}}\right) - \mathscr{I}_1\left(\frac{1}{\sqrt{\mathrm{Bo}}}\right)\mathscr{K}_1\left(\frac{r^\star}{\sqrt{\mathrm{Bo}}}\right)}{\mathscr{I}_1\left(\frac{1}{\sqrt{\mathrm{Bo}}}\right)\mathscr{K}_1\left(\frac{r_i}{r_o\sqrt{\mathrm{Bo}}}\right) - \mathscr{I}_1\left(\frac{r_i}{r_o\sqrt{\mathrm{Bo}}}\right)\mathscr{K}_1\left(\frac{1}{\sqrt{\mathrm{Bo}}}\right)},$$

$$C(r^\star) = \frac{\mathscr{K}_1\left(\frac{1}{\sqrt{\mathrm{Bo}}}\right)}{\mathrm{Bo}} \frac{\mathscr{I}_1\left(\frac{r^\star}{\sqrt{\mathrm{Bo}}}\right)\mathscr{K}_1\left(\frac{r_i}{r_o\sqrt{\mathrm{Bo}}}\right) - \mathscr{I}_1\left(\frac{r_i}{r_o\sqrt{\mathrm{Bo}}}\right)\mathscr{K}_1\left(\frac{r^\star}{\sqrt{\mathrm{Bo}}}\right)}{\mathscr{I}_1\left(\frac{1}{\sqrt{\mathrm{Bo}}}\right)\mathscr{K}_1\left(\frac{r_i}{r_o\sqrt{\mathrm{Bo}}}\right) - \mathscr{I}_1\left(\frac{r_i}{r_o\sqrt{\mathrm{Bo}}}\right)\mathscr{K}_1\left(\frac{1}{\sqrt{\mathrm{Bo}}}\right)},$$

$$D(r^\star) = -\frac{\mathscr{I}_1\left(\frac{1}{\sqrt{\mathrm{Bo}}}\right)}{\mathrm{Bo}} \frac{\mathscr{I}_1\left(\frac{r^\star}{\sqrt{\mathrm{Bo}}}\right)\mathscr{K}_1\left(\frac{r_i}{r_o\sqrt{\mathrm{Bo}}}\right) - \mathscr{I}_1\left(\frac{r_i}{r_o\sqrt{\mathrm{Bo}}}\right)\mathscr{K}_1\left(\frac{r^\star}{\sqrt{\mathrm{Bo}}}\right)}{\mathscr{I}_1\left(\frac{1}{\sqrt{\mathrm{Bo}}}\right)\mathscr{K}_1\left(\frac{r_i}{r_o\sqrt{\mathrm{Bo}}}\right) - \mathscr{I}_1\left(\frac{r_i}{r_o\sqrt{\mathrm{Bo}}}\right)\mathscr{K}_1\left(\frac{1}{\sqrt{\mathrm{Bo}}}\right)},$$

$\mathscr{I}_1$ and $\mathscr{K}_1$ being the modified Bessel functions of first and second kinds, respectively.

Appendix C. Shercliff's modelling of the MHD flow in a square duct

In this appendix, the theoretical analysis of an electroconductive square-duct flow with all insulating walls, subjected to an outer DC field $\vec{B}_0 = B_0\vec{e}_z$, originally performed by Shercliff [33] for a rectangular duct. A typical geometrical layout is given in Fig. D.16 (if we preclude the gaseous inclusion and the boundary conditions presented in this figure). The typical length, pressure, velocity, and induced magnetic field are L, P, $V = PL/\eta$, and $\mu V\sqrt{\sigma\eta}$, respectively. The governing equations for the velocity field $\vec{v}^\star = v_x^\star(y^\star, z^\star)\vec{e}_x$ and the induced magnetic field $\vec{b}^\star = b_x^\star(y^\star, z^\star)\vec{e}_x$ are dimensionless induction equation and momentum equation:

$$\Delta^\star b_x^\star + \mathrm{Ha}\frac{\partial v_x^\star}{\partial z^\star} = 0, \quad \Delta^\star v_x^\star + \mathrm{Ha}\frac{\partial b_x^\star}{\partial z^\star} = -1,$$

where $\mathrm{Ha} = LB_0\sqrt{\sigma/\eta}$. The dynamic boundary conditions consists of no-slip boundary conditions at the duct walls. With respect to the electromagnetic BCs, let us first remark that Eq. (MA) yields:

$$\vec{j}^\star = \frac{1}{\mathrm{Ha}}\overrightarrow{\mathrm{curl}}\left(\vec{b}^\star\right) = \frac{1}{\mathrm{Ha}}\left(\frac{\partial b_x^\star}{\partial z^\star}\vec{e}_y - \frac{\partial b_x^\star}{\partial y^\star}\vec{e}_z\right), \tag{C.1}$$

meaning that the induced magnetic field can be considered as a current stream function. As shown in Eq. (II.A.36), this leads to a vanishing induced magnetic field at the walls. Finally, the development in Fourier series leads to the following solution:

$$v_x^\star(y^\star, z^\star) = \sum_{n=0}^{\infty} f_n(z^\star)\cos(\alpha_n y^\star),$$
$$b_x^\star(y^\star, z^\star) = \sum_{n=0}^{\infty} g_n(z^\star)\cos(\alpha_n y^\star),$$

where

$$f_n(z^\star) = \frac{\beta_n}{\alpha_n^2}\left(1 - \frac{\sinh(\gamma_n)\cosh(\delta_n z^\star) - \sinh(\delta_n)\cosh(\gamma_n z^\star)}{\sinh(\gamma_n - \alpha_n)}\right),$$
$$g_n(z^\star) = \frac{\beta_n}{\alpha_n^2}\frac{\sinh(\gamma_n)\sinh(\delta_n z^\star) - \sinh(\delta_n)\sinh(\gamma_n z^\star)}{\sinh(\gamma_n - \alpha_n)},$$

with

$$\alpha_n = \frac{(2n+1)\pi}{2}, \quad \beta_n = \frac{2\sin(\alpha_n)}{\alpha_n},$$
$$\gamma_n = \frac{1}{2}\left(\mathrm{Ha} + \sqrt{\mathrm{Ha}^2 + 4\alpha_n^2}\right), \quad \delta_n = \frac{1}{2}\left(\mathrm{Ha} - \sqrt{\mathrm{Ha}^2 + 4\alpha_n^2}\right).$$

The electric current density is deduced from Eq. (C.1).

Appendix D. A first approach to bubble MHD

In this appendix, our purpose is to complete the investigation of the coupling between surface rheology and MHD, highlighted in the main matter of this thesis work for a stratified MHD flow, by focusing this time on a dispersed topology. The physical outlines related to the MHD flow past a gas bubble, referred to as the "bubble MHD" problem, are discussed. The MHD flow past a gaseous inclusion constitutes actually an insightful topic, in many respects. As explained in the introduction, this substantial work has been placed in the appendices, the lack of time preventing us from investigating the coupling between full interfacial dynamics and bulk MHD.

It is first shown that the bubble MHD problem represents the natural complement to the work performed on the MHD viscometer. Then, we detail the typical bubble MHD flow configuration on which we shall focus in this work. The main notations and assumptions are outlined, along with our approach to the problem. It is particularly shown how the most insightful features are strongly related to the respective orientations of the velocity field and the outer magnetic field. Afterwards, a state-of-the-art of the dynamics of particulate media is drawn, first for simple hydrodynamics (with a special emphasis on varying interfacial BC), then for MHD, in order to constitute a basis of reference benchmarks for subsequent numerical studies. Some hints at the numerical implementation of the bubble MHD problem, and particularly the full interfacial dynamics (driven by surface rheology), are finally discussed, as the first step towards the description of dispersed MHD flows.

D.1. Motivation, physical issues and assumptions for the bubble MHD problem

D.1.a. A key topic with promising features for future R&D prospects, in link with the annular MHD viscometer

As emphasised in the global introduction (see Sec. I.A.1.b), dispersed MHD flows are likely to become one of the cornerstones of MHD in a close future, given the numerous fundamental and industrial applications potentially involved. The capacity of heterogeneous media to transfer mass, momentum and heat is well-known. The addition of an outer magnetic field, in order to drive the multiphase flow by making the most of the outstanding properties of MHD boundary layers, aims at improving these remarkable properties. However, it is necessary to describe properly the varying liquid/gas interface dynamics, governed by surface rheology (*e.g.* in the case of liquid metals, subjected to oxidation), if we want to capture the physical behaviour of these atypical layers. By the way, the guiding principle of this thesis results from the lack of available information to tackle the physical issues raised partly by the bubble MHD

problem: how does the surface rheology of a gradually oxidising liquid metal impact a supporting MHD flow? All along this work, our ambition is to propose an approach allowing for the description of the two asymptotic topologies of multiphase flows, *i.e.* the dispersed and stratified flows. A first part of answer has been given for stratified flows, with the main matter of this thesis work about the annular MHD viscometer. The bubble MHD problem is the natural complement for proposing an exhaustive first approach towards the description of multiphase MHD flows.

Apart from this common thread, the two study cases are strongly connected to each other. Indeed, the results obtained with the annular viscometer are intended to feed the bubble MHD problem. Madip has clearly demonstrated the wide range of possible values for the surface viscous shear of a gradually oxidising interface. This makes credible our approach to the varying BC at the bubble surface, where we consider a liquid metal/gas interface evolving from a slip (pure) to a no-slip (oxidised) condition. Besides, the accurate description of the bubble interfacial dynamics definitely depends on the ability of identifying Bo_{η_S} and $\mathrm{Bo}_{\varkappa_S}$ with respect to the oxidation state of the interface, which is the primary goal of Madip. Thus, the consistency of our twofold strategy appears more obvious.

D.1.b. Typical flow configuration and main approximations

Geometry

In this part, we shall investigate the coupling between a gaseous inclusion (made of *e.g.* $\mathrm{Ar/O_2}$ mixtures) and the suspending MHD (square) duct flow of an electroconductive fluid (*e.g.* Galinstan), with varying mechanical boundary conditions at the liquid/gas interface. A very general layout is given in Fig. D.1.

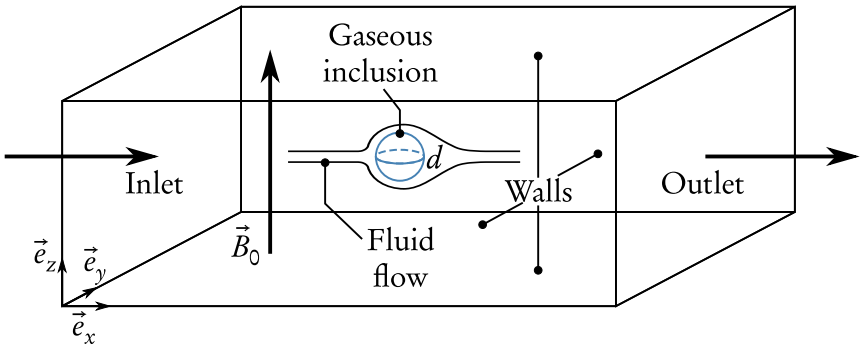

Figure D.1 – Overall layout of the bubble MHD problem. $\vec{B}_0$ and d are the outer DC magnetic field and the bubble apparent diameter, respectively.

In order to describe the MHD flow past the gas bubble, several hypotheses are admitted. In addition to the overall assumptions exposed in the general introduction (see Sec. I.C.2) and in the fundamental part (Part II) about classical MHD and the modelling of the interfacial behaviour, there are several approximations specific to the bubble MHD problem, that we must now clarify.

Internal motion, terminal velocity, rectilinear path and fluid flow past a stationary unconfined sphere

First of all, the internal bubble motion is of no interest to us. We are primarily interested in the surrounding fluid dynamics, and the viscosity of the gas is several order of magnitudes lower than that of the surrounding fluid, so that the contribution of the gas dynamics to the jump momentum balance (JMB) is indeed totally negligible, and can be left aside. Now, let us consider the case of a gas inclusion rising freely under the influence of buoyancy in a viscous fluid. This bubble ultimately attains a terminal settling velocity, when all the forces exerted on the bubble counterbalance each other. In this study, we suppose that the bubble under investigation has reached its terminal velocity $-V\vec{e}_x$; from now on, V shall be used as the typical flow velocity. The order of magnitude of this terminal velocity is discussed in the following section, in link with the bubble shape. Moreover, we suppose that this bubble always follows a rectilinear path along the $\vec{e}_x$ axis. These strong approximations allow us to considerably simplify the problem, by regarding the bubble as being at rest with fluid streaming past to it. The latter attains a typical core-flow velocity V far from the obstacle, in the (positive) $\vec{e}_x$ direction, which actually represents the relative velocity between the bubble and the flow motion, as described in Fig. D.2. The reasoning will not suffer from any loss of generality, for the absolute motions of either the liquid metal or the bubble can be deduced from this configuration using arguments explained *e.g.* in [91]. Note that the influence of confinement due to the duct walls shall be discussed in Sec. D.2.c.

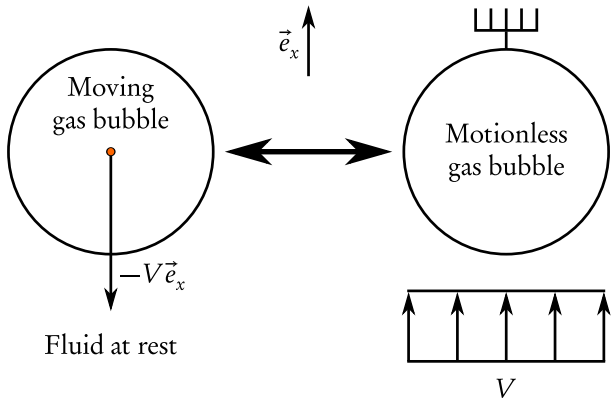

Figure D.2 – Equivalence between a bubble rising in a fluid at rest at its terminal velocity, and the flow past a stationary bubble.

Bubble shape and particulate Reynolds number

As explained in Sec. I.C.2, all along the present work, we assume that the shape of the liquid/gas interface is *a priori* given. In the particular case of the bubble MHD problem, this allows us to circumvent the modelling issue of deforming bubbles. For the sake of consistency, we must check whether this strong assumption proves relevant or not, and, if so, we must determine an appropriate shape for the gaseous inclusion.

Let us momently go back to the case of a bubble rising freely under the influence of buoyancy, in an infinite medium. The shape of this bubble is governed by 6 parameters (we omit the gas bubble density, because it is much lower than Galinstan density). Three parameters are physical properties of the surrounding fluid: η, ρ, γ; the last three are d, g and V ($g = 9.81\,\mathrm{m{\cdot}s^{-2}}$ being the local acceleration of gravity). A first basic calculation based on the capillary length $l_c = \sqrt{\gamma/\rho g}$ gives a first hint at the size of bubbles that can be obtained inside Galinstan, whose physical properties (except $\gamma = 0.535\,\mathrm{N{\cdot}m^{-1}}$ [29]) have been previously gathered in Tab. I.B.1. The numerical application gives a relatively high value (due to surface tension) $l_c = 2.9\,\mathrm{mm}$, which makes us expect bubbles with typical equivalent diameter $d \sim 1\,\mathrm{cm}$.

In parallel, three dimensionless parameters can be defined, that govern the shape of the bubble. These three parameters are:

$$\mathrm{Re_p} = \frac{\rho V d}{\eta}, \quad \mathrm{Mo} = \frac{\eta^4 \rho g}{\rho^2 \gamma^3}, \quad \mathrm{Eo} = \frac{\rho g d^2}{\gamma}, \tag{D.1}$$

where $\mathrm{Re_p}$, Mo and Eo are the particulate Reynolds number, the Morton number and the Eötvös number, respectively. The numerical application gives $\mathrm{Mo} = 2.1 \times 10^{-13}$ and $\mathrm{Eo} = 11.7$. The extrapolation of the flow regime map [25] (see Fig. D.3) gives access to a first estimation of the particulate Reynolds number $\mathrm{Re_{p,real}} \sim 10^4$, leading to a terminal velocity $V \sim$ a few $10^2\,\mathrm{mm{\cdot}s^{-1}}$, corresponding to a wobbling shape. This order of magnitude is consistent with experimental observations (see *e.g.* [46]).

In this study, however, we shall restrict our attention to much lower particulate Reynolds number, $\mathrm{Re_{p,max}} = 1.3 \times 10^2$, corresponding to $V \sim 1\,\mathrm{mm{\cdot}s^{-1}}$. There are many reasons justifying such a strong approximation, all of them being clarified in the subsequent section concerning the state-of-the-art of bubble (magneto)hydrodynamics in link with surface rheology:

- this work is a first approach to the bubble MHD problem. As such, we want to focus only on steady flow regimes, for a non-deforming gaseous inclusion, so that neither instabilities nor turbulence must be taken into account. As pointed out hereafter, such flow regimes past a sphere are valid up to the value $\mathrm{Re_{p,max}} = 1.3 \times 10^2$;
- for such low $\mathrm{Re_p}$ values, the bubble is not wobbling, but tends towards a spherical shape, for which a consequent amount of theoretical, numerical and experimental benchmarks exists;
- one aim of this study is to consider the influence of a transverse magnetic field on the bubble dynamics. As shown in Sec. D.3.b, a transverse magnetic field acts to make a bubble more spherical;
- another long-term goal is to investigate the influence of surface rheology on the bubble dynamics. It is now well-known that a bubble subjected to surface contamination may reach a (sometimes considerably) lower terminal velocity than a bubble with a pure interface.

Consequently, in addition to the approximations made for the sake of simplicity, there are several physical phenomena involved in the coupling between MHD and

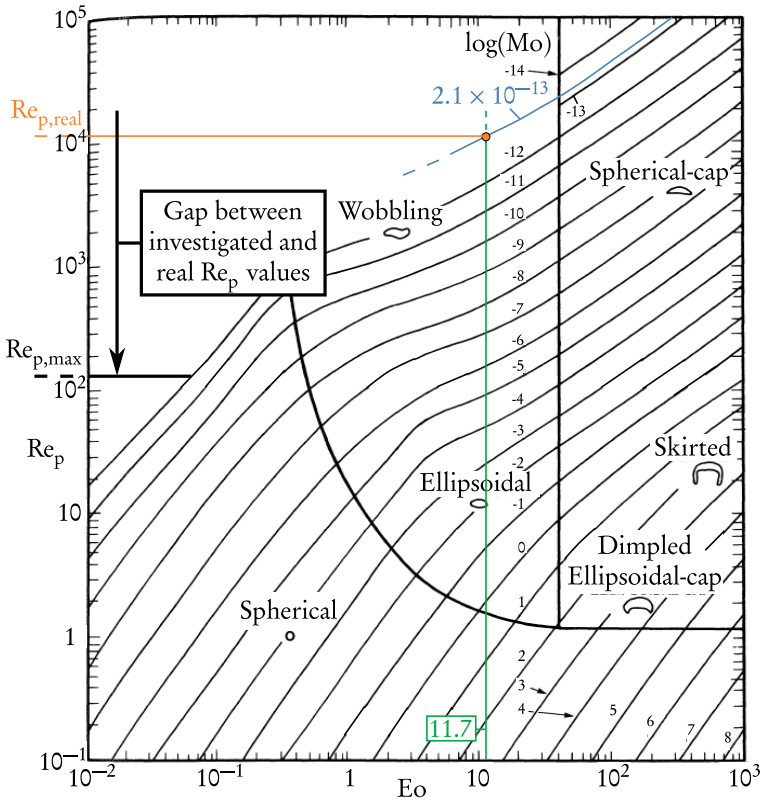

Figure D.3 – Shape regimes for bubbles and drops in unhindered gravitational motion through liquids [25]. The real working conditions $\mathrm{Re}_{\mathrm{p,real}}$ for the motion of a gas bubble in Galinstan are pointed out, along with the maximum value $\mathrm{Re}_{\mathrm{p,max}}$ investigated in this study.

surface rheology which tend to correct the shape of the bubble into a spherical shape. Henceforth, we shall only consider a non-deforming spherical inclusion with radius $R = d/2$.

Definition of flow coefficients

In this section, we introduce different flow coefficients, whose evolution with respect to Re and Ha reflects typical aspects of the flow dynamics, and allows for the comparison with benchmarking studies.

The first parameter is defined for those cases where Re_{p} has a moderate value, typically $20 \leq \mathrm{Re}_{\mathrm{p}} \leq 130$. These values correspond the flow regime of the steady recirculation regions, which develop in the sphere wake (see hereafter). This parameter is the length of the steady recirculation area, denoted L_w, measured between the rear point of the sphere and the tail of the recirculation region.

The sphere is subjected to a force $\vec{F}$, exerted by the surrounding flow, due to both pressure and viscous forces. The streamwise projection of this hydrodynamic force is called the drag force, while the transverse projection is called the lift force. In this

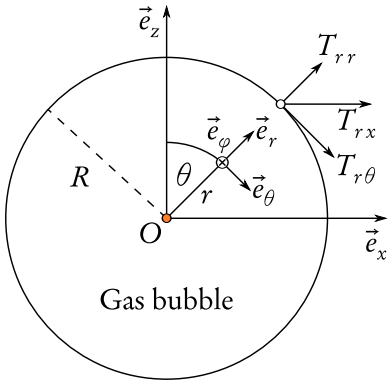

Figure D.4 – Projection of the mechanical stress tensor leading to the definition of the drag force.

preliminary work, the lift force is neglected, for symmetry reasons. If the fluid far from the obstacle flows along the $\vec{e}_x$ direction, the drag force is generally defined as:

$$\vec{F}_d = \left(\vec{F}\cdot\vec{e}_x\right)\vec{e}_x = \left(\iint_S \left(\overrightarrow{\overrightarrow{T}}\cdot\vec{e}_r\right)\cdot\vec{e}_x\right)\vec{e}_x, \tag{D.2}$$

where $\overrightarrow{\overrightarrow{T}}$ is the bulk mechanical stress tensor defined in Eq. (II.A.25), S is the surface of the sphere and $\vec{e}_r$ the outer normal to this surface. For instance, in the case of an axisymmetric flow past the inclusion, Eq. (D.2) writes:

$$\vec{F}_d = F_d\vec{e}_x = \int_0^\pi 2\pi R^2\sin(\theta)T_{rx}(R,\theta)\,\mathrm{d}\theta\,\vec{e}_x, \tag{D.3}$$

where r and θ are the spherical coordinates attached to the sphere, and T_{rx} is the projection of the bulk mechanical stress tensor defined as (see Fig. D.4):

$$T_{rx} = T_{r\theta}\cos(\theta) + T_{rr}\sin(\theta), \tag{D.4}$$

$$T_{rr} = -p + 2\eta\frac{\partial v_r}{\partial r},\ T_{r\theta} = \eta\left(r\frac{\partial(\frac{v_\theta}{r})}{\partial r} + \frac{1}{r}\frac{\partial v_r}{\partial\theta}\right). \tag{D.5}$$

In practise, the dimensionless group related to the drag force is preferentially used. This dimensionless coefficient is called the drag coefficient, and is defined as follows:

$$C_d = \frac{|F_d|}{\frac{1}{2}\rho V^2\pi R^2}. \tag{D.6}$$

D.1.c. Respective orientation of the velocity field and of the outer magnetic field

To conclude this section, let us highlight an issue of particular interest in view of magnifying the coupling between MHD and surface rheology, related to the respective orientation of the velocity field *ad infinitum* and of the outer DC field. We must

determine whether a streamwise or a transverse configuration seems more insightful. Let us momently consider the case of a bubble rising freely in an unbounded medium, and let us investigate the streamwise configuration, where the velocity and the outer magnetic field are aligned (along the $\vec{e}_x$ direction) far from the inclusion.

The spherical system of coordinates attached to the bubble, defined in Fig. D.4, is used, and a potential formulation of the MHD problem is selected. After an appropriate scaling, the potential formulation leads to the equation for the electric potential (see Eq. (II.A.20)):

$$\Delta^\star \phi^\star = \mathrm{div}^\star\left(\vec{v}^\star \times \vec{e}_x\right).$$

Let us develop further this equation, by projecting $\vec{e}_x$ on the spherical basis: classically, $\vec{e}_x = \sin(\theta)\vec{e}_r + \cos(\theta)\vec{e}_\theta$, and here $\vec{v}^\star = v_r^\star(r^\star,\theta)\vec{e}_r + v_\theta(r^\star,\theta)\vec{e}_\theta$ for symmetry reasons. Consequently, the vector $\vec{v}^\star \times \vec{e}_x$ is oriented along the single $\vec{e}_\phi$ component, but depends on r and θ alone. Its divergence is consequently zero, resulting in:

$$\Delta^\star \phi^\star = 0. \tag{D.7}$$

The electric current density writes (see Eq. (II.A.21)):

$$\vec{j}^\star = -\frac{\partial \phi^\star}{\partial r^\star}\vec{e}_r - \frac{1}{r^\star}\frac{\partial \phi^\star}{\partial \theta}\vec{e}_\theta + \left(v_r^\star \sin(\theta) - v_\theta^\star \cos(\theta)\right)\vec{e}_\varphi. \tag{D.8}$$

Finally, the electromagnetic boundary condition at the surface of the insulating bubble is written $\vec{j}\cdot\vec{e}_r = 0$, which yields using Eq. (D.8):

$$\left.\frac{\partial \phi^\star}{\partial r^\star}\right|_{r^\star=1} = 0. \tag{D.9}$$

As a result, Eq. (D.7) does not bring any source term due to velocity into play. Moreover, the BC (D.9) at the surface of the bubble is independent of velocity as well, which leads us to the conclusion that the form of the electric potential is not conditioned by velocity, neither in the ruling equation nor in the boundary conditions. Finally, the electric current densities, given in Eq. (D.8), do not depend on velocity as far as the in-plane components are concerned. As such, implementing the JMB at the gas/liquid interface is not worthwhile considering the expected effects on the electric current, because only the out-of-plane component would be affected by this change. This would result in a passive matching between the boundary layer surrounding the sphere and the outer MHD flow, and would not deeply alter the core-flow topology.

Finally, in the light of these remarks, the streamwise configuration is not expected to be the most insightful layout. This is the reason why we shall focus on the transverse configuration, where $\vec{B}_0 = B_0\vec{e}_z$. However, this choice has a major drawback: the axisymmetry of the problem is broken, which considerably compromises an analytical approach to the problem. Anyway, the addition of the duct walls would have broken this symmetry, and implementing the surface rheology equations would certainly lead to a tedious (if even possible) analytical reasoning. This is the reason why a numerical approach should be favoured in future prospects.

Now that the reference layout is definitely settled on, let us draw a state-of-the-art of the most significant existing achievements about bubble dynamics.

D.2. Hydrodynamic flow past a sphere: state-of-the-art

In this section, the focus is set upon the typical patterns linked to the hydrodynamic flow past a gaseous sphere, in the case where no outer magnetic field is present ($B_0 = 0$). A distinction is made between two flow regimes, based on the values of the particulate Reynolds number. On the one hand, when $\mathrm{Re_p}$ is low (typically $\mathrm{Re_p} < 1$), the classical creeping flow regime is introduced. On the other hand, for intermediate values ($1 < \mathrm{Re_p} < 130$), the so-called steady wake regime gradually intensifies. Finally, the most salient features concerning the coupling between surface rheology and bubble hydrodynamics are highlighted.

D.2.a. The creeping flow regime: $\mathrm{Re_p} < 1$

The problem of the streaming flow past a stationary sphere is a classical problem in fluid mechanics, first solved by Stokes [24], and discussed later on in such reference textbooks as [91, 25, 19]. Because $\mathrm{Re_p} < 1$, the inertial terms are neglected, allowing for the analytical investigation of the flow patterns.

Rigid sphere and no-slip BC at the gas/liquid BC

This case corresponds to the historical layout solved by Stokes, who introduced the Stokes stream function $\psi(r,\theta)$ such as:

$$v_r = \frac{1}{r^2 \sin(\theta)} \frac{\partial \psi}{\partial \theta}, \quad v_\theta = -\frac{1}{r \sin(\theta)} \frac{\partial \psi}{\partial r}, \tag{D.10}$$

to solve for the resulting mathematical problem. The solution in terms of the dimensionless stream function with respect to $(r^\star = r/R, \theta)$ writes:

$$\psi^\star_{\mathrm{St}} = \frac{1}{2} \sin^2(\theta) \left(r^{\star 2} - \frac{3}{2} r^\star + \frac{1}{2r^\star} \right). \tag{D.11}$$

An overview of the flow streamlines (solid lines) is given in Fig. D.5. Concerning the drag force now, its expression can be found by using Eqs. (D.2), (D.4), (D.5), and (D.11), which leads to the well-known Stokes' law of resistance:

$$|F_{d,\mathrm{St}}| = 6\pi\eta R V,$$

and to the following value of the drag coefficients:

$$C_{d,\mathrm{St}} = \frac{24}{\mathrm{Re_p}} \text{ for } \mathrm{Re_p} \ll 1. \tag{D.12}$$

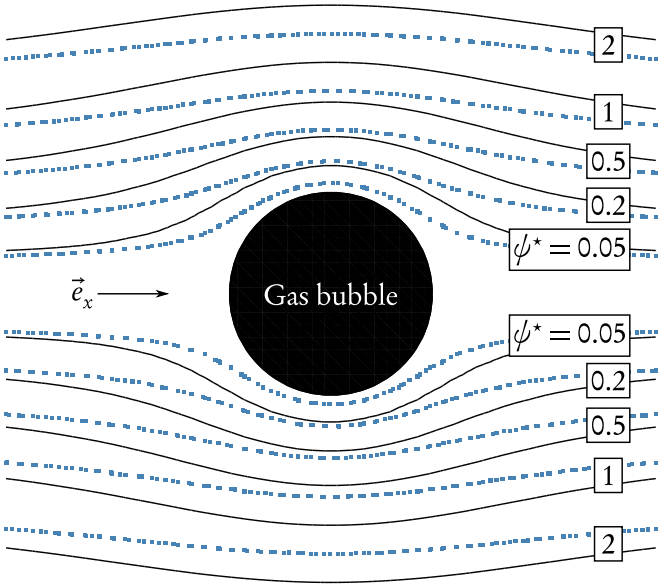

Figure D.5 – Flow streamlines in the case of a no-slip (solid lines: Stokes) or a perfect slip (dotted lines: Basset) BC at the bubble surface.

Gaseous sphere and perfect slip at the gas liquid interface

This case, solved by Basset by introducing the sliding friction coefficient β [92], and which can be derived from the Hadamard-Rybczynski theory [22, 23], differs from the Stokes solution in that a slip condition is implemented at the surface of the sphere, whose gaseous nature is thus more accurately described. When $\beta \to \infty$, corresponding to a no-slip BC at the surface, the previous Stokes solution is recovered. When $\beta \to 0$, corresponding to a perfect slip at the bubble surface, the solution for the dimensionless stream function is:

$$\psi^\star_{\mathrm{Ba}} = \frac{1}{2}\sin^2(\theta)\left(r^{\star 2} - r^\star\right). \tag{D.13}$$

An overview of the flow streamlines (dotted lines) is given in Fig. D.5. It can be noticed that for a given value $\psi^\star = \mathrm{Cst}$, the streamlines are closer to the bubble than they are in the Stokes solution. Empirically, a perfectly sliding interface is actually expected to exert less influence on the flow in its vicinity than when a strong friction occurs at the surface. More formally, this difference is explained by the conservation of momentum written on an elementary surface surrounding the bubble. In the case of a perfect slip, the expression of the drag coefficient is:

$$C_{d,\mathrm{Ba}} = \frac{16}{\mathrm{Re_p}} \text{ for } \mathrm{Re_p} \ll 1. \tag{D.14}$$

D.2.b. The steady wake regime: $1 < \mathrm{Re_p} < 130$

The previous analytical solutions for flow around gaseous spheres are limited to $\mathrm{Re_p} < 1$. For higher $\mathrm{Re_p}$ values, the inertial effects must be taken into account, leading to the flow separation and to the apparition of two steady recirculation regions, valid up to $\mathrm{Re_{p,max}} = 130$ [25]. Because of the inertial effects, the main sources of information include experimental observations and numerical solutions. The flow patterns are investigated through the flow coefficients previously introduced.

Rigid sphere

In the case of rigid spheres, the development of flow field with $\mathrm{Re_p}$ can be divided into two steps. The first interval $1 < \mathrm{Re_p} < 20$ corresponds to an unseparated flow regime. The flow still sticks to the whole sphere surface, and no separation is visible. Asymmetry becomes more marked. At the onset value $\mathrm{Re_p} = 20$ [25], flow separation occurs at the rear stagnation point, and recirculation begins. Finally, as $\mathrm{Re_p}$ increases beyond 20, the recirculation regions appear. These regions are symmetric with respect to the wake centreline, and develop at the rear of the sphere and lengthen downstream, as shown in Fig. D.6.

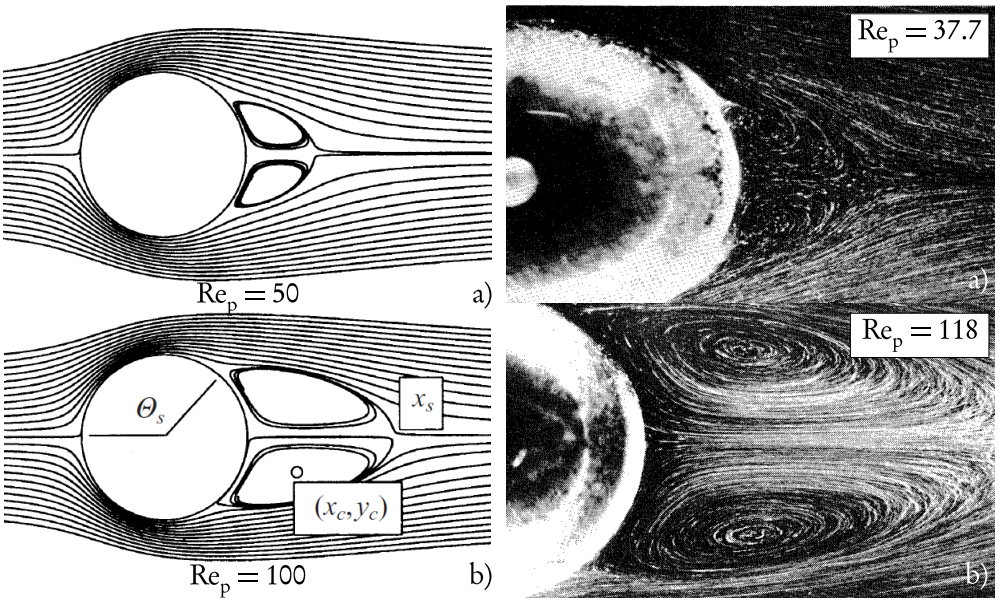

(a) – Computed axisymmetric streamlines past a solid sphere [93].

(b) – Photographs showing the development of the attached wake behind rigid spheres [94].

Figure D.6 – Numerical and experimental evidence of the steady recirculation regions at differente intermediate $\mathrm{Re_p}$ values.

Let us quantify the development of the steady recirculation area by means of the parameter L_w. The evolution of L_w with respect to $\mathrm{Re_p}$ is shown in Fig. D.7(a). Let

us focus on the data for which $\mathrm{Re_p} < 130$. The following correlation can be derived from this experimental data:

$$\frac{L_{w,\mathrm{sphere}}}{d} = c_1\left(\mathrm{Re_p}\right) = 0.5494 \ln\left(\mathrm{Re_p}\right) - 1.6694 \;\forall\, \mathrm{Re_p}. \tag{D.15}$$

With respect to the drag coefficient, the following piecewise correlation is proposed by Clift *et al.* in [25], which encompasses a large set of experimental data:

$$C_{d,\mathrm{Clift,s}} = c_2\left(\mathrm{Re_p}\right) = \begin{cases} \frac{24}{\mathrm{Re_p}}\left(1 + 0.1315\ \mathrm{Re_p}^{0.82-0.05\log_{10}\left(\mathrm{Re_p}\right)}\right) & \text{if } \mathrm{Re_p} \leq 20, \\ \frac{24}{\mathrm{Re_p}}\left(1 + 0.1935\ \mathrm{Re_p}^{0.6305}\right) & \text{if } \mathrm{Re_p} \in \,]20, 130]. \end{cases} \tag{D.16}$$

The resulting drag coefficient curve is shown in Fig. D.7(b).

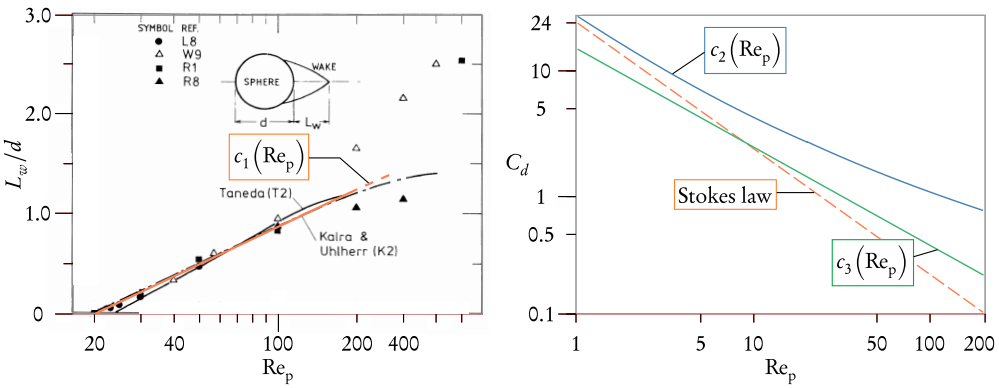

(a) – Length of sphere wake [25].

(b) – Drag coefficient of a sphere [25].

Figure D.7 – Flow coefficients of a sphere at intermediate $\mathrm{Re_p}$ values.

Gaseous sphere

Contrary to the creeping flow regime, where the rigid or fluid nature of the sphere does not radically alter the flow topology, both qualitative and quantitative aspects of the flow patterns past a gaseous sphere noticeably differ from the case of a rigid sphere. As previously said, the internal circulation of the gas bubble is not of primary interest to us, because it does not directly impact the JMB. Nonetheless, the slip BC detailed in Sec. D.2.a stems from this internal circulation, which in turn causes a delay of flow separation and wake formation in the external fluid. In the case of a bubble with a very pure surface, the separation of flow seems even absent [25], as shown in Fig. D.8.

With respect to the drag coefficient, a good fit to numerical predictions on spherical gas bubbles is provided by the following correlation:

$$C_{d,\mathrm{Clift,g}} = c_3\left(\mathrm{Re_p}\right) = 14.9\ \mathrm{Re_p}^{-0.78},\ \mathrm{Re_p} > 1. \tag{D.17}$$

The resulting drag coefficient curve is shown in Fig. D.7(b).

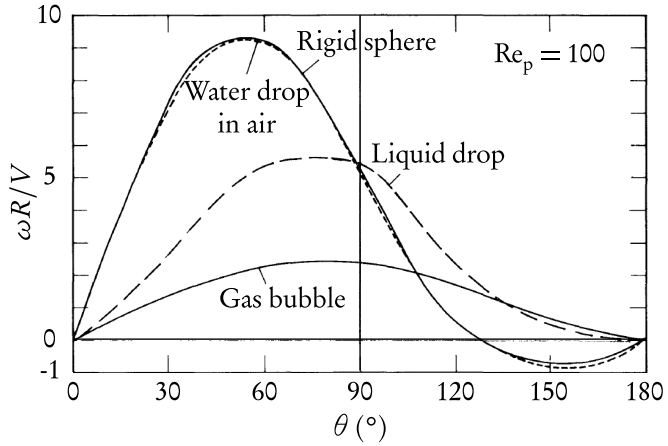

Figure D.8 – Vorticity ω distribution at the surface of different spheres for $\mathrm{Re_p} = 100$ [25]. The absence of separation for the bubble is indicated by the fact that the sign of ω remains unchanged.

D.2.c. Impact of flow confinement

Influence on overall flow patterns

Up to now, the flow domain has been considered unbounded, so that the typical velocity of the flow far from the inclusion has been considered uniform. In practise, the flow domain is bounded by ducts, whose typical transverse extent is $2L$, as shown in Fig. D.9. Depending on the value of the so-called *blockage ratio*:

$$\lambda = \frac{d}{2L}, \tag{D.18}$$

the confinement may deeply alter the flow patterns past the spherical inclusion. It is thus important to assess this influence.

Let us consider the typical layout described in Fig. D.9. At the inlet, the hydrodynamic velocity profile vary now in accordance with the parabolic Poiseuille velocity profile. The typical velocity V corresponds now to the maximum velocity reached at the inlet, *i.e.* at the duct centreline. Moreover, the core-flow between the sphere and the duct walls is locally accelerated, in link with the momentum balance. Finally, the boundary layers at the walls can also interfere in the overall flow patterns. Given the relatively low value of λ that shall be adopted in this work, we do not expect the impact of the confinement on the flow dynamics to be significant, from a qualitative point of view.

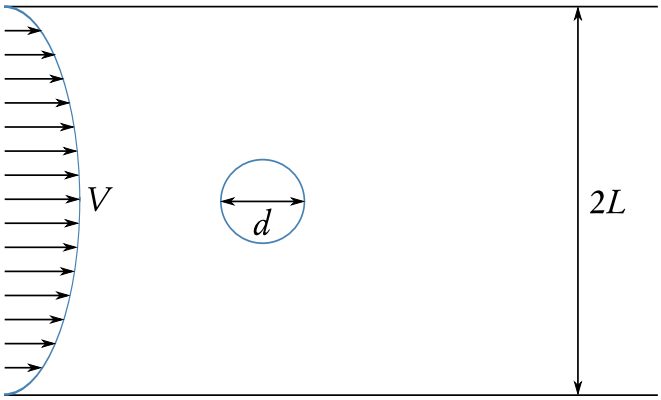

Figure D.9 – Cross-section of the duct flow past a sphere: confinement effects.

Influence on flow coefficients

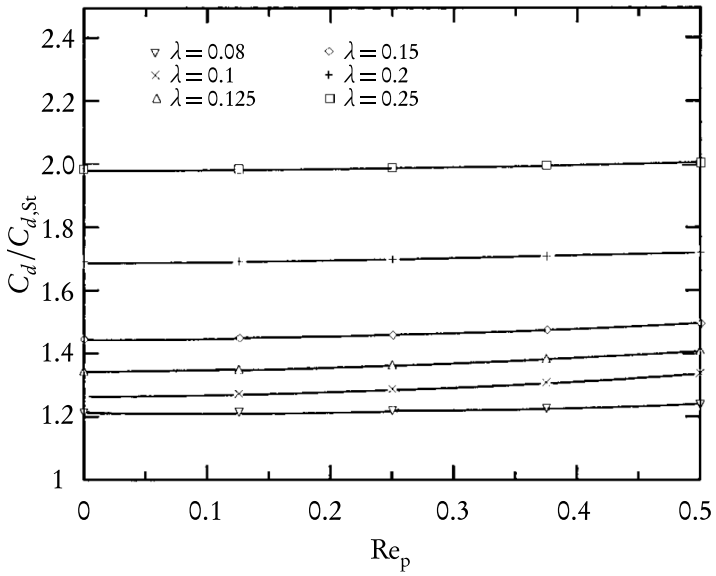

Figure D.10 – Drag correction for a falling sphere at small Re_p numbers for several blockage ratios [95].

From a quantitative point of view however, the non-uniform inlet velocity profile generates an additional pressure gradient along the transverse direction, and viscous effects at the duct walls. These two combined effect impact the values of the flow coefficients, beginning with the length of the recirculation area L_w, for the steady wake regime. An increase of λ causes a shortening of the steady recirculation region, and thus a decrease of L_w, at a given Re_p. For instance, for $\lambda = 0.125$, L_w differs within $5-10\,\%$ from its value in the $\lambda = 0$ (unbounded) case [96].

Now, with respect to the drag coefficient, the difference with the unbounded configuration can be significant. Indeed, for $\lambda = 0.125$, C_d can reach up to 35 % higher values than in the unbounded case, as shown as shown by Wham *et al.* [95] (see Fig. D.10).

These authors propose to apply the following correction factor K to the unbounded solution, in order to take the blockage ratio into account:

$$K = \frac{1 - 0.75857\lambda^5}{1 - \left(0.6628 + 1.458\,\mathrm{e}^{-0.02818\mathrm{Re_p}}\right)\lambda + 2.0865\lambda^3 - 1.7086\lambda^5 + 0.72603\lambda^6},$$

which leads to the following correlation:

$$C_{d,\mathrm{Wham}} = C_{d,0}.K\left(\mathrm{Re_p}\right) \;\forall\, \mathrm{Re_p}. \tag{D.19}$$

Eq. (D.19) has been validated in the case of rigid spheres. In the absence of similar information in the case of gaseous (slipping) bubbles, $C_{d,0}$ may represent Eq. (D.16) for rigid spheres, Eq. (D.14) in the case of gaseous spheres for $\mathrm{Re_p} < 1$ and (D.17) in the case of gaseous spheres for $\mathrm{Re_p} > 1$.

D.2.d. Impact of surface contamination: the coupling with surface rheology

Up to now, the liquid/gas interface has been considered either totally rigid, leading to the flow patterns observed past a rigid sphere, or totally sliding, corresponding to the case of a gaseous sphere. In practise, the interface BC is profoundly affected by the presence of surface contaminants, or surfactants. The fluids exhibiting high surface tension, *e.g.* liquid metals, are particularly concerned. When these surfactants are absent, the liquid/gas interface is pure, but when they are present even in small proportions, they may adsorb at the interface, conferring it a rigid behaviour. As it has been previously highlighted, this change in the interfacial behaviour leads to significant changes in the hydrodynamic flow patterns, especially at intermediate $\mathrm{Re_p}$ values. This is the reason why we focus now on the most salient features implied by the coupling between the surface rheology of the liquid/gas interface and the suspending flow hydrodynamics.

Neglecting the Marangoni effect

We remind here that we are not interested in surface properties gradients, and that the surface tension γ is not brought into play, because the spherical shape of the interface is *a priori* assumed. This is a very strong approximation: as emphasised in the overall introduction in Fig. I.B.3, surface tension gradients do exist in practise at the surface of the sphere. These gradients are generated by the convective sweeping of the surfactants at the rear of the sphere, because of the bubble motion. These gradients would normally interfere with surface dynamics, inducing a tangential stress due to Marangoni effect. The latter would thus retard surface, increase the drag coefficient, and the terminal velocity of the bubble would be lowered (which is quite positive, for it brings back the real gas bubble to lower $\mathrm{Re_p}$ values on the map of flow regimes presented in Fig. D.3). Nevertheless, because the primary objective of this thesis is to give a first glance at the coupling between MHD and surface rheology, we leave such gradients apart from the following analysis, allowing us to ignore chemical transport issues. The modelling of the interfacial transport of species is left for future prospects.

Surface rheology and gaseous spheres in the creeping flow regime

Let us place in the case of a gas bubble whose surface exhibits Newtonian rheological behaviour, rising at a terminal velocity V, such as $\mathrm{Re_p} < 1$. Let us use the spherical system of coordinates, typically described in Fig. D.4. The bulk equations are the classical Stokes equations, while the jump momentum balance written at the interface can be deduced from Eq. (II.B.6) written in spherical coordinates, after an appropriate scaling [20]:

$$\left(\mathrm{Bo}_{\varkappa_S} + \mathrm{Bo}_{\eta_S}\right) \frac{\partial}{\partial \theta} \left[\frac{1}{\sin(\theta)} \frac{\partial \left(\sin(\theta) v_\theta^\star \right)}{\partial \theta} \right] = \frac{\partial \left(\frac{v_\theta^\star}{r^\star} \right)}{\partial r^\star}, \tag{D.20}$$

where:

$$\mathrm{Bo}_{\varkappa_S} = \frac{\varkappa_S}{\eta R}, \; \mathrm{Bo}_{\eta_S} = \frac{\eta_S}{\eta R} \tag{D.21}$$

are the surface dilatational and shear numbers, respectively. Owing to the axisymmetric nature of the fluid motion, the mathematical problem can be solved using a Stokes stream function formulation, which leads to [20]:

$$\psi_{\mathrm{Ed}}^\star = \frac{1}{2} \sin^2(\theta) \left(r^{\star 2} - \frac{3\left(1 + \mathrm{Bo}_{\varkappa_S}\right)}{3 + 2\mathrm{Bo}_{\varkappa_S}} r^\star + \frac{\mathrm{Bo}_{\varkappa_S}}{3 + 2\mathrm{Bo}_{\varkappa_S}} \frac{1}{r^\star} \right). \tag{D.22}$$

The first remark that can be drawn is that interfacial shear viscosity is absent from Eq. (D.22). This result has been confirmed in more recent studies [97]. This reveals that the interfacial motion is in this case purely dilatational. The lack of any η_S term may be related to the fact that the azimuthal surface velocity $v_\theta^\star$ does not depend on φ. In practise, when the axisymmetric asumption is broken, *e.g.* when the spherical bubble experiences an external shear field, the surface viscous shear is solicited. Besides, the variations of $\mathrm{Bo}_{\varkappa_S}$ covers the entire spectrum of interfacial behaviour: when $\mathrm{Bo}_{\varkappa_S} \to 0$, the interface BC is equivalent to a pure slip, and Eq. (D.22) becomes equivalent to Eq. (D.13). Conversely, when $\mathrm{Bo}_{\varkappa_S} \to \infty$, the bubble surface is so contaminated that it behaves like a rigid sphere, and Eq. (D.11) is recovered. The same assessment can be made with the drag coefficient:

$$C_{d,\mathrm{Ed}} = \frac{24}{\mathrm{Re_p}} \frac{2 + \mathrm{Bo}_{\varkappa_S}}{3 + \mathrm{Bo}_{\varkappa_S}}. \tag{D.23}$$

Surface rheology and gaseous spheres in the steady wake regime

When $\mathrm{Re_p} > 1$, the difference between the drag coefficients for rigid and gaseous spheres becomes nearly 50 % wider as $\mathrm{Re_p}$ increases, as shown in Fig. D.7(b). The influence of surfactants can be then even more marked than at low $\mathrm{Re_p}$. However, it is very difficult to have an accurate control over the exact quantity of surfactants introduced

in the system, so that the different flow patterns observed in various experimental investigations cannot be related to a well-known concentration of surfactants [25]. Nonetheless, all the available data confirm that the presence of surfactants causes a strong drop of the terminal velocity value, up to 50 % lower than in the case of a pure interface [98].

In conclusion, we have seen how surface rheology may drive the interfacial dynamics. The boundary condition at the surface of the sphere may evolve from pure slip to no-slip, depending on its rate of contamination, which strongly affects the hydrodynamic flow in the vicinity of the interface. Let us now see what happens when an outer magnetic field is added.

D.3. MHD flow around an obstacle in the presence of a transverse magnetic field

The addition of an external DC magnetic field significantly changes the core flow topology, regardless of the presence of the bubble. As emphasised in the overall introduction (see Sec. I.B.1.a), in the case of a duct flow with insulating walls, the Hartmann layers exert an active control over the core-flow, leading to a typical order of magnitude $V_C^\star \sim O(1/\mathrm{Ha})$ (see App. C). The presence of the gaseous bubble (assimilated with an obstacle) is expected to alter deeply the topology of the MHD core-flow. Indeed, Hartmann layers may develop at the surface of the spherical inclusion, (most likely) depending on the liquid/gas interface BC, *i.e.* in strong interaction with surface rheology. These Hartmann layers may modify the core-flow. Conversely, because the surrounding electroconductive liquid is affected by Lorentz forces, immersed insulating objects can experience noticeable MHD effects in an indirect way. Thus, the interplay between bubble and bulk dynamics (and ultimately surface rheology) is expected to magnify particularly original flow patterns.

In the literature, there are few existing theoretical works describing the MHD of an electroconductive flow past a rigid sphere subjected to an outer transverse DC field, and virtually none past a gaseous sphere (not to mention surface rheology), because of the complexity of the mathematical system of equations. Nonetheless, there is a certain amount of numerical and experimental data, for both aligned and transverse configurations. As previously enhanced, the streamwise (aligned) orientation of the outer field is left aside from the analysis (see [7, 46, 99, 100] for a non-exhaustive list of references). Eventually, all the results presented in this section consider a no-slip BC at the surface of the obstacle; to our knowledge, there are no existing study on the MHD flow past obstacles, which consider a *mechanically* varying BC at the interface between the immersed body and the surrounding fluid. The most significant achievements concerning the transverse layout are now highlighted, beginning with an insightful analytical approach to the 3-D flow around an obstacle in the case $\mathrm{Ha} \gg \mathrm{Re}$ and $\mathrm{Ha} \gg 1$, for which the most salient features appear.

D.3.a. Analytical approach to the 3-D MHD flow past an obstacle when $\mathrm{Ha} \gg \mathrm{Re}$ and $\mathrm{Ha} \gg 1$

The following analysis mainly bears on the reference article written by Hunt and Ludford [55], and clarified later in such classical MHD textbooks as [4]. The main steps of the calculation are included, in as much they unveil significant properties of the original MHD flow patterns emerging past a 3-D obstacle.

Flow structure

In the original article, an obstacle of arbitrary shape is considered. In the following section, though, we shall only consider a motionless rigid spherical obstacle with diameter d, so that a no-slip BC is implemented at the surface. This obstacle is placed in a square duct electro-conductive flow, with typical extent L along $\vec{e}_y$ (corresponding to half the width of the duct), and unbounded in the $\vec{e}_x$ and in the $\vec{e}_z$, with a typical (maximum) velocity V far from the obstacle, and subjected to an external DC magnetic field $\vec{B}_0$. A sketch of the geometrical layout is displayed in Fig. D.11. The usual dimensionless numbers describing the MHD flows are:

$$\mathrm{Ha} = B_0 L \frac{\sigma}{\eta},\ \mathrm{Re} = \frac{\rho V L}{\eta},\ \mathrm{N} = \frac{\mathrm{Ha}^2}{\mathrm{Re}} = \frac{\sigma B_0^2 L}{\rho V}, \tag{D.24}$$

where Ha, Re and N are the Hartmann, Reynolds and Stuart numbers, respectively. Within the assumption $\mathrm{N}, \mathrm{Ha} \gg 1$ (which only implies $\mathrm{Ha}^2 \gg \mathrm{Re}$, Re being potentially large), some original features appear. The flow is indeed structured into two main regions, where the velocity $\vec{v}$ gradients and current density $\vec{j}$ gradients are weak: a column C, whose axis is aligned with $\vec{B}_0$, circumscribing the sphere, and the region E external to this column. The gradients of $\vec{v}$ and $\vec{j}$ are actually located in thin layers: the Hartmann layer between the obstacle and the column C, denoted HS, the (classical) Hartmann layers located near the duct walls, called HW, and an intermediate region SL constituting a parallel (or Shercliff) layer between C and E. The Hartmann layers exhibit a typical thickness $\delta_H^\star = 1/\mathrm{Ha}$, while the Shercliff layer is $\delta_{SL}^\star = 1/\sqrt{\mathrm{Ha}}$-thick. The different flow areas are highlighted in Fig. D.11. The most insightful properties pertaining to each region are now detailed. Note that here $\vec{B}_0$ is aligned with the $\vec{e}_y$ axis, meaning that we shall take $y \to z$, $z \to -y$ for the sake of comparisons with our own approach where $\vec{B}_0$ shall be aligned with $\vec{e}_z$.

Regions C and E

These regions constitute the core-flow areas, E and C being the internal and external core-flow regions, respectively. They are deeply impacted by the different boundary layers, and are of primary interest in view of analysing the impact of the spherical obstacle on the bulk MHD flow. We shall then introduce the most significant physical features common to the two regions, then we shall detail the properties pertaining to each separate area.

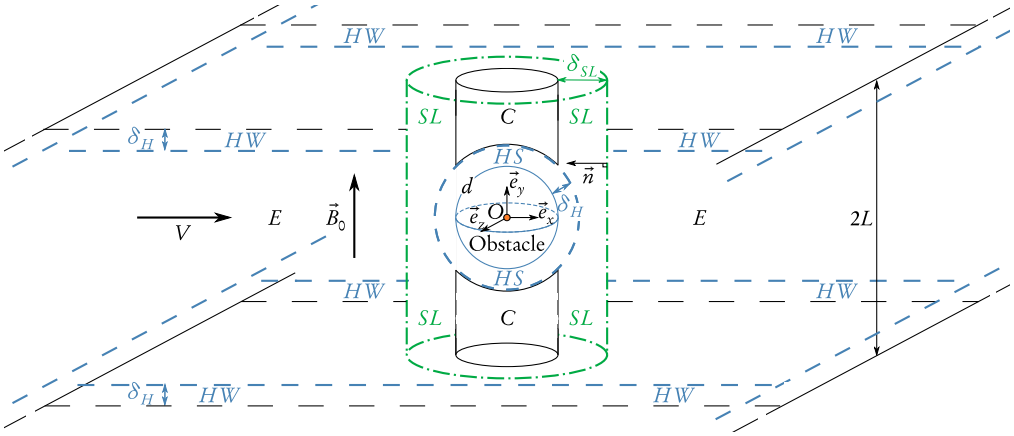

Figure D.11 – Different regions of the MHD flow (not to scale) around a sphere when $\mathrm{Ha}, \mathrm{N} \gg 1$ [55].

On the general solution for flow between two non-conductive surfaces

In these areas, viscosity effects are negligible, and after an appropriate scaling, the dimensionless Navier-Stokes equation can be written within the assumption $\mathrm{N} \gg 1$:

$$0 = -\overrightarrow{\mathrm{grad}}\left(\frac{p^\star}{\mathrm{N}}\right) + \vec{j}^\star \times \vec{e}_y. \tag{D.25}$$

It immediately follows that $\partial(p^\star/\mathrm{N})/\partial y^\star = 0$, and by taking the curl of Eq. (D.25), $\partial \vec{j}^\star/\partial y^\star = 0$. The $\vec{j}$-formulation of the induction equation writes (see Eq. (II.A.14)):

$$\overrightarrow{\mathrm{curl}}^\star\left(\vec{j}^\star\right) = \frac{\partial \vec{v}^\star}{\partial y^\star}, \tag{D.26}$$

which leads to:

$$\frac{\partial^2 \vec{v}^\star}{\partial {y^\star}^2} = 0. \tag{D.27}$$

We can now deduce the general form of the core solution:

$$\begin{aligned} v_x^\star &= -\frac{\partial \phi}{\partial x^\star} - \frac{\partial \psi}{\partial z^\star} + y^\star \frac{\partial g}{\partial z^\star}, \quad v_y^\star = h + y^\star\left(\frac{\partial^2 \phi}{\partial {x^\star}^2} + \frac{\partial^2 \phi}{\partial {z^\star}^2}\right), \\ v_z^\star &= -\frac{\partial \phi}{\partial z^\star} + \frac{\partial \psi}{\partial x^\star} - y^\star \frac{\partial g}{\partial z^\star}, \quad p^\star = \mathrm{N}\phi, \end{aligned} \tag{D.28}$$

where ϕ, ψ, g and h are unknown functions of $x^\star$ and $z^\star$ only. Ohm's law leads to:

$$j_x^\star = \frac{\partial \phi}{\partial z^\star}, \quad j_y^\star = -g, \quad j_z^\star = -\frac{\partial \phi}{\partial x^\star}. \tag{D.29}$$

Let us consider the general solution for the flow between two non-conductive surfaces of arbitrary shape, described by $y^\star = y_1(x^\star, z^\star)$ and $y^\star = y_2(x^\star, z^\star)$ (or equivalently $f_i(x^\star, y^\star, z^\star) = y^\star - y_i(x^\star, z^\star) = 0, i = 1, 2$). At leading order, the Hartmann

layer HS imposes that $\vec{v}^\star \cdot \vec{n}$ and $\vec{j}^\star \cdot \vec{n}$ go to zero when $y^\star \to y_i$ ($\vec{n}$ being the outer normal to the surface circumscribing a given area). In the vicinity of the surfaces, these conditions are written [4]:

$$\vec{v}^\star \cdot \vec{n} = \left(\vec{v}^\star \cdot \overrightarrow{\text{grad}^\star}\right) f_i = -\left(\vec{v}^\star \cdot \overrightarrow{\text{grad}^\star}\right) y_i + v_y^\star = 0, \quad -\left(\vec{j}^\star \cdot \overrightarrow{\text{grad}^\star}\right) y_i + j_y^\star = 0,$$

so that four equations can be deduced from Eqs. (D.28) and (D.29) ($i = 1,2$):

$$\frac{\partial y_i}{\partial x^\star}\left(y_i \frac{\partial g}{\partial z^\star} - \frac{\partial \phi}{\partial x^\star} - \frac{\partial \psi}{\partial z^\star}\right) + \frac{\partial y_i}{\partial z^\star}\left(-y_i \frac{\partial g}{\partial x^\star} - \frac{\partial \phi}{\partial z^\star} + \frac{\partial \psi}{\partial x^\star}\right) = y_i \Delta\phi + h, \tag{D.30}$$

and

$$\frac{\partial y_i}{\partial x^\star}\frac{\partial \phi}{\partial z^\star} - \frac{\partial y_i}{\partial z^\star}\frac{\partial \phi}{\partial x^\star} = -g, \tag{D.31}$$

Subtracting the two equations (D.31) leads to $\overrightarrow{\text{grad}}(y_1 - y_2) \times \overrightarrow{\text{grad}}(\phi) = 0$, meaning that $\phi(x^\star, y^\star)$ does only depend on the local thickness $e = y_1 - y_2$. We can thus denote $\phi(x^\star, y^\star) = \Phi(e)$. The two relations (D.31) are then reduced to:

$$g = \frac{\mathrm{d}\Phi}{\mathrm{d}e}\left(\frac{\partial y_1}{\partial x^\star}\frac{\partial y_2}{\partial z^\star} - \frac{\partial y_1}{\partial z^\star}\frac{\partial y_2}{\partial x^\star}\right). \tag{D.32}$$

Eventually, when $\Phi(e)$ is known, the three equations Eqs. (D.30) and (D.32) lead to the solution for ψ, g, and h.

The external region E

In the region far from the obstacle, and comprised between the walls $y_1 = 1$ and $y_2 = -1$, Eqs. (D.28), (D.29) and (D.32) give:

$$g = j_y^\star = \frac{\partial v_x^\star}{\partial y^\star} = \frac{\partial v_z^\star}{\partial y^\star} = 0.$$

The sum of the two equations (D.30) reduces to $h = 0$, and the BCs for $v_y^\star$ at the walls require $\Delta\phi = 0$. The flow in E is thus planar ($v_y^\star = 0$), and is derived from a stream function $\Psi = \psi + \overline{\phi}$, where $\overline{\phi}$ is the harmonic conjugate of ϕ, such as:

$$\Delta\Psi = 0, \; v_x^\star = -\frac{\partial \Psi}{\partial z^\star}, \; v_z^\star = \frac{\partial \Psi}{\partial x^\star}. \tag{D.33}$$

The Hartmann layers at the walls impose also that the flow is a curl-free. Finally, to solve for Eq. (D.33), the conditions on the contour of the column C must be known, which leads us to the analysis of C and of the parallel layer.

The internal region C

For the sake of simplicity, we shall only focus on the $y^\star > 0$ part (the reasoning being symmetric for $y^\star < 0$). In this area, $y_1^\star = 1$, but this time $y^\star = y_2(x^\star, z^\star)$ at the surface of the obstacle, so that Eqs. (D.30) and (D.32) do not degenerate. They imply:

$$g = 0, \quad \phi = \Phi(1 - y_2) = \overline{\Phi}(y_2),$$

so that

$$v_x^\star = -\frac{\mathrm{d}\overline{\Phi}}{\mathrm{d}y_2}\frac{\partial y_2}{\partial x^\star} - \frac{\partial \psi}{\partial z^\star}, \quad v_z^\star = -\frac{\mathrm{d}\overline{\Phi}}{\mathrm{d}y_2}\frac{\partial y_2}{\partial z^\star} + \frac{\partial \psi}{\partial x^\star}. \tag{D.34}$$

The constraint imposed by the Hartmann layers allow to close the problem in the C region. Indeed, only $\overline{\Phi} = \mathrm{Cst}$ is acceptable. Any other choice gives circulating currents in C, closing themselves on cylinders with $\vec{e}_y$-axis, accompanied by non-zero total mass flux across them, according to Eq. (D.34). This is incompatible with the condition $\vec{v}^\star \cdot \vec{n} = 0$ at the boundary of both HS and HW layers, which cannot feed the flow rate from the ends of the cylinder section. The only possibility is:

$$v_x^\star = v_y^\star = v_z^\star = j_x^\star = j_y^\star = j_z^\star = 0. \tag{D.35}$$

The column C is at rest, and no electric current can flow through it. We refer to this area as Hunt's wake, using thereby the terminology adopted by Dousset and coworkers [58].

***The parallel layer** S*

A planar curl-free flow in the external core region E, a motionless column in the internal core region C: the existence of the parallel layer S stems from the observation of the velocity discontinuity between these two regions. Provided that the electric current in the core $\vec{j}^{\star(E)} = O(1/\mathrm{Ha})$ (which is the case for duct flows with insulating walls, as shown in Sec. I.B.1.a or in App. C), the balance between electromagnetic and viscous forces in this layer can be written [55]:

$$\frac{\partial^4 v_\zeta^\star}{\partial {\xi^\star}^4} - \mathrm{Ha}^2 \frac{\partial^2 v_\zeta^\star}{\partial {y^\star}^2} = 0, \tag{D.36}$$

where $\xi^\star = x^\star \delta_{SL}^\star, y^\star$ and $\zeta^\star$ represent the (curvilinear) coordinates respectively normal to the boundary of C, parallel to the generatrices of C, and tangent to C in the $(\vec{e}_x, \vec{e}_z)$ plane, and where $v_\xi^\star, v_y^\star$ and $v_\zeta^\star$ are the velocity components along these curvilinear directions.

The boundary conditions impose the asymptotic matching with the values in the core regions:

$$\lim_{\xi^\star \to +\infty} \vec{v}^\star = 0, \tag{D.37}$$

$$\lim_{\xi^\star \to -\infty} v_\xi^\star = v_\xi^{\star(E)}, \lim_{\xi^\star \to -\infty} v_y^\star = 0, \lim_{\xi^\star \to -\infty} v_\zeta^\star = v_\zeta^{\star(E)} = O(1). \tag{D.38}$$

The last BC $\lim_{\xi^\star\to-\infty} v_\zeta^\star = O(1)$ is particularly significant, for it ensures that no velocity component can be $O(\delta_{SL}^\star)$ in the core-flow (where $\vec{v}^\star = O(1)$ by hypothesis). Finally, the HW layers require that:

$$v_y^\star(y^\star = \pm 1) = 0. \tag{D.39}$$

The mathematical problem is thus definitely closed, and the asymptotic matched expansion based on $1/\mathrm{N} \ll 1$ provides the following solution [55]:

$$v_\xi^\star = \frac{v_\xi^{\star(E)}}{2}\left(1-\mathrm{erf}\left(\frac{\xi^\star}{2}\sqrt{\frac{\mathrm{Ha}}{y^\star}}\right)\right), \quad v_y^\star = 0, \quad v_\zeta^\star = \frac{W(\xi^\star)}{2}\sqrt{\frac{\mathrm{Ha}}{\pi y^\star}}\,\mathrm{e}^{-\frac{\xi^{\star 2}\mathrm{Ha}}{4y^\star}}, \tag{D.40}$$

where $\mathrm{d}W/\mathrm{d}\xi^\star = v_\xi^{\star(E)}$. The electric current component follow by invoking the induction and the continuity equations. From Eq. (D.40), we can deduce that the requirement that no velocity component can be $O(\delta_{SL}^\star)$ in the core-flow leads to:

$$v_\zeta^{\star(E)} = 0. \tag{D.41}$$

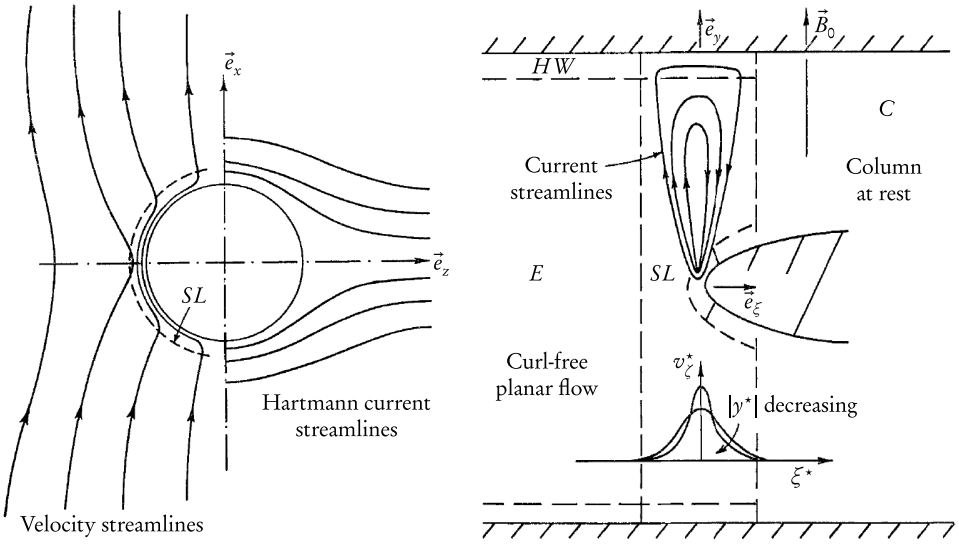

(a) – Streamlines and current lines for flow over a non-conducting sphere.

(b) – Flow in the shear layer: current streamlines and graph of $v_\zeta^\star$ at constant values of $y^\star$.

Figure D.12 – Typical flow patterns past a spherical obstacle when $\mathrm{Ha}, \mathrm{N} \gg 1$[55].

Completion of the solution and insightful results

Eq. (D.41) reads:

$$\frac{\partial \Psi}{\partial n^\star} = 0, \tag{D.42}$$

where $\vec{n}$ is the normal to the cylinder circumscribing the SL region, pointing from E towards SL (see Fig. D.11). The surface of this cylinder is thus an equipotential surface of the curl-free plane flow. The last condition is

$$\Psi = V z^\star \text{ at large distances,} \tag{D.43}$$

The flow is then entirely determined. An overview of the most significant results is proposed in Fig. D.12. As shown in Fig. D.12(a), the velocity field in the external core region is analogous to the electric field in vacuum around a perfectly conducting cylinder. The streamlines penetrate into the column perpendicularly to its boundary, but circles round the internal core to concentrate in the shear layer, where a large component $v_\zeta^\star = O(\delta_{SL}^\star)$ appears, as confirmed by Fig. D.12(b). In this layer, the electric current streamlines close themselves up; these $O(1)$ currents cannot be extracted neither by the inner ($j^{\star(E)} = O(1/\mathrm{Ha})$) or outer ($j^{\star(C)} = 0$) core regions, nor by the HW layers, which carry an electric current in coherence with the flow *ad infinitum* [4]. Such original flow patterns are really specific to MHD phenomena, and illustrate once again the promising features of two-phase MHD flows, in link with the outstanding properties of the Hartmann layers. In the case of a (rigid) bubble rising in a quiescent flow subjected to a strong outer magnetic field, Hunt's wake should follow the bubble trajectory along its ascent in the duct. The addition of surface rheology at the bubble surface is expected to add even more salient features.

Drag coefficient and other flow regimes

The emergence of Hunt's wake leads to a considerable increase of the drag coefficient. The progressive formation of a *ghost* [58] cylinder at rest encapsulating the bubble leads to very strong velocity gradients with the outer core region. These gradients are smoothed over the $O(1/\sqrt{\mathrm{Ha}})$-thin shear layer, leading to a an intensifying tangential stress with increasing Ha. For the sake of consistency with the pure hydrodynamic case, where the drag coefficients are given with respect to a particulate Reynolds number, based on the bubble diameter, let us define:

$$\mathrm{Ha_p} = B_0 d \sqrt{\frac{\sigma}{\eta}},\ \mathrm{N_p} = \frac{\mathrm{Ha_p}^2}{\mathrm{Re_p}}. \tag{D.44}$$

$\mathrm{Ha_p}$ and $\mathrm{N_p}$ are the particulate Hartmann and Stuart numbers, respectively. The drag coefficient due to the electromagnetic contribution that derives from this asymptotic theory is [101]:

$$C_{d,\mathrm{Hunt}} = 8\frac{\mathrm{Ha_p}}{\mathrm{Re_p}} \text{ for } \mathrm{Ha_p} \gg \mathrm{Re_p}, \mathrm{Ha_p} \gg 1. \tag{D.45}$$

Note that this "electromagnetic drag coefficient" must be added to the corresponding hydrodynamic drag coefficient for the same $\mathrm{Re_p}$, in order to obtain the global drag coefficient. Now, regarding the electromagnetic drag coefficient, we can cite other

analytical works, allowing us to complete the asymptotic approach of Hunt and Ludford. Thus, the case $\mathrm{Re_p}, \mathrm{Ha_p} \ll 1$, corresponding to the electromagnetic Stokes flow, has been analytically solved, and leads to the electromagnetic drag coefficient [102]:

$$C_{d,\mathrm{Gotoh}} = \frac{27}{2}\frac{\mathrm{Ha_p}}{\mathrm{Re_p}} \text{ for } \mathrm{Re_p}, \mathrm{Ha_p} \ll 1. \tag{D.46}$$

Finally, the case $\mathrm{N_p} \ll 1, \mathrm{Re_p} \gg 1$ is investigated in [103], leading to:

$$C_{d,\mathrm{Reitz}} = \frac{3}{10}\mathrm{N_p} \text{ for } \mathrm{N_p} \ll 1, \mathrm{Re_p} \gg 1. \tag{D.47}$$

Let us now describe the numerical and experimental results allowing for exploring other combinations of (Re, Ha, N) values.

D.3.b. Numerical and experimental results of MHD flows past an obstacle

Numerical investigations

In every numerical simulation dealing with MHD flows, the most challenging issue is always connected to the modelling of the Hartmann layers. The typical thickness of these layers is indeed $O(1/\mathrm{Ha})$, which means that they can become very thin relative to the typical size of the numerical layout, even for relatively small Ha. However, as it has been enhanced throughout this entire work, Hartmann layers exert an active control over the bulk flow. Despite their thinness, it is most important to mesh properly these regions (or implement equivalent wall-functions, such as [104]), so that the essential physics is captured.

Provided this issue is correctly addressed, the numerical simulations allow to extrapolate the results obtained in the asymptotic theory for different N values. In a rather different context, Dousset and co-workers [58] have numerically confirmed the progressive emergence of Hunt's wake. In this case, the obstacle consists of a truncated cylinder. Depending on the Re value, the blocked column appears above the cylinder upper face, up to the top Hartmann walls (see Fig. D.13(a)). Outside this region, the flow is quasi 2-D. When Re is increased at a given Ha, so that N decreases, Hunt's wake is gradually pushed downstream by the free stream (see Fig. D.13(b)). The flow may thus switch from a vertical (electromagnetic) to a horizontal (hydrodynamic) steady wake. To our knowledge, this is the only numerical evidence of Hunt's wake available in the literature.

In addition to the velocity profiles, the typical distribution of electric current densities and Lorentz force past an obstacle can be determined, as shown in Fig. D.14. It may be first noted that the results of Dousset *et al.* [58] are also added, despite the quite different flow configurations (duct flow past an insulating truncated square-cylinder of typical width w). The interest of the latter simulations is that they allow to show the electric current streamlines in different cross-sections of the duct, located upstream, across and downstream (not shown) the obstacle, for Ha values corresponding to the maximum values used in our upcoming numerical approach to the bubble

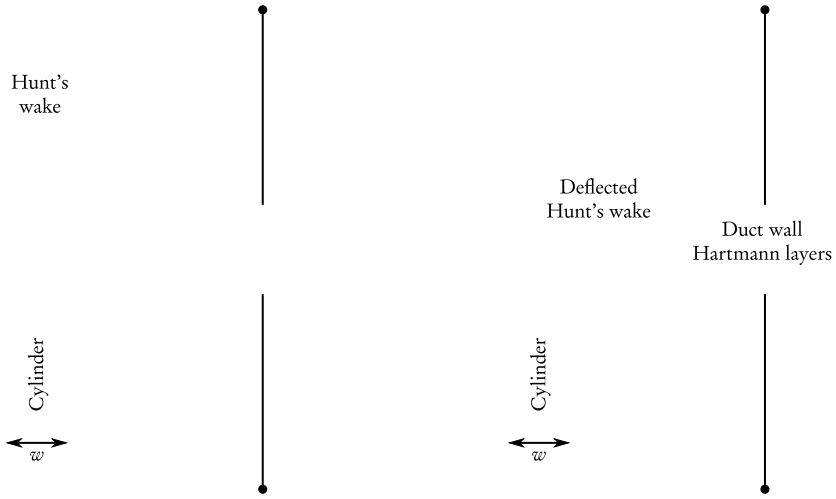

(a) – Streamwise velocity magnitude, $\mathrm{Re_w} = 1$. **(b)** – Streamwise velocity magnitude, $\mathrm{Re_w} = 50$.

Figure D.13 – Hunt's wake past a truncated cylinder, at $\mathrm{Ha} = 200$, for different $\mathrm{Re_w} = \rho V w/\eta$ (flow from left to right, color-scale: higher magnitude from blue to red) [58].

MHD problem. Upstream the cylinder (Fig. D.14(c)a)), the characteristic flow patterns of the Shercliff flow are observed. Similarly, downstream of the cylinder, the perturbations induced by the obstacle gradually dissipates, and the Shercliff flow patterns are gradually recovered (not shown). With respect to the section across the cylinder (Fig. D.14(c)b)), and keeping in mind the comparison with the spherical obstacle case, let us only focus on the upper half of the duct. The electric current streamlines accumulates in the region above the cylinder tip, which explains the flow braking observed with the emergence of Hunt's wake. Finally, at the trailing edge of the cylinder upper face, the flow "washes down" into the rear of the cylinder. Similar flow patterns are expected in the case of a spherical obstacle.

Now, back to the spherical obstacle, a numerical study at low-to-moderate particulate Hartmann numbers values ($\mathrm{Ha_p} < 20$) about the magnetohydrodynamics of insulating spheres is proposed in [89, 106]. The distribution of electric currents past the sphere (Fig. D.14(b)) leads to an increase of the drag coefficient with increasing Ha, due to velocity gradients along the azimuthal direction. The evolution of the drag coefficient with respect to $\mathrm{N_p}$ is shown in Fig. D.15(a). The drag coefficients calculated from Eqs. (D.45) and (D.47) are also indicated as asymptotic references, and the agreement between the numerical modelling and the theoretical predictions seems quite satisfying. As expected, for a given $\mathrm{Re_p}$, the electromagnetic drag coefficient increases with $\mathrm{N_p}$. This increase could be fitted with a power function of the parameter $\mathrm{N_p}$:

$$C_{d,\mathrm{em}} = C_d - C_{d,\mathrm{Wham}} = f(\mathrm{Re_p})\mathrm{N_p}^n.$$

The last interesting feature of numerical studies concerns the shape of gas bubbles rising in a liquid metal subjected to an outer transverse DC field. Recent simulations [105] (Fig. D.14(a)) based on the VOF method to track the interface show that a transverse magnetic field acts to make a bubble more spherical. This observation

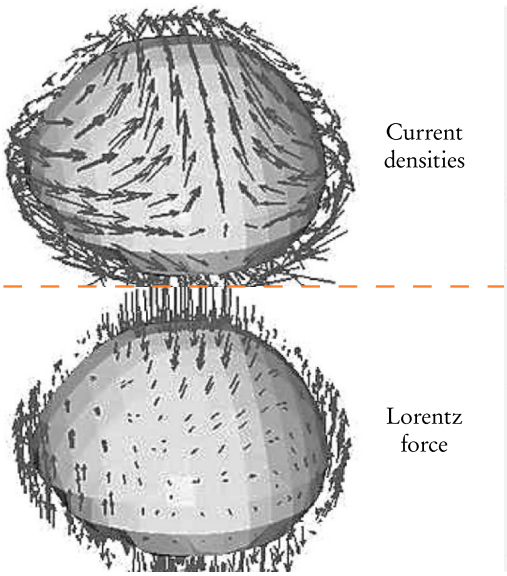

(a) – Distribution of eddy currents and Lorentz force at the surface of gas bubbles rising in a liquid metal [105].

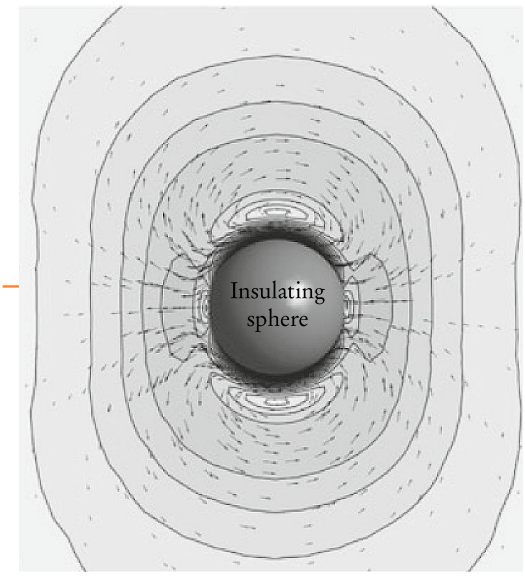

(b) – Current densities vectors (arrows) and magnitude (greyscale) in the vicinity of an insulating sphere with diameter d: $\mathrm{Re}_p = 10$, $\mathrm{Ha}_p = 2$ [89].

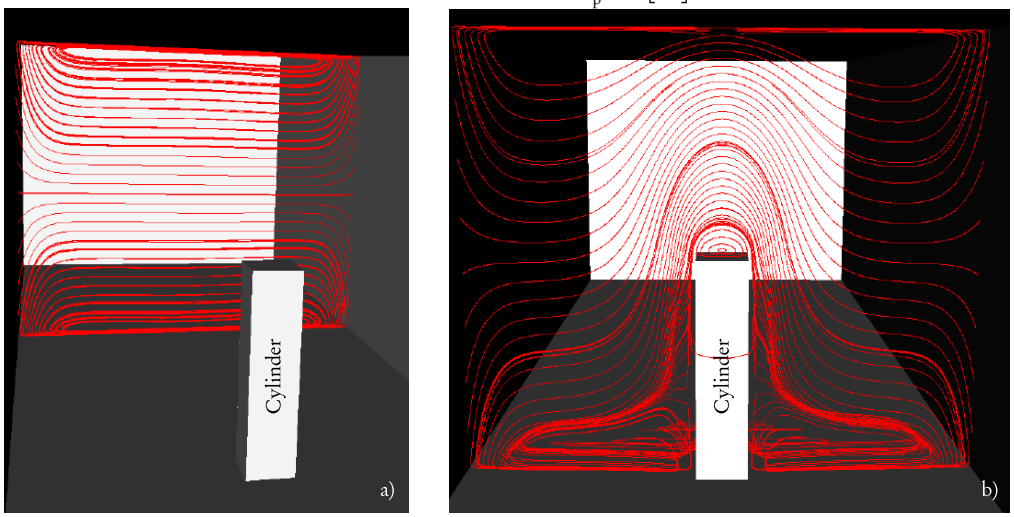

(c) – Electric streamlines of the MHD flow past a truncated cylinder, $\mathrm{Re}_w = \rho V w/\eta = 100$, $\mathrm{Ha} = 100$ [58]. a): upstream the obstacle, b): across the obstacle. Flow from back to front.

Figure D.14 – Electric current streamlines for different MHD flows past obstacles.

actually endorses our assumption of a spherical bubble. Let us now end this review of MHD flows past obstacles in a transverse magnetic field with some significant experimental results.

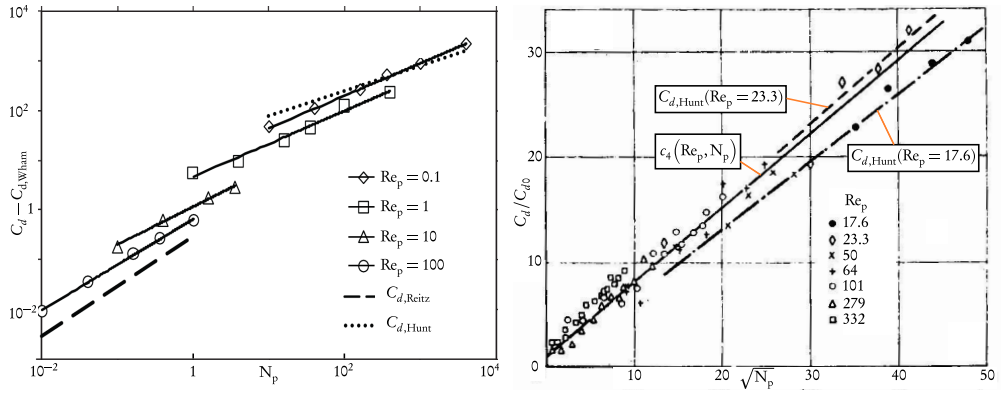

(a) – Drag coefficient: numerical simulations [89]. **(b)** – Drag coefficient: experimental data [4, 107].

Figure D.15 – Drag coefficients of spheres placed in a MHD flow: numerical and experimental results.

Experimental investigations

Obviously, the most challenging issues faced by MHD experiments on liquid metals is the opaque nature of the fluid. The access to the velocity field is possible, but requires more sophisticated methods, such as ultra-sound Doppler velocimetry (UDV) (see, *e.g.* [46]) or X-ray radioscopy [108]. It thus reveals quite complicated to access to detailed flow patterns. However, it is possible to determine some global properties of the liquid metal flow. Thus, in the case of the drag on spheres immersed in a liquid metal, in the presence of a strong transverse magnetic field, a reference study carried out by Branover *et al.* [107] has given rise to the following empirical law for the global drag coefficient, valid for a wide range of $(\mathrm{Re_p}, \mathrm{Ha_p}, \mathrm{N_p})$ values in most practical cases:

$$C_{d,\mathrm{Br}} = c_5\left(\mathrm{Re_p}, \mathrm{N_p}\right) = C_{d,\mathrm{Wham}} \cdot \left(1 + 0.7\sqrt{\mathrm{N_p}}\right), \ \forall (\mathrm{Re_p}, \mathrm{Ha_p}, \mathrm{N_p}), \tag{D.48}$$

where $C_{d,\mathrm{Wham}}$ corresponds to the drag coefficient of Eq. (D.19), in the absence of the magnetic field, at a given $\mathrm{Re_p}$ value. The experimental results found in [107], along with the correlation (D.48), are displayed in Fig. D.15(b). For the sake of comparison, the two curves corresponding to the drag coefficient calculated from Eq. (D.45) at $\mathrm{Re_p} = 17.6$ and $\mathrm{Re_p} = 23.3$ are also shown. The agreement is excellent between experimental results and theoretical predictions.

In conclusion, the previous analytical, numerical and experimental results about the bubble (magneto)hydrodynamics has allowed us to constitute a review of the most salient physical features in link with the bubble MHD problem. All the previous qualitative and quantitative observations about the typical hydrodynamic or MHD flow patterns past a spherical obstacle shall serve as multiple benchmarks for upcoming numerical studies. Let us finally discuss about the typical physical modelling of the bubble MHD problem, and point out some insightful numerical issues in link with the implementation of surface dynamics.

D.4. Some hints at the numerical implementation of the bubble MHD problem

In this section, the typical bubble MHD layout is introduced, along with the governing equations and boundary conditions. A final comment is also added, about a general weak formulation of the JMB. The following approach constitutes in fact the preparatory work for future FEM simulations of the bubble MHD problem.

D.4.a. Geometry, notations, governing equations and boundary conditions

Geometry

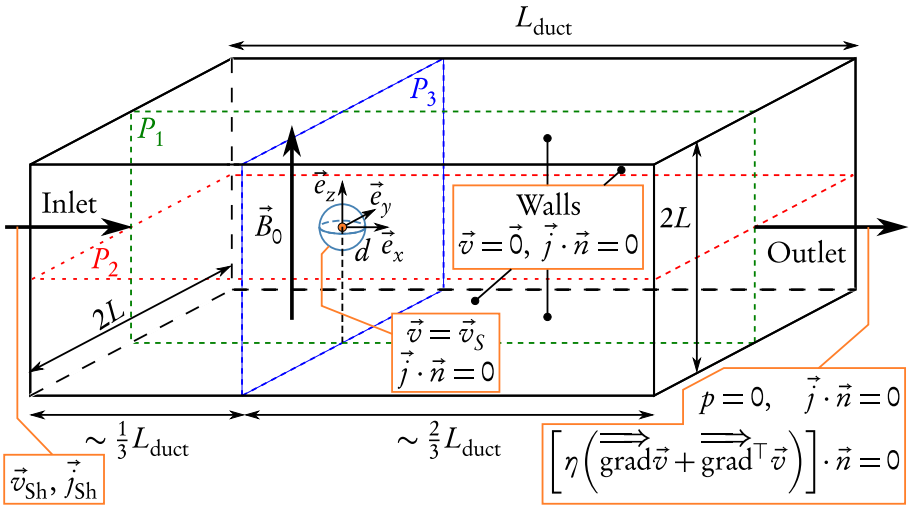

Figure D.16 – Geometry (not to scale), boundary conditions, and cutting planes for post-treatment.

The suspending fluid under consideration is Galinstan, whose physical properties are collected in Tab. I.B.1. A typical geometrical layout is given in Fig. D.16, along with the electromagnetic and dynamic BCs. The bubble with diameter d (typically: $d=10^{-2}$ m) is placed in the duct, whose typical length L (*e.g.* : $L\in[4d,6d]$) is the half-height of the square cross-section. The blockage ratio is $\lambda=d/2L$. Typically, $\lambda\in[0.08,0.125]$: if it is larger, the confinement would greatly influence the hydrodynamic flow, if it is smaller, mesh size could rapidly become prohibitive. The origin of the Cartesian system of coordinates $(O,\vec{e}_x,\vec{e}_y,\vec{e}_z)$ is located at the centre of the spherical inclusion. The bubble should be slightly shifted from the centre of the duct, whose streamwise extension along the $\vec{e}_x$ axis is L_{duct}. The latter should be equal to a couple of times the length L, so that the development of the wake at the rear of the sphere is undisturbed by the outlet boundary condition. The flow far from the sphere flows along the $\vec{e}_x$ direction, while the outer magnetic field is oriented along the $\vec{e}_z$ direction. Finally, the following cutting planes could be defined for post treatment, as shown in Fig. D.16: P_1, P_2 and P_3 refer to the (xz), (xy) and (yz) planes passing through O.

Notations, dimensionless parameters and flow regimes

The physical quantities of interest are expressed in the Cartesian system of coordinates: first, the velocity field $\vec{v} = v_x(x,y,z)\vec{e}_x + v_y(x,y,z)\vec{e}_y + v_z(x,y,z)\vec{e}_z$, then, the pressure $p = p(x,y,z)$, and at length, using generalised Ohm's law, the electric current densities $\vec{j} = j_x(x,y,z)\vec{e}_x + j_y(x,y,z)\vec{e}_y + j_z(x,y,z)\vec{e}_z$, the latter being deduced from the electric potential $\phi = \phi(x,y,z)$.

With respect to bulk dimensionless quantities, two typical lengths can be chosen to scale the governing equations, *i.e.* the sphere diameter d or the typical duct length L. This leads to two set of dimensionless parameters, *i.e.* the Reynolds, Hartmann and Stuart numbers Re, Ha and N, based on L, or the particulate Reynolds, Hartmann and Stuart numbers, *i.e.* $\mathrm{Re_p}$, $\mathrm{Ha_p}$ and $\mathrm{N_p}$, based on the diameter d of the spherical inclusion. Depending on their respective values, different flow regimes should be distinguished. If $\mathrm{Ha} = \mathrm{N} = \mathrm{Ha_p} = \mathrm{N_p} = 0$, two distinct hydrodynamic flow regimes could be investigated, whatever the surface BC: the Stokes flow regime for $\mathrm{Re_p} < 1$, and the steady wake regime for $1 \leq \mathrm{Re_p} \leq \mathrm{Re_{p,max}} = 130$, the latter corresponding to the onset of wake instability, which does no enter the scope of this thesis work. When the outer magnetic field is added, in the limit $\mathrm{N}, \mathrm{N_p} \gg 1$ and for a no-slip BC at the surface of the sphere, Hunt's wake flow regime should be gradually reached, with the emergence of the blocked column on both sides of the sphere. Other combinations of bulk dimensionless parameters correspond to intermediate flow regimes. Concerning surface quantities, the Boussinesq numbers $\mathrm{Bo}_{\eta_S}, \mathrm{Bo}_{\varkappa_S}$ defined in Eq. II.B.10 allow for the accurate description of surface dynamics, from perfect slip to no-slip BC.

All the bulk physical quantities should seemingly be scaled with the length L (along with $\vec{v}_S$), which reveals more convenient to discuss the MHD flow patterns, while d is more convenient for purely hydrodynamic patterns. The latter observation explains why a mixed terminology ($\mathrm{Re_p}$, Ha) should be favoured to set the flow regime, $\mathrm{Re_p}$ characterising the hydrodynamic flow regimes, Ha determining the transition towards Hunt's wake. However, as far as drag coefficients C_d are concerned, particulate dimensionless numbers should be preferred, based on the sphere diameter. It seems indeed more consistent to express the drag coefficients evolution with respect to d, a length characterising the body subjected to the drag force. By the way, benchmarking studies always refer to a dependence on the particulate numbers. Similarly, the Boussinesq numbers should be also based on the sphere diameter (or radius, see Eq. (D.21)). The dimensionless quantities of interest could thus be defined as:

- the Cartesian coordinates: $-L_{\mathrm{duct}}/3L \leq x^\star = x/L \leq 2L_{\mathrm{duct}}/3L$ (for instance), $-1 \leq y^\star = y/L \leq 1$ and $-1 \leq z^\star = z/L \leq 1$;
- the velocity $\vec{v}^\star = \vec{v}/V$, where V corresponds to the maximum value of the inlet velocity;
- the pressure $p^\star = p/\rho V^2$;
- the electric potential $\phi^\star = \phi/LB_0V$
- and finally, the electric current densities: $\vec{j}^\star = \vec{j}/\sigma VB_0$;

MHD equations

A potential formulation based on the electric potential ϕ should be favoured. The basic MHD equations are derived in Sec. II.A.1.d (see Eqs. (II.A.20) for the induction equation and (II.A.28) for Navier-Stokes equations):

$$\Delta^\star \phi^\star = \mathrm{div}^\star\left(\vec{v}^\star \times \vec{e}_z\right), \tag{D.49}$$

$$\left(\vec{v}^\star \cdot \overrightarrow{\mathrm{grad}}^\star\right)\vec{v}^\star = -\overrightarrow{\mathrm{grad}}^\star p^\star + \frac{1}{\mathrm{Re}}\vec{\Delta}^\star \vec{v}^\star + \frac{\mathrm{Ha}^2}{\mathrm{Re}}\vec{j}^\star \times \vec{e}_z. \tag{D.50}$$

These equations are completed the continuity equation for the velocity field:

$$\mathrm{div}\left(\vec{v}^\star\right) = 0, \tag{D.51}$$

and by generalised Ohm's law for the electric current densities:

$$\vec{j}^\star = -\overrightarrow{\mathrm{grad}}(\phi^\star) + \vec{v}^\star \times \vec{e}_z. \tag{D.52}$$

Boundary conditions

The electromagnetic boundary conditions are quite straightforward. The duct walls and the bubble are actually all insulating so that the boundary condition:

$$\vec{j}^\star \cdot \vec{n} = 0, \tag{D.53}$$

is valid everywhere, even at the inlet and the outlet boundaries (see the discussion of Sec. II.A.3.b). In terms of the electric potential, Eq. (D.53) yields:

$$\vec{n} \cdot \overrightarrow{\mathrm{grad}}(\phi^\star) = 0, \tag{D.54}$$

where $\vec{n}$ is the unit normal outer to the considered surface. Eq. (D.54) is true everywhere, except at the outlet, where:

$$\frac{\partial \phi^\star}{\partial x^\star} = v_y^\star, \tag{D.55}$$

and at the surface of the sphere, where (with $\vec{n} = \vec{e}_r$):

$$-\vec{e}_r \cdot \overrightarrow{\mathrm{grad}}(\phi^\star) = -v_y^\star\left(\vec{e}_x \cdot \vec{e}_r\right) + v_x^\star\left(\vec{e}_y \cdot \vec{e}_r\right). \tag{D.56}$$

Now, as far as dynamic conditions are concerned, a no-slip BC is applied at the duct walls:

$$\vec{v}^\star = \vec{0}. \tag{D.57}$$

The inlet and boundary conditions for velocity are (see the discussion pertaining to the inlet/outlet dynamic BCs in Sec. II.A.3.b):

$$\vec{v}^\star\big|_{\mathrm{inlet}} = \vec{v}_{\mathrm{Sh}}^\star,\ p_{\mathrm{outlet}}^\star = 0,\ \left(\overrightarrow{\overrightarrow{\mathrm{grad}}}\vec{v}^\star + \overrightarrow{\overrightarrow{\mathrm{grad}}}^{\star\top}\vec{v}^\star\right)\cdot \vec{n}\Big|_{\mathrm{outlet}} = 0, \tag{D.58}$$

corresponding to the Shercliff velocity profile at the inlet (see App. C) and to a zero-pressure, no viscous stress outlet. Finally, the dynamic BC a the surface of the sphere is generally written:

$$\vec{v}^{\star}\big|_S = \vec{v}_S^{\star}. \tag{D.59}$$

The surface velocity field $\vec{v}_S^{\star}$ is governed by the JMB, whose possible numerical implementation is finally discussed.

D.4.b. 3-D Interfacial dynamics in FEM simulations

Numerical issues

The ultimate aim of numerical investigations about the bubble MHD problem is to highlight the different flow patterns which may result from the original coupling between bubble interfacial dynamics (driven by Bo_{η_S} and $\mathrm{Bo}_{\varkappa_S}$), and the MHD core-flow. For this purpose, and for the same reasons as those exposed in the previous numerical work about the annular MHD viscometer, we have decided to implement the weak form of Eq. (II.B.6) in the selected FEM software, *i.e.* Comsol. However, in this 3-D case, such an implementation has revealed a much more tedious process.

In the numerical investigations of Secs. III.B.2 and III.C, the (natural) system of coordinates is cylindrical for both the bulk flow and the surface dynamics equations. In the present case, the Cartesian coordinates constitute the natural system of coordinates for describing the square-duct flow, while the spherical coordinates are more natural to describe the spherical bubble interfacial dynamics. This conflict between the two system of coordinates has led us to choose the Cartesian system, more convenient for post-treatment, which implies the projection of Eq. (II.B.6) in the $(\vec{e}_x, \vec{e}_y, \vec{e}_z)$ basis. This time-consuming process has not allowed us to implement the full surface rheology formulation.

As it happens, in recent works, the improvement of calculation capacities has leaded to the modelling of deforming bubble dynamics occurring at large Re_p, even for turbulent configurations, through such numerical methods as the volume of fluid (VOF) or level-set methods to capture the interface dynamics. Surface rheology is often taken into account only through surface tension, *e.g.* through a surface tension force term integrated in the bulk equations (see for instance [105]). The deformation of gas bubble is far from the scope of this study, nevertheless one work has retained our attention: in [109], Reusken and Zhang investigate different bubbly flows configuration, by taking into account a Boussinesq-Scriven interface tensor, including both surface and dilatational viscosities. As they perform FEM-based simulations, they explicitly derive the surface stress tensor functional, corresponding to the weak form of the left-hand term of the JMB (see Eq. (II.B.3)). Note that these authors do not focus on the right-hand jump term, because they adopt a level-set method allowing them to circumvent this issue. In the following, we complete their results by adding this jump term to the overall weak form. The resulting expression is valid whatever the considered 3-D geometry, which reveals most valuable when considering the flow past a sphere in a square duct, where two system of coordinates (Cartesian for the duct, spherical for the gaseous inclusion) enter in competition. The only prerequisite is to

be able to define properly the normal to a given surface, which reveals a challenging issue for deforming interfaces, but which does not cause any particular difficulty in the case of a non-deforming bubble. The corresponding mathematical foundations are now briefly exposed, because they shall constitute the cornerstone of future FEM simulations involving the coupling between MHD and surface rheology.

General weak form of the JMB

The $\mathbb{R}^3$ basis is generally denoted $(e_1, e_2, e_3)^\top$, with $\vec{e}_i$ being the ith basis vector. S indicates the liquid/gas interface. Let us project the right-hand term of the JMB (see Eq. (II.B.3)) on the basis of test functions $\vec{w} = (w_1, w_2, w_3)^\top$, from the finite element velocity $\vec{v}$ space. The surface stress tensor functional takes the form:

$$F_S(\vec{w}) = \int_S f_S(\vec{w})\,\mathrm{d}S = \int_S \overrightarrow{\mathrm{div}}_S\left(\overrightarrow{\overrightarrow{T_S}}\right)\cdot\vec{w}\,\mathrm{d}S.$$

After integrating by parts, and making use of mathematical arguments, the previous expressions can be written:

$$F_S(\vec{w}) = -\int_S \mathrm{tr}\left(\overrightarrow{\overrightarrow{T_S}}\bullet\overrightarrow{\overrightarrow{\mathrm{grad}}}(\vec{w})\right)\mathrm{d}S,$$

where tr stands for the matrix trace. The previous equation can be developed by using Eq. (II.B.1), which introduces surface tension γ, and surface shear and dilatation viscosities η_S and $\varkappa_S$:

$$F_S(\vec{w}) = -\int_S \gamma\,\mathrm{tr}\left(\overrightarrow{\overrightarrow{I_S}}\bullet\overrightarrow{\overrightarrow{\mathrm{grad}}}(\vec{w})\right)\mathrm{d}S - \int_S (\varkappa_S-\eta_S)\,\mathrm{div}_S(\vec{v})\,\mathrm{tr}\left(\overrightarrow{\overrightarrow{I_S}}\bullet\overrightarrow{\overrightarrow{\mathrm{grad}}}(\vec{w})\right)\mathrm{d}S$$
$$-\int_S \eta_S\,\mathrm{tr}\left(\left[\overrightarrow{\overrightarrow{I_S}}\bullet\left(\overrightarrow{\overrightarrow{\mathrm{grad}}}_S(\vec{v}) + \overrightarrow{\overrightarrow{\mathrm{grad}}}_S^\top(\vec{v})\right)\bullet\overrightarrow{\overrightarrow{I_S}}\right]\bullet\overrightarrow{\overrightarrow{\mathrm{grad}}}(\vec{w})\right)\mathrm{d}S = I_1 + I_2 + I_3.$$

Let us first explicit the surface tension term by using the trace operator definition:

$$I_1 = -\int_S \sum_{i=1}^{3}\gamma\left(\overrightarrow{\overrightarrow{I_S}}\bullet\vec{e}_i\right)^\top\cdot\overrightarrow{\mathrm{grad}}(w_i)\,\mathrm{d}S.$$

The other terms follow, by using the following identities linked to $\overrightarrow{\overrightarrow{I_S}}$, the surface projection tensor :

$$\overrightarrow{\overrightarrow{I_S}}\bullet\overrightarrow{\overrightarrow{\mathrm{grad}}}_S = \overrightarrow{\overrightarrow{I_S}}\bullet\overrightarrow{\overrightarrow{\mathrm{grad}}},\ \text{and}\ \mathrm{div}_S(\vec{v}) = \left(\overrightarrow{\overrightarrow{I_S}}\bullet\overrightarrow{\overrightarrow{\mathrm{grad}}}\right)\cdot\vec{v}.$$

This yields:

$$I_2 = -\int_S \sum_{i=1}^{3}(\varkappa_S-\eta_S)\left(\left(\overrightarrow{\overrightarrow{I_S}}\bullet\overrightarrow{\overrightarrow{\mathrm{grad}}}\right)\cdot\vec{v}\right)\left(\overrightarrow{\overrightarrow{I_S}}\bullet\vec{e}_i\right)^\top\cdot\overrightarrow{\mathrm{grad}}(w_i)\,\mathrm{d}S,$$

and

$$I_3 = -\int_S \sum_{i=1}^{3} \eta_S \left(\left[\overrightarrow{\overrightarrow{I_S}} \bullet \left(\overrightarrow{\overrightarrow{\mathrm{grad}}}(\vec{v}) + \overrightarrow{\overrightarrow{\mathrm{grad}}}^{\top}(\vec{v}) \right) \bullet \overrightarrow{\overrightarrow{I_S}} \right] \bullet \vec{e}_i \right)^{\top} \cdot \overrightarrow{\mathrm{grad}}(w_i)\, \mathrm{d}S.$$

Finally, the weak form of the surface stress tensor contribution is written by adding the three previous contributions, and the jump term weak contribution, denoted $F_{[\![]\!]}$. The latter is quite straightforward, as it only involves first-order derivatives of the velocity components. Taking the integrand yields:

$$\begin{aligned} f_S(\vec{w}) - f_{[\![]\!]} = -\sum_{i=1}^{3} \Bigg\{ & \gamma \left(\overrightarrow{\overrightarrow{I_S}} \bullet \vec{e}_i \right)^{\top} + (\varkappa_S - \eta_S) \left(\left(\overrightarrow{\overrightarrow{I_S}} \bullet \overrightarrow{\overrightarrow{\mathrm{grad}}} \right) \cdot \vec{v} \right) \left(\overrightarrow{\overrightarrow{I_S}} \bullet \vec{e}_i \right)^{\top} \\ & + \eta_S \left(\left[\overrightarrow{\overrightarrow{I_S}} \bullet \left(\overrightarrow{\overrightarrow{\mathrm{grad}}}(\vec{v}) + \overrightarrow{\overrightarrow{\mathrm{grad}}}^{\top}(\vec{v}) \right) \bullet \overrightarrow{\overrightarrow{I_S}} \right] \bullet \vec{e}_i \right)^{\top} \Bigg\} \cdot \overrightarrow{\mathrm{grad}}(w_i) - \left[\!\!\left[\overrightarrow{\overrightarrow{T}} \cdot \vec{n} \right]\!\!\right] \cdot \vec{w}. \end{aligned} \tag{D.60}$$

Eq. (D.60) is the weak form that should be implemented, *e.g.*, in Comsol, at the interface between two media, to take the influence of a Newtonian interface into account. As previously said, it strongly relies on the possibility of defining the normal $\vec{n}$, which enters in the definition of the surface projection tensor. The main advantage of Eq. (D.60) is that it enables to work in the usual Cartesian basis, without the difficulty of a tedious projection of the surface rheology equations (written normally in spherical coordinates) at the surface of the sphere.

In conclusion, it has been shown how the coupling between MHD and surface rheology, within the framework of the bubble MHD problem, could reveal insightful. When considering separately in the literature the outstanding properties of the MHD flow past an obstacle, and the significant impact of surface rheology on bubble dynamics, salient physical features would certainly arise if the two approaches were merged. The present appendix is thought of as a background step, gathering theoretical, numerical and experimental benchmarks, and constituting guidelines in order to tackle the bubble MHD problem, towards the description of MHD dispersed flows. Because of a lack of time, this remains as an outlook of the present project.

Appendix E. Electrical conductivity of liquid metals: the Micmac experiment

In this appendix, an experimental set-up, called the Micmac (for *Mesure inductive de la conductivité des matériaux (électro)conducteurs* in French) experiment, is proposed as an experimental test-bench for measuring the electrical conductivity of liquid metals. Micmac is based on the eddy-current method, first introduced by Bean *et al.* [110]. After a brief review of the theoretical foundations of this method, the technical developments of Micmac are introduced. The first results obtained for different metallic samples, including the liquid metal Galinstan, are unveiled.

E.1. Motivation and state-of-the-art

E.1.a. Physical issues

In the literature, there are some discrepancies about the value of the electrical conductivity σ of Galinstan [28, 29, 43, 44, 49]. This may be explained by the fact that this liquid metal is an eutectic alloy, and beyond the commercial denomination, the name "Galinstan" has become generic to qualify the alloy based on Tin, Gallium and Indium. The values of σ may significantly vary with the alloy composition. The most usual chemical composition in wt % is $Ga_{67\%}In_{20.5\%}Sn_{12.5\%}$, which corresponds to the particular alloy used in this thesis work. The corresponding usual value of σ for pure Galinstan is indicated in Tab. I.B.1: $\sigma = 3.29 \times 10^6\,\mathrm{S{\cdot}m^{-1}}$. It has been established by means of a standard contact-method in accordance with the four-point scheme [28].

In the latter work, the authors particularly highlight that measurements of the thermophysical properties of Galinstan greatly depend on the oxidation rate of the interface, though they do not quantify such a dependence. As explained in Sec. I.B.2.b, surface oxidation deeply alters the wettability of Galinstan. For contact methods, this wettability is expected to play a significant role in the determination of σ, by introducing an artificial contact resistance.

To the best of our knowledge, there seems to be no available data about the conductivity of gradually oxidising liquid metals. The variation of σ has been apparently considered only from the thermal point of view. Therefore, there is a need to determine the electrical conductivity of the alloy with respect to the purity of the surrounding atmosphere. This is all the more justified when considering the coupling between surface rheology and bulk MHD: the strong gradients of σ near the interface, left aside from the analysis in this thesis work, could actually impact the current density patterns, thus modifying the electric circuit inside the liquid metal. Conse-

quently, we need to set up a contactless, accurate, non-destructive (given the cost of Galinstan samples) experimental method, in order to determine σ in various experimental conditions (temperature, oxidation…). The selected method is based on the eddy-current approach, which is now detailed.

E.1.b. Typical experimental layout and associated physical features

Geometry

The typical experimental set-up under consideration is displayed in Fig. E.1. It derives from the original layout proposed by Bean *et al.* [110]. It essentially consists of a primary circuit, including a DC voltage power supply denoted G, a resistor R_1, a switch, and a primary coil with N_1 turns and inductance L_1. This primary circuit shall also be referred to as the "power circuit" hereafter. A secondary coil with N_2 turns and inductance L_2 is placed into the primary one, and with the associated monitoring and processing unit, they constitute the secondary circuit, or "measurement circuit". Finally, the sample is placed into a chemically neutral and electrically insulating crucible, which is in turn inserted inside the secondary coil.

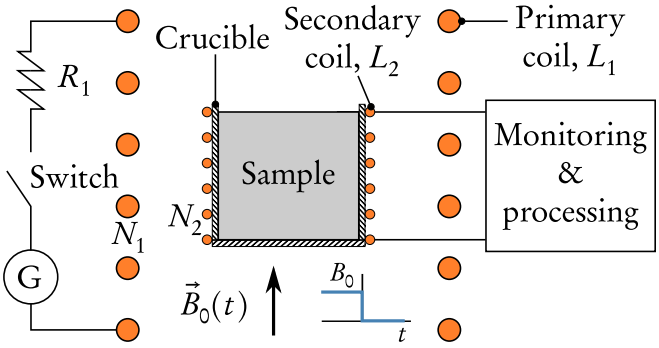

Figure E.1 – Typical layout of eddy current method [110].

Principle

As its name suggests, the eddy-current method bears on the decay of induced electric current in a metallic sample, which is subjected to a sudden magnetic field step. In the original layout, the sample is primarily exposed to a uniform outer DC magnetic field $\vec{B}_0$, generated by the primary coil. This magnetic field is switched off very rapidly, inducing eddy currents in the sample, according to generalised Ohm's law for time-dependent problems:

$$\vec{j} = \sigma \left(-\overrightarrow{\text{grad}}(\phi) + \vec{v} \times \vec{B} - \frac{\partial \vec{A}}{\partial t} \right). \tag{E.1}$$

In this case, the transient term $\partial \vec{A}/\partial t$ constitutes the most significant contribution. The decay of these eddy currents generates a voltage through Faraday's principle,

which can be measured across the secondary coil. The electrical conductivity of the metallic sample can be deduced from the signal, by means of the following theory. In the literature, this method has been used for a collection of solid samples (see, *e.g.*, [111, 112]). As suggested in [113], our aim here is to extend the original scope to liquid samples.

E.1.c. Theory for solid samples

In this section, the original layout considered by Bean *et al.* [110] is analytically investigated. The outer magnetic field $\vec{B}_0$ is instantly switched off.

Governing equations

The magnetic induction equation II.A.8 is used to determine the rate of change of the magnetic flux inside a cylindrical sample with radius R. The rate of change of the magnetic induction is governed by a diffusion-like equation, assuming an isotropic resistivity and permeability and neglecting the displacement currents. It is furthermore assumed that the magnetic induction is only oriented along the $\vec{e}_z$ axis, and that the problem is axisymmetric relative to this axis. Thus: $\vec{B} = (b_z(r,t) + B_0(t))\vec{e}_z$. The ruling equation for the magnetic induction is a diffusion-like equation:

$$\frac{\partial b_z}{\partial t} = \frac{1}{\mu\sigma}\left(\frac{\partial^2 b_z}{\partial r^2} + \frac{1}{r}\frac{\partial b_z}{\partial r}\right). \tag{E.2}$$

Once Eq. (E.2) is solved, $b_z(r,t)$ is known. The voltage measured at the coil terminals is then found through Maxwell-Faraday (MF) equation:

$$\overrightarrow{\text{curl}}\left(\vec{E}\right) = -\frac{\partial \vec{b}}{\partial t},$$

which is integrated for the secondary solenoid with N_2 turns into:

$$V = N_2\frac{\mathrm{d}\Phi}{\mathrm{d}t}, \quad \text{with} \quad \Phi = \iint_S B_z \,\mathrm{d}S. \tag{E.3}$$

for a circular cross-section of the sample with radius R.

Boundary conditions

The boundary conditions for b_z are as follows:

$$b_z(r,0) = B_0 \quad \text{for} \quad r \in [0;R[\,, \tag{E.4}$$

$$b_z(R,t) = 0 \quad \text{for} \quad t > 0. \tag{E.5}$$

Solution

The integration of equation (E.2) has been performed *e.g.* by Wwedensky [114], and yields:

$$b_z(r,t) = \sum_{n=1}^{\infty} A_n \mathscr{J}_0(\alpha_n r) \exp\left(-\frac{\alpha_n^2}{\mu\sigma} t\right),$$

where A_n and α_n are constants, and $\mathscr{J}_0$ is the zero-order Bessel function. Using the theory of Bessel functions (see *e.g.* Gray *et al.* [115]), BC (E.5) yields that $\alpha_n R = \lambda_n$, where λ_n are the successive roots of the zero-order Bessel function. Finally, the boundary condition (E.4) provides:

$$A_n = \frac{2}{\mathscr{J}_0'^2(\lambda_n)} \int_0^R B_0 \mathscr{J}_0\left(\frac{\lambda_n r}{R}\right) r \, \mathrm{d}r = \frac{2B_0}{\lambda_n \mathscr{J}_1(\lambda_n)}.$$

Consequently, the magnetic induction is written:

$$b_z(r,t) = \sum_{n=1}^{\infty} \frac{2B_0}{\lambda_n \mathscr{J}_1(\lambda_n)} \mathscr{J}_0\left(\frac{\lambda_n r}{R}\right) \exp\left(-\frac{\lambda_n^2}{\mu\sigma R^2} t\right). \tag{E.6}$$

Now the magnetic induction is known, Eq. (E.3) is used to determine the voltage. The total magnetic flux across one elementary coil is:

$$\begin{aligned}
\Phi(t) = \iint_S B_z \, \mathrm{d}S &= 2\pi \int_0^R r B_z(r,t) \, \mathrm{d}r \\
&= \sum_{n=1}^{\infty} \frac{4\pi B_0}{\lambda_n \mathscr{J}_1(\lambda_n)} \left[\int_0^R r \mathscr{J}_0\left(\frac{\lambda_n r}{R}\right)\right] \exp\left(-\frac{\lambda_n^2}{\mu\sigma R^2} t\right) \\
&= \sum_{n=1}^{\infty} \frac{4\pi B_0}{\lambda_n \mathscr{J}_1(\lambda_n)} \left[\frac{R^2 \mathscr{J}_1(\lambda_n)}{\lambda_n}\right] \exp\left(-\frac{\lambda_n^2}{\mu\sigma R^2} t\right) \\
&= 4\pi R^2 B_0 \sum_{n=1}^{\infty} \frac{1}{\lambda_n^2} \exp\left(-\frac{\lambda_n^2}{\mu\sigma R^2} t\right).
\end{aligned}$$

The voltage at the terminals of the N_2 spires of the secondary coil is then found by differentiation with respect to time of the previous expression, which leads to:

$$V(t) = \frac{4\pi B_0 N_2}{\mu\sigma} \sum_{n=1}^{\infty} \exp\left(-\frac{\lambda_n^2}{\mu\sigma R^2} t\right).$$

At long times, only the first term remains, and the voltage can be written:

$$V(t) = V_0 \exp\left(-\frac{t}{\tau}\right), \tag{E.7}$$

with $V_0 = 4\pi B_0 N / \mu\sigma$ and $\tau = \mu\sigma R^2 / \lambda_1^2$, where $\lambda_1 = 2.405$ when approximated to the third significant digit.

E.1.d. Applicability to liquid metals

Eq. (E.7) is valid for solid materials. Is it still valid as far as liquid metals are concerned? To address this critical issue, we must check whether the magnetic Reynolds number remains negligibly small or not. The transient Lorentz force $\vec{j} \times \vec{B}$ due to the magnetic field step could put the fluid into motion, so that the magnetic field could be significantly convected.

Let us suppose a balance between viscous and electromagnetic effects in Navier-Stokes equation. This assumption requires that $\mathrm{Re} < 1$, where Re is the Reynolds number based on the radius of the sample. Such an approximation gives $1\,\mathrm{m{\cdot}s^{-1}}$ for the typical velocity, leading to $\mathrm{Re} \sim 10^5$, which enters in contradiction with the small Reynolds assumption. If now, we suppose an equilibrium between inertial and electromagnetic effects, the new velocity order of magnitude is $10^{-2}\,\mathrm{m{\cdot}s^{-1}}$, which gives a consistent value $\mathrm{Re} \sim 10^3$. The corresponding magnetic Reynolds number is $\mathrm{Rm} \lesssim 10^{-2}$. Consequently, we consider that Eq. (E.7) still holds for liquid metals.

E.2. The Micmac experiment

E.2.a. Global electric circuit

The global electric circuit of Micmac is shown in Fig. E.2. Further details about technical developments are given in [116].

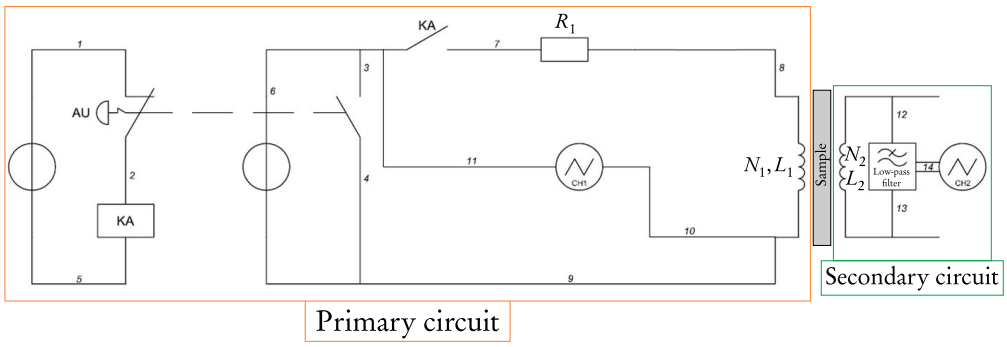

Figure E.2 – Global electric circuit of Micmac [116].

E.2.b. Experimental requirements

Some experimental precautions must be taken, in order to measure the signal corresponding to the decay of eddy currents in the metallic sample. The most significant are the following: first, the secondary coil must be designed with its inductance and distributed capacity being low enough so that its resonant frequency is much higher than $1/\tau$. Besides, the resistance R_1 must be high enough to damp instantly the transient magnetic flux decay of the primary coil, seen by the secondary coil. The characteristics of the primary circuit stem from these requirements:

$$N_1 = 183, L_1 = 938\,\mu\mathrm{H}, R_1 = 22.82\,\Omega, N_2 = 500, L_2 = 7.4\,\mathrm{mH}.$$

The radius of the different cylindrical metallic samples is $R = 12.5\,\text{mm}$.

E.2.c. First experimental results

Experimental protocol

Contrary to Bean *et al.*, the outer magnetic field is instantly switched on in the Micmac experiment. However, the form of the solution is identical to Eq. (E.7), except for the sign. Signals are measured on an oscilloscope after low-pass filtering to reduce experimental noise, and transferred to a processing computer. Then, the data are fitted by means of a least-mean square method, which gives access to the electrical conductivity of the sample.

First results

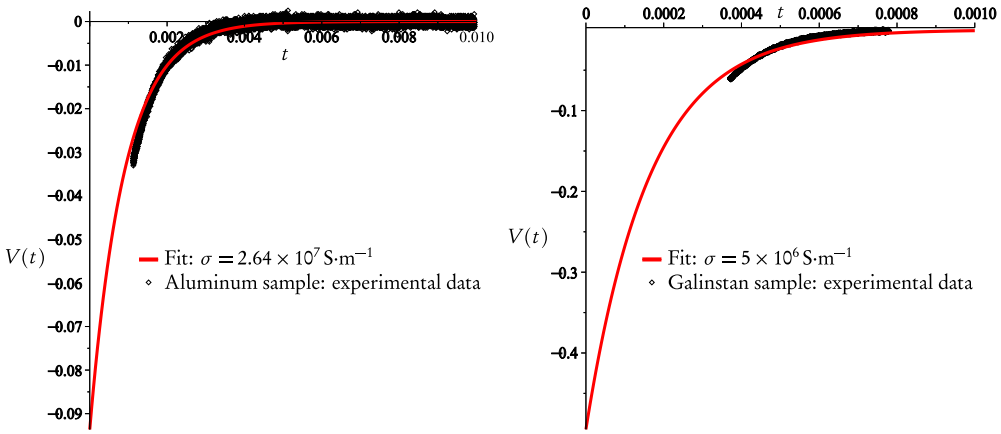

(a) – Solid aluminium sample.

(b) – (Liquid) Galinstan sample.

Figure E.3 – Some Micmac results: t is given in seconds, V in volts.

Some results obtained with Micmac are shown in Fig. E.3. As far as solid samples with high conductivity are concerned, Micmac provides satisfying results, for instance with aluminium in Fig. E.3(a). The fitted curve gives $\sigma = 2.64 \times 10^7\,\text{S·m}^{-1}$, close to the manufacturer data $\sigma = 2.61 \times 10^7\,\text{S·m}^{-1}$. However, for solid samples with low conductivity values, such as stainless steel, the agreement is far worse, with a measured value twice as high as the expected value. This problem is also found with Galinstan exposed to ambient air: as shown in Fig. E.3(b), the fitting gives $\sigma = 5 \times 10^6\,\text{S·m—1}$, to be compared with the usual value $\sigma = 3.29 \times 10^6\,\text{S·m—1}$. This might be explained by the fact that the lower conductivity is, the lower the time constant corresponding to the decay of eddy currents in the sample. Consequently, it becomes difficult to make a distinction between the signal characterising the decay and other fast transient signals, such as the switch closing, or despite the experimental precautions taken, the primary transient. For future prospects, it could be worthwhile to increase R_1, and to change for a faster switch, to recover an acceptable accuracy for low σ values. The influence of oxidation is also an outlook of the present thesis work.

References

Bibliography

[1] Sintef website. Stratified flow photograph. Technical report, Sintef, 2013.

[2] R. Zenit research group website. Bubble flow photograph. Technical report, Universidad Nacional Autónoma de México, 2015.

[3] B. Lehnert. An instability of laminar flow of mercury caused by an external magnetic field. *P. Roy. Soc. Lond. A. Mat.*, 233:299–302, 1955.

[4] R. Moreau. *Magnetohydrodynamics*, chapter 1, 4, 5, pages 1–31, 110–150, 179–189. Kluwer academic publishers, Dordrecht, 1990.

[5] C. Zhang, V. Shatrov, J. Priede, S. Eckert, and G. Gerbeth. Intermittent behavior caused by surface oxidation in a liquid metal flow driven by a rotating magnetic field. *Metall. Mater. Trans. B*, 42:1188–1200, 2011.

[6] J. Etay and Y. Fautrelle. Contrôle électromagnétique des interfaces libres. *Tech. Sci. Ing.*, MB1, RE41:1–11, 2005.

[7] J. Zhang and M-J. Ni. Direct simulation of single bubble motion under vertical magnetic field: Paths and wakes. *Phys. Fluids*, 26:102102–1 – 102102–24, 2014.

[8] Advanced Reactors Information System. Depiction of the MSFR system. Technical report, IAEA, 2015.

[9] B. Roger, X. Deschanels, F. Lemort, R. Piccinato, Y. Fautrelle, J. Etay, D. Perrier, and R. Ernst. Dispositif électromagnétique de fusion et d'agitation interfaciale de systèmes diphasiques, notamment pour l'accélération de processus métallurgiques ou pyrochimiques. Patent number: FR2840821, 2003.

[10] ITER website. Technical description of the ITER machine. Technical report, ITER, 2015.

[11] S. Smolentsev, N. B. Morley, M. A. Abdou, and S. Malang. Dual-Coolant Lead-Lithium (DCLL) blanket status and R&D needs. *Fusion Eng. Des.*, Article in press:1–11, 2015.

[12] Plasma diagnostic group website. View of the ITER reactor. Technical report, UC Davis, 2015.

[13] Y. Poitevin. ITER TBM. Technical report, Fusion for energy, 2013.

[14] J. D. Bender and M. A. Hoffman. A two-phase flow cooling concept for fusion reactor blankets. Technical report, LLNL Report UCRL-78892, 1977.

[15] F-C. Li, T. Kunugi, and A. Serizawa. MHD effect on flow structures and heat transfer characteristics of liquid metal-gas annular flow in a vertical pipe. *Int. J. Heat Mass. Tran.*, 48:2571–2581, 2005.

[16] D. Delage and R. Ernst. Modélisation électrique d'un système de fusion par induction en creuset froid destiné à l'élaboration de matériaux de haute pureté. *Rev. Gen. Elec.*, 4:266–272, 1983.

[17] J. Hartmann. Hg-Dynamics I. Theory of the laminar flow of an electrically conductive liquid in a homogeneous magnetic field. *Det. Kgl. Danske Vid. Sels. Mat.-Fys. Medd.*, 15(6):1–27, 1937.

[18] J. Hartmann and F. Lazarus. Hg-Dynamics II. Experimental investigations on the flow of mercury in a homogeneous magnetic field. *Det. Kgl. Danske Vid. Sels. Mat.-Fys. Medd.*, 15(7):1–45, 1937.

[19] G. Batchelor. *An introduction to fluid dynamics*, chapter 3,5, pages 148–151, 367–370. Cambridge University Press, Cambridge, 1967.

[20] D. A. Edwards, H. Brenner, and D. T. Wasan. *Interfacial Transport Processes and Rheology*, chapter 1-14, pages 1–367. Butterworth Heinemann, Stoneham, 1991.

[21] L. E. Scriven. Dynamics of a fluid interface. *Chem. Eng. Sci.*, 12:98–108, 1960.

[22] J. Hadamard. Mouvement permanent lent d'une sphère liquide et visqueuse dans un liquide visqueux. *Comp. Rend. Acad. Sci. (Paris)*, 152:1735–1738, 1911.

[23] W. Rybczynski. Über die fortschreitende Bewegung einer flüssigen Kugel in einem zähen Medium. *Bull. Int. Acad. Sci. (Cracovice)*, Ser. A, 1:40–46, 1911.

[24] G. G. Stokes. On the effect of the internal friction of fluids on the motion of a pendulum. *Trans. Cambr. Phil. Soc.*, 9:8–27, 1851.

[25] R. Clift, J. R. Grace, and M. E. Weber. *Bubbles, drops, and particles*, chapter 2,3, pages 16–68. Academic Press, Inc., New-York, 1978.

[26] J. Boussinesq. Vitesse de la chute lente, devenue uniforme, d'une goutte liquide sphérique, dans un fluide visqueux de poids spécifique moindre. *Comp. Rend. Acad. Sci. (Paris)*, 156:1124–1130, 1913.

[27] A. Frumkin and V. G. Levich. On surfactants and interfacial motion. *Zh. Fiz. Khim.*, 21:1183–1204, 1947.

[28] Y. Plevachuk, V. Sklyarchuk, S. Eckert, G. Gerbeth, and R. Novakovic. Thermophysical properties of the liquid Ga-In-Sn eutectic Alloy. *J. Chem. Eng. Data*, 59:757–763, 2014.

[29] T. Liu, P. Sen, and C-J. Kim. Characterization of Nontoxic Liquid-Metal Alloy Galinstan for Applications in Microdevices. *J. Microelectromech. S.*, 21:443–450, 2012.

[30] R. P. Woodward. Surface tension measurement using the drop shape method. Technical report, FTA, 2015.

[31] R. J. Mannheimer and R. S. Schechter. An improved apparatus and analysis for surface rheological measurements. *J. Colloid Interf. Sci.*, 32:195–211, 1970.

[32] J. M. Lopez and A. H. Hirsa. Direct determination of the dependence of the surface shear and dilatational viscosities on the thermodynamic state of the interface: theoretical foundations. *J. Colloid Interf. Sci.*, 206:231–239, 1998.

[33] J. A. Shercliff. Steady motion of conducting fluids in pipes under transverse magnetic fields. *J. Fluid Mech.*, 49:136–144, 1953.

[34] S. Y. Molokov and J. E. Allen. On the theory of the Heiser and Shercliff experiment. I: MHD flow in an open channel in a strong uniform magnetic field. *J. Phys. D: Appl. Phys*, 25:393–400, 1992.

[35] J. C. R. Hunt and K. Stewartson. Magnetohydrodynamic flows in rectangular ducts. II. *J. Fluid Mech.*, 23:563–581, 1965.

[36] P. Tabeling and J-P. Chabrerie. Magnetohydrodynamic secondary flows at high Hartmann numbers. *J. Fluid Mech.*, 103:225–239, 1981.

[37] V. Kolevzon and G. Gerbeth. Light-scattering spectroscopy of a liquid gallium surface. *J. Phys. D: Appl. Phys.*, 29:2071–2082, 1996.

[38] V. Kolevzon, G. Gerbeth, and G. Podzniakov. Light-scattering study of the mercury liquid-vapor interface. *Phys. Rev. E*, 55:3134–3142, 1997.

[39] M. D. Dickey, R. C. Chiechi, R. J. Larsen, E. A. Weiss, D. A. Weitz, and G. M. Whitesides. Eutectic Gallium-Indium (EGaIn): a liquid metal alloy for the formaiton of stable structures in microchannels at room temperature. *Adv. Funct. Mater.*, 18:1097–1104, 2008.

[40] R. J. Larsen, M. D. Dickey, G. M. Whitesides, and D. A. Weitz. Viscoelastic properties of oxide-coated liquid metals. *J. Rheol.*, 53:1305–1326, 2009.

[41] K. Doudrick, S. Liu, E. M. Mutunga, K. L. Klein, V. Damle, K. K. Varanasi, and K. Rykaczewski. Different Shades of Oxide: From Nanoscale Wetting Mechanisms to Contact Printing of Gallium-Based Liquid Metals. *Langmuir*, 30:6867–6877, 2014.

[42] R. Moreau, Y. Bréchet, and L. Maniguet. Eurofer corrosion by the flow of the eutectic alloy Pb-Li in the presence of a strong magnetic field. *Fusion Eng. Des.*, 86:106–120, 2011.

[43] Geratherm. Safety Data Sheet acc, to Guideline 93/112/EC. Technical report, Geratherm Medical AG, 2004.

[44] T. Alboussière, P. Cardin, F. Debray, P. La Rizza, J-P. Masson, F. Plunian, A. Ribeiro, and D. Schmitt. Experimental evidence of Alfven wave propagation in a gallium alloy. *Phys. Fluids*, 23:096601, 2011.

[45] N. Terzija, W. Yin, G. Gerbeth, F. Stefani, K. Timmel, T. Wondrak, and A. Peyton. Electromagnetic inspection of a two-phase flow of GaInSn and argon. *Flow Meas. Instrum.*, 22:10–16, 2010.

[46] C. Zhang, S. Eckert, and G. Gerbeth. Experimental study of single bubble motion in a liquid metal column exposed to a DC magnetic field. *Int. J. Multiphas. Flow*, 31:824–842, 2005.

[47] K. Timmel, S. Eckert, G. Gerbeth, F. Stefani., and T. Wondrak. Experimental modelling of the continous casting process of steel using low melting point metal alloys - the LIMMCAST Programm . *ISIJ. Int*, 50:1134–1141, 2010.

[48] J.-U. Mohring and A. Pothérat. Stability of a liquid metal free surface in an annulus affected by an alternating magnetic field. In *The 6th International pamir conference on fundamental and applied MHD, Aluminium reduction cells*, 2005.

[49] N. B. Morley, J. Burris, L. C. Cadwallader, and M. D. Nornberg. GaInSn usage in the research laboratory. *Rev. Sci. Instrum..*, 79:056107–1 – 056107–3, 2008.

[50] Les Echos website. Matières premières. Technical report, Groupe Les Echos, 2015.

[51] M. D. Dickey. Emerging applications of liquid metals featuring surface oxides. *ACS Appl. Mater. Interfaces*, 6:18369–18379, 2014.

[52] M. J. Regan, H. Tostmann, P. S. Pershan, O. M. Magnussen, E. DiMasi, B. M. Ocko, and M. Deutsch. X-ray study of the oxidation of liquid-gallium surfaces. *Phys. Rev. B*, 55:10786–10790, 1997.

[53] Q. Xu, N. Oudalov, Q. Guo, H. M. Jaeger, and E. Brown. Effect of oxidation on the mechanical properties of liquid gallium and eutectic gallium-indium. *Phys. Fluids*, 24:063101, 2012.

[54] J. A. Shercliff. *A textbook of magnetohydrodynamics*, chapter 2, pages 9–30. Pergamon Press Ltd, 1965.

[55] J. C. R. Hunt and G. S. S. Ludford. Three-dimensional MHD duct flows with strong transverse magnetic field. Part 1. Obstacles in a constant area channel. *J. Fluid Mech.*, 33:693–714, 1968.

[56] J. A. Shercliff. The flow of conducting fluids in circular pipes under transverse magnetic fields. *J. Fluid Mech.*, 1:644–666, 1956.

[57] B. Mück, C. Günther, U. Müller, and L. Bühler. Three-dimensional MHD flows in rectangular ducts with internal obstacles. *J. Fluid Mech.*, 418:265–295, 2000.

[58] V. Dousset. *Numerical simulations of MHD flows past obstacles in a duct under externally applied magnetic field*. PhD thesis, Coventry University, 2009.

[59] Comsol Support. Comsol 4.2 Documentation. Technical report, Comsol Inc., 2012.

[60] M. Fleischer and H. Meixner. Gallium oxide thin films: a new material for high-temperature oxygen sensors. *Sensor. Actuator. B-Chem.*, 4:437–441, 1991.

[61] A. M. Albano and D. Bedeaux. Non-equilibrium electro-thermodynamics of polarizable multicomponent fluids with an interface. *Physica A*, 147:407–435, 1987.

[62] C. Picard. *Ondes capillaires à une interface fluide fonctionnalisée: détection micromécanique de brins d'ADN*. PhD thesis, Institut National Polytechnique de Grenoble - INPG, 2007.

[63] I. Benjamin. Molecular dynamics of liquid surfaces and interfaces. In *Solvent Extraction for the 21st century*, 2001.

[64] J. C. Slattery, L. Sagis, and E. Oh. *Interfacial transport phenomena*, chapter 1, 4, B, pages 22, 360, 712. New York: Springer-Verlag, 2007.

[65] I. B. Ivanov, K. D. Danov, K. P. Ananthapadmanbhan, and A. Lips. Interfacial rheology of adsorbed layers with surface reaction: On the origin of the dilatational surface viscosity. *Adv. Colloid. Interfac.*, 114-115:61–92, 2005.

[66] R. Aris. *Vectors, Tensors and the basic equations of Fluid Mechanics*. Prentice-Hall, Englewood Cliffs, NJ, 1962.

[67] W. D. Harkins and J. Robert. Viscosity of monomolecular films. *Nature*, 140:465, 1937.

[68] A. H. Hirsa, J. M. Lopez, and R. Miraghaie. Determination of surface shear viscosity via deep-channel flow with inertia. *J. Fluid Mech.*, 470:135–149, 2002.

[69] J. M. Lopez, R. Miraghaie, and A. H. Hirsa. Non-newtonian behavior of an insoluble monolayer: effects of inertia. *J. Colloid Interf. Sci.*, 248:103–110, 2002.

[70] L. Drazek, J-F. Legrand, and L. Davoust. A first attempt to enhance the 2-D single-crystal growth of a protein at an air/water interface from hydrodynamics. *J. Cryst. Growth*, 275:e1467–e1472, 2005.

[71] L. Davoust, Y-L. Huang, and S-H. Chang. Flow-induced melting of condensed domains within a dispersed Langmuir film. *Phys. Fluids*, 20:082105, 2008.

[72] L. Davoust, Y-L. Huang, and S-H. Chang. Shearing of a stratified layer of amphiphilic (bio)molecules. *Surf. Sci.*, 603:2777–2788, 2009.

[73] L. Davoust, J-L. Achard, and L. Drazek. Low-to-moderate Reynolds number swirling flow in an annular channel with a rotating end wall. *Phys. Rev. E*, 91:023019–1 – 023019–17, 2015.

[74] A. H. Hirsa, J. M. Lopez, and R. Miraghaie. Measurement and computation of hydrodynamic coupling at an air/water interface with an insoluble monolayer. *J. Fluid Mech.*, 443:271–292, September 2001.

[75] E. Serre, E. Crespo del Arco, and P. Bontoux. Annular and spiral patterns in flows between rotating and stationary discs. *J. Fluid Mech.*, 434:65–100, 2001.

[76] B. Launder, S. Poncet, and E. Serre. Laminar, transitional and turbulent flows in rotor-stator cavities. *Ann. Rev. Fluid. Mech*, 42:229–248, 2010.

[77] J. Delacroix and L. Davoust. Electrical activity of the Hartmann layers relative to surface viscous shearing in an annular magnetohydrodynamic flow. *Phys. Fluids*, 26:037102–1 – 037102–21, 2014.

[78] A. H. Nayfeh. *Perturbation methods*, chapter 1,3,4, pages 1–19,56–154. Wiley-Intersciences, New York, 1973.

[79] M. Van Dyke. *Perturbation methods in fluid mechanics*, chapter 5. Wiley-Intersciences, New York, 1975.

[80] L. Pamela Cook, G. S. S. Ludford, and J. S. Walker. Corner regions in the asymptotic solution of $\epsilon\nabla^2 u = \frac{\partial u}{\partial y}$ with reference to MHD duct flow. In *Proc. Camb. Phil. Soc.*, volume 72, pages 117–122. Cambridge University Press, Cambridge, 1972.

[81] J. C. R. Hunt and W. E. Williams. Some electrically-driven flows in magnetohydrodynamics. Part 1. Theory. *J. Fluid Mech.*, 31:705–722, 1968.

[82] I. Stakgold. *Boundary value problems of mathematical physics*, volume 1, chapter 1, pages 64–78. SIAM, Philadelphia, 2000.

[83] A. J. Pintar. *The measurement of surface viscosity*. PhD thesis, Illinois Institute of Technology, 1968.

[84] MUMPS Support. MUltifrontal Massively Parallel Solver (MUMPS 4.10.0) User's guide. Technical report, ENS-Lyon and ENSEEIHT, 2011.

[85] J. Delacroix and L. Davoust. On the role of surface rheology in a magnetohydrodynamic swirling flow. *Phys. Fluids*, 27:062104–1 –062104–22, 2015.

[86] G. Vitter. *Jauges électrochimiques à oxygène pour contrôles industriels*. PhD thesis, INPG, 1980.

[87] I. F. Sbalzarini and P. Koumoutsakos. Feature point tracking and trajectory analysis for video imaging in cell biology. *J. Struct. Biol.*, 151:182–195, 2005.

[88] D. J. Brown and R. F. Tefft. The densities, equivalent conductances and relative viscosities at 25 °C, of solution of hydrochloric acid, potassium chloride and sodium chloride, and of their binary and ternary mixtures of constant chloride-ion-constituent content. *J. Am. Chem. Soc.*, 48:1119–1128, 1926.

[89] J. W. Haverkort and T. W. J. Peeters. Magnetohydrodynamics of insulating spheres. *Magnetohydrodynamics*, 45:111–126, 2009.

[90] LnCMI website. LnCMI hybrid magnet. Technical report, LnCMI, 2015.

[91] J. Happel and H. Brenner. *Low Reynolds number hydrodynamics with special applications to particulate media*, chapter 4, pages 111–113, 145–149. Martinus Nijhoff Publishers, The Hague, 1983.

[92] A. B. Basset. *A Treatise on Hydrodynamics: Vol. 2*, chapter 20, page 248. New York: Dover, 1961.

[93] T. A. Johnson and V. C. Patel. Flow past a sphere up to a Reynolds number of 300. *J. Fluid Mech.*, 378:19–70, 1999.

[94] S. Taneda. Experimental investigation of the wake behind a sphere at low Reynolds numbers. *J. Phys. Soc. Jpn.*, 11:1104–1108, 1956.

[95] R. M. Wham, O. A. Basaran, and C. H. Byers. Wall effects on flow past solid spheres at finite Reynolds number. *Ind. Eng. Chem. Res.*, 35:864–874, 1996.

[96] A. Maheshwari, R. P. Chhabra, and G. Biswas. Effect of blockage on drag and heat transfer from a single sphere an an in-line array of three spheres. *Powder Technol.*, 168:74–83, 2006.

[97] J. T. Schalbe, F. R. Phelan, P. M. Vlahovska, and S. D. Hudson. Interfacial effects on droplet dynamics in Poiseuille flow. *Soft Matter*, 7:7797–7804, 2011.

[98] R. B. Fdhila and P. C. Duineveld. The effect of surfactants on the rise of a spherical bubble at high reynolds and peclet numbers. *Phys. Fluids*, 8:310–321, 1996.

[99] X. Miao, D. Lucas, Z. Ren, S. Eckert, and G. Gerbeth. Numerical modeling of bubble-driven liquid metal flows with external static magnetic field. *Int. J. Multiphas. Flow*, 48:32–45, 2013.

[100] T. V. S. Sekhar, T. V. R. Ravikumar, and H. Kumar. MHD flow past a sphere at low and moderate Reynolds numbers. *Comput. Mech.*, 31:437–444, 2003.

[101] J. C. R. Hunt. Bluff body drag in a strong transverse magnetic field. *Magneto-hydrodynamics*, 6:35–38, 1970.

[102] K. Gotoh. Stokes flow of an electrically conducting fluid in a uniform magnetic field. *J. Phys. Soc. Jpn*, 15:696–705, 1960.

[103] J. Reitz and L. Foldy. The force on a sphere moving through a conducting fluid in the presence of a magnetic field. *J. Fluid Mech.*, 11:133–142, 1961.

[104] O. Wildlund. Wall functions for numerical modeling of laminar MHD flows. *Eur. J. Mech. B-Fluid*, 22:221–237, 2003.

[105] K. Takatani. Mathematical modeling of incompressible MHD flows with free surface. *ISIJ International*, 4:545–551, 2007.

[106] J. W. Haverkort and T. W. J. Peeters. Magnetohydrodynamic effects on insulating bubbles and inclusions in the continuous casting of steel. *Metall. Mater. Trans. B*, 41:1240–1246, 2010.

[107] G. Branover, N. Slyusarev, and A. Tsinober. Drag of a sphere in a magnetohydrodynamic flow. *Magnetohydrodynamics*, 2:149–150, 1966.

[108] M. Bertherat, T. Odievre, M. Allibert, and P. Le Brun. A radioscopic technique to observe bubbles in liquid aluminium. *Light Met.*, 3:861–867, 2002.

[109] A. Reusken and Y. Zhang. Numerical simulation of incompressible two-phase flows with a Boussinesq-Scriven interface stress tensor. *Int. J. Numer. Meth. Fluids*, 73:1042–1058, 2013.

[110] C. P. Bean, R. W. DeBlois, and L. B. Nesbitt. Eddy-current method for measuring the resistivity of metals. *J. Appl. Phys*, 30:1976–1980, 1959.

[111] G. Fleury and M-E. Davoust. Model selection for inductive conductivity measurement. *AIP Conf. Proc.*, 557:1413–1420, 2001.

[112] A. B. Kos and F. R. Fickett. Improved Eddy-current decay method for resistivity characterization. *IEEE. T. Magn.*, 30:4560–4562, 1994.

[113] J-L Bretonnet. Conductivité électrique des métaux liquides. *Tech. Sci. Ing.*, M69:1–8, 2005.

[114] B. Wwedensky. Über die Wirbelströme bei der spotanen Änderung der Magnetisierung. *Ann. Phys.*, 369:609–620, 1921.

[115] A. Gray and G. B. Mathews. *A treatise on Bessel functions and their applications to physics*, chapter 6, pages 51–58. Macmillan & Co, London, 1895.

[116] E. Rostan. Mesure de la conductivité électrique d'un métal liquide. Master's thesis, Grenoble-INP ENSE3, 2015.

Publications and conferences

Peer-reviewed journals

J. Delacroix and L. Davoust. *Electrical conductivity of the Hartmann layers relative to surface viscous shearing in an annular magnetohydrodynamic flow.* Physics of Fluids, 26: 037102, 2014.

Abstract: As a first step towards two-phase magnetohydrodynamics (MHD), this paper addresses an original analytical coupling between surface rheology, *e.g.* a gradually oxidizing liquid metal surface, ruled by the Boussinesq number B_o, and a supporting annular MHD flow, ruled by the Hartmann number H_a, in the general layout of a classical annular deep-channel viscometer, as developed by Mannheimer *et al.*, in *J. Colloid Interface Sci.*, 32:195–211, 1970. Using a matched asymptotic expansion based on the small parameter $1/H_a$, we can express the surface velocity as a coupling variable in the jump momentum balance (JMB) at the liquid surface. By solving the latter through the determination of the Green's function, the whole flow can be analytically calculated. A modified Boussinesq number, $\tilde{B_o}$, is produced as a new non-dimensional parameter that provides the balance between surface viscous shearing and the Lorentz force. It is shown that the $\tilde{B_o}$ number drives the electrical activation of the Hartmann layers, heavily modifying the MHD flow topology and leading to the emergence of the Lorentz force, for which interaction with the flow is not classical. Finally, the evolution laws given in this study allow the determination of scaling laws for an original experimental protocol, which would make it possible to accurately determine the surface shear viscosity of a liquid metal with respect to the quality of the ambient atmosphere.

J. Delacroix and L. Davoust. *Impact of surface viscosity upon an annular magnetohydrodynamic flow.* Magnetohydrodynamics, 51: 195-202, 2015.

Abstract: Using a matched asymptotic expansion based on the small parameter $1/Ha$, this paper addresses an original analytical coupling between surface rheology of *e.g.* a gradually oxidizing liquid metal surface, and a supporting annular MHD flow. It is shown that the level of surface viscosity drives the electrical activation of the Hartmann layers, heavily modifying MHD flow topology and leading to the emergence of a Lorentz force, for which interaction with the flow is not classical. These analytical results are compared to a 2-D numerical study, highlighting a fair agreement as soon as $Ha \geq 10$.

J. Delacroix and L. Davoust. ***On the role of surface viscosity in a magnetohydrodynamic swirling flow.*** **Phys. Fluids, 27: 062104, 2015.**

Abstract: The original coupling between the surface rheology of a liquid metal surface and a supporting annular Couette magnetohydrodynamic (MHD) flow is theoretically and numerically investigated in this paper, in the general layout of the classical annular viscometer, as developed by Mannheimer *et al.* [*J. Colloid Interface Sci.*, 32:195–211, 1970]. The purely hydrodynamic interplay between the main azimuthal flow (induced by a rotating floor) and the secondary overturning flow (generated by centrifugation) is found to be strongly affected by both surface viscous shear and surface viscous dilatation. When the flow is subjected to an outer vertical magnetic field, the impact of varying interface boundary conditions (through the surface shear and dilatational viscosities) at the gas/liquid interface profoundly alters the MHD flow topology. Particularly, when centrifugation competes with electromagnetic effects, advection of the main flow by the secondary flow is proved to affect significantly the core MHD flow, leading to a variety of atypical MHD flow patterns.

J. Delacroix and L. Davoust. ***Surface viscometry in a uniform magnetic field.*** **Mechanics and Industry, submitted, 2nd review.**

Abstract: This paper addresses an original numerical coupling between surface mechanics of a gradually oxidizing liquid metal surface, and a supporting annular MHD flow, in the general layout of the classical annular viscometer, originally developed by Mannheimer *et al.* [*J. Colloid Interface Sci.*, 32:195–211, 1970]. A purely hydrodynamic interplay between a main azimuthal flow (induced by a rotating floor) and a secondary overturning flow generated by centrifugation is found to be strongly affected by both surface viscous shear and surface viscous dilatation. When centrifugation competes with electromagnetic effects, advection of the main flow by the secondary flow is proved to affect significantly the core MHD flow, leading to original MHD flow patterns. The latter phenomenology reveals to be relevant to characterise the surface viscosities of a gradually oxidising liquid metal surface.

Peer-reviewed conferences

- 9th PAMIR International Conference on fundamental and applied MHD, Riga, Latvia, June 16-20,2014. One oral presentation.
- 10th European Fluid Mechanics Conference, Copenhagen, Denmark, September 14-18, 2014. One oral presentation.
- Congrès français de mécanique (CFM) 2015, Lyon, France, August 24-28,2015. One oral presentation.

On the role of surface rheology in a two-phase MHD flow.

Abstract: In this thesis work, a first approach towards the description of magnetohydrodynamic (MHD) multiphase flows is proposed, based on the investigation of the role of surface rheology in permanent regime. The study of the coupling between bulk MHD and surface rheology is particularly motivated by the development of an annular surface viscometer devoted to liquid metals topped with an oxidation layer. First, theoretical foundations of MHD and of surface rheology are separately introduced. The modelling brings out a strong coupling between bulk and surface velocities, the latter being dependent on two interfacial parameters: the surface shear and dilatational viscosities. Their respective influence is analytically and numerically investigated in the case of a permanent annular (stratified) MHD end-driven flow. In the considered geometry, a vertical (uniform) magnetic field is imposed, perpendicular to the gradually oxidising liquid surface. The contribution of planar surface viscous stresses to the possible electrical activation of Hartmann layers is demonstrated, leading to a variety of atypical MHD flow patterns. The annular MHD viscometer is then developed as a first device able to perform selective measurement of the surface viscosities of electroconductive fluids. First experiments lead to an estimated value of the surface shear viscosity for a liquid alloy (GaInSn) at room temperature. Some hints are finally given to investigate the study case of a MHD flow past a rigid fluid sphere, with varying interfacial conditions governed by surface rheology, as an additional work constituting a first step towards the description of dispersed MHD flows.

Keywords: magnetohydrodynamics, surface rheology, multiphase flows, Hartmann layers, surface viscosities, liquid metal.

Rôle de la rhéologie de surface dans un écoulement diphasique MHD.

Résumé: Dans les travaux de recherche développés durant cette thèse, une première approche des écoulements magnétohydrodynamiques (MHD) multiphasiques est proposée. Cette approche se concentre sur les phénomènes liés à l'interaction entre une dynamique interfaciale et un écoulement de cœur MHD. Le couplage induit entre rhéologie de surface et MHD de sous-phase est particulièrement illustré par le développement d'un viscosimètre annulaire surfacique, dédié à l'étude des métaux liquides progressivement oxydés. En premier lieu sont introduits les éléments théoriques propres à la MHD et à la rhéologie de surface. La modélisation de leur couplage fait intervenir deux paramètres interfaciaux : les viscosités surfaciques dilatationnelle et de cisaillement. L'influence respective de ces deux paramètres sur l'écoulement MHD de sous-phase est étudiée analytiquement et numériquement dans le cas d'un écoulement (stratifié) annulaire MHD permanent. Dans la configuration retenue, un champ magnétique uniforme vertical est imposé, perpendiculairement à la surface liquide graduellement oxydée. Le rôle décisif des contraintes visqueuses interfaciales concernant l'(in)activation des couches de Hartmann est démontré, conduisant à des topologies atypiques d'écoulement MHD. Le viscosimètre annulaire MHD est ensuite proposé en tant que méthode expérimentale originale, permettant la mesure sélective des viscosités surfaciques de fluides électroconducteurs. Les premières campagnes expérimentales aboutissent à une estimation de la viscosité de cisaillement interfacial d'un alliage métallique (GaInSn) liquide à température ambiante. Finalement, une ouverture sur l'écoulement MHD à proximité d'une inclusion gazeuse sphérique rigide est discutée en annexe de ce projet, en lien avec des conditions mécaniques variables à l'interface liquide/gaz pilotées par la rhéologie de surface, constituant une première approche vers la description des écoulements MHD dispersés.

Mots-clés: magnétohydrodynamique, rhéologie de surface, écoulement multiphasique, couches de Hartmann, viscosités de surface, métal liquide.